

**Resolved stellar populations of dwarf galaxies
in the Centaurus A/M83 group**



Denija Crnojević

Dissertation
submitted to the
Combined Faculties of the Natural Sciences and Mathematics
of the Ruperto-Carola-University of Heidelberg, Germany
for the degree of
Doctor of Natural Sciences

Put forward by
Denija Crnojević
born in: Šibenik, Croatia
Oral examination: 10th December, 2010

Resolved stellar populations of dwarf galaxies
in the Centaurus A/M83 group

Referees: Prof. Dr. E. K. Grebel
Prof. Dr. H.-W. Rix

Abstract

Dwarf galaxies, fundamental ingredients of galactic structures in our Universe, are ubiquitous and surprisingly heterogeneous systems. The study of such objects in nearby groups is a powerful way of investigating their formation and evolutionary mechanisms. The Centaurus A/M83 group is denser and in a more advanced evolutionary phase than our own Local Group, thus being an appealing target for the study of dwarf galaxies. Its more than 50 dwarf members, with different morphologies and stellar contents, can still be resolved into individual stars (at an average Galactocentric distance of ~ 4 Mpc).

We use optical (HST/ACS) and near-infrared (VLT/ISAAC) photometric data to derive physical properties and evolutionary histories for sixteen dwarfs in this group. Specifically, the predominantly old populations of our target early-type dwarfs show metallicity contents that resemble what is found for Local Group members. However, they intriguingly contain lower intermediate-age population fractions than those found in morphologically similar dwarfs around the Milky Way, thus being more comparable to the M31 companions. We also apply our analysis techniques to the deeper photometric data available for M31 early-type dwarfs. The star formation histories derived for our star-forming late-type dwarf targets reveal that the star formation is quenched for galaxies currently found in the densest group regions. The time-dependent spatial distribution of their stellar populations points toward a stochastic star formation mode in these objects.

Our results show that the evolution of dwarf galaxies depends on their mass but that it is, at the same time, heavily influenced by the surrounding environment. The Centaurus A/M83 group, along with other nearby galaxy groups, deserves further attention in order for us to ultimately gain deeper insights into the processes that regulate the evolution of dwarf galaxies.

Zusammenfassung

Zwerggalaxien sind die fundamentalen Bestandteile galaktischer Strukturen in unserem Universum und sind allgegenwärtige und erstaunlich verschiedenartige Systeme. Das Studium dieser Objekte in benachbarten Galaxiengruppen ist eine leistungsfähige Methode, um deren Bildungs- und Evolutionsmechanismen zu erforschen. Die Centaurus A/M83 Gruppe ist im Vergleich zu unserer Lokalen Gruppe dichter und befindet sich in einem fortgeschritteneren Entwicklungsstadium. Deshalb ist sie ein attraktiver Ort um Zwerggalaxien zu untersuchen. Ihre mehr als 50 zugehörigen Zwerggalaxien besitzen verschiedene Morphologien und Sternpopulationen und einzelne Sterne können noch aufgelöst werden (die mittlere galaktozentrische Entfernung der Gruppe ist ~ 4 Mpc).

Wir benutzen optische (HST/ACS) und nah-infrarote (VLT/ISAAC) photometrische Daten um die physikalischen Eigenschaften und die Entwicklungsgeschichte von sechzehn Zwerggalaxien in dieser Gruppe herzuleiten. Die vorwiegend alte Population der frühen Zwerge zeigt einen Metallgehalt ähnlich desjenigen der Zwerge der Lokalen Gruppe. Ihr Anteil an mittel-alten Populationen ist jedoch niedriger als derjenige in morphologisch ähnlichen Zwerggalaxien in Milchstraßennähe, und sind eher mit M31 Begleitern vergleichbar. Wir wenden unser Verfahren auch auf tiefere photometrische Daten von frühen M31 Begleitern an. Die Sternentstehungsgeschichte unserer aktiv Sterne bildenden späten Zwerge zeigt auf, dass die Sternentstehung für Galaxien in den dichtesten Regionen der Gruppe gedämpft ist. Die zeit-abhängige räumliche Verteilung ihrer Sternpopulationen weist auf einen stochastischen Sternentstehungsmodus dieser Objekte hin.

Unsere Ergebnisse zeigen, dass die Entwicklung von Zwerggalaxien abhängig ist von ihren Massen, sie wird aber auch von ihren Umgebungen stark beeinflusst. Die Centaurus A/M83 Gruppe, wie auch andere benachbarte Gruppen, benötigt weitere Aufmerksamkeit damit tiefere Einblicke in die Prozesse gewonnen werden können, welche die Entwicklung von Zwerggalaxien bestimmt.

*Alla mia famiglia e a Stefano:
per avermi sempre, pazientemente tenuta per mano.*

Contents

1	Introduction	1
1.1	Why go for the dwarfs?	1
1.2	Resolved stellar populations	3
1.3	The Local Group	8
1.4	Nearby groups of galaxies	15
1.4.1	The Centaurus A/M83 group of galaxies	16
1.5	Motivation for this Thesis	18
2	Data analysis	19
2.1	Optical data	20
2.1.1	Photometry	21
2.1.2	Artificial star tests	26
2.1.3	Optical color-magnitude diagrams	27
2.1.3.1	Galactic foreground contamination	27
2.1.3.2	Early-type dwarfs	29
2.1.3.3	Late-type dwarfs	31
2.2	NIR data	34
2.2.1	Photometry	35
2.2.2	Artificial star tests	36
2.2.3	Near-infrared color-magnitude diagrams	37
3	Early-type dwarfs	43
3.1	Optical data	43
3.1.1	Metallicity distribution functions	43
3.1.2	Possible sources of error	47
3.1.3	Stellar spatial distributions	53
3.1.3.1	Metallicity gradients?	53
3.1.3.2	Population gradients?	56
3.1.4	Discussion	61
3.2	NIR data	65
3.2.1	Combined CMDs	65
3.2.2	Intermediate-age populations	69
3.2.2.1	Variable candidates	70
3.2.2.2	Absolute bolometric magnitudes	70
3.2.2.3	Spatial distribution	73
3.2.3	Discussion	75
4	M31 dwarf spheroidal companions	79
4.1	Color-magnitude diagrams	79
4.2	Metallicity distribution functions and ages	83
4.2.1	And V	86
4.2.2	And III	88
4.2.3	And VI	89
4.2.4	And I	89

4.2.5	And II	90
4.2.6	And VII	91
4.3	Discussion	93
5	Late-type dwarfs	97
5.1	Recent star formation histories	97
5.1.1	The M83 subgroup	99
5.1.2	The CenA subgroup	108
5.2	Spatial distribution of stellar populations as a function of time	115
5.3	Discussion	121
6	Summary and outlook	131
	Bibliography	138
	Acknowledgements	151

“Equipped with his five senses, man explores the universe around him and calls the adventure Science.”

E. P. Hubble, *The Nature of Science*
(1954)

1

Introduction

If the taste of a cake depends primarily on its ingredients, then the study of dwarf galaxies deserves a very careful attention. These objects are indeed believed to be the smallest baryonic counterparts of the dark matter structures in our Universe. Just as cooking ingredients, they like to congregate and form groups, or clusters, together with their more massive counterparts. In particular, the role of the cake in this Thesis is played by groups of galaxies, and as every good cook would do, we will try to catch the secret details of an intriguing recipe.

1.1 Why go for the dwarfs?

The definition of dwarf galaxy is not strict, and is generally based on luminosity and structural parameters. The (somewhat arbitrary) limit for a galaxy to be called dwarf is $M_V \sim -17$ mag (e.g., Grebel 2001), but more than a clear cut we observe a continuum between the properties of stellar clusters, low-mass galaxies, larger spheroidal systems and disks of spirals (e.g., Binggeli 1994; Kormendy et al. 2009). Dwarf galaxies are definitely the most numerous type of galaxy in the Universe, and since the first detailed studies of these smaller counterparts of the well-studied giant galaxies, they have revealed an unexpected amount of intriguing properties. These objects span a considerable range of morphologies, luminosities, metallicities, gas content, kinematic properties, and thus discard the naive idea of being the simplest type of galaxy just as a consequence of their small size.

As already mentioned, dwarf galaxies inhabit the smallest dark matter subhaloes in a Λ CDM (i. e., Cold Dark Matter) cosmology, and appear to be the most dark matter dominated objects in the Universe (see e.g. Wilkinson et al. 2004; Gilmore et al. 2007; Wolf et al. 2010). In the current cosmological paradigm, dark matter structures grow hierarchically, in the sense that the smallest gravitationally bound systems are the first to be born, and successively merge together to form larger objects. In particular, the mass of these dark matter haloes depends on the intrinsic physical properties of their constituent particles. Those characterized as cold dark matter are expected, as seen from cosmological simulations, to become non-relativistic (slow-moving) soon after the Big Bang. In these simulations, however, they form haloes that may be several orders of magnitude less massive than the least luminous observed haloes, and that moreover are much more numerous (see Moore et al. 1999; Klypin et al. 1999). This is also known as the “missing satellite problem”. One among the possible explanations is that a large fraction of such small haloes is actually not hosting visible baryonic matter and thus remains undetectable for us, but on the other hand the physical mechanisms that lead to or truncate gas cooling and subsequent star formation in such low-mass dark matter haloes are still largely



Figure 1.1: *Left panel.* Phoenix, transition-type dwarf galaxy belonging to the Local Group. Its predominantly old population has a rather regular distribution. *Right panel.* NGC 1705, late-type dwarf at a distance of ~ 5.1 Mpc from us. Its actively star forming regions are bright and distributed in clumps (images taken from the web).

uncertain (e.g., Bullock et al. 2000; Kravtsov et al. 2004; Mayer et al. 2007). However, in the last few years an increasing number of extremely low-mass and low-luminosity satellites has been discovered in the vicinity of our Galaxy, the Milky Way (MW), and of its giant neighbor Andromeda (M31) (see e.g. Willman et al. 2005; Belokurov et al. 2006; Zucker et al. 2006a,b, 2007; Martin et al. 2009; Belokurov et al. 2010), which in part alleviates the missing satellite problem. A complementary solution for this discrepancy is given by the observational limits for the detection of these low-mass objects (Koposov et al. 2008; Tollerud et al. 2008; Bullock 2010). The luminosity function of dwarf galaxies can thus provide constraints on cosmological models, and the properties of the dwarfs may help us to understand the formation history of our MW.

We briefly summarize the various flavors that dwarf galaxies can have (see, e.g., Grebel 2001). Early-type dwarfs have a rather regular, elliptical shape, contain predominantly old ($\gtrsim 10$ Gyr) and intermediate-age ($\gtrsim 1$ Gyr) populations, and lack a significant neutral (HI) gas content. This class is further divided into two subclasses. Dwarf spheroidal galaxies have lower surface brightnesses ($\mu \gtrsim 22$ mag arcsec $^{-2}$) and total luminosities than dwarf ellipticals, which show more pronounced central concentrations. The morphological class of dwarf irregulars (or late-type dwarfs) is, on the other hand, named after their optical appearance. Their young populations form in clumpy and scattered bright regions, on top of an old population that is less luminous, and more regularly distributed within the galaxy. Dwarf irregulars do contain large amounts of neutral gas (up to $\sim 10^9 M_{\odot}$) and they usually show the presence of solid-body rotation (see, e.g., Skillman et al. 1988). On the other hand, early-type dwarfs normally are pressure-supported objects, although recent studies have shown the presence of rotation also for some of these objects (e.g., Battaglia et al. 2008; Geha et al. 2010). An additional subclass of this classification is constituted by the transition-type dwarfs, which have intermediate properties between early-type and late-type dwarfs. This type of galaxies is dominated by older populations, but also contains small amounts of neutral gas. It has been suggested that these

galaxies are undergoing a morphological transformation, being born as low-mass irregulars and then slowly turning into spheroidals. This process could be caused by an exhaustion or expulsion of the gas due to star formation, although neither of the two processes would be efficient enough to lead to a complete removal of neutral gas. Alternatively, external forces could act on late-type dwarfs that are falling toward a group or a cluster of galaxies, like for example ram-pressure stripping by an intra-group/intra-cluster medium or tidal stripping by a massive companion (see, e.g., Grcevich & Putman 2009). Although there are shortcomings for each of these mechanisms (see the discussion in Grebel et al. 2003), it is possible that a combination of all of the mentioned processes contributes to the transformation from late-type to early-type dwarf. An example of how different types of dwarfs look like can be seen in Fig. 1.1, where we show a predominantly old transition-type dwarf and a dwarf irregular that hosts several star forming regions.

For the sake of completeness, we mention that additional types of dwarfs are present in our Universe, although we will not concentrate on them in this study. Ultra-faint dwarfs are very faint dwarf spheroidals that, as mentioned before, have just recently revealed their presence within our Local Group through the study of the Sloan Digital Sky Survey (SDSS, e.g. Adelman-McCarthy et al. 2008). These objects (about twenty discovered until now) are very faint (down to $M_V \sim -1.5$) and diffuse (down to $\mu_V \sim 30$ mag arcsec $^{-1}$), which explains why their discovery happened only in the last few years. More of them are awaiting to be found, and there is a major effort in this direction with the design of the latest surveys (e.g., LSST, PAndAS, PanSTARRS, Southern Sky Survey). Finally, blue compact dwarfs (BCDs) and ultra-compact dwarfs (UCDs) are, as suggested by their name, very concentrated and actively star-forming objects.

Given the diversity that dwarf galaxies display, the study of their physical properties results in an appealing task that can lead to a deeper understanding of how galaxies evolve and of the main processes that drive this evolution. Our cook's paradise is undoubtedly, in this case, the Local Group we inhabit. Our closest neighborhood consists of two giant spirals, the MW and M31 with similar masses of the order of $\sim 10^{12}M_\odot$, with M31 being slightly more massive. These giants are surrounded by more than 50 dwarf members, and many more may still await discovery. Several efforts have been made to analyze the physical properties of the dwarf companions of the MW and of M31, ideal targets due to their proximity (the turnover radius of the Local Group is ~ 1.0 Mpc, assuming a spherical potential, Karachentsev et al. 2009). We will briefly summarize the main properties of this delicious sample, but first of all let us get acquainted with the cutlery.

1.2 Resolved stellar populations

As mentioned before, the vicinity of the Local Group dwarfs allows us, together with the use of state-of-the-art instrumentation and the development of sophisticated analysis techniques, to delve deep into the secrets of their evolution. Stars play a fundamental role in the understanding of galactic evolution, since they retain the imprints of evolutionary parameters such as age, metallicity or initial mass function. A simple stellar population is defined as a group of stars where all the stars have the same age and initial chemical composition. They will then evolve differently based on their individual masses. The recipe to make a galaxy however is not that simple, and requires multiple stellar populations, with different ages and possibly different

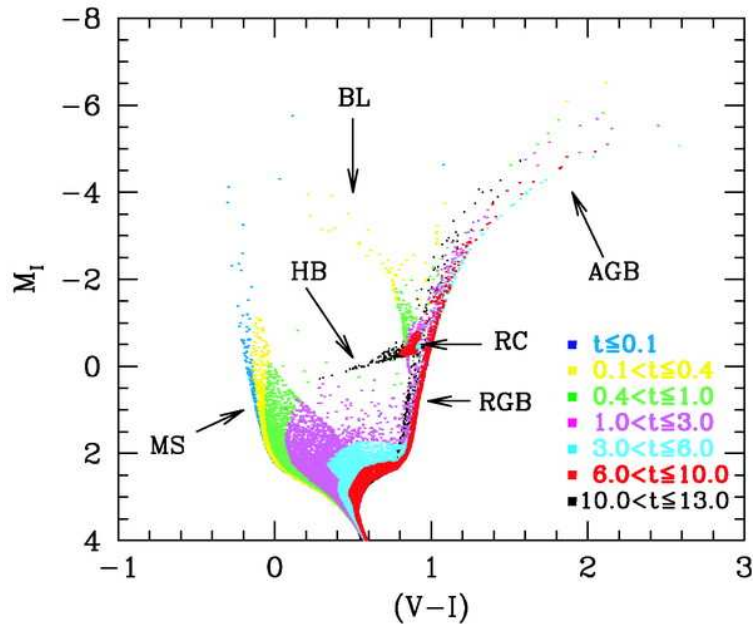


Figure 1.2: Simulated CMD computed assuming a constant star formation rate from 13 Gyr ago until present-day, and with metallicity increasing with time. The main evolutionary stages are labeled (see text for their descriptions), and stars of different ages are color-coded as indicated in the legend. Figure taken from Aparicio & Gallart (2004).

metallicities. After all, a higher complexity level adds on the flavor.

The goal of astronomers is, in this case, to measure and quantify the flux coming from the stellar sources. The measurement of the brightness, or luminosity intensity, of a star in a particular wavelength range is called “photometry” (see also next Chapter). From such measurements at different wavelength ranges we can then infer the temperature and the luminosity of a star, which is often reported as the logarithm of the flux (= magnitude). The relation between luminosity and effective temperature (or spectral type) of a star characterizes its physical properties, as first discovered one century ago by Hertzsprung and Russel by studying Galactic globular clusters (i.e., old stellar associations). These two researchers thus give their names to the theoretical version of this relation, while its observational counterpart is commonly called color-magnitude diagram (CMD). The name stems from the color (i.e., difference between magnitudes in two bands, directly related to the effective temperature of a star) and the magnitude of a stellar object. As a star evolves, it will trace different and specific paths (= evolutionary tracks) in the color-magnitude space, depending on its mass, its chemical composition, and its age (since its luminosity and temperature change with time). By looking at the CMD of a simple stellar population (i.e., stars found at approximately the same distance from the observer) we are thus able to obtain important information about its constituents. An example of a simulated CMD is shown in Fig. 1.2.

The evolutionary stages of a stellar population can be briefly summarized in the following phases (also marked in Fig. 1.2). For a comprehensive description of stellar evolution, see e.g. Salaris & Cassisi (2005). Stars spend most of their lives along the main sequence (MS), where they burn hydrogen in their cores. The amount of time spent in this stage is connected to the mass of a star. For example, stars with masses $\lesssim 1M_{\odot}$ remain on the MS for tens of Gyr, while stars with masses $\gtrsim 20M_{\odot}$ spend only a few Myr in this stage. A star along the

MS is more luminous when its mass is higher, and its position in this evolutionary phase also depends on its chemical composition. A low-mass star evolves toward higher luminosities and higher temperatures as the hydrogen burns in the core, while for stars with masses $\gtrsim 1.5M_{\odot}$ the temperature decreases. When hydrogen is consumed in the stellar core, the evolutionary track of the star on the CMD turns toward lower temperatures (MS turnoff, or MSTO). For stars with masses $\lesssim 1.8 - 2.2M_{\odot}$ (depending on the chemical composition), the evolution goes on toward lower temperatures at an almost constant luminosity. This phase is called sub-giant branch (SGB), during which the stellar envelope expands to counteract the contraction of the inert core. There is a physical limit (Hayashi limit) that stops the star from cooling further, and thus the evolution now proceeds toward higher luminosities, but at an almost constant temperature. The star now starts to burn hydrogen in a shell around the core. This phase is called red giant branch (RGB), during which the star expands and loses mass, and its envelope turns from radiative into convective. In these low-mass objects, the core contracts gravitationally until the helium becomes degenerate, and eventually it gets ignited in an explosive way (the so-called helium-flash). This happens at the tip of the RGB (TRGB), whose luminosity mainly depends on the helium-core mass. Since stars that ignite the helium in a degenerate way have all a similar helium-core mass, the TRGB is widely used as a distance indicator (particularly in *I*-band, where the dependence on metallicity is minimal, see next Chapter). The star subsequently experiences a core expansion and thus an envelope contraction, which make its luminosity fade and the temperature increase. This phase, where helium is burned in the core and hydrogen in a surrounding shell, is the horizontal branch (HB). During the HB phase the stars keep a nearly constant luminosity, but will be found at different positions depending primarily on their metallicity, with metal-poor stars being hotter compared to metal-rich ones. The amount of mass lost during the RGB phase also influences the location of a star along the HB, although this mechanism is still poorly understood. Depending on the initial mass of the star, the time needed to reach the HB will vary. In the case of old objects ($\gtrsim 10$ Gyr and $M \lesssim 0.9 - 1.0M_{\odot}$, depending on the chemical composition), the HB will appear extended toward the blue end of the HB, while for intermediate-age stars ($\sim 1 - 9$ Gyr and $0.9 \lesssim M \lesssim 2.0M_{\odot}$) the core helium-burning phase will mostly concentrate on the red side (also called red clump, RC, overlapping with old and metal-rich stars).

The situation is different for higher mass stars ($M \gtrsim 2.2M_{\odot}$). The helium ignition will in this case not happen in a degenerate core, and the star will spend less time to get to the core helium-burning phase (less than ~ 1 Gyr). As the stellar mass increases, the star will be able to subsequently ignite more and more massive elements in its core, starting from the products of helium (i.e. carbon and oxygen), continuing with neon and silicon, and stopping at iron-peak elements. For a star with $5 \lesssim M \lesssim 20M_{\odot}$, the path along the CMD will be characterized by an evolution toward higher temperatures every time that one of the mentioned elements is ignited in the core. After an element stops burning in the core and before the product of this burning gets ignited, the star evolves back toward lower temperatures. This leads to loops within the CMD that are called blue loops (BL). For stars with masses $\gtrsim 5M_{\odot}$, the evolutionary time after the MS phase is no longer than a few Myr. For masses above $\sim 20M_{\odot}$, the evolution in the core is so fast that the outer envelope does not have time to be significantly affected, and the evolutionary track has an almost constant luminosity.

On the other hand, when low-mass stars cease the core helium-burning, they ignite a helium-burning shell below the hydrogen-burning shell and evolve toward lower temperatures and higher luminosities. During this stage their track follows the RGB sequence, but at slightly

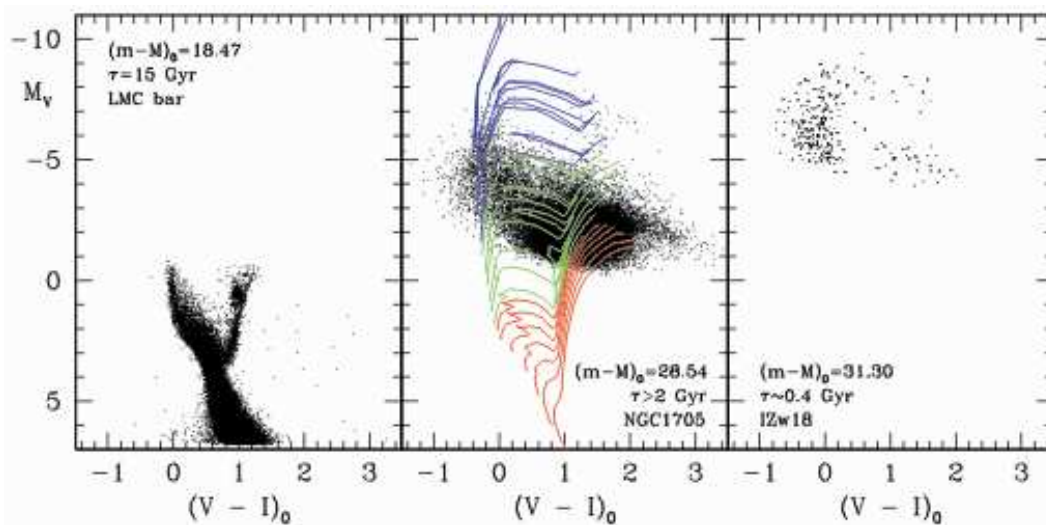


Figure 1.3: CMDs for three late-type dwarf galaxies at different distances (images obtained with the Hubble Space Telescope). Distance modulus and lookback time (i.e., age of the oldest stars resolvable) are reported for each object. The LMC lies at ~ 50 kpc from the MW, NGC 1705 is at ~ 5.1 Mpc, while IZw 18 has a distance of ~ 18 Mpc. The effect of an increasing distance is a decreasing depth of the CMD, i.e., for the farthest object only the brightest and youngest stars are resolvable. In the central panel, stellar evolutionary tracks are overlaid to the CMD (red: low-mass stars with $M \lesssim 2M_{\odot}$; green: intermediate-mass stars with $2 \lesssim M \lesssim 7M_{\odot}$; blue: massive stars with $M \gtrsim 7M_{\odot}$). Figure taken from Cignoni & Tosi (2010).

hotter temperatures. This is the so-called asymptotic giant branch (AGB) phase. Depending on its initial mass, a star could then be able to ignite carbon and oxygen. While evolving toward higher luminosities, the star will then become thermally unstable and experience a strong mass loss. The end of its life the star will eventually cool down to death as a white dwarf (if the final mass is below $\sim 1.4M_{\odot}$), an inert degenerate core that constitutes the stellar remnant after the outer envelope has been expelled (planetary nebula phase).

When the light coming from a source is expressed as a function of wavelength (or frequency), we call this a spectrum. A spectrum can be produced by splitting the electromagnetic radiation of a stellar source by dispersing it through a so-called spectrograph. The technique of “spectroscopy” studies the position and the width of the spectral absorption lines in a spectrum. Namely, these are caused by absorption of the stellar radiation by the gas present in the star’s atmosphere. This phenomenon happens when the photons have the right frequency to bump an electron of an atom of a specific element present in the gas up to a higher energy level, with the photon thus being absorbed by the gas. The intensity of a spectral line is a measure of the abundance of an element, and can be used to derive the chemical composition and the kinematics of the stellar gas. The advantage of spectroscopy compared to photometry is that one can get more detailed information about the chemical content of a star, and moreover about its radial velocity. It is rather complicated to derive the exact metallicity of a star only from its position on the CMD, since in many evolutionary phases stars with different ages and metallicities have overlapping positions (e.g., during the MS or the RGB, see also Fig. 1.2). However, a practical drawback of spectroscopy is that a significant amount of integration time is needed to reach the signal-to-noise ratio necessary to derive the mentioned properties. With the presently available instrumentation, it is only possible to acquire spectra for individual RGB stars within the boundaries of the Local Group, while spectra for bright supergiants and for ionized gas regions

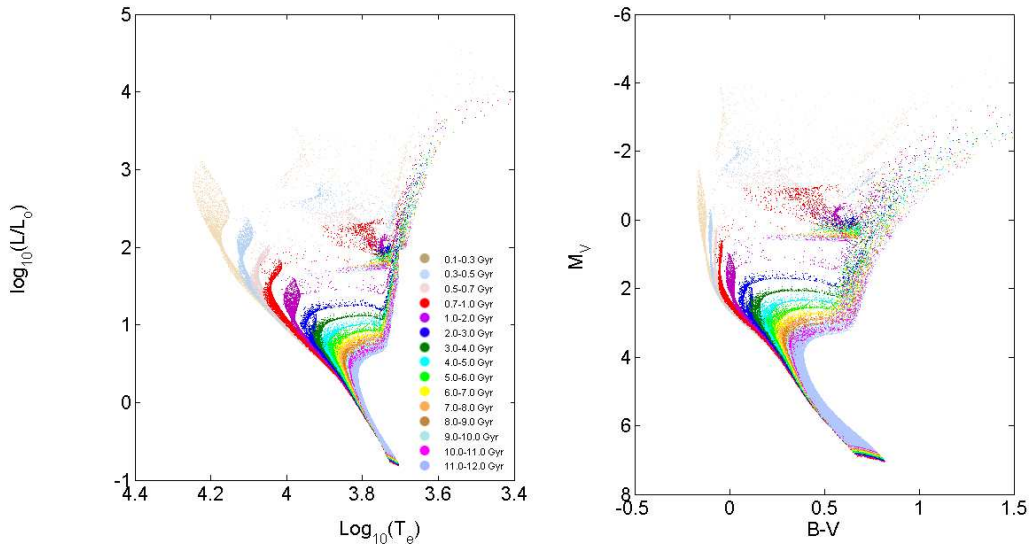


Figure 1.4: Synthetic CMDs computed starting from the Padova stellar evolutionary models (Marigo et al. 2008). The star formation rate is constant over the galaxy’s lifetime, and the metallicity is increasing with time. Stars of different ages are color-coded as indicated in the legend. In the *left panel*, a theoretical version of the CMD is plotted, while in the *right panel* we show the conversion to the observational plane. Courtesy of S. Pasetto.

(e.g., around hot and massive young stars or planetary nebulae) can still be obtained beyond the Local Group. Photometry allows us, instead, to resolve individual stars down to the RGB in stellar populations for objects as far as ~ 15 Mpc. However, an increasing distance makes the resolution drop, so that for the farthest objects only the brightest stars (supergiants, RGB stars at the TRGB and AGB stars) are resolvable, and we are only able to extract the galactic properties for a short lookback time. The take-home message is that, the deeper the observed CMD for a galaxy, the more information we are able to get about its less massive and thus older stellar populations, and thus about their past life. This is illustrated clearly in the example of Fig. 1.3.

In Fig. 1.3 we can also see some evolutionary tracks, which help to distinguish the various features in a composite CMD. Originally, fiducials (= mean locus of a CMD sequence) derived for the CMDs of Galactic globular clusters were compared to the CMDs of target galaxies to recognize their different stellar populations and the relative physical properties. This is justified by the fact that globular clusters are essentially simple stellar populations at a first approximation (although recent studies revealed an unexpected complexity also in these objects, see e.g. Piotto 2009 for a review). In the past decades, several groups have independently developed a number of theoretical models that reproduce evolutionary tracks for stars of different masses (e.g., VandenBerg et al. 2000; Pietrinferni et al. 2004; Dotter et al. 2008; Marigo et al. 2008). We call isochrones those paths in a CMD that follow the evolution of stars with a range of masses but with the same age. The fiducials are thus now accompanied in their role by isochrones.

Since in this Thesis we will mainly concentrate on the photometric properties of resolved stellar populations, we introduce the most sophisticated tool used to derive the star formation histories (SFHs) of dwarf galaxies. The technique of synthetic CMD modeling was pioneered some twenty years ago, and since then it has been further developed and improved by many

different groups (e.g., Tosi et al. 1989, 1991; Dohm-Palmer et al. 1997; Aparicio et al. 1996; Aloisi et al. 1999; Schulte-Ladbeck et al. 1999; Aloisi & Leitherer 2001; Dolphin 2002; Harris & Zaritsky 2002; Cole et al. 2007). Comparisons of different SFHs recovery methods have shown that, within the observational and theoretical uncertainties, the results are in excellent agreement among each other (see, e.g., Skillman et al. 2003; Monelli et al. 2010). This method consists in the generation of synthetic CMDs with a large range of different physical properties, starting from a set of theoretical isochrones. These sets of CMDs are then converted from the theoretical to the observational plane (an example is shown in Fig. 1.4), which is a delicate passage given the uncertainties involved in such transformations. Moreover, the synthetic CMDs have to take into account the observational errors and incompleteness effects that come with the photometry process. The following step is to then statistically compare the observed number of stars found in each evolutionary stage with the values produced in the simulated CMDs (usually this is done by subdividing the CMD into a grid, where the size of each box depends on the amount of information available from the observed CMD). In this way, the best-fitting solution quantifies the amount of stars produced as a function of time in a galaxy (i.e., the star formation rate, SFR). We stress that an accurate age dating for a galaxy is only obtainable when the CMD reaches the MSTO for the oldest stars. For a review about this technique, its advantages and its limitations, see e.g. Gallart et al. (2005); Cignoni & Tosi (2010).

1.3 The Local Group

Many efforts have been made to analyze the physical properties of the dwarf companions of the MW and of M31, ideal targets due to their proximity. Our Galaxy, the MW, is surrounded by about 15 “classical” dwarfs (i.e., not considering the newly discovered ultra-faints) within a distance of ~ 500 kpc, out of which about 3/4 are dwarf spheroidals and the rest dwarf irregulars. The first thing to note is that these two subsamples have different distributions within the entire Local Group. Namely, dwarf irregulars are usually found at greater distances from the giant dominant galaxy, whereas early-type dwarfs are located mostly within the inner ~ 300 kpc from the giant spirals (e.g., Einasto et al. 1974; Karachentsev et al. 2002b). There are outliers to this relation, namely the two Magellanic Clouds, which are irregulars closer than 100 kpc to the MW, and the early-type dwarfs Cetus, Tucana and And XVIII, located at the edges of the Group. More generally, the distribution of dwarf galaxies could be explained by environmental effects that act on their evolution (e.g., Grebel et al. 2003). On the other hand, M31 has dwarf irregular, dwarf spheroidal and dwarf elliptical companions (the MW has instead none of the latter). A sketch of our Local Group is shown in Fig. 1.5.

The deep high-resolution images from the Hubble Space Telescope (HST) provided us, in the past two decades, with a wealth of data on the resolved stellar populations of Local Group dwarf members. These deep observations permit us both to have a broad and detailed view of the physical properties of dwarf galaxies and to investigate how they form and evolve in this type of environment (Grebel 1997; Mateo 1998; van den Bergh 1999; Tolstoy et al. 2009). One of the perhaps most astonishing properties discovered for such small objects is that there are no two dwarfs that are alike, as they exhibit a wide range of diverse evolutionary histories (e.g., Grebel 1997; Mateo 1998; Dolphin 2002; Tolstoy et al. 2009). As explained in the previous Section, deep CMDs permit us to derive the detailed SFHs for dwarf galaxies in the Local Group. We are thus able to put strong constraints on the star formation epochs and star formation efficiency

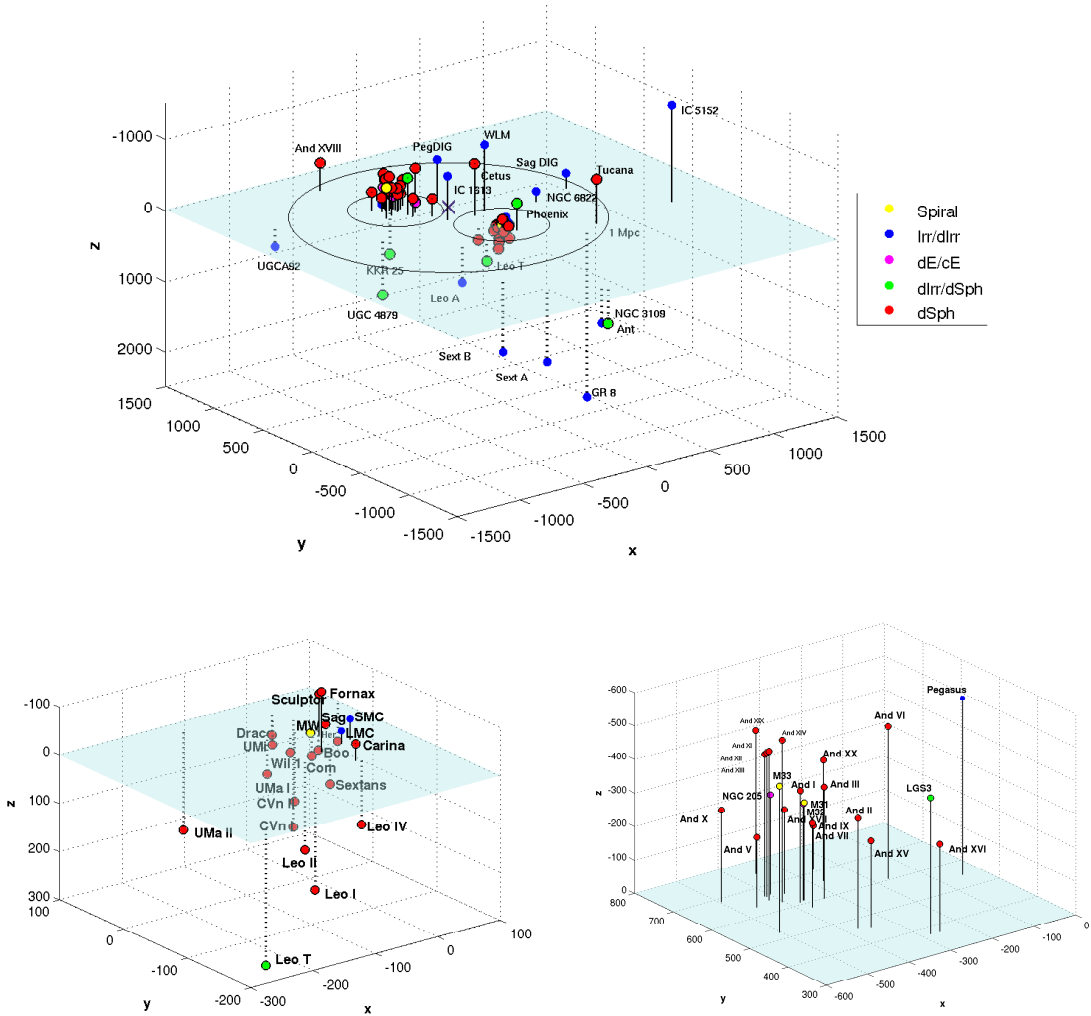


Figure 1.5: 3D distribution of Local Group members. Shown are a global view (*upper panel*), and a zoom-in of both the MW and the M31 subgroups (*lower panels*, see legend for the morphological type color-coding). The axes are in units of kpc. Courtesy of K. Glatt.

for dwarf galaxies, provided that the photometry reaches the oldest MSTO.

None of the Local Group dwarfs of each morphological type studied in detail so far (i.e., within the accuracy of photometric age-dating techniques) seems to lack an ancient population with age $\gtrsim 10$ Gyr, even though their fractions vary strongly from galaxy to galaxy (e.g., Grebel 1997; Mateo 1998; Grebel & Gallagher 2004; Orban et al. 2008; Tolstoy et al. 2009). It is interesting to find out that most of the early-type dwarfs in the Local Group contain mainly old populations, which is the case for, e.g., Draco, Ursa Minor and Sculptor (see e.g. Grillmair et al. 1998; Mighell & Burke 1999; Aparicio et al. 2001; Bellazzini et al. 2002; Carrera et al. 2002; Ikuta & Arimoto 2002). On the other hand, there are objects that also show prominent intermediate-age populations (IAPs, $\sim 1 - 9$ Gyr) that make up for up to $\sim 50\%$ of their stellar populations, like the dwarf spheroidals Carina, Fornax, Leo I, Leo II (e.g. Mighell & Rich 1996; Hurley-Keller et al. 1998; Gallart et al. 1999; Saviane et al. 2000; Dolphin 2002; Pasetto et al. 2010) and the dwarf ellipticals NGC 205, NGC 185 and NGC 147 (Demers et al. 2003;

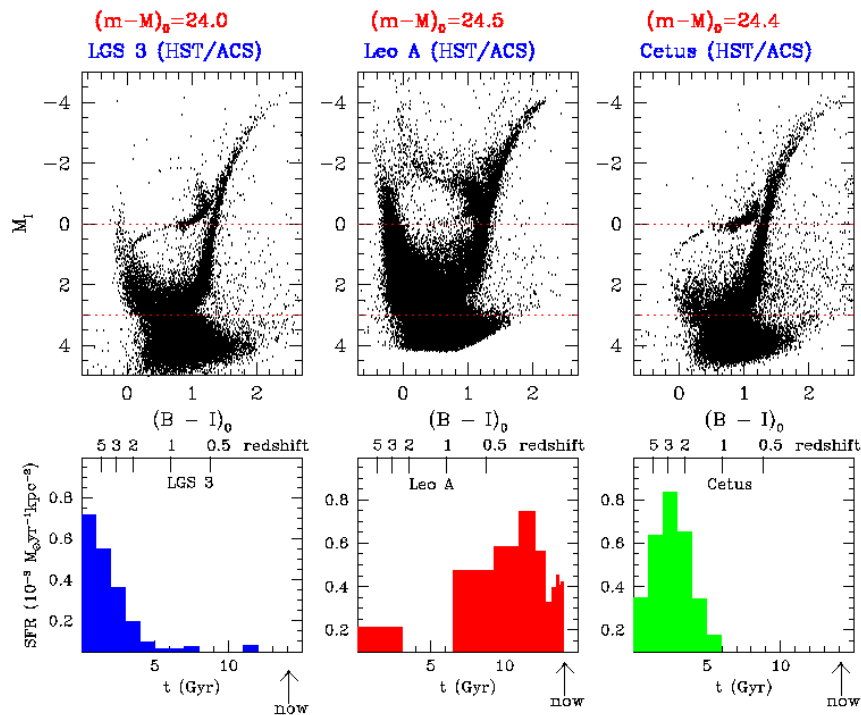


Figure 1.6: *Upper panels.* CMDs for three Local Group dwarfs, from exquisitely deep images reaching the oldest MSTO (obtained with the Hubble Space Telescope). LGS3 is a transition-type dwarf, Leo A a late-type dwarf, and Cetus a dwarf spheroidal. *Lower panels.* Star formation histories (i.e., star formation rate as a function of time) derived for the three galaxies with the synthetic CMD modeling technique. Figure taken from Tolstoy et al. (2009).

Nowotny et al. 2003; Davidge 2005).

The synthetic CMD modeling was preferentially performed on MW early-type dwarf companions, since it requires long exposure times and thus is easier to apply for closer objects. As for late-type dwarfs, generally found in the outskirts of the Local Group, their CMD-modeling census has not yet been completed. For example, detailed SFHs have already been determined from deep CMDs for the Magellanic Clouds (e.g., Smecker-Hane et al. 2002; Harris & Zaritsky 2004, 2009; Noël et al. 2009; Sabbi et al. 2009), IC1613 (Skillman et al. 2003), Leo A (Cole et al. 2007), IC10 (Cole 2010). From these and other works we learn that late-type dwarfs use to form stars slowly over long periods, separated by short quiescent phases, the so-called “gasp-ing” regime (Marconi et al. 1995). The average SFR for late-type dwarfs is $\sim 10^{-3} M_\odot \text{yr}^{-1} \text{kpc}^{-2}$ (Hunter & Elmegreen 2004). An example of the variety of SFHs for Local Group dwarf members is shown in Fig. 1.6 (where the SFHs are derived with the synthetic CMD modeling).

Regarding the chemical content of Local Group dwarf galaxies, it has first been photometrically estimated, and then spectroscopically confirmed that they all tend to be metal-poor, with average iron abundance ($[\text{Fe}/\text{H}]$) values of $\lesssim -1.0$ dex (see, e.g., Mateo 1998; Koch 2009). The chemical composition of stars in MW companions has been well studied with detailed spectroscopic and kinematic data. All these objects show wide metallicity spreads, which indicate their capacity of retaining part of the material produced from stellar evolution (e.g., Shetrone et al. 2001; Sarajedini et al. 2002; Tolstoy et al. 2004; Battaglia et al. 2006; Helmi et al. 2006; Koch

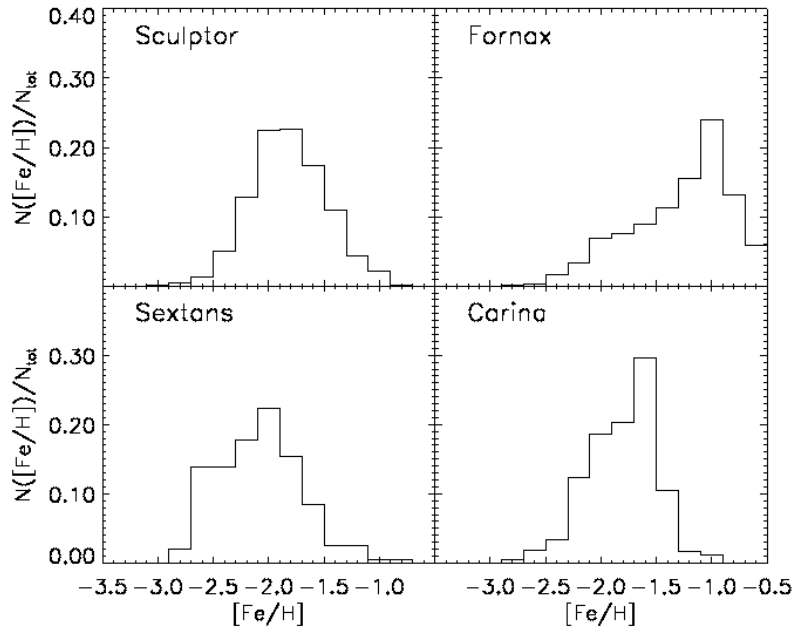


Figure 1.7: Differential metallicity distribution functions for four Local Group dwarf spheroidals. Each of the objects presents unique features. Figure taken from Helmi et al. (2006).

et al. 2006; Bosler et al. 2007; Koch et al. 2007a,b; Gullieuszik et al. 2009). Their metallicity distribution functions (MDFs) often show a slow increase toward higher metallicities and then a steeper decline, but there are many individual differences reflecting a wide range of complex SFHs, as can be seen from the example in Fig. 1.7 (e.g., Helmi et al. 2006; Koch et al. 2006, 2007a,b; Tolstoy et al. 2009). Detailed models of chemical evolution have been developed and applied to MW dwarf spheroidals (e.g., Lanfranchi & Matteucci 2004; Marcolini et al. 2006; Marcolini et al. 2008; Revaz et al. 2009), and they are able to reproduce the shape of the observed MDFs. The above-mentioned asymmetry of the MDFs with a steeper fall-off on the metal-rich side may be explained by an evolution that is regulated by supernova explosions, stellar winds and galactic outflows (e.g., Dekel & Silk 1986; Lanfranchi & Matteucci 2004).

Moreover, detailed abundances for individual stars in the MW dwarf spheroidals can be obtained spectroscopically with high-resolution and high-signal-to-noise data. Different chemical elements can then be used as indicators for the processes of chemical enrichment (e.g., the expulsion of gas from giant stars, planetary nebulae, or supernovae) and of their time variation. In particular, the relation between α -elements and mean metallicity $[\text{Fe}/\text{H}]$ is a powerful tool to infer the evolutionary history of a galaxy. Namely, it strongly depends on the ratio of supernovae type II (i.e., stars with masses $\gtrsim 8M_{\odot}$ experiencing core-collapse after having burned all the nuclear fuels until iron-peak elements, with a subsequent catastrophic explosion and expulsion of the envelope) to supernovae type Ia (i.e., white dwarf in a binary system that accretes mass from a red giant companion, until the degenerate core of the dwarf gets ignited leading to an explosion). The supernovae type II produce significant amounts of α -elements and thus enrich the intergalactic medium when they explode, on timescales of a few Myr, while the explosion of supernovae type Ia depends on the time necessary for the less massive of the two stars to reach the white dwarf stage ($\sim 10^8 - 10^9$ yr). Supernovae type Ia produce significant amounts

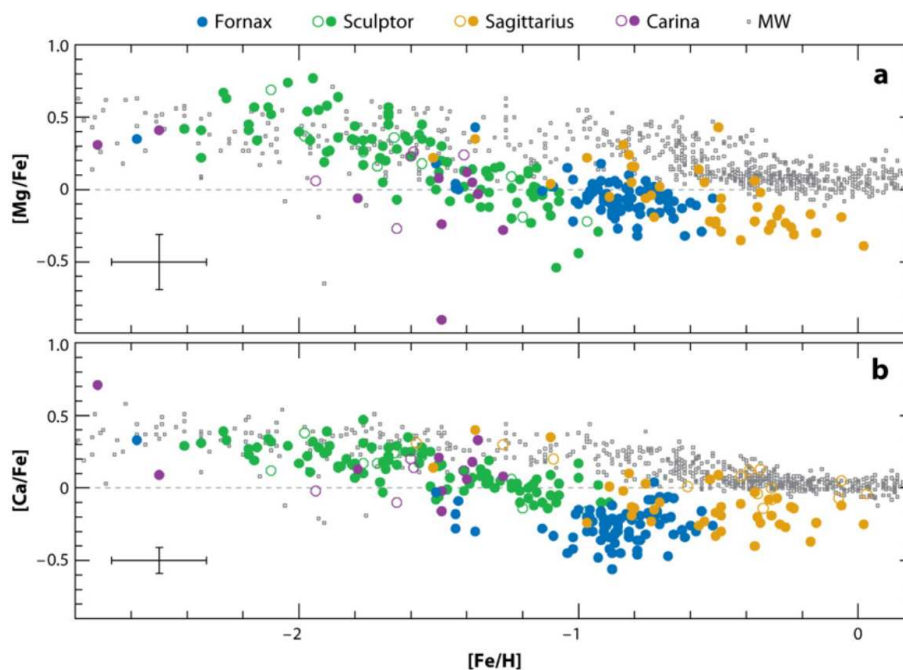


Figure 1.8: α -element (Mg and Ca) abundances plotted as a function of metallicity for four dwarf spheroidal galaxies and for MW disk and halo stars (color-coding as in the legend). Open symbols refer to single-slit spectroscopy measurements, filled circles to multiobject spectroscopy. For the latter, a representative errorbar is shown on the left side of each panel. Figure taken from Tolstoy et al. (2010).

of iron, and as they explode the α -element abundance decreases, since no subsequent star formation episode is able to enhance again this value with respect to the iron abundance. When we thus plot the α -element abundance as a function of $[\text{Fe}/\text{H}]$, the onset of supernovae type Ia explosions is seen as a “knee”, that indicates the amount of enrichment achieved until that moment by the galaxy (see, e.g., Matteucci & Brocato 1990). If the galaxy has been able to retain metals before supernovae type Ia start to dominate the iron production, then the position of the knee will be found at a higher metallicity with respect to a galaxy that has lost most of its metals through, e.g., galactic winds, or that has had a low SFR. In Fig. 1.8 we show an example of such a plot for both MW stars and different dwarf spheroidals, from which it is clear that all of the objects considered have had varied SFHs. Moreover, from this plot we can notice that all the dwarfs have different α -element abundances, scattering from super- to sub-solar values also within the same galaxy and having on average solar values ($[\alpha/\text{Fe}] \sim 0.0$) for metallicities $-1.5 \lesssim [\text{Fe}/\text{H}] \lesssim -1.0$.

On the other hand, also the MDFs of the MW and of its dwarf spheroidal companions are compared to each other, to look for possible connections. If dwarf galaxies similar to those observed today have in the past contributed to build up the halo of a MW-like giant spiral, then the signature of such a process should be still imprinted in the chemical composition of both types of objects. For many years, it was believed that stars coming from dwarf spheroidals were not able to reproduce the MDF seen for MW halo stars, since they were lacking the low-metallicity end ($[\text{Fe}/\text{H}] \leq -3.0$) observed in the latter (e.g., Shetrone et al. 2001; Helmi et al. 2006). However, recent studies have shown that with an increasing amount of data and most importantly more accurate analysis techniques, this discrepancy is not anymore present (Starkenburger et al. 2010; Tafelmeyer et al. 2010). Moreover, stars with very low metallicities have also been found

in MW ultra-faint companions (e.g., Kirby et al. 2008; Frebel et al. 2010; Norris et al. 2010). This is thus a confirmation that both this type of objects and the classical dwarf spheroidals are indeed candidate ingredients for the hierarchical build-up of our Galaxy. The same accretion mechanism is probably also taking place for similar systems, starting from our companion M31 and going on with spirals outside the Local Group, which show the presence of stellar streams possibly stemming from the disruption of accreted dwarf companions (e.g. Brown et al. 2006; Martínez-Delgado et al. 2010; Mouhcine et al. 2010).

The estimation of metallicity is slightly more difficult for late-type dwarfs due to their larger distance. Spectra for individual stars can be obtained only for the brightest supergiants, and more commonly their chemical content is extracted from regions of ionized gas (HII regions, surrounding young and hot stars) or planetary nebulae. The usual value derived in these cases is an oxygen abundance. Late-type dwarfs usually have considerable metallicity spreads, and in particular their localized actively star forming regions show a range of metallicity values (e.g., Kniazev et al. 2005; Glatt et al. 2008a; Koch et al. 2008b). To be able to compare the oxygen abundance values to the metallicities found for the old, unevolved populations of early-type dwarfs, one needs to convert it into a $[\text{Fe}/\text{H}]$ estimate (e.g., Mateo 1998). However, this procedure is unavoidably affected by intrinsic uncertainties, and the best way of comparing metallicity for different morphological types is to derive them for the same old stellar populations (although the metallicities derived photometrically are not as precise as the spectroscopic ones). This is exactly what is done by Grebel et al. (2003), who study the metallicity-luminosity relation for Local Group dwarfs (see also Mateo 1998). There is, namely, a linear relation between these two physical quantities, such that more luminous objects have also a higher mean metal content. This can be intuitively explained if a higher luminosity implies a deeper gravitational potential well, or a higher SFR, such that the metal enrichment is more efficient as is also the capacity of the galaxy to retain the products of stellar evolution (e.g., Dekel & Silk 1986). On the other side, as the study by Grebel et al. (2003) shows and extensively discusses, late-type dwarfs appear to be systematically more metal-poor compared to early-type dwarfs at a fixed luminosity. The reason for this offset could be reconducted to an evolutionary transition (see also previous Section), which would be supported by the evidence that several transition-type dwarfs share the same position with early-type dwarfs in the metallicity-luminosity diagram (see Fig. 1.9).

Literature studies have also looked at possibly distinct stellar spatial distributions of different stellar populations in both early-type (e.g., Stetson et al. 1998; Hurley-Keller et al. 1999) and late-type (e.g., Dohm-Palmer et al. 1997; van Dyk et al. 1998; Dohm-Palmer et al. 2002; Weisz et al. 2008; Glatt et al. 2010; Sanna et al. 2010) dwarf galaxies. The first systematic study of a large sample of early-type dwarfs was carried out by Harbeck et al. (2001), who investigated morphological gradients based on HB and RGB stars for a sample of nine galaxies. They showed that if gradients are present they are always such that the more metal-rich and/or younger populations are more centrally concentrated. Later on, spectroscopic studies were able to also confirm chemically, and in some cases also kinematically, distinct subpopulations for various dwarfs, like Fornax, Sculptor, and Sextans (e.g., Tolstoy et al. 2004; Battaglia et al. 2006). However, there are also cases for which such distinct populations were not found, but only weak metallicity gradients as a function of radius were present (e.g., Harbeck et al. 2001; Koch et al. 2006, 2007a,b). Theoretical models are able to explain the presence of metallicity gradients and stellar subpopulations (e.g. Marcolini et al. 2008) as a product of the chemical homogenization of the intergalactic medium and of the inhomogeneous pollution by the explo-

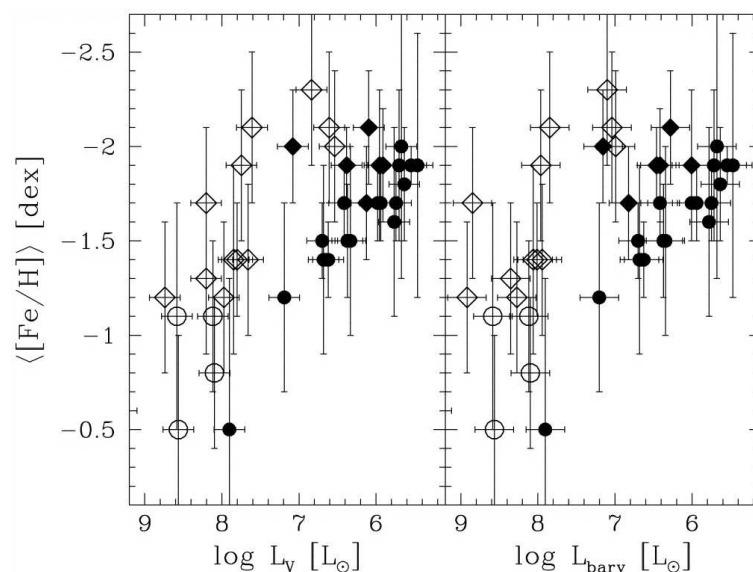


Figure 1.9: V -band luminosity (*left panel*) and baryonic luminosity (i.e., corrected for baryon contribution of gas not yet turned into stars, *right panel*) as a function of metallicity for Local Group dwarf members. The metallicities are derived from old stellar populations. The errorbars in metallicity indicate the measured spread in the metallicity distribution function, not the uncertainty of the measurement (which is typically < 0.2 dex). Filled circles denote dwarf spheroidals, filled diamonds transition-type dwarfs, and open diamonds late-type dwarfs. Note the bimodality of the relation. Figure taken from Grebel et al. (2003).

sion of supernovae type Ia. Regarding late-type dwarfs within and at the edges of the Local Group, stellar populations of different ages have also been found to show distinct spatial extents. The youngest stars are always located in clumps, preferentially toward the center of the galaxy, while the oldest stars are uniformly distributed along the whole galaxy's body, reflecting the migration and redistribution of stars with time (see, e.g., Payne-Gaposhkin 1972; Isserstedt 1984; Dohm-Palmer et al. 1997, 2002; Weisz et al. 2008). Looking at the spatial distribution of the youngest stars in different time steps, it can even be seen that the SFR varies in time and space in a way that suggests a stochastic, in some cases self-propagating, star formation mode (e.g., Seiden et al. 1979; Weisz et al. 2009a,b). This picture gains further support from abundance studies in late-type dwarfs, which indicate that these objects are not well-mixed on global scales.

We already mentioned that dwarf galaxies are dark-matter dominated objects, and their total mass can be computed from their velocity dispersions assuming a spherical symmetry and virial equilibrium. It has recently been suggested that dwarf spheroidal galaxies share a common mass scale of $\sim 10^7 M_\odot$ within 0.3 kpc of their center (Strigari et al. 2008), result based on both classical and newly discovered ultra-faint objects. However, caution should be used when dealing with observational uncertainties and theoretical assumptions (see, e.g., Adén et al. 2009; Collins et al. 2010), and more data are needed to definitely confirm the suggested trend (for a brief review, see e.g. Bullock 2010). Alternatively, we might just have been looking at the wrong recipe from the beginning, while the correct one actually does not include the classical Newtonian dynamics among the ingredients. More specifically, the theory of modified Newtonian dynamics (MOND, see Milgrom 1983a,b; Begeman et al. 1991) postulates a breakdown of the classical dynamics for accelerations below a threshold of $a_0 \sim 10^{-8} \text{cm s}^{-2}$. This is enough to avoid the evocation of an unseen mass in order to explain, for example, the flat rotation curves of spiral galaxies.

This short introduction is not by any means supposed to give a comprehensive picture of the Local Group. For a complete overview, see the reviews by Grebel (1997); Mateo (1998); van den Bergh (1999); Tolstoy et al. (2009) (and references therein). We, however, now understand a bit more about the ingredients of our own cake. At this point, why not to look at the recipes of our closest neighbors to find out similarities and differences?

1.4 Nearby groups of galaxies

Beyond the Local Group, both the integrated and the resolved properties of dwarf galaxies in nearby groups have been studied extensively (e.g., Karachentsev et al. 2002b,a; Trentham & Tully 2002; Makarova et al. 2002; Karachentsev et al. 2003a,b,c, 2004; Karachentsev 2005; Makarova et al. 2005; Grebel 2007; Sharina et al. 2008; Bouchard et al. 2009; Weisz et al. 2008; Dalcanton et al. 2009; Koleva et al. 2009; Crnojević et al. 2010; Lianou et al. 2010). The main purpose of most of these studies was to catalog and characterize new objects in nearby groups and to look for possible environmental effects on galaxy evolution. Due to the distance, their resolved stellar populations can be studied in detail only with advanced space instrumentation (HST), and even in those cases, only the brightest stars are resolvable within a distance of ~ 18 Mpc (see Fig. 1.3).

The first goal of the mentioned observations is to derive individual distances for dwarf galaxies by taking advantage of the constant luminosity of the TRGB in I -band. Apart from their distances, the study of the resolved stellar populations via deep imaging offers insights to the SFHs of these systems. The first attempts of deriving SFHs via synthetic modeling beyond the Local Group were already made more than a decade ago (e.g., Tosi et al. 1989, 1991; Dohm-Palmer et al. 1997; Aloisi et al. 1999; Schulte-Ladbeck et al. 1999; Aloisi & Leitherer 2001), and recently there has been an increasing effort in this kind of studies (e.g., Weisz et al. 2008; Dalcanton et al. 2009; McQuinn et al. 2009; Tolstoy et al. 2009, and references therein), but we are still very far from having a complete census. Even though the limiting absolute magnitude dramatically decreases with their distance, we can still observe these galaxies down to comparable sensitivity levels as we used to see much closer dwarf galaxies in our own Local Group, as recently as only a decade ago (e.g., Dohm-Palmer et al. 1997), and the results of such studies can still shed light on how dwarf galaxies evolve in different neighborhoods.

Are the SFHs of dwarf galaxies influenced by the surrounding environment? I.e., do loose, filamentary structures (like the Canes Venatici Cloud or the Sculptor group, see Karachentsev et al. 2003a,c) have similar properties in their galaxy populations as the denser, more evolved groups we know (the Local Group itself, or the Centaurus A group, e.g., Karachentsev et al. 2002b), or are there striking differences in the way they spend their lives? Until now, there is no evidence for big differences among the properties of dwarfs within diverse galaxy groups (see, for example, the extended sample analyzed by Sharina et al. 2008, or the comparison between the Local Group and the M81 group in Weisz et al. 2008). This similarity could lead us to the conclusion that internal properties like mass or stellar feedback are the ones governing the star formation in these objects. On the other hand, the dwarf galaxy types do seem to depend on environment. For example, very loose groups such as the Sculptor group and Canes Venatici Cloud host primarily late-type dwarfs (see Karachentsev et al. 2003a,c), whereas more evolved, higher density groups like the Local Group, the highly interacting M81 group and the Centaurus A group have a sizeable fraction of early-type dwarfs (Karachentsev et al. 2002a,b). Ongoing

and future studies should be able to answer this and many further questions by looking closely at nearby groups.

1.4.1 The Centaurus A/M83 group of galaxies

The Centaurus A/M83 group of galaxies is, together with the more sparse Sculptor group, the nearest prominent galaxy group in the southern sky (located at an average Galactic latitude of $b \sim 20^\circ$). It consists of two smaller subgroups, whose dominant galaxies are Centaurus A (CenA, or NGC 5128) and M83 (NGC 5236), even though it is not clear whether they are receding from or approaching each other (e.g., Karachentsev et al. 2007). The peculiar, radio-loud giant elliptical galaxy CenA shows a very perturbed morphology and has probably undergone several merger events in its recent past (e.g., Meier et al. 1989; Mirabel et al. 1999; Karachentsev 2005). It is found at a Galactocentric distance of 3.8 Mpc (Hui et al. 1993; Karachentsev et al. 2002b, 2007; Harris et al. 2009), while the giant spiral M83 is at 4.8 Mpc (Karachentsev et al. 2007). At these distances, the group members are still resolvable into stars. A sketch of the group is presented in Fig. 1.10. Karachentsev et al. (2007) find an orbital/virial mass of $(6.4 - 8.1) \times 10^{12} M_\odot$ for the CenA subgroup, with a mass-to-light ratio of $\sim 125 M_\odot/L_\odot$. The M83 subgroup shows instead values of $(0.8 - 0.9) \times 10^{12} M_\odot$ and $\sim 34 M_\odot/L_\odot$, respectively. Finally, the zero-velocity surface radius for the group lies at ~ 1.4 Mpc.

Recent searches for new members of this group have been published by Côté et al. (1997), Banks et al. (1999), and Jerjen et al. (2000a). The current list of members of the CenA group contains 62 galaxies with radial velocities in the Local Group rest frame of $V_{LG} < 550 \text{ km s}^{-1}$ and angular distances from CenA of $< 30^\circ$ (Karachentsev et al. 2007). When looking at the luminosity function of the entire group, we can note that there are more luminous early-type dwarfs than in our own Local Group or in the Sculptor group, as expected for an evolved group (Jerjen et al. 2000a; Rejkuba et al. 2006). Moreover, many more faint early-type dwarfs could possibly be found if more sensitive surveys were available. In particular, we know now that the Local Group contains about 20 dwarfs with $M_B > -10$ (with many more probably still awaiting discovery), while, due to its distance, only 4 such faint objects have been detected so far in the CenA group. The fraction of early-type dwarfs found within the CenA/M83 group is higher than the fraction of late-type dwarfs, another indication for an advanced dynamical state of the group. With respect to the Local Group, this group is thus a denser and possibly more evolved environment.

The CenA/M83 dwarf population, displaying a variety of morphologies and stellar contents, has already been studied in the past (Côté et al. 1997; Karachentseva & Karachentsev 1998; Banks et al. 1999; Côté et al. 2000; Jerjen et al. 2000a,b; Karachentsev et al. 2002b; Lee et al. 2003; Karachentsev et al. 2004; Karachentsev 2005; Rejkuba et al. 2006; Bouchard et al. 2007; Grossi et al. 2007; Karachentsev et al. 2007; Lee et al. 2007; Makarova & Makarov 2008; Sharina et al. 2008; Bouchard et al. 2009; Makarova et al. 2009; Côté et al. 2009). Most of the mentioned works concentrated on large samples of objects at different wavelengths, not investigating their physical properties individually. The main conclusions from these datasets are that the scaling relations (e.g., morphology-density, metallicity-luminosity) are comparable to those observed in the Local Group and in other nearby groups. Rejkuba et al. (2006) study the resolved stellar populations of two early-type dwarfs at both optical and near-infrared (NIR) wavelengths. From the combination of these two datasets, they are able to disentangle the galactic luminous AGB stars from the foreground contaminants belonging to the MW, and to

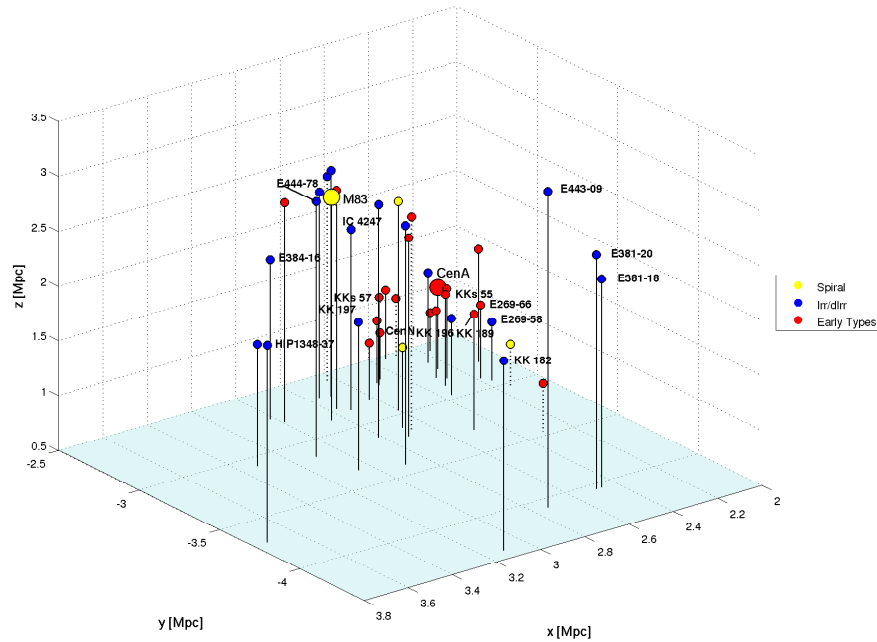


Figure 1.10: 3D distribution for members of the Centaurus A/M83 group (see legend for the morphological type color-coding). The dwarfs studied in this Thesis are labeled in the plot. Courtesy of K. Glatt.

quantify the amount of intermediate-age SFR for the two targets. It turns out that the IAP fractions are quite low (up to $\sim 15\%$) compared to some of the MW dwarf spheroidals. These are preliminary results due to the low-number statistics, but are interesting if we look at them from the perspective of possible environmental effects on the evolution of dwarf galaxies. Bouchard et al. (2007) find that in the CenA group there is an apparent gap in HI masses: the detected galaxies have gas masses of about $10^7 M_{\odot}$, or they are not detected at all (which permits them to put an upper limit of $\sim 10^6 M_{\odot}$). Bouchard et al. (2007) conclude that the CenA group environment must favor an efficient gas stripping from its dwarf companions. However, they also point out that the limits of the HI survey make it currently impossible to detect transition-type dwarfs in the CenA group (with no ongoing star formation but with neutral gas). Thus, knowledge of only the stellar content of early-type dwarfs does not tell us with certainty whether they are “contaminated” by residual gas. Grossi et al. (2007) find that some of the CenA late-type dwarfs contain an unexpectedly large fraction of neutral gas, but are not able to find an explanation for this trend. Bouchard et al. (2009) have collected literature data for dwarfs in the CenA and Sculptor groups and analyzed them along with new observations. Again, there is no significant ongoing star formation for early-type galaxies. Bouchard et al. (2009) investigate the dependence of several physical properties (optical luminosity, neutral gas and $H\alpha$ content) on environment. In a similar way to the Local Group, they are able to confirm: that galaxies in denser regions of these groups have, in general, lower values of HI; that the star formation in these objects is lower; and that they probably formed their stellar content earlier, with respect to galaxies in low-density regions. However, these correlations with environment do not rule out the simultaneous impact of internal processes that act to shape their evolution. Despite the fact that the giant members of the group all show elevated star formation rates and hints for

recent interaction events, the H α fluxes of the late-type dwarf population do not reveal any sign of enhanced activity with respect to other groups (Côté et al. 2009).

There is already a lot of information about the global appearance of this cake and about its fragrance, but we have a refined taste and we are thus keen to know more about it. This is the simple reason for this Thesis. The resolved stellar populations of the CenA/M83 dwarf ingredients can still reveal a vast amount of details about their metallicity content and stellar spatial distribution, their SFHs, and about how these properties relate to their home environment.

1.5 Motivation for this Thesis

- Dwarf galaxies are fundamental ingredients of our Universe, are ubiquitous and numerous, and exhibit a considerable variety in their physical properties despite their small sizes.
- The dwarf members of the Local Group have now been extensively studied, allowing a more detailed understanding about the (internal and external) processes that shape their evolution.
- *How typical is the Local Group? Does dwarf galaxy evolution proceed differently in other groups? To what extent does environment affect (dwarf) galaxy evolution, and to what extent do intrinsic properties and processes dominate?*
- The Local Group being only one particular realization of a range of possible environments, it would be a real pity not to aim for a more complete vision of the evolution of dwarf galaxies. Within a distance of ~ 18 Mpc, it is possible to resolve the stellar populations of such objects, and it is desirable to investigate their lifetime physical properties in different neighborhoods in order to answer the above listed questions.
- The Centaurus A/M83 group (~ 4 Mpc from us) is home to more than 50 dwarf galaxies, and offers thus an appealing possibility to ultimately put further constraints on the evolution of these low-mass objects, and look for potential environmental influences on the derived properties.

This Thesis is organized as follows. We present the data in § 2, where we also describe the photometry reduction and analysis and show the derived CMDs for our targets. The six target early-type dwarfs are analyzed in § 3. We present our results about the metallicity content and the metallicity gradients of their old stellar populations, and estimate their IAP fractions. We additionally study a sample of early-type companions of M31 in § 4 with the same method used for the CenA targets. In this way we check the validity of our analysis tools, and at the same time we look for common properties between the two groups of galaxies. Ten late-type dwarfs, companions of both CenA and M83, are then analyzed in § 5. We derive their SFHs with the synthetic CMD modeling technique and investigate their spatially resolved SFHs, discussing our results as a function of environment. Our conclusions are summarized in § 6, where we also illustrate possible new recipes along the lines of the cake studied.

“One must still have chaos in oneself to be able to give birth to a dancing star.”

F. Nietzsche, Thus Spoke Zarathustra
(1885)

2

Data analysis

This work is based on the light emitted at optical and NIR wavelengths by stellar sources in nearby galaxies, which are close enough to be resolved (see previous Chapter). We will hereafter concentrate on their *photometric* properties, since spectra for individual stars such faint ($I \sim 24$) are beyond the instrumental capabilities nowadays. On the other hand, integrated light spectra for the studied galaxies could in principle be obtained, although the physical properties of their stellar populations are less easily disentangleable with this method. We will not consider in more detail this technique here, but we mention that dwarf galaxies in the M81 group have been observed both through their resolved stellar populations as well as in their integrated light properties, and the results stemming from the two analysis have been found to be in very good agreement (Makarova et al. 2010). We are aware of the existence of integrated field spectroscopy observations for some of our target early-type and transition-type dwarfs, and we plan to compare the results presented below to these spectroscopic studies (M. Koleva, private communication).

One of the pioneers of automated point source photometry on Charge-Coupled Device (CCD) images was P. Stetson, who developed a series of semi-automated programs and tools devoted to quantify the light emitted by stars in crowded fields (DAOPHOT, see e.g. Stetson 1987, 1994). A further version of this software was included in the IRAF¹ environment (IRAF/DAOPHOT), permitting to perform aperture and PSF fitting photometry in a more flexible and interactive way (e.g. Davis 1993). Recently, A. Dolphin created his own version of these codes, specifically tuned for HST images (HSTPHOT, Dolphin 2000), and more automated than the previous versions especially in the PSF modeling and in the choice of the PSF stars themselves. Later on, the ultimate package DOLPHOT was released, which requires very little input from the user and is now available for the main HST instruments (ACS, WFPC2 and the newly installed WFPC3, Dolphin 2002). In the next Sections, we perform PSF-fitting photometry for our datasets using the DAOPHOT software as well as the DOLPHOT package.

For this Thesis, HST archival data obtained from the STScI Multi-Mission Archive (MAST²) have been used as our optical dataset, while VLT proprietary data (PI: H. Jerjen) were analyzed for NIR wavelengths. We give below the details of our target dwarf galaxies and of the data analysis as follows: in § 2.1 we describe the optical data, illustrate the photometry process, and present the resulting CMDs. Similarly, in § 2.2 we summarize the NIR observations, provide the details of the photometry, and give the results for the resolved photometry. The material presented in this Chapter is partly included in the following papers: Crnojević et al. (2010),

¹IRAF is supported by the National Optical Astronomy Observatories, which are operated by the Association of Universities for Research in Astronomy, Inc., under cooperative agreement with the National Science Foundation.

²<http://archive.stsci.edu/hst>.

Crnojević et al. (2010b), A&A submitted, Crnojević et al. (2010c), A&A submitted, and Crnojević et al. (2010d), in preparation.

2.1 Optical data

We look for existing HST observations of CenA group galaxies in order to study their resolved stellar populations. HST is the only telescope with which it is possible to reach faint enough magnitudes ($I \sim 29$) and to still resolve individual stars in crowded fields at a distance of ~ 4 Mpc. This permits us to resolve at least the upper part of the RGB or the most massive young stars within a reasonably short exposure time. For example, the RC or HB apparent magnitude at these distances is $I \sim 28$, which requires an observing time of ~ 8.5 hours (or 12 full HST orbits) in one filter to be observed (see, e.g., the deep HST observations of CenA presented in Rejkuba et al. 2005).

We choose our targets starting from the catalogs compiled by Karachentsev et al. (2002b), Karachentsev (2005), Karachentsev et al. (2007). In the latter of the mentioned papers there is an updated list of all the dwarf members of the CenA/M83 group, and moreover a series of CMDs for those of them which were observed with the Wide Field Channel (WFC) of the Advanced Camera for Surveys (ACS) instrument in order to obtain their distances (TRGB method, see Chapter 1). The ACS/WFC consists of two chips with a total field of view of ~ 11 arcmin² and a resolution of 0.049 arcsec/pixel. Observations with this instrument are available for 21 dwarfs in the CenA group (programs GO-9771 and GO-10235). Each galaxy has a 1200 seconds exposure in the $F606W$ filter (corresponding to the V -band in the Johnson-Cousins system) and a 900 seconds exposure in the $F814W$ filter (corresponding to the I -band). This choice of filters was made to optimally target RGB stars and to detect the TRGB (which has a fixed absolute magnitude in I -band), which is the most prominent component seen for the target galaxies. We decide not to consider observations carried out with the Wide Field Planetary Camera 2 (WFPC2) aboard the HST, since its field of view is smaller, three of its chips have lower resolution and it is less sensitive than the ACS. Earlier studies of dwarfs in the CenA group based on WFPC2 data were published by, e.g., Karachentsev et al. (2002b), Karachentsev et al. (2003b), Rejkuba et al. (2006).

Out of the dwarf galaxies observed with ACS/WFC, we choose six early-type dwarfs (companions of CenA) and ten late-type dwarfs (five companions of CenA and five companions of M83) as our dataset. The main properties of the target galaxies are listed in two Tables, depending on their morphology and on the subgroup to which they belong (following the subdivision of Karachentsev 2005). The properties for early-type dwarfs are reported in Table 2.1 as follows: column (1): name of the galaxy; (2-3): equatorial coordinates (J2000); (4): morphological de Vaucouleurs type; (5): I -band magnitude at the TRGB (from Karachentsev et al. 2007); (6): distance of the galaxy derived by Karachentsev et al. (2007) with the TRGB method; (7): de-projected distance from CenA, derived starting from the radial distance in column (6) and the angular distance reported by Karachentsev et al. (2002b); (8) foreground extinction in I -band from Schlegel et al. (1998); (9): absolute B magnitude from Karachentsev (2005); (10): absolute V magnitude from Georgiev et al. (2008); and (11): tidal index (i.e., degree of isolation), taken from Karachentsev et al. (2007); the latter was defined by Karachentsev & Makarov (1999) as

$$\Theta_i = \max\{\log(M_k/D_{ik}^3)\} + C, \quad k = 1, 2, \dots, N,$$

for the galaxy i , where M_k and D_{ik} refer to the mass and deprojected distance of any of its neighboring galaxies, respectively. This parameter thus quantifies the maximum density enhancement produced by the companions of the object under study. Finally, the constant C is such that it is equal to zero when the Keplerian cyclic period of the target galaxy with respect to its main disturber is equal to a cosmic Hubble time.

We then list the general properties of the late-type target galaxies in Table 2.2, which contains the following columns: (1): name of the galaxy; (2-3): equatorial coordinates (J2000); (4): morphological type; (5-6): distance and distance modulus of the galaxy derived by Karachentsev et al. (2007) with the TRGB method; (7): deprojected distance from M83/CenA, again derived from the radial distance in column (5); (8) Galactic foreground extinction in I -band from Schlegel et al. (1998); (9): absolute B magnitude (converted from Bouchard et al. 2009 with the distance modulus listed in column 6); (10): HI mass obtained from different sources (Banks et al. 1999; Beaulieu et al. 2006; Georgiev et al. 2008; Bouchard et al. 2009); where the HI flux values (S_{HI} , in Jy km s^{-1}) have been originally taken from (Banks et al. 1999), we recompute the HI gas mass with updated values of the distance (in Mpc), given that the relation between these quantities is the following

$$M_{HI} = (2.356 \times 10^5) D^2 S_{HI}$$

(see, e.g., Bouchard et al. 2007); (11): tidal index from Karachentsev et al. (2007); and (12) references for the individual HI masses.

2.1.1 Photometry

We performed PSF-fitting stellar photometry using the ACS module of the DOLPHOT package (Dolphin 2002) for crowded field photometry. The reduced and pre-processed **.fits* files can be downloaded from the HST MAST (i.e., Multimission Archive at Space Telescope Science Institute) web archive. The photometry can be run on either the original, single pointing flat-fielded images (**_flt.fits*), or on the cosmic ray-cleaned images (**_crj.fits*). Moreover, the datasets obtained from the archive already contain the images that are corrected for geometrical distortion and combined from the different pointings (multi-drizzled images, **_drz.fits*). The photometry can be performed on either the **_flt.fits* or the **_crj.fits* single images. It is recommended not to perform the photometry on the drizzled images, since stars at different locations in the field of view can be resampled in different ways by the process, and the signal in adjacent pixels is correlated. We decide to work on the **_flt.fits* files, since the *splitgroups* DOLPHOT task (see below) assigns a wrong readout noise value to the **_crj.fits* images derived from the respective **_flt.fits* files, resulting in too high a signal-to-noise ratio for the sources. The cosmic rays can be then recognized and eliminated in the post-photometry processing using appropriate quality cuts (see below).

The preparatory steps for the photometry include the masking of the bad pixels on the original images (*acsmask* task), the splitting of each image into the two different chips (*splitgroups* task), and the (not mandatory) computation of the sky level (*calcsky* task). The latter has been discarded after some tests, since the program can calculate the sky while running the photometry process automatically, and the preliminary computation did not improve the final quality of the photometry. Finally, a first estimate of the offset between the reference image and the single chips for each of the pointings and each of the filters has to be evaluated using the task

Table 2.1: Fundamental properties of the target early-type dwarf galaxies (companions of CenA).

Galaxy	RA (J2000)	DEC (J2000)	T	I_{TRGB}	D (Mpc)	D_{CenA} (kpc)	A_I	M_B	M_V	Θ
KK189, CenA-dE1	13 12 45.0	-41 49 55	-3	24.40 ± 0.07	4.42 ± 0.33	676 ± 483	0.22	-10.52	-11.99	2.0
ESO269-66, KK190	13 13 09.2	-44 53 24	-5	24.04 ± 0.04	3.82 ± 0.26	113 ± 412	0.18	-13.85	-13.89	1.7
KK197, SGC1319.1-4216	13 22 01.8	-42 32 08	-3	24.19 ± 0.04	3.87 ± 0.27	198 ± 112	0.30	-12.76	-13.04	3.0
KKs55	13 22 12.4	-42 43 51	-3	24.21 ± 0.03	3.94 ± 0.27	176 ± 450	0.28	-9.91	-11.17	3.1
KKs57	13 41 38.1	-42 34 55	-3	24.10 ± 0.05	3.93 ± 0.28	257 ± 290	0.18	-10.07	-10.73	1.8
CenN	13 48 09.2	-47 33 54	-3	24.10 ± 0.04	3.77 ± 0.26	399 ± 24	0.27	-10.89	-11.15	0.9

Notes. Units of right ascension are hours, minutes, and seconds, and units of declination are degrees, arcminutes, and arcseconds. The references for the reported values are Karachentsev (2005) and Karachentsev et al. (2007), and Georgiev et al. (2008) for the absolute V magnitude. The deprojected distance from CenA is computed in this study.

Table 2.2: Fundamental properties of the target late-type dwarf galaxies (companions of M83 and CenA).

Galaxy	RA (J2000)	DEC (J2000)	T	D (Mpc)	$(m - M)_0$	$D_{M83/CenA}$ (kpc)	A_I	M_B	M_{HI} ($10^6 M_\odot$)	Θ	Ref.
ESO381-18	12 44 42.7	-35 58 00	10	5.32 ± 0.51	28.63 ± 0.14	1156 ± 125	0.12	-12.91	27/29	-0.6	1,2
ESO381-20	12 46 00.4	-33 50 17	10	5.44 ± 0.37	28.68 ± 0.14	1100 ± 144	0.13	-14.44	157/251	-0.3	1,2
ESO443-09, KK170	12 54 53.6	-28 20 27	10	5.97 ± 0.46	28.88 ± 0.17	1212 ± 415	0.13	-11.82	14	-0.9	2
IC4247, ESO444-34	13 26 44.4	-30 21 45	10	4.97 ± 0.49	28.48 ± 0.21	277 ± 437	0.12	-14.07	34/37	1.5	1,2
ESO444-78, UGCA365	13 36 30.8	-29 14 11	10	5.25 ± 0.43	28.60 ± 0.17	107 ± 499	0.10	-13.11	18/21	2.1	2,3
KK182, Cen6	13 05 02.9	-40 04 58	10	5.78 ± 0.42	28.81 ± 0.15	2048 ± 555	0.20	-12.48	42/55	-0.5	1,3
ESO269-58	13 10 32.9	-46 59 27	10	3.80 ± 0.29	27.90 ± 0.16	316 ± 44	0.21	-14.60	24	1.9	2
KK196, AM1318-444	13 21 47.1	-45 03 48	10	3.98 ± 0.29	28.00 ± 0.15	255 ± 391	0.16	-11.90	-	2.2	-
HIPASS J1348-37	13 48 33.9	-37 58 03	10	5.75 ± 0.66	28.80 ± 0.24	2053 ± 738	0.15	-11.90	8/33	-1.2	1,2
ESO384-16	13 57 01.6	-35 20 02	10	4.53 ± 0.31	28.28 ± 0.14	1038 ± 352	0.14	-13.17	4/6	-0.3	3,4

Notes. Units of right ascension are hours, minutes and seconds, and units of declination are degrees, arcminutes and arcseconds. The reference for the M_B values is Bouchard et al. (2009); the M_{HI} values are obtained from different sources, indicated in the last column as follows: (1) Banks et al. (1999); (2) Georgiev et al. (2008); (3) Bouchard et al. (2009); and (4) Beaulieu et al. (2006); all the remaining reported values are taken from Karachentsev et al. (2007).

acsfitdistort. This is then further refined during the photometry run. We choose the deepest multi-drizzled frame (i.e., the *F814W*-filter exposure) as the reference frame for the photometry, as suggested in the DOLPHOT User’s Guide³. The parameters chosen for the photometry also follow the prescriptions of the User’s Guide. The program then locates automatically the stars, adjusts the PSF (originally produced by TinyTim, Krist 1995) based on the image, iterating the photometry until it converges and applying the aperture corrections.

The program runs the photometry simultaneously on all of the input images, giving as an output a first block containing the combined photometry, and following the blocks with the results for the single input images. After the instrumental magnitudes, the output also contains the transformed and calibrated magnitudes. The transformations to the Johnson-Cousins system are made following Sirianni et al. (2005), and then charge transfer efficiency corrections are applied. The output from the program also contains quality parameters for each star, both for the combined photometry block as well as for the photometry for each of the filters. The “object type” tells whether a star is good or not: it has a value of 0 when the star’s shape is pointlike, and its value increases when the star is sharp or extended. There is an “error flag” which has a value of 0 only when the star is well recovered in the image, i.e., for which the photometry is not saturated or does not extend beyond the chip. The next quality parameters are signal-to-noise ratio and χ . The sharpness parameter is negative when a star is too sharp (this is the case for cosmic rays or detector defects) and positive when it is too extended (for example, background galaxies), while a good star has a value of 0. Finally, the crowding parameter quantifies how much brighter (in mag) the star would be if isolated when measured, as opposed to the true measurement in which the light of the neighboring object affects the photometry.

In order to reject non-stellar detections and to have a clean final sample of stars for our CMDs, the stars that we then want to retain from the original photometry have to simultaneously satisfy the required cuts for different quality parameters in both wavelengths. These limits are the following: the “object type” has to be ≤ 2 ; the “error flag” is set to 0; the object’s signal-to-noise ratio has to be at least 5; its sharpness parameter has to be $|sharp| \leq 0.3$; the crowding parameter is set to a value lower than 0.5; and finally the χ has to be ≤ 2.5 . This selection choice leaves us with fairly clean CMDs.

However, for some of the target late-type dwarfs (ESO381-18, IC4247, ESO384-16 and ESO269-58) the standard parameters for the photometry do not give satisfying results. More specifically, the stars found in central, crowded regions are rejected by our adopted quality cuts, resulting in a loss of information especially for the bluest young stars found in these regions. For these galaxies, we change the DOLPHOT photometry parameter Force1 from the value suggested in the User’s Guide. This would normally force the code to retain only “good” objects, meaning not too faint for the PSF determination, not too sharp or too elongated. By changing this parameter, also sharp/extended objects are classified as “good” objects in the output of the photometry, so that the final photometry will now retain valid objects in the crowded regions, but will also add spurious objects. To avoid the latter, we apply stricter quality cuts (using $-0.2 \leq |sharp| \leq 0.2$), and remove spurious objects by hand when these selection criteria are not enough (e.g., in the cases where pointlike objects are detected in the tails of saturated foreground stars). In this way, we do not lose precious information about the bluest part of the CMD, with the only disadvantage of having a diagram slightly less clean.

³<http://purcell.as.arizona.edu/dolphot/>.

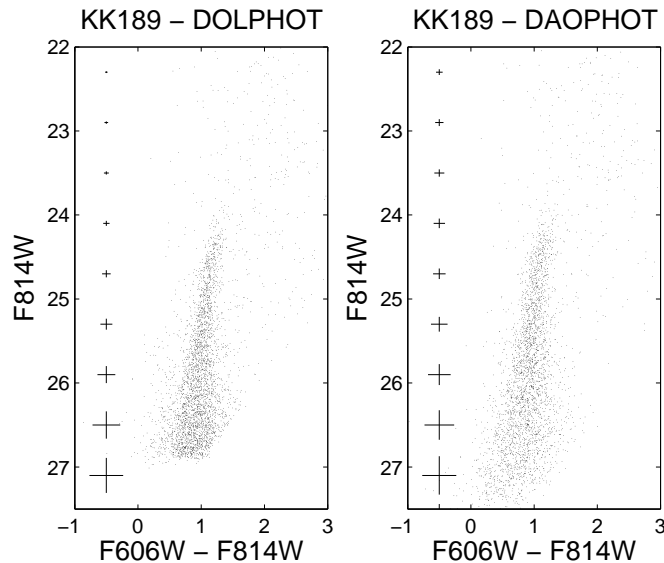


Figure 2.1: Color magnitude diagram of the early-type dwarf KK189. The photometry has been derived both with the DOLPHOT package (*left panel*), and with the IRAF/DAOPHOT package (*right panel*). Representative errorbars, as given by the photometry output, are shown aside the CMDs.

DOLPHOT vs DAOPHOT

We just point out that DOLPHOT is not the only photometry package that could be used for analyzing our data. However, it has the advantage to be more automated and thus quicker than, for example, DAOPHOT. Literature studies, moreover, show that the two packages do not give significantly different results for PSF photometry (e.g., Monelli et al. 2010, and references therein), although small discrepancies will always be present due to the different approaches of the photometry programs. As a quick comparison, we decide to run the photometry with IRAF/DAOPHOT for one of our early-type target galaxies (KK189).

We work on the drizzled images. We first find ~ 150 PSF stars (i.e., bright, not saturated, evenly distributed on the image) with the task DAOFIND, and iteratively compute the PSF for each filter until the subtraction of the PSF model to the stars on the image leaves us with no spurious features (e.g., oversubtracted stars or wings). We then run ALLSTAR to perform PSF fitting photometry on the whole image. The resulting photometry for each filter is calibrated with aperture corrections and photometric zero-points from Sirianni et al. (2005). We then combine the two subcatalogs into a final list of stars with the CataXcorr and CataComb programs (P. Montegriffo, private communication). The quality cuts applied in this case are: the photometric errors given by the photometry program have to be < 0.3 ; we set $\chi < 3$; and the sharpness parameter has an absolute value < 2 . The final CMD is shown in Fig. 2.1, together with the one derived using the DOLPHOT package (see previous Section). Note that the quality parameters have slightly different definitions within the two photometry packages, but with this combination of values the two CMDs still agree very well with each other, and show no systematic differences. It can be noticed that, in general, the CMD derived with DAOPHOT shows a larger scatter in its features, and reaches slightly fainter magnitudes; on the other hand, the photometric errors given by this program are also somewhat larger than the ones stemming from DOLPHOT. Overall, the differences are not significant (or at least less significant than many other factors, see next Chapter) for the purposes of our study, and we will thus not return

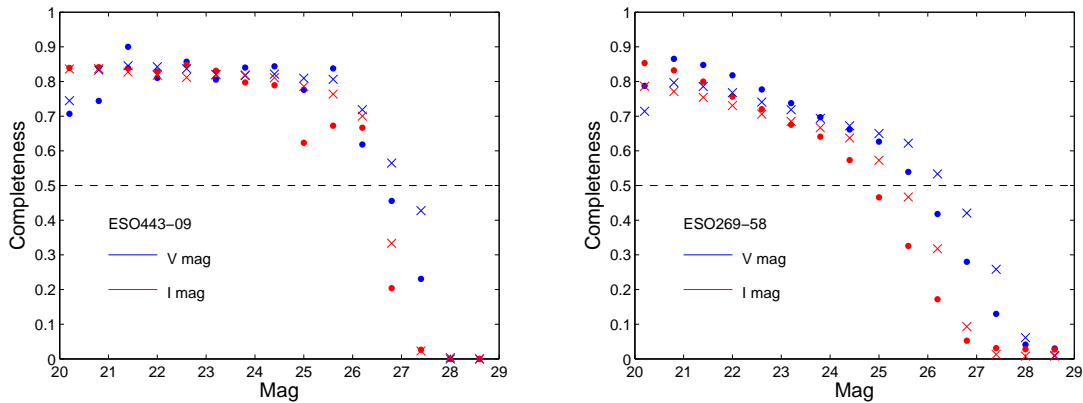


Figure 2.2: V - and I -band completeness curves for the least and most crowded galaxies in our sample, ESO443-09 (*left panel*) and ESO269-58 (*right panel*), respectively. The dashed line shows the 50% completeness level. Dots represent curves that were computed using stars from the central region of the galaxy, while crosses are for stars located in the outskirts of the galaxy (see text for details). The completeness curve falls off more rapidly in the case of ESO269-58, and it is steeper for the central regions of the galaxy, dominated by crowding.

to this point.

2.1.2 Artificial star tests

The DOLPHOT output includes photometric errors for each star, however, these errors do not account for systematic errors of the point spread function. Thus, extensive artificial star tests are performed for each of the studied objects, using the same photometry parameters and quality cuts of the original image, in order to estimate the photometric uncertainties and to assess the incompleteness effects. For each galaxy, we add $\sim 5 - 10$ times the number of observed stars to the images (after quality cuts), distributing them evenly across the ACS field of view and such that they cover the whole color and magnitude range of the observed stars. Moreover, the artificial stars are simulated also up to ~ 1 mag below our detection limit, in order to take into account objects that are actually fainter than what we observe, but that are detected because of an addition of noise. The artificial stars we add are measured one at a time by the DOLPHOT routine, in order to avoid artificial crowding. After running the photometry again with the artificial stars, we apply the same quality cuts as before.

We then derive completeness curves as a function of magnitude, and also as a function of radius, since we are interested in the radial properties of the galaxies' stellar populations (see, in particular, Chapter 3). We show an example of the magnitude-dependent completeness curves in both bands for the least crowded (ESO443-09, with a peak density of ~ 2 stars per arcsec^2 , corresponding to ~ 167 stars per 0.1 kpc^2) and the most crowded (ESO269-58, peak density of ~ 10 stars per arcsec^2 , or ~ 2520 stars per 0.1 kpc^2) of the studied galaxies in Fig. 2.2. Both these objects are late-type dwarfs. The fraction of recovered objects never reaches 1 because of bad pixels and cosmic rays. We can see that the completeness function is decreasing more rapidly in the case of a crowded field. At a 50% completeness level, the limiting magnitude for ESO443-09 is ~ 27.2 mag (~ 26.8 mag) for the V -band (I -band). At the mentioned I -band magnitude, the representative 1σ photometric error amounts to ~ 0.18 mag in magnitude and ~ 0.23 mag in color. For ESO269-58, the 50% completeness level is reached at ~ 26.2 mag (~ 25.3 mag) for

the V -band (I -band), while the corresponding 1σ photometric errors for this I -band magnitude are ~ 0.20 mag in magnitude and ~ 0.28 mag in color. In the same Figure, also the dependence of the completeness on galactic radius is shown. We compute the completeness for two subsamples of stars, which are located within and outside an ellipse corresponding to an isophote level of 25 mag arcsec $^{-1}$ in I -band (taken from Sharina et al. 2008), respectively. For ESO443-09 the two resulting curves differ very little, while for ESO269-58 the 50% completeness level is ~ 0.5 mag fainter for the outer sample than that for the central one due to the high crowding of the central regions.

Considering the early-type dwarfs, the limiting magnitude taken at a 50% completeness level is at ~ 27.3 (~ 26.8) mag in the V -band for the least (most) crowded objects of this sample, and at ~ 26.4 (~ 26.0) mag in I -band. The mentioned galaxies are Kks55 and ESO269-66, with peak stellar densities of ~ 390 and ~ 1240 stars per 0.1 kpc 2 . At a completeness level of 50%, the 1σ extremes of the photometric errors amount to ≤ 0.23 mag (≤ 0.16 mag) in I -band magnitude and ≤ 0.30 mag (≤ 0.21 mag) in $V - I$ color, for these two galaxies. The mean photometric errors ($\pm 1\sigma$) for all of the target galaxies are indicated by representative errorbars in the CMDs in the next Sections.

2.1.3 Optical color-magnitude diagrams

2.1.3.1 Galactic foreground contamination

Before presenting our optical CMDs, we discuss the Galactic foreground contamination issue. The CenA group lies at a low Galactic latitude on the sky ($b \sim 20^\circ$), and is thus affected by a substantial amount of Galactic foreground stars acting as contaminants. To give a first estimate, we use the TRILEGAL models (Girardi et al. 2005). TRILEGAL is a theoretical tool that was initially meant to produce stellar isochrones, synthetic photometry, and simulations of stellar populations (star clusters and external galaxies), and has recently turned into a Galaxy population synthesis star counts model. The photometry can be produced for many different broad- and intermediate-band systems, including non-standard ones. At the sky position of the target objects, and within the ACS field of view ($\sim 3 \times 3$ arcmin), there are between 170 and 260 simulated foreground dwarf stars (depending on the galaxy considered). Additionally, the TRILEGAL models provide the photometry of the simulated stars, so that we are able to check which regions of the CMD would be most affected by foreground stars. One has to carefully compare the mentioned number of contaminants to what is seen in the CMD of each galaxy. Let us begin considering the late-type dwarfs. We show as an example the original CMD for the dwarf ESO443-09 in Fig. 2.3: this is the least luminous late-type galaxy in our sample, the one with the smallest number of detected stars and thus one of the objects most affected by foreground contamination. We use a neighbor-counting algorithm to compute a density diagram (=Hess diagram), overlay it to make the features in the CMD more apparent, and plot the simulated Galactic foreground stars from TRILEGAL as red crosses. Overall, the contaminant fraction is less than 10% and is only affecting the red part of the CMD. However, when looking at the strip with magnitudes $23 < I < 25$ and colors in the range $1 < V - I < 1.3$ (red supergiant or RSG region, see description below), we clearly see that the ratio between number of dwarf galaxy stars (corrected for incompleteness) and number of foreground stars is quite high, as much as $\sim 22\%$ in this case. The same is true also for ESO381-18, ESO444-78, KK182, KK196, HIPASS J1348-37, and ESO384-16, ESO269-58 (respectively with contami-

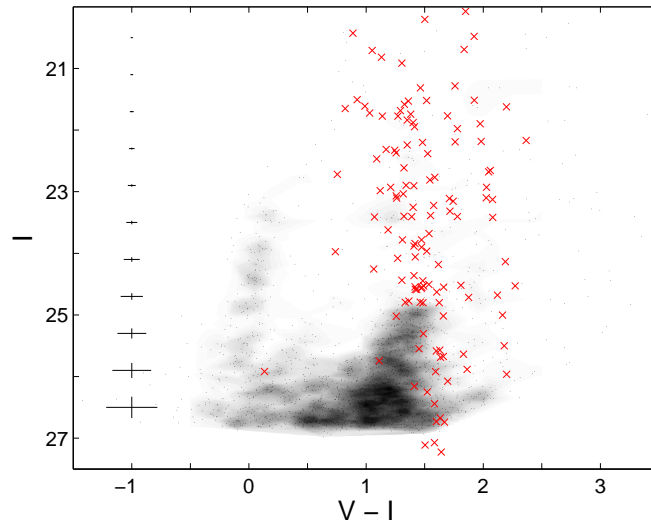


Figure 2.3: Color-magnitude diagram of the dwarf irregular galaxy ESO443-09 (black dots), overlaid by a Hess density diagram of its stars (gray areas). Overplotted are also Galactic foreground stars (red crosses), simulated with the TRILEGAL models. We do not include incompleteness effects or photometric errors in the simulations. The expected foreground contamination affects in particular the region above the tip of the red giant branch (see text for details). On the left side of the diagram, typical 1σ photometric uncertainties are reported.

nant fractions of $\sim 20\%$ and $\sim 25\%$, $\sim 12\%$, $\sim 11\%$, $\sim 13\%$, $\sim 16\%$, and $\sim 22\%$). For IC4247 and ESO381-20, the CMDs are well populated, and the fraction of Galactic foreground objects in the RSG region rather small (5% and 2%, respectively). The foreground contamination is also affecting the AGB region, although this is less critical than for the RSG region. Below we will see that this is particularly important for the early-type dwarfs.

We thus decide to perform a statistical foreground subtraction over the whole CMD for the galaxies where the contaminant fractions are not negligible. We adopt the following method: we first randomly extract a subsample of objects from the list of foreground stars simulated by the TRILEGAL models, in order to account for the incompleteness of our observations (different values for different color and magnitude ranges). Then, we consider the observed galaxy stars that are found in a circle around each simulated foreground object, with a radius equal to two times the error in color at that position in the CMD. If more than one observed star is found within that circle, we simply subtract one of them randomly. We test this procedure a number of times for the same galaxy, to check whether the random choice of the subtracted stars would change the overall shape of the RSG region, but it does not. Finally, we point out that the decontamination process for IC4247 and ESO381-20 would leave all of our results unchanged because the contaminants fractions are very low, so we decide not to perform it in these cases.

The final result of this statistical “decontamination” will be to slightly degrade the quality of the fit when deriving their SFHs (see Chapter 5), without however adding a significant bias. On the other side, we expect the foreground contaminants to be distributed rather uniformly across the ACS field of view, so their subtraction will not change the main features of the stellar density maps presented in the next Chapters.

Coming to the early-type dwarfs, their predominant stellar population consists of RGB stars and a few AGB stars more luminous than the TRGB (see next Section). When looking at

Fig. 2.3, we already see from the CMD of ESO443-09 that the amount of Galactic foreground stars overlapping with the RGB region is very small. In the next Chapter, we will derive photometric MDFs starting from RGB stars, and thus this is the part of the early-type dwarfs' CMDs in which we are most interested.

From Fig. 2.3 we also see that the contamination is not negligible for the upper part of the CMD above the TRGB, and this is especially problematic for the early-type dwarfs since their number of luminous AGB stars is very low (see also Fig. 2.4). It is impossible from the optical observations alone to thus clearly distinguish between real AGB stars and foreground contaminants. This point will be considered again below, where we investigate the contribution from intermediate-age objects in more detail. We will discuss the effects that Galactic foreground stars could have on our resulting MDFs in Chapter 3, but given that the predicted contaminants are few in the RGB, we just mention here that we do not statistically subtract them from the CMDs of our target early-type dwarfs.

On the other hand, we stress that the foreground contamination for these galaxies is substantial in the region above the TRGB, where intermediate-age, luminous AGB stars are found. Since the statistical decontamination is not a unique process, from the optical data alone it is not possible to unambiguously estimate the number and/or true membership of these AGB stars, and we have to use alternative methods if we want to obtain more precise information about their IAPs. Previous studies have shown that luminous AGB stars, indicative of such an IAP, are brighter in the NIR bands, and that the foreground is easier to separate from the galactic stellar content with this kind of data (e.g., Rejkuba et al. 2006; Boyer et al. 2009). The combination of optical and NIR data is thus a powerful tool to investigate to which extent and at which ages the target dwarfs produced their IAPs. This is the reason why we analyze data at these wavelengths for our target early-type dwarfs. We will extensively return to this point in the next Sections.

2.1.3.2 Early-type dwarfs

The CMDs of the six early-type target galaxies are shown in Fig. 2.4, ordered by increasing absolute V magnitude of the galaxies. The number of stars in the final (after quality cuts) photometric catalogs is 2720, 10401, 6684, 3675, 26713 and 39064 for KKs57, KKs55, CenN, KK189, KK197 and ESO269-66, respectively. The CMDs all show prominent RGBs, where stars may encompass a wide range of ages, starting with ages as young as 1 – 2 Gyr. An accurate age-dating is not possible for these stars due to the metallicity-age degeneracy present in the RGB (see below). The observations reach ~ 2.5 mag (I -band) below the TRGB. The latter is computed by Karachentsev et al. (2007) using the same dataset to derive the distances of the galaxies. We recompute the TRGB from the I -band luminosity function using a Sobel edge-detection filter. We find $I_{0,TRGB} = 24.02 \pm 0.12, 23.93 \pm 0.13, 23.76 \pm 0.13, 24.13 \pm 0.12, 23.96 \pm 0.13$ and 23.83 ± 0.12 for KKs57, KKs55, CenN, KK189, KK197 and ESO269-66, respectively, where the errors come from a combination of observational uncertainties and the luminosity function bin size. Not surprisingly, our results agree with the results of Karachentsev et al. (2007) (see Table 2.1, where we report the not dereddened values), although their technique for estimating the errors is more accurate (see, e.g., Karachentsev et al. 2007) and we will thus continue to use the values given in their study.

Populations with ages of a few Gyr (“intermediate-age stars”, $\sim 1-9$ Gyr) can be recognized by several additional features including more luminous MSTOs, RC and vertical RC stars, and luminous AGB stars with luminosities greater than the TRGB. Unfortunately, the HST data

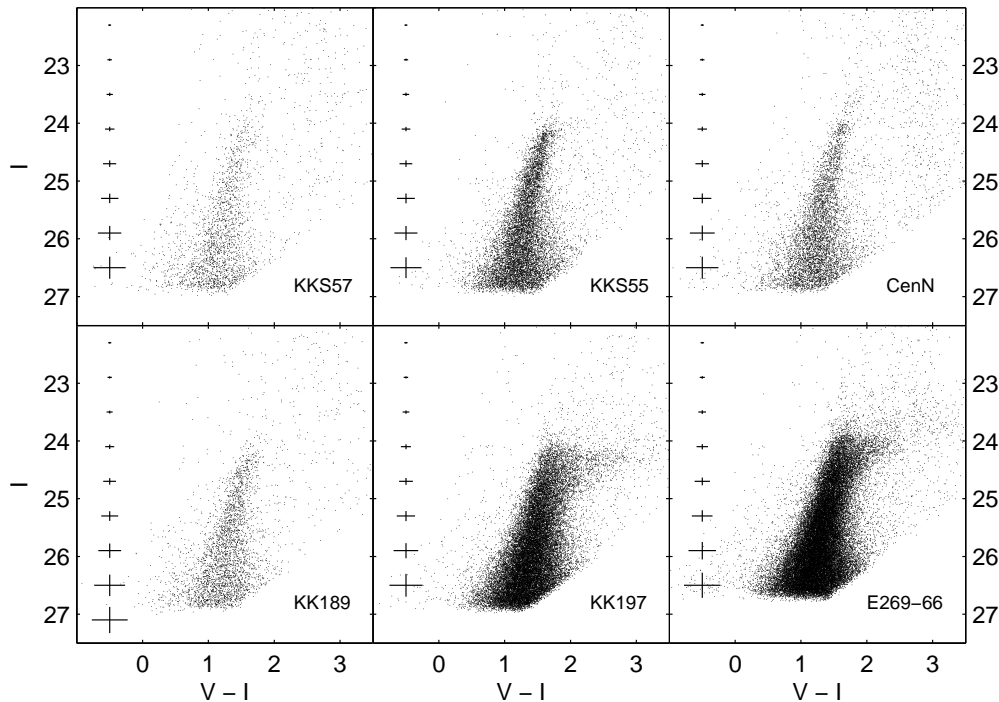


Figure 2.4: Color-magnitude diagrams of the six early-type dwarf galaxies studied here, ordered by increasing absolute V magnitude of the galaxies. The main feature visible in all of the CMDs is a prominent RGB, while luminous AGB stars are less numerous (see text for an estimate for each galaxy). Representative errorbars derived from artificial star experiments are shown on the left side of the diagrams. At an I -band magnitude of 25.5, the 1σ photometric errors (from artificial tests) are ~ 0.1 mag in magnitude and ~ 0.15 mag in color (see text for details).

are not deep enough to reach the MSTOs or the RC stars of the IAPs, as these are below our detection limit of ~ 27 I -band apparent magnitude (the RC would be expected to have a magnitude of ~ 28 in the same band). However, we can infer the presence or absence of IAPs from the presence or absence of luminous AGB stars. Even younger stars (< 1 Gyr) are definitely not present in these galaxies, as there are no objects found in the region blueward of the RGB (i.e., upper MS, or massive blue and red helium-burning stars, see also next Section). A quantitative evaluation of the amount of intermediate-age stars, and how it affects our results, is presented in Chapter 3. Similar evidence of intermediate-age components has also been found in some of the dwarf spheroidals and dwarf ellipticals of the Local Group, such as Leo I, Leo II, Fornax, Carina, NGC 147, NGC 185 and NGC 205 (e.g., Han et al. 1997, see also Chapter 1).

In the CMDs of Fig. 2.4, we also show representative photometric errors derived from artificial star tests. The (1σ) error is ~ 0.1 mag in magnitude and ~ 0.15 mag in color at an I -band magnitude of 25.60 for KKS57, 25.55 for KKS55, 25.50 for CenN, 25.55 for KK189, 25.45 for KK197 and 25.30 for ESO269-66. The RGB is thus partly broadened by photometric errors in the observed CMDs. However, the broadening does not come entirely from the errors, so is also associated with the physical properties of the galaxies. In particular, the color spread across the RGB could stem from either age or metallicity. There is a well known degeneracy in this evolutionary stage, such that stars that are younger and more metal-rich may be found in

the same RGB region as stars that are older and more metal-poor. Ideally, for a “simple” stellar population a spread in age would produce a narrower RGB at the same metallicity than would a spread in metallicity at a constant age (see, for example, Vandenberg et al. 2006). Owing to the relatively small number of luminous AGB stars above the TRGB, we may assume that the majority of the RGB stars belong to old populations (~ 10 Gyr or older). Because of this, and also because early-type dwarfs in the Local Group all display metallicity spreads, we assume that the color spread across the RGB is predominantly caused by a metallicity range within these galaxies. Our final goal is then to derive photometric MDFs from the optical CMDs.

We want to stress that a spread in metallicity would imply the presence of an age spread as well ($\sim 1 - 2$ Gyr), such that the first generation of stars born in the galaxy would have time to evolve and pollute the surrounding interstellar medium, making it possible for the next star formation episodes to produce more metal-rich stars (see, e.g., Ikuta & Arimoto 2002; Marcolini et al. 2006, 2008). This spread at such old ages is, however, not resolvable from the upper part of the RGB alone, and from the optical data we can only try to put some constraints on the age range of the IAPs from the number and brightness of the luminous AGB stars. The unresolvable spread in age for old populations could have the effect of inflating the derived metallicity spreads by 10 – 20% (as computed in the next Chapter). On the other side, the possible presence of intermediate-age stars would also affect the metallicity spreads in a way that depends on each individual galaxy’s characteristics, and it deserves more careful attention. Both these aspects will be discussed in detail in the next Chapter.

2.1.3.3 Late-type dwarfs

The CMDs for our ten late-type target galaxies, ordered by absolute magnitude, are presented in Fig. 2.5 (M83 companions in the upper panel and CenA companions in the lower panel). For ESO443-09, ESO381-18, ESO444-78, HIPASS1348-37, KK196, KK182, ESO384-16 and ESO269-58 we show the foreground subtracted diagrams (see previous Section). The number of stars resolved for the target galaxies is 1931 for ESO443-09, 7312 for ESO381-18, 11370 for ESO444-78, 17813 for IC4247, 19936 for ESO381-20, 3271 for HIPASS1348-37, 7328 for KK196, 4079 for KK182, 17194 for ESO384-16 and 136298 for ESO269-58. The reported numbers are the final values after the foreground decontamination, except for IC4247 and ESO381-20, for which we do not perform a subtraction. Also shown on the left-hand side of each diagram are the mean photometric uncertainties for each magnitude bin, as derived from the artificial star tests. In particular, the 1σ error is ~ 0.1 mag in magnitude and ~ 0.15 mag in color at different I -band magnitudes for different galaxies, and more precisely: 25.50 for ESO443-09, 25.30 for ESO381-18, 25.45 for ESO444-78, 25.30 for IC4247, 25.35 for ESO381-20, 25.40 for HIPASS1348-37, 25.40 for KK196, 25.55 for KK182, 25.30 for ESO384-16, and 24.30 for ESO269-58. These error limits will be used in Chapter 5 to define different stellar subsamples.

The CMDs of all of the late-type dwarf galaxies exhibit the following evolutionary stages:

- upper MS: a blue plume of MS candidates (and blue helium-burning stars) is found in the color range of $-0.5 \leq V - I \leq 0$ and at magnitudes of $I \geq 22$ (Fig. 2.5). The youngest and most massive stars detected in our CMDs have estimated ages of ~ 4 Myr (as derived in Chapter 5);

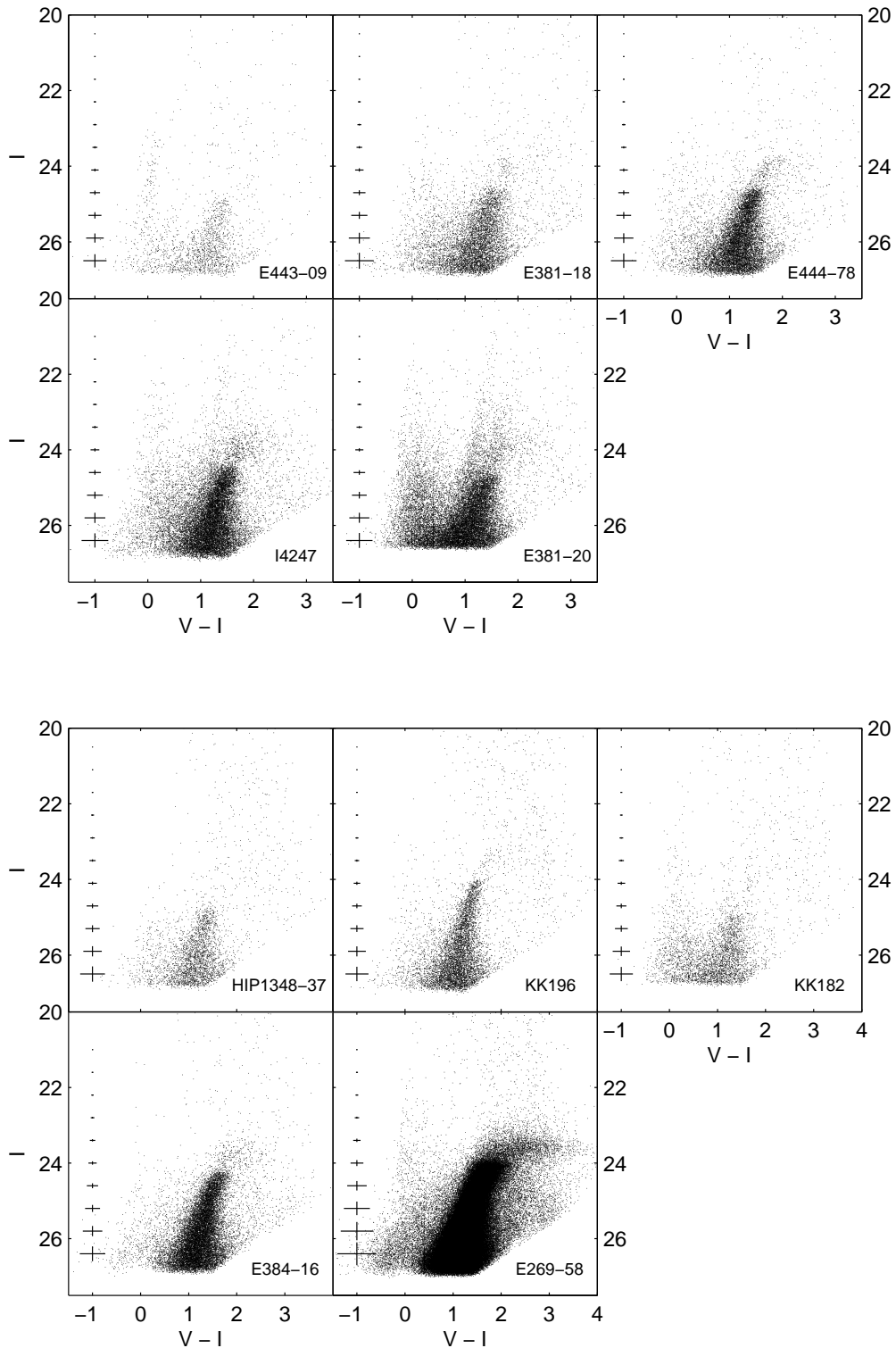


Figure 2.5: Color-magnitude diagrams for the ten late-type dwarf galaxies studied here, ordered by (increasing) absolute magnitude. The companions of M83 are shown in the *upper panel*, while the companions of CenA are in the *lower panel*. The galaxies ESO443-09, ESO381-18, ESO444-78, HIPASS J1348-37, KK196, KK182, ESO384-16 and ESO269-58 have been statistically “decontaminated” from foreground stars. The main features visible in all of the diagrams are the blue plume (main sequence and blue helium-burning stars, very sparsely populated for HIPASS1348-37, KK196, and ESO384-16), the upper red giant branch, the luminous asymptotic giant branch (in all but for ESO443-09 and HIPASS1348-37) and for IC4247 and ESO381-20 also a prominent red supergiant region. On the left side of each diagram, representative 1σ photometric errorbars as derived from artificial star tests are shown.

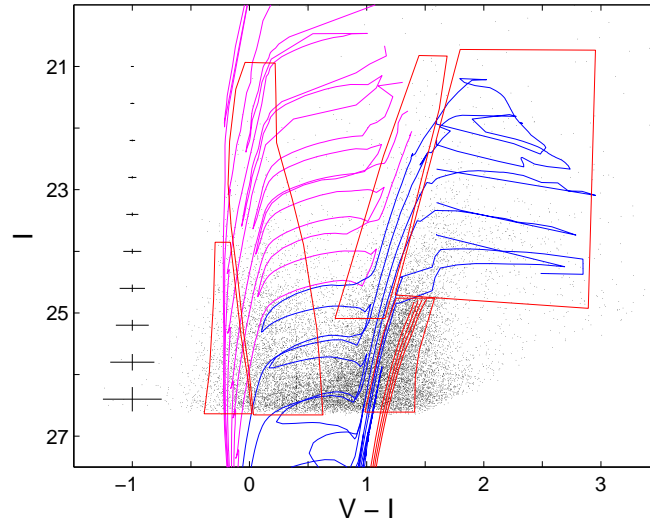


Figure 2.6: Color magnitude diagram of the dwarf irregular galaxy ESO381-20. Overlaid are Padova stellar isochrones, with a fixed metallicity of $Z=0.0008$ and varying ages. Ages of 4, 8, 15, 20, 35, 55 and 85 Myr (proceeding from the blue to the red part of the CMD) are drawn in magenta, ages of 130, 200, 350, 550, 800 Myr and 1.3 Gyr are in blue, and ages of 4, 7, 10 and 14 Gyr are in red (see text for details). Also plotted are selection boxes (red) that separate different evolutionary stages (MS, BL, RSG, RGB and AGB, from the blue to the red part of the CMD). On the left side of the diagram, typical 1σ photometric uncertainties are reported. For example, they are of ~ 0.1 mag in magnitude and ~ 0.15 mag in color at a magnitude of $I \sim 25.35$ (see text for details).

- helium-burning stars: massive stars with ages from ~ 20 to 500 Myr are visible in the CMDs in the so called “blue-loop” phase, burning helium in their core. These evolved supergiants comprise blue ($V - I \sim 0$ to 0.5) and red ($V - I \sim 1$ to 1.3) supergiants. The latter are however not prominent for the galaxies in which the star formation was low some ~ 100 to 500 Myr ago (on the contrary, this feature is very well populated for IC4247 and ESO381-20);
- AGB: lower mass stars with ages between ~ 0.1 and ~ 9 Gyr are found along the RGB and above its tip. The latter (luminous AGB stars) are well visible at colors of $1.3 \leq V - I \leq 2.5$, except for ESO443-09 and HIPASS1348-37, which contain very few of these objects;
- upper RGB: these are evolved stars with colors in the range $V - I \sim 1$ to 1.8, and indicative of intermediate-age and old ($\geq 1 - 2$ Gyr) low-mass stars which have not yet commenced core helium-burning. Up to $\sim 20\%$ of the stars along the apparent upper RGB are in fact faint AGB stars in the same age range as the RGB stars (e.g. Durrell et al. 2001, see also the discussion in the next Chapter).

To help the eye recognize the various features, we plot the CMD of the galaxy ESO381-20 in Fig. 2.6 and overlay Padova isochrones. We choose a metallicity of $Z=0.0008$ (which roughly corresponds to $[\text{Fe}/\text{H}] \sim -1.4$, assuming $Z_{\odot}=0.019$), since this is the best-fit average metallicity resulting from our synthetic CMD modeling (see Chapter 5). The isochrone ages range from 4 Myr to 14 Gyr (from the blue to the red side of the CMD). We draw the “very young” ages (4 to 85 Myr, encompassing upper MS and most of the blue helium-burning stars)

in magenta, the “young” ages (130 Myr to 1.3 Gyr, clearly showing where most of the red helium-burning stars and the most luminous AGB stars lie) in blue, and the “intermediate” and “old” ages (4 to 14 Gyr, for which only the upper RGBs and luminous AGB stars are visible at this photometric depth) in red. These isochrones were truncated at the TRGB omitting the thermally pulsing AGB stars, to avoid overcrowding in the plot. We point out that the previous color-coding of “very young”, “young”, “intermediate” and “old” ages is arbitrary, and simply meant to illustrate the diverse features of the CMD, which were described above.

In Fig. 2.6 we also show the selection boxes that separate different evolutionary stages for ESO381-20, which are used in Chapter 5. We select different evolutionary stages in the CMDs following the stellar sequences for each individual galaxy and referring to the Padova isochrone models. The stellar content of each galaxy is divided in: RGB, MS, blue helium-burning stars (or blue loop, BL), red helium-burning stars (or RSG), and luminous AGB. We stress that the upper RSG region is not well reproduced by the models, in the sense that the observed stars are redder than predicted (e.g. Úbeda et al. 2007, and references therein), and we thus follow the stellar sequence on the CMD to define our selection box.

The presence of many different evolutionary stages clearly indicates the presence of a prolonged star formation, and each one represents a range of stellar ages. Depending on the number of stars that are found in each stage and depending on the time resolution that the CMD offers, it is possible to quantitatively constrain the star formation rate (SFR) of a galaxy during its past history. In the analysis of Chapter 5, our purpose is to derive the SFHs of the target late-type galaxies, making use of a code written by A. A. Cole.

2.2 NIR data

Within the ESO observing programme 073.B-0131 we collected NIR observations of 14 early-type dwarfs in the CenA Group. We now choose to study in detail here those galaxies that could be fully resolved (due to good seeing conditions) in their stellar content from these observations, and for which archival HST data are available, similarly to what was already done by Rejkuba et al. (2006). The sample consists of three objects, namely KK189, KK197 and ESO269-66 (in order of increasing luminosity). Their general properties were already reported in Table 2.1.

Deep NIR images of the target dwarfs were taken in service mode with the short wavelength arm of ISAAC NIR array at the VLT at ESO Paranal Observatory. The field of view of the short wavelength arm of ISAAC is 2.5×2.5 arcmin² and the detector has a pixel scale of 0.148 arcsec. Each galaxy was observed once in the J_S -band using 4 coverages of 35 sec exposures at 15 different dither positions, amounting thus to a total exposure time of 2100 sec per galaxy. K_S -band images were taken at two different epochs with 7 coverages of 12 sec exposures at 28 different dither positions, amounting to a total exposure time of 4704 sec per galaxy. For KK197 the J_S -band observation had to be repeated because of violated seeing constraint, while for KK189 one K_S -band observation was repeated because other observational constraints were violated. The observing log is reported in Tab. 2.3, with the following columns: (1): galaxy name; (2): date of observation; (3): filter; (4): exposure time; (5): airmass; and (6): seeing of the combined images.

The standard procedure in reducing IR data consists of dark subtraction, flat-field correction, sky subtraction, registering and combining the images (performed by M. Rejkuba). The details of ISAAC data reduction with IRAF are described by Rejkuba et al. (2001). At the end of the

Table 2.3: NIR imaging observing log.

Galaxy	Date dd/mm/yy	F	t_{exp} sec	AM	Seeing arcsec
KK189	21/04/04	K_S	2352	1.23	0.59
	11/05/04	K_S	2352	1.08	0.34
	27/05/04	K_S	2352	1.21	0.41
	27/05/04	J_S	2100	1.11	0.44
KK197	14/05/04	K_S	2352	1.44	0.43
	10/07/04	K_S	2352	1.11	0.47
	10/07/04	J_S	2100	1.20	0.77
	19/07/04	J_S	2100	1.32	0.44
ESO269-66	11/05/04	K_S	2352	1.20	0.41
	31/05/04	K_S	2352	1.12	0.34
	31/05/04	J_S	2100	1.21	0.41

Notes. For each galaxy all the dithered sequences for both filters (F) are listed in order of observing dates. Airmass (AM) is given for the central image in each sequence. Exposure time (t_{exp}) is in sec and seeing in arcsec as measured on the combined images.

reduction all the images taken in a single dithered sequence were combined. From now on when we refer to an image in J_S -band or K_S -band we always refer to these combined dithered sequences, and we also drop the “s” subscript and just use the nomenclature convention J - and K -band.

2.2.1 Photometry

For all the targets PSF fitting photometry was done (by M. Rejkuba) using the suite of DAOPHOT and ALLFRAME programmes (Stetson 1987, 1994). The steps for each galaxy target included the following. For each image we detected all the point sources and determined its PSF using at least 30 relatively bright, non-saturated stars, well spread across the field (using the FIND, PHOT and ALLSTAR tasks). For the observations in both filters the coordinate transformations were derived with DAOMATCH and DAOMASTER. The complete star list was then created from the median combined image obtained with MONTAGE2, which is deeper than the single images. In case of large variations of seeing between different images, the worst seeing image was not used in the median combination. PSF fitting photometry using this star list and these coordinate transformations was performed simultaneously on each image using ALLFRAME. The final photometric catalog for each galaxy contains all the sources that could be measured in both J -band and at least one K -band image. We further apply the following quality cuts to the catalog: the photometric errors (as measured by ALLFRAME) are smaller than 0.3 mag in both bands; the sharpness parameter has an absolute value ≤ 2 ; and we impose $\chi \leq 1.5$. The number of stars from the NIR photometry in each galaxy is: 347 (KK189), 1505 (KK197) and 3428 (ESO269-66).

We have tied our photometry to the 2MASS photometric system (Carpenter 2001)⁴ by

⁴http://www.ipac.caltech.edu/2mass/releases/allsky/doc/sec6_4b.html/.

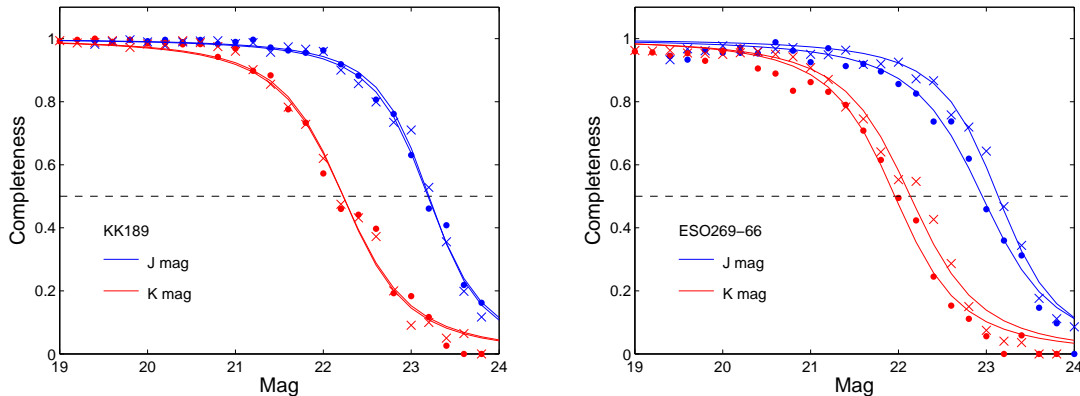


Figure 2.7: J - and K -band completeness curves for the least and most crowded galaxies in our sample, KK189 (*left panel*) and ESO269-66 (*right panel*), respectively. The dashed line shows the 50% completeness level. Dots represent curves that were computed using stars from the central region of the galaxy, while crosses are for stars located in the outskirts of the galaxy (see text for details). We overplot to the curves the best-fitting analytic completeness functions as solid lines (Fleming et al. 1995). Even for the most crowded field, the two curves differ very little.

matching all the point sources from 2MASS observed in our fields with our J -band and K -band detections. Zero points for each galaxy included thus the correction for the atmospheric extinction. Typically more than 7 stars had 2MASS magnitudes, resulting in errors of the order of 0.02 to 0.1 mag in the J -band and 0.03 to 0.15 mag in the K -band.

2.2.2 Artificial star tests

Completeness and magnitude errors were measured using artificial star tests. Fake stars were added to each image using its measured PSF and adding the expected noise. They are located on a grid, separated by at least $2 \times \text{PSF}$ in order not to increase the crowding artificially, for a total number of $\sim 5 - 10$ times the observed number of stars subdivided into 30 runs. Photometry of all the stars was then performed and typical photometric errors derived as the difference between input and recovered magnitude. We also compute the percentage of recovered simulated stars, and test to which extent stellar crowding affects the completeness of the observations. KK189 is the least crowded galaxy of this sample, while ESO269-66 the most crowded. We choose an elliptical radius that divides the stellar sample into a central subsample (which should be the most affected by crowding) and a subsample containing stars in the outskirts of the galaxies. To define this radius, we use the stellar density profiles computed in the next Chapter. KK189 is off-center in the ISAAC field of view, so we can use the galaxy limiting (=tidal) radius, beyond which almost only field stars are found. ESO269-66 is more extended than the field of view, so we adopt the half-light radius (see again next Chapter). The completeness curves are shown in Fig. 2.7, for both J - and K -band and for both central and external stellar subsamples. This function is well represented (see Fleming et al. 1995) by an analytical function of the form

$$f = \frac{1}{2} \left[1 - \frac{\alpha(m - m_0)}{\sqrt{1 + \alpha^2(m - m_0)^2}} \right].$$

We fit our completeness curves with this analytical function, and overplot the best-fit solu-

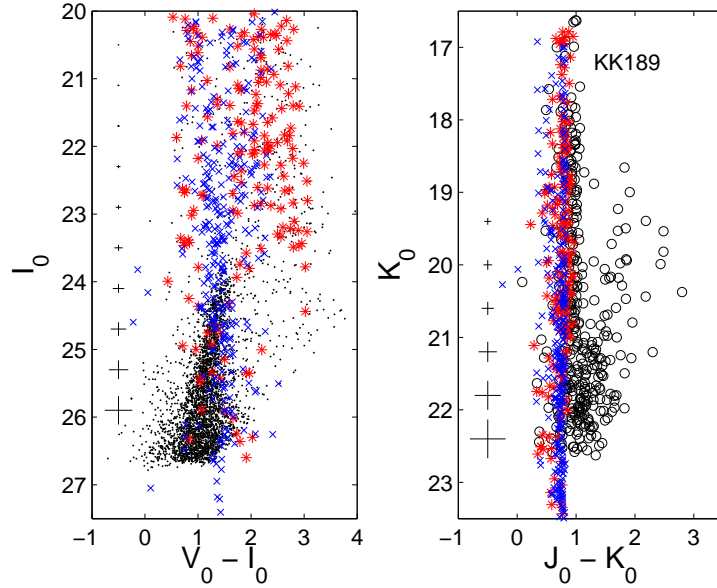


Figure 2.8: Optical (*left panel*) and NIR (*right panel*) dereddened CMDs for KK189. Representative photometric errorbars are plotted on the left side of the CMDs. The blue crosses represent the Galactic foreground contamination as predicted by TRILEGAL models, while the red asterisks are simulated using the Besançon models. Note that the simulated data do not include corrections for photometric errors, nor are corrected for incompleteness. The models show that the optical CMD is heavily contaminated by foreground objects in the region above the TRGB, while in the NIR CMD it is easier to disentangle foreground stars from the stars belonging to KK189.

tions in Fig. 2.7. Also in the case where the crowding is higher, namely for ESO269-66, the completeness is not changing significantly as a function of galactic radius. For example, for ESO269-66 the 50% completeness limit (in both bands) is only ~ 0.2 mag fainter for the external subsample than for the central one. From now on we will thus assume the completeness to be constant with radius. The photometric errors we derive are shown for each galaxy in Fig. 2.9, along the CMDs.

2.2.3 Near-infrared color-magnitude diagrams

We already mentioned that the low galactic latitude of the CenA group ($b \sim 20^\circ$) means that a non negligible amount of Galactic foreground stars contaminates the CMDs of our target galaxies. In Section 2.1.3.1 we claimed that this contamination would not influence the results about the metallicity content of our early-type target galaxies, but it certainly does affect the upper part of the observed CMDs. As pointed out in the previous Section, from the current optical observations (see Fig. 2.4) we can exclude the presence of stars younger than ~ 1 Gyr in these galaxies from the absence of an upper MS or supergiant stars, but above the TRGB of each galaxy we can see a number of stars that are probably luminous AGB stars. They are the bright tip of the iceberg of an IAP (~ 1 to 9 Gyr), which we expect to find at this position for metal-poor stellar populations. For populations more metal-rich than $[\text{Fe}/\text{H}] \sim -1.0$, some old and metal-rich stars may also be found above the TRGB, but our target objects are predominantly metal-poor (as computed in the next Chapter), so we conclude that the presence of such stars is not significant in our sample.

To show the effects of the foreground contamination on our CMDs, we simulate the expected foreground using both the TRILEGAL models (Girardi et al. 2005) and the Besançon models (Robin et al. 2003). The stellar population synthesis model developed by the Besançon group is used to elaborate a global view of the Galaxy including dynamical and evolutionary aspects. The derived theoretical distribution functions are directly compared with survey observations of different types (photometry, kinematics, abundance distributions), and permit thus to derive observational predictions from an overall description of Galactic structure and evolution. For our purposes, the TRILEGAL and Besançon models produce similar outputs, but there are small differences in the implementation of the underlying physics involved in the simulations. An example of the contamination on our CMDs is shown in Fig. 2.8. We plot both optical and NIR (dereddened) CMDs for KK189, and overplot the positions of foreground stars predicted by the two models (blue crosses for TRILEGAL and red asterisks for Besançon), without taking into account incompleteness and photometric errors. Just for comparison purposes, we only plot stars simulated by Besançon models that have masses $> 0.15M_{\odot}$, since the TRILEGAL models do not include them in their computation. These few, very low-mass stars would have the effect of extending the Besançon plotted sequence to slightly redder colors. We can notice that at magnitudes $K_0 \lesssim 20.5$ and colors $J_0 - K_0 \lesssim 1$ (where only foreground stars are found), the number counts resulting from the models are comparable to each other, and similar to the number of observed stars. We stress, however, that the models give slightly different results, and in particular the Besançon model reaches slightly redder colors, but a comparison between the models is beyond the goals of this study. Overall, it is clear from the left panel that the luminous AGB region is the most affected in the optical, and we have no way of determining which stars belong to the dwarf galaxy and which are part of the foreground.

The NIR CMDs for the target galaxies are presented in Fig. 2.9. We have corrected the magnitudes for foreground reddening, referring to the NED values derived from the Schlegel extinction maps (Schlegel et al. 1998). For all of the galaxies, the upper part of the RGB is visible at $J_0 \gtrsim 23$ and $K_0 \gtrsim 22$, and the stars above this limit are likely belonging to their IAPs. We also overplot the 50% completeness limits in all of the panels. We further show three isochrones on each CMD: the first has the lowest metallicity value for that galaxy (corresponding to the lowest metallicity available from the isochrone set), the second represents the median metallicity (derived in the next Chapter and found in Table 3.1), and the last the highest metallicity value found.

We compute the expected TRGB magnitude in both bands using the formulae given in Valenti et al. (2004), assuming the distance moduli derived in the previous Section and the median metallicities which we derive in the next Chapter (Table 3.1). The resulting values are: $J_{0,TRGB} = 22.96 \pm 0.18$, 22.56 ± 0.18 and 22.56 ± 0.18 , and $K_{0,TRGB} = 22.00 \pm 0.18$, 21.50 ± 0.18 and 21.52 ± 0.18 for KK189, KK197 and ESO269-66, respectively. We emphasize that the TRGB is not constant as a function of metallicity in these bands, in other words its luminosity depends on the metallicity value of the galaxy and all of our targets have a considerable metallicity spread within them. However, as can be seen from the MDFs presented in the next Chapter, most of the stars in a galaxy have metallicity values around the median value, so that in the luminosity function of the galaxy the TRGB will still be recognizable as a fall-off (although not a neat one, as would be the case in I -band). We thus check our resulting values by additionally plotting the luminosity function for both bands in Fig. 2.10. The luminosity functions have been dereddened, and for each magnitude bin the number of predicted Galactic foreground stars from TRILEGAL (similar to that given by Besançon) has been subtracted,

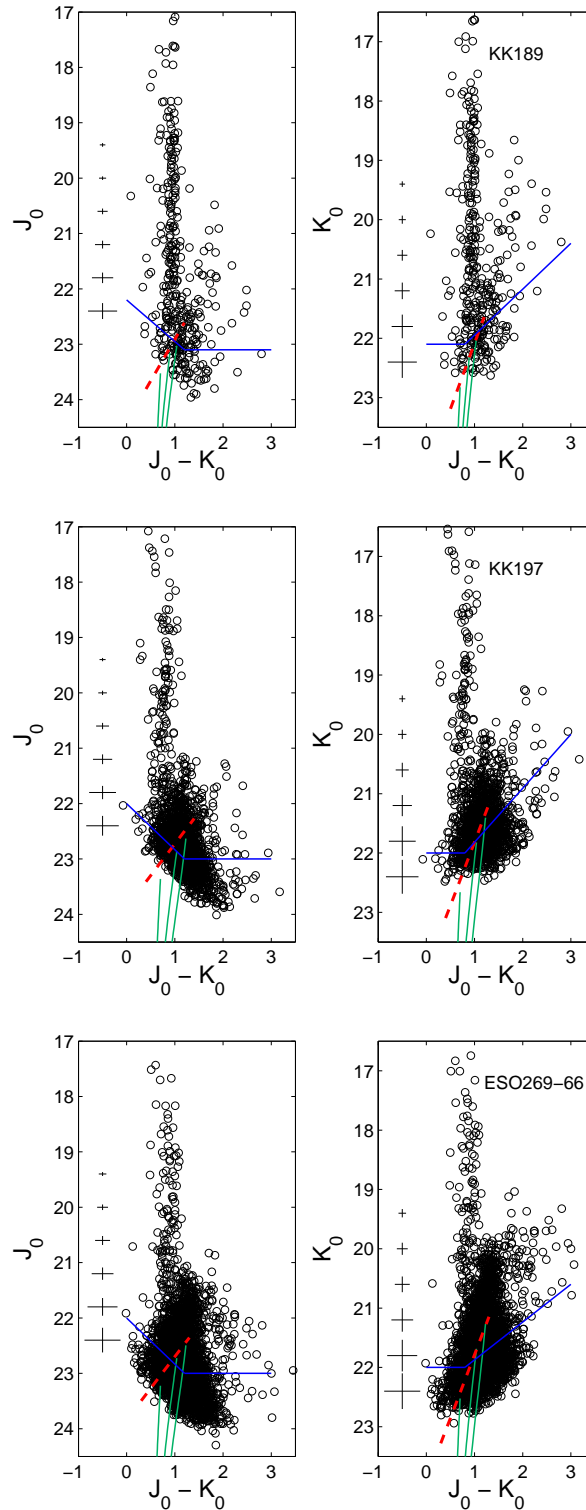


Figure 2.9: NIR (dereddened) CMDs of the target galaxies, ordered by increasing luminosity. Representative photometric errorbars are plotted along the CMDs. The red dashed lines indicate the expected position of the TRGB as a function of metallicity (see text for details). The green lines are isochrones with a fixed age of 10 Gyr and spanning the metallicity range of each target galaxy. They have the following values: $[\text{Fe}/\text{H}] = -2.5, -1.52$ and -1.1 (from the blue to the red side) for KK189; $[\text{Fe}/\text{H}] = -2.5, -1.08$ and -0.4 for KK197; $[\text{Fe}/\text{H}] = -2.5, -1.21$ and -0.4 for ESO269-66. The blue solid lines indicate the 50% completeness limits.

after considering incompleteness effects. The expected values derived with the Valenti et al. (2004) formula using the median metallicities are shown in Fig. 2.10 as arrows, and agree well with the observations. We moreover overlay a line to the arrows indicating the possible range of TRGB values stemming from the range of metallicities, again computed following the Valenti et al. (2004) TRGB calibration equation. In addition, the NIR CMDs suffer from much larger incompleteness and photometric errors than the optical CMDs (Fig. 2.4), such that the most metal-poor end of the RGB is below the detection limit in KK189 and KK197, while it is close to detection limit for ESO269-66. As a reference, in Fig. 2.9 we also overplot stellar isochrones on the CMDs to indicate the metallicity range of the galaxies, and we draw a dashed line passing through the TRGB values computed from the lowest, the median and the highest metallicities found for each galaxy with the Valenti et al. (2004) formula, finding a good agreement with the theoretical isochrones (see next Chapter).

Also the NIR CMDs are contaminated by Galactic foreground, but this time the luminous AGB region is not as heavily affected as it is in the optical observations (see right panel of Fig. 2.8). The vertical feature extending from $J_0 - K_0 \sim 0.3$ to ~ 1.0 in Fig. 2.8 and 2.9 and over the whole magnitude range is mainly due to Galactic old disk turnoff stars ($J_0 - K_0 \sim 0.36$), Galactic RGB and RC stars ($J_0 - K_0 \sim 0.65$), and low-mass dwarfs with $M \leq 0.6M_\odot$ ($J_0 - K_0 \sim 0.85$, Girardi et al. 2005). The fact that these stars are distributed in vertical sequences is due to the range of distances and luminosities that they span. In the next Chapter, for our analysis of the stellar populations of the early-type target galaxies, we will take advantage of the fact that the Galactic foreground contamination is more easily recognizable in the NIR CMDs to look for AGB candidates.

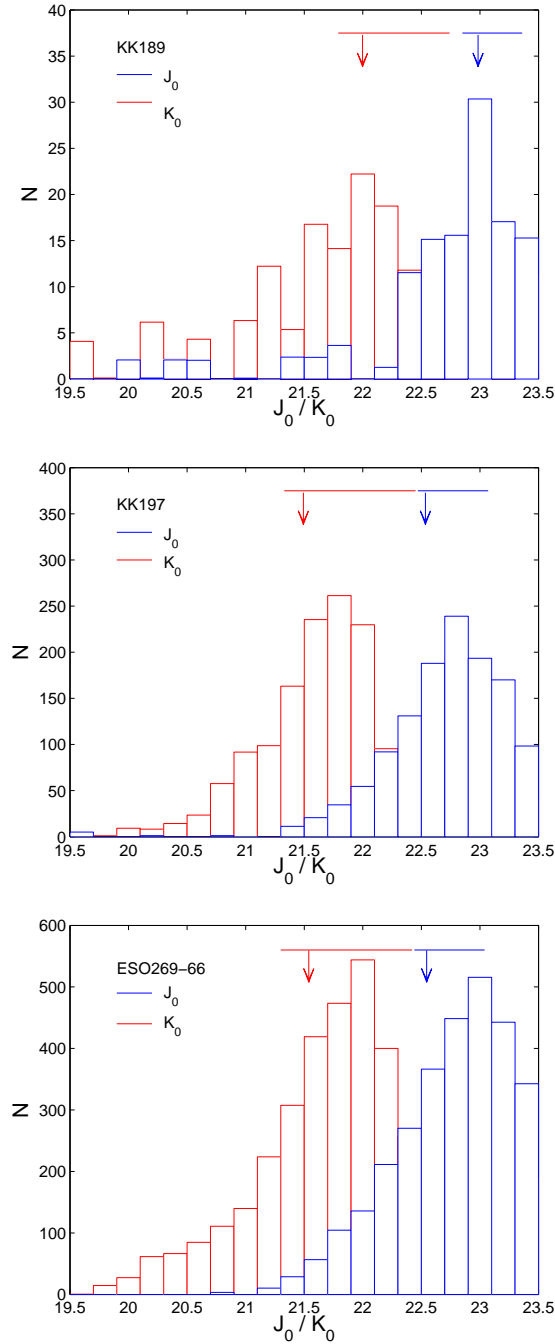


Figure 2.10: NIR luminosity functions for the J_0 - and K_0 -bands of the target galaxies, ordered by increasing luminosity. The numbers have been corrected for incompleteness and Galactic foreground contamination. The arrows indicate the predicted values for the TRGB at the median metallicity of the galaxy, while the overlaying lines show the range of TRGB values that stem from the spreads in metallicity (see text for details).

“We are all in the gutter, but some of us
are looking at the stars.”

O. Wilde, *Lady Windermere’s Fan*
(1892)

3

Early-type dwarfs

In the previous Chapter we have seen that the CMDs for early-type dwarf members of the CenA group show a prominent RGB and little sign of an IAP, as revealed by the luminous AGB population. We will now concentrate on the physical properties that can be inferred from the CMDs. We first consider optical data in order to study the metallicity content of these objects (Section 3.1), and then analyze in more detail their IAPs thanks to NIR data for a subsample of target dwarfs in Section 3.2. The material presented in this Chapter is partly included in the following papers: Crnojević et al. (2010), and Crnojević et al. (2010b), A&A submitted.

3.1 Optical data

3.1.1 Metallicity distribution functions

At the distance of the CenA group (~ 3.8 Mpc on average, Karachentsev et al. 2007), there is no possibility of obtaining individual stellar absorption line spectra for red giants using the current instrumentation within reasonable integration times (compare I_{TRGB} in Table 2.1). Moreover, genuine early-type dwarf galaxies usually do not contain neutral gas reservoirs or show ongoing star formation. As a result, we cannot directly measure their present-day metallicity from spectroscopy of HII regions around massive young stars. Finally, a reconstruction of the SFH from CMDs would be almost impossible, given the small amount of information that comes from the RGBs alone.

The only tool we have for constraining metallicity in this type of galaxy and at these distances is thus photometry combined with isochrones. Once we have a set of isochrones from an evolutionary model, we can overlay them on the observed CMDs, as shown in Fig. 3.1. In the case of a single stellar population with a narrow RGB, one would try to find the one best-fitting isochrone. However, early-type dwarf galaxies, at least in the Local Group, are known to have wide spreads in their metallicities (e.g., Grebel 1997; Mateo 1998). As our RGBs look quite broad and there are no young population features in the CMDs (i.e., stars younger than ~ 1 Gyr, as argued in the previous Chapter), we make the simplified assumption of a single, fixed old age and then let the metallicity of the isochrones vary to cover the whole RGB color range. In this way we are able to derive the metallicity of each star on the RGB via interpolation among the isochrones. This method is widely used for studies of predominantly old populations, for which spectroscopy is not available (e.g., Durrell et al. 2001; Sarajedini et al. 2002; Rejkuba et al. 2005; Harris et al. 2007; Richardson et al. 2009), to derive photometric MDFs.

In this method, there are some weaknesses that have to be taken into account. First, we have a small ($\sim 22\%$, see e.g. Durrell et al. 2001) contamination from old ($\gtrsim 10$ Gyr), low-

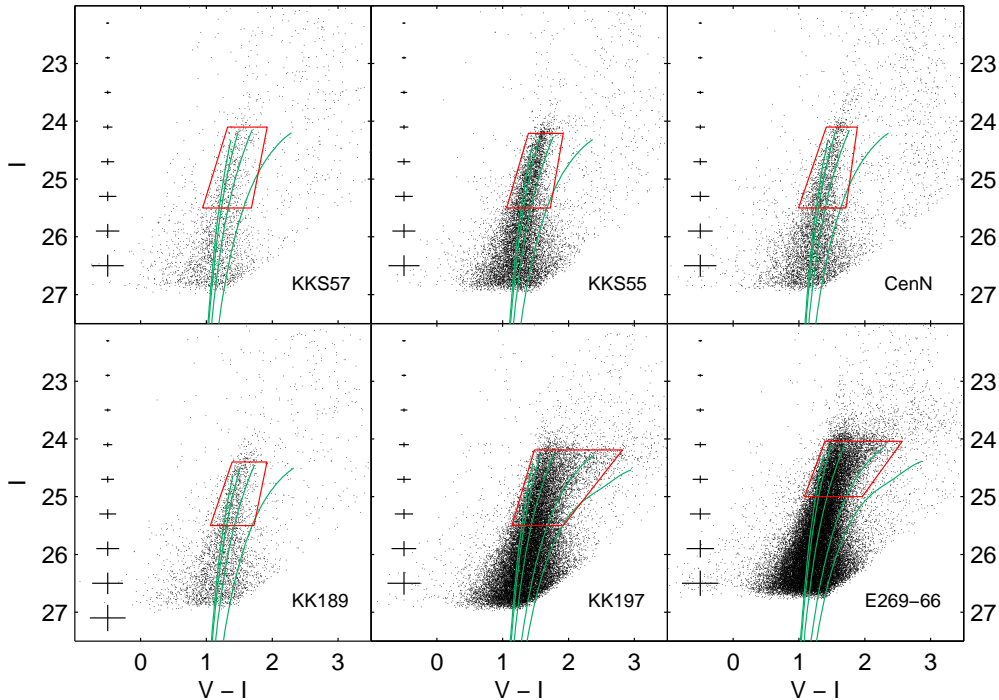


Figure 3.1: Color-magnitude diagrams of the six early-type dwarf galaxies studied in this paper, ordered by absolute V magnitude of the galaxies. Overlaid are Dartmouth stellar isochrones (green solid lines) with a fixed age of 10 Gyr, shifted to the distance of the galaxies and reddened according to the values listed in Table 2.1. Their metallicities have values of $[\text{Fe}/\text{H}] = -2.5, -1.9, -1.3$ and -0.7 (proceeding from the blue to the red parts of the CMD). For KK197 and ESO269-66, the isochrone with $[\text{Fe}/\text{H}] = -0.4$ is also shown, because of the broader RGB. Drawn in red is the selection box within which we interpolate metallicity values for the individual RGB stars (see text for details).

luminosity AGB stars that overlap with our RGB. With the available photometry it is impossible to distinguish them from RGB stars, and our main conclusions are not affected by this inevitable contamination since it would introduce a systematic bias toward slightly lower metallicities within the investigated metallicity range. That is, we would have an approximately equally overestimated number of stars for each metallicity bin. Second, we observe luminous AGB stars above the TRGB, which resemble an intermediate-age, metal-poor population (going up almost straight to higher luminosities), meaning that there will be a non-negligible contribution from such stars also at lower luminosities, hence affecting the most metal-poor bins of our resulting metallicity distribution functions. This effect has to be quantified more accurately for each galaxy and is considered in the next Section.

In Fig. 3.1 we overplot on the observed CMDs, which have been shown in the previous Chapter, the boxes (in red) used to select the putative stars for which we derive metallicities. Their width in color is chosen by constructing Hess diagrams for the galaxies, so as to approximately contain stars that lie within $\sim \pm 3\sigma$ from the mean locus of the RGB. Their vertical size is such that the stars in the selection boxes have 1σ photometric errors of ≤ 0.1 mag in magnitude and ≤ 0.15 mag in color, and go up to the TRGB (the apparent magnitude of the latter has been adopted from Karachentsev et al. 2007). In the selected region, the I -band completeness

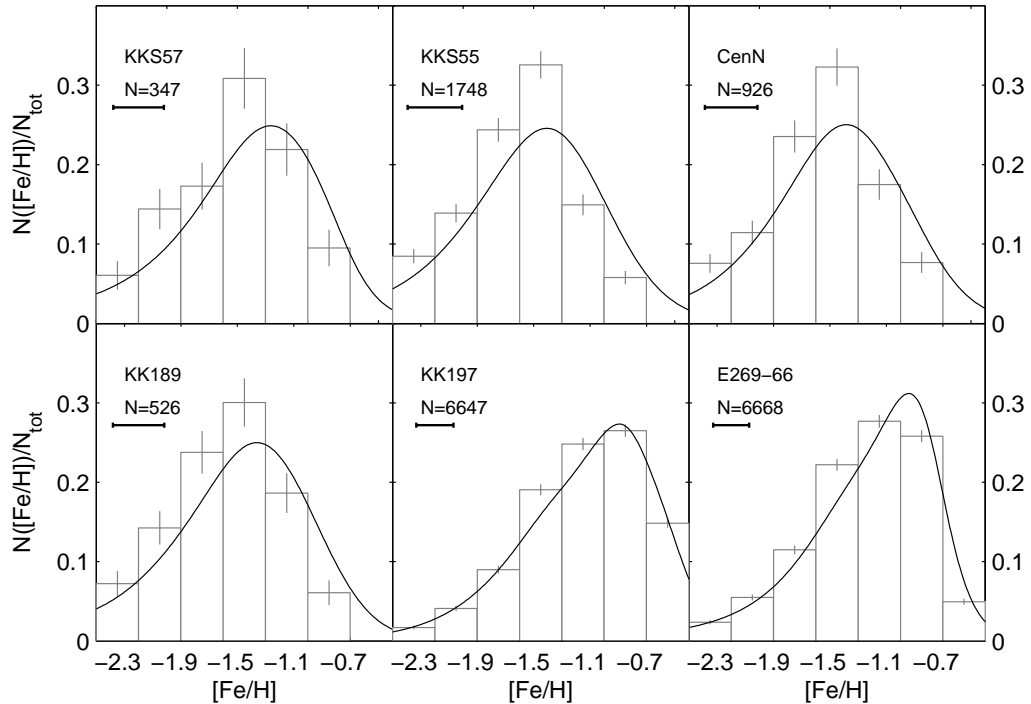


Figure 3.2: Normalized metallicity distribution functions of the six early-type dwarfs, derived via interpolation of isochrones at a fixed age (10 Gyr) and varying metallicity. Overlaid (black lines) are the MDFs convolved with the observational errors. Also plotted in the left upper corner is the median error on the individual values of $[\text{Fe}/\text{H}]$, and the total number of stars considered (for details see text).

is above the $\sim 70\%$ level and the theoretical isochrones are more widely separated from each other than at lower luminosities, providing a better resolution in metallicity.

In Fig. 3.1 we further show the adopted stellar isochrones, taken from the Dartmouth evolutionary models (Dotter et al. 2008). We chose isochrones for which the transformations from the theoretical to the observational plane are based on synthetic model atmosphere grids, in favor of the empirical transformations (see Dotter et al. 2008, for details). This was decided after some tests, in which we recompute the metallicity of a set of isochrones with different ages and metallicities by using the empirical formula $[\text{Fe}/\text{H}] = -12.64 + 12.6(V - I)_{-3.5} - 3.3(V - I)_{-3.5}^2$ (Lee et al. 1993). This relation is based on Galactic globular cluster fiducials, and it allows one to infer the mean metallicity from the mean color of the RGB at an absolute magnitude of $M_I = -3.5$. We find that the metallicity extracted with this method for isochrones with a known input metallicity are closer to the true values for the set with synthetic transformations, and thus adopt those for the subsequent analysis. We also chose not to use α -enhanced tracks, because nothing is known about the level of the α -enhancements in our target galaxies. The effects of this arbitrary choice will be discussed in the next Section.

The isochrones are shifted to the distance of each observed galaxy and reddened by the respective foreground reddening value. Distances and reddening values are taken from Karachentsev et al. (2007) and from the Schlegel extinction maps (Schlegel et al. 1998), respectively. The Dartmouth set of evolutionary models is able to reproduce the populations of old and

Table 3.1: Metallicity values derived for the studied sample of galaxies.

Galaxy	N_{RGB}	% _{cont}	$\langle[\text{Fe}/\text{H}]\rangle_{med}$	$\sigma[\text{Fe}/\text{H}], obs$	$\sigma[\text{Fe}/\text{H}], int$
KKs57	347	9	-1.45	0.46	0.28
KKs55	1748	2	-1.56	0.40	0.1
CenN	926	5	-1.49	0.40	0.15
KK189, CenA-dE1	526	5	-1.52	0.42	0.2
KK197, SGC1319.1-4216	6647	1	-1.08	0.49	0.41
ESO269-66, KK190	6668	0.5	-1.21	0.42	0.33

intermediate-age clusters particularly well, while other models generally fail to simultaneously reproduce all features of the CMD for the correct, spectroscopically measured metallicity (e.g., Glatt et al. 2008a; Glatt et al. 2008b; Sarajedini et al. 2009). We choose a fixed age of 10 Gyr, and metallicities ranging from $[\text{Fe}/\text{H}] = -2.5$ to -0.3 in solar units. The implications of this simplistic, single age assumption are discussed in detail in the next section. The isochrone grid is finely spaced (0.2 dex steps), in order to get good interpolation values for each star. We interpolate linearly among the isochrones. We also only retain stars that fall within the range of our isochrone grid, while rejecting those with extrapolated values (meaning values blueward of the most metal-poor isochrone and redder than the most metal-rich one), to avoid artificially metal-poor or -rich extremes in the results.

After deriving the metallicity values for each RGB star through interpolation, we show in Fig. 3.2 the MDFs for our galaxies (each normalized to the total number of considered stars). The galaxies are again ordered by increasing absolute V magnitude. We chose not to correct the MDFs for completeness, since the latter changes very little within the magnitude range of the selection box. The errors in $[\text{Fe}/\text{H}]$ we derived as follows: we performed 1000 Monte Carlo realizations of the interpolation process, varying the position of the stars on the CMD within their respective photometric errors (assuming Gaussian distributions), thus accounting for random errors. We plotted the median 1σ measurement errors of the individual values of $[\text{Fe}/\text{H}]$ in the left corner of each subpanel. They range from ~ 0.26 to ~ 0.39 dex. The vertical (random) counting errors of each histogram bin were also taken from the Monte Carlo realizations. Finally, in the figure we also draw the MDFs convolved with observational random errors (black lines). The effects of the systematic errors (on distance and reddening of the galaxy, taken from Karachentsev et al. 2007) on the MDFs are discussed in the next Section.

All six galaxies contain populations that are on average metal-poor, with median values ranging from $\langle[\text{Fe}/\text{H}]\rangle_{med} = -1.56$ to -1.08 (the median value is more meaningful since the MDFs are not symmetric). There is no galaxy that appears to contain stars with a metallicity higher than $[\text{Fe}/\text{H}] = -0.4$. This result is influenced by our choice of the selection box, but for clarity in Fig. 3.1 we also overplot (for the galaxies KK197 and ESO269-66) an isochrone with $[\text{Fe}/\text{H}] = -0.4$; indeed, it can be seen how few stars lie redwards of this isochrone, so we conclude that our cutoff is reasonable. On the other side, the few stars that lie bluewards of the bluest isochrone (see Fig. 3.1) have probably been scattered there by photometric errors. Some may also be old AGB stars and some of them may be genuinely metal-poor RGB stars. We have no way of identifying the nature of such stars in our photometry. As stated earlier, we simply avoid extrapolating toward putative metallicities lower than covered by our isochrones.

The spreads in metallicity are quite broad. The nominal ranges of the metallicity covered

in each galaxy are $\Delta[\text{Fe}/\text{H}],_{obs} \sim 2$ dex, and typically reach from $[\text{Fe}/\text{H}] = -2.5$ to values as high as $[\text{Fe}/\text{H}] = -0.7$ to -0.4 . In the classical dwarf spheroidals in the Local Group, the full spectroscopically measured RGB metallicity range typically exceeds 1 dex (e.g., Grebel et al. 2003), so this wide range is in good agreement with what one might expect. When calculating a formal Gaussian dispersion, the metallicity spreads derived here are on the order of $\sigma[\text{Fe}/\text{H}],_{obs} \sim 0.4\text{--}0.5$ dex. This result requires some further attention. That is, we have to take the median error into account on the individual metallicity estimates, which comes from both photometric errors and from the close spacing of the isochrones on the CMDs. This simply means that the true metallicity dispersion is in fact narrower than derived. For a better estimate of the global intrinsic spread of the galaxy, $\sigma[\text{Fe}/\text{H}],_{int}$, we thus subtract in quadrature the median metallicity error from the observed dispersion. The final values range from $\sigma[\text{Fe}/\text{H}],_{int} \sim 0.10$ dex to ~ 0.41 dex. This implies that the observed broadening of the RGBs is not only an effect of photometric errors.

In Table 3.1 we summarize the results as follows: column (1): name of the galaxy; (2): number of RGB stars for which we derive individual metallicity values; (3): percentage of Galactic foreground contaminants with respect to the number of stars in the selection box (see next Section); (4): median $[\text{Fe}/\text{H}]$ value computed from the MDF; (5): observed metallicity dispersion of the MDF (from Gaussian fit); and (6): intrinsic metallicity dispersion, after subtraction of the median measurement error.

The six histograms shown in Fig. 3.2 show a slow decline in the metal-poor direction, and a steeper slope on the metal-rich side. The results found here are similar to what has been observed in dwarf galaxies of the Local Group, both in terms of metallicity ranges and of MDF shape (e.g., Shetrone et al. 2001; Sarajedini et al. 2002; Tolstoy et al. 2004; Battaglia et al. 2006; Helmi et al. 2006; Koch et al. 2006; Bosler et al. 2007; Koch et al. 2007a,b; Gullieuszik et al. 2009). Theoretical models predict such a steep fall-off on the metal-rich end for the MDFs, which can be explained by galactic outflows blowing out gas and thus preventing further enrichment in the galaxy (see, e.g., Lanfranchi & Matteucci 2004). However, since in our work we are only able to present results based on limited assumptions because of the age–metallicity degeneracy, we do not compare the shapes of our MDFs to theoretical models or to Local Group members in more detail. We just note that the overall shapes of the MDFs resemble the MDFs of Galactic dwarf spheroidals, which suggests that similar evolutionary processes may have governed their star formation and enrichment histories.

3.1.2 Possible sources of error

The results presented in Table 3.1 will unavoidably be affected by the assumptions we made in the first place, i.e. a single old age, a negligible contribution to the MDFs by intermediate-age stars, and a scaled solar value for the α -element abundances. We now discuss the effects that these assumptions may have on the derived results in more detail.

Foreground contamination

For the HST/ACS data used here, we do not expect a high number of unresolved background galaxies in such a small field of view. In fact, they will mostly be rejected by the DOLPHOT quality cuts, leaving a contamination of the CMDs of less than 3% (see, e.g., Dalcanton et al. 2009).

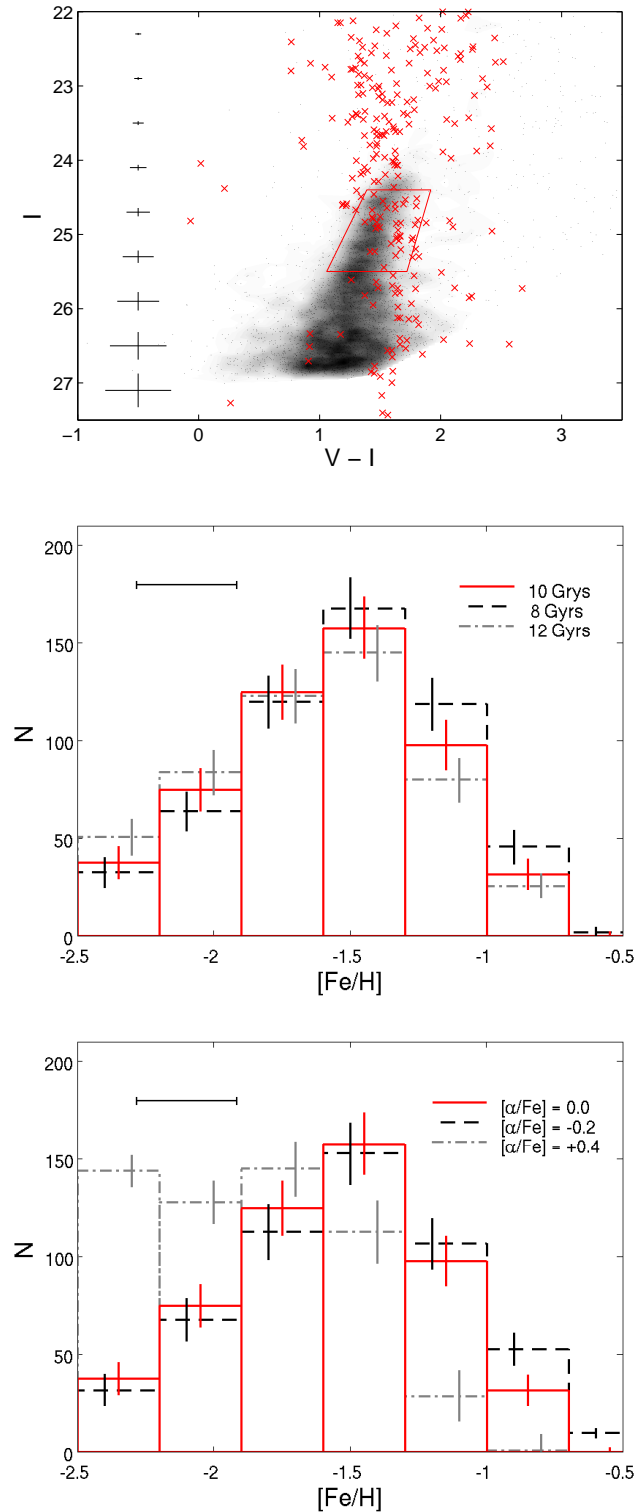


Figure 3.3: *Top panel.* Color-magnitude diagram of the dwarf spheroidal galaxy KK189 (black dots), overlaid by a Hess density diagram of its stars (gray areas). Shown also is the expected location of Galactic foreground stars (red crosses), estimated from the TRILEGAL models, and the selection box within which we derived metallicities. *Central panel.* Metallicity distribution function of KK189, derived via interpolation of isochrones at a fixed age and varying metallicity. The results are shown for 3 different ages (8, 10, and 12 Gyr), and the errorbars are computed considering photometric errors. Also plotted in the left corner is the median individual metallicity error. *Bottom panel.* As for the central panel, but keeping the age fixed at 10 Gyr and varying the α -enhancement abundance ($[\alpha/Fe] = -0.2, +0.0$ and $+0.4$).

Regarding Galactic foreground contamination, as already mentioned in the previous Chapter, we obtained estimates using the TRILEGAL models (Girardi et al. 2005). In the direction of the CenA group and within the entire ACS field of view, there are on average ~ 200 foreground stars expected. In particular, we computed the percentage of contaminant stars found in the RGB selection boxes for each early-type galaxy, after taking completeness effects into account (not all of the foreground stars would in fact be detected by the instrument), and we report the values in Table 3.1. They range from $< 1\%$ to $\sim 9\%$, depending on the total number of stars in each galaxy.

In the top panel of Fig. 3.3 we take the galaxy KK189 as an example. We plot a Hess density diagram of its stars on top of the CMD to illustrate its main features more clearly, and overplot the expected location of Galactic foreground stars derived from the TRILEGAL models. The predicted contaminants are few and are relatively uniformly distributed within the selection box, so we decided not to statistically subtract them from our RGB sample. Given the errorbars on the MDFs, the few stars that would be subtracted in such a procedure would indeed not change significantly our final results. With respect to the density maps presented in the next Section, the lowest contour level is always well above the value inferred for foreground contamination.

It could be argued that the Galactic models are not always able to reproduce the observed contamination perfectly. In particular, the TRILEGAL models underestimate the amount of objects with colors $V - I > 2$, partly because the contribution from thick disk and halo stars is uncertain at these colors and partly because there could be unresolved galaxies among them. However, the predicted star counts will differ in different color bins as a function of the slope of the adopted Galactic IMF. Thus, the underestimation at red colors does not necessarily mean that the models are incorrectly reproducing the contamination at the position of our RGBs.

From Fig. 3.3, and as pointed out in the previous Chapter, we also see that the contamination is higher in percentage for the upper part of the CMD above the TRGB, since the number of luminous AGB stars is very low. We underlined that it is difficult from the optical observations alone to thus clearly distinguish between real AGB stars and foreground contaminants. This point will be extensively considered again below, where we investigate the contribution from intermediate-age objects in more detail.

We also investigate the possible foreground contamination by projected halo stars of the dominant galaxy CenA. This contamination may happen for the dwarfs that are found at very close projected distances from the giant elliptical, as in the case of KKs55 and KK197 (~ 48 and ~ 58 kpc, respectively). The RGB of CenA has been investigated in detail in a series of papers (Harris et al. 1999; Harris & Harris 2000, 2002; Rejkuba et al. 2005) in order to derive the MDFs for fields at different galactocentric distances (8, 21, 31 and 38 kpc). If we assume that the halo of the giant elliptical extends further (see, e.g., Gerhard 2010), out to the projected distances at which KKs55 and KK197 are found, and that the MDF shape of CenA will not be very different from the more internal ones at these distances (e.g., Harris 2010), we may then try to look for a possible contamination in the CMDs of our dwarfs. The photometric data collected for CenA show a range in magnitude and color that is very similar to those of the dwarfs in our study. Thus, if the contamination from the CenA halo stars is relevant, we should tentatively observe the RGB features of the giant elliptical even in our CMDs, i.e. we should see a very broad RGB with an extended metal-rich population (the peak metallicity for the outermost field of the galaxy is of $[\text{Fe}/\text{H}] \sim -0.6$). This is not found for the closest dwarf in projection, KKs55, which displays quite a narrow RGB, so we do not expect it to be true either for KK197. For the sake of completeness, we checked the radial distribution of the most metal-rich stars found

in the CMD of KK197 and find them to be centrally concentrated, thus excluding a possible, diffuse contamination from the CenA field.

Age assumption

In our metallicity derivation, we may be neglecting the stellar populations younger than the adopted age of 10 Gyr. In the CMDs of our targets (Fig. 2.4), some luminous AGB stars are indeed visible above the TRGB. The RGB could be contaminated by the stars coming from these IAPs that are on the RGB or ascending to the AGB phase, after having burned off the He in their cores. This contamination will be mostly in the metal-poor part of the derived MDFs, as relatively metal-poor, intermediate-age stars in their RGB/AGB stage would overlap the old, most metal-poor isochrones (age-metallicity degeneracy). For example, on the upper part of the RGB a 10 Gyr isochrone with a metallicity of $[\text{Fe}/\text{H}] = -2.3$ overlaps with a 4 Gyr isochrone with $[\text{Fe}/\text{H}] = -1.7$.

From our optical data we can give a first rough estimate of the number of luminous AGB stars. However, we underline that the best way to look in more detail at luminous intermediate-age stars is instead to combine optical with near-infrared filters, because they are more luminous in the infrared and more easily separated from foreground contamination in the latter (e.g., Rejkuba et al. 2006; Boyer et al. 2009). We will thus make use of the NIR data to better constrain the epoch and strength of the more recent star formation episodes for our target galaxies in Section 3.2. We now consider Padova stellar evolutionary models (Marigo et al. 2008), since the Dartmouth isochrones do not model stages later than the RGB phase. We select stars in a box that extends (in magnitude) from ~ 0.1 mag above the TRGB (this is greater than the photometric error in magnitude at these luminosities, so we make sure we are not picking RGB stars upscattered by photometric errors) up to ~ 1.1 mag above the TRGB. The range in color goes from the bluest edge of the RGB to $V - I \sim 3$. This selection criterion should still retain luminous AGB stars with ages from 1 to 10 Gyr, and with metallicities that are around the median metallicities derived for our galaxies (we assume that the IAPs will on average be slightly more enriched than the oldest and most metal-poor RGB stars).

We first compute the bolometric magnitudes for the candidate AGB stars with the empirical correction formula by Da Costa & Armandroff (1990) (for I -band magnitude). We then construct the bolometric luminosity function for the AGB stars, subtracting the number of predicted foreground stars for each magnitude bin. Since the star counts from the TRILEGAL models could be uncertain, we also try a second method, subtracting the number of stars that are found in a box with the same size of the AGB selection box, but just above it on the CMD. The two methods give results that are almost identical.

Having done this, we can now use the empirical relation derived in Rejkuba et al. (2006) (their Fig. 19), which connects the tip luminosity of the AGB and their age (for ages ≥ 1 Gyr). This method gives us a rough quantitative idea about the fraction of an IAP. Finally, we use an approximation for the formula of the fuel consumption theorem (Armandroff et al. 1993, originally from Renzini & Buzzoni 1986) to compute the expected number of luminous AGB stars per magnitude, given their fraction relative to the entire galaxy population. We then compare the results from our AGB counting to the predictions from this theorem, varying the fraction of the intermediate-age contaminants until the two values are similar.

With this method we obtain for each galaxy an estimate of the presence of stars with ages in the range $\sim 4 - 8$ Gyr. Younger stars are probably not present, as seen from our data, if

we assume our foreground subtraction is correct. The results are as follows. For KK189, KKs57 and KK197, the estimated fraction of the IAP relative to the entire population is $\sim 10\%$; ESO269-66 has a probable fraction of $\sim 15\%$, while for KKs55 and CenN this number grows to $\sim 20\%$. All of the stated fractions could possibly be lower limits to the true values, since the luminous AGB phase is short, so this stage could be poorly populated in the observed CMDs. These numbers are lower than what is observed in those few Local Group early-type dwarf galaxies with pronounced intermediate-age star formation (e.g., Leo I, Leo II, Fornax, Carina, NGC 205, NGC 147, and NGC 185, with fractions up to $\sim 50\%$), but in line with previous studies of other early-type dwarfs in the CenA group (Rejkuba et al. 2006).

At this point, in our MDFs we simply subtract the fraction of intermediate-age stars from the metallicity bins that are more metal-poor than the median metallicity. If we then recompute median metallicities and spreads for each galaxy, we find that for KK189, KKs57 and KK197, the median metallicities values would not change significantly since there are few intermediate-age stars, and the spreads would be slightly narrower ($\sim 5 - 10\%$); for ESO269-66 the new median metallicity is higher by $\sim 5\%$ and the spread is smaller by $\sim 10\%$; finally, KKs55 and CenN would be only slightly more metal-rich ($\sim 2 - 3\%$), but the Gaussian metallicity spreads would practically go to zero.

The assumption of one single age for the galaxies' populations is also a strong simplification. To account for the spread in metallicity, extended SFHs are needed. For early-type dwarf galaxies in the Local Group, complex SFHs have been derived, and it was shown that no two dwarfs are alike, not even within the same morphological subtype (Grebel 1997). Although there are examples of Local Group dwarf spheroidals with predominantly old and metal-poor populations (e.g., Ursa Minor, Draco), the case of a single, ancient starburst is quite unlikely for most of them; on the contrary, large metallicity spreads have been detected, and the early star formation appears to have been low and continuous (e.g., Ikuta & Arimoto 2002; Grebel et al. 2003; Koch et al. 2006; Coleman & de Jong 2008; Koleva et al. 2009). Different models arrive at different durations to explain the observed metallicity spread (e.g., Ikuta & Arimoto 2002; Lanfranchi & Matteucci 2004; Marcolini et al. 2008). Assuming that the spread in metallicity is predominantly due to a spread in age, we repeated the metallicity interpolation process by choosing the three most metal-poor isochrones to have an age of 12 Gyr, and the most metal-rich ones an age of 8 Gyr. The result of this simple test is that, as one would expect, the peak of the MDF is less pronounced, and the intrinsic dispersion is slightly larger ($\sim 15\%$ in dex). However, since the observations are not deep enough to permit us to resolve the age-metallicity degeneracy from photometry of MSTO stars, a single age is the simplest assumption we can make without going into pure speculation. Moreover, as mentioned earlier, metallicity is the main contributor to the shape and width of the RGB; age has much less of an effect.

Having clarified this, our choice of setting the isochrone age to 10 Gyr is arbitrary, but as we can see from the central panel of Fig. 3.3, we may make such an assumption. We plot three different MDFs for KK189: one is derived from our chosen age, the other two are derived from ages slightly lower (8 Gyr) and slightly higher (12 Gyr) than the chosen one. It is clear that we do not introduce a significant bias when choosing one isochrone age over a slightly older or slightly younger one. Only in the case of an assumed younger age, there will be a higher number of metal-rich stars, but this will not significantly change the median metallicity value (the amount of change is $\sim 5\%$ in dex) or the shape of the distribution. The reason for this relatively small dependence on age is that a decrease or an increase in age by a few Gyr has very little effect on the isochrones for these high ages. E.g., at the TRGB a change in age from 5

to 14 Gyr for isochrones with fixed metallicity translates into a shift of ~ 0.1 mag in $V - I$ color. Similarly, the same shift in color is achieved with a change in metallicity from $[\text{Fe}/\text{H}] = -1.9$ to -1.5 for 10 Gyr isochrones. Hence a change in metallicity is much more noticeable, as it will have a stronger effect on the isochrones.

α -enhancement

For our adopted set of isochrones, we chose not to use α -enhanced tracks, because nothing is known about the level of the α -enhancements in our target galaxies. In the Local Group, the dwarf spheroidals present a broad range of $[\alpha/\text{Fe}]$ ratios at the metallicities of our galaxy sample (e.g., Shetrone et al. 2001, 2003; Sadakane et al. 2004; Geisler et al. 2007; Koch et al. 2008a). In particular they can vary from sub- ($[\alpha/\text{Fe}] \sim -0.2$) to super-solar ($[\alpha/\text{Fe}] \sim +0.4$) values within the same dwarf, and the observed $[\alpha/\text{Fe}]$ ratios show a correlation with the $[\text{Fe}/\text{H}]$ ratios, such that the α -element abundance tends to decrease for increasing $[\text{Fe}/\text{H}]$ (e.g., Tolstoy et al. 2009; Koch 2009). The exact shape of this relation depends on the details of the SFH (see Chapter 1 for a more detailed explanation about the effects of supernovae explosions). Overall, as shown in Fig. 1.8, the $[\alpha/\text{Fe}]$ values for Local Group dwarf spheroidals scatter around an average value of $[\alpha/\text{Fe}] \sim 0.0$ for $-1.5 \lesssim [\text{Fe}/\text{H}] \lesssim -2.0$.

We again try the simple test described above for a choice of different ages, and let the α -element abundances vary for our isochrones. With a fixed age of 10 Gyrs, we compute the metallicities for isochrones again with $[\alpha/\text{Fe}] = -0.2, +0.2, \text{ and } +0.4$. The resulting MDFs are shown in the bottom panel of Fig. 3.3 for $[\alpha/\text{Fe}] = -0.2, +0.0, \text{ and } +0.4$. Changing the α -element abundances by ± 0.2 from the solar values gives a similar result as a change in age, such that lower (higher) α -element abundances would mimic a younger (older) set of isochrones, and the median metallicities would accordingly be higher (lower) by less than $\sim 5\%$. When choosing $[\alpha/\text{Fe}] = +0.4$, the median metallicity is lower by $\sim 30\%$, and the metallicity spread is almost doubled. However, this is a rather extreme assumption, since the most probable case is the one where we have a spread of α -enhancement values. This could again be included in our computation by choosing the most metal-poor and oldest isochrones to have subsolar α -enhancement, and the most metal-rich and youngest to have super-solar α -enhancement. Our simple test is primarily intended to explore the parameter range. It demonstrates that the resulting median metallicities would be slightly lower ($\sim 15\%$ in dex), while the metallicity spread would be much greater (3-4 times) when a range of $[\alpha/\text{Fe}]$ values is considered.

Systematic errors

In our analysis, we adopt the values for distance and foreground reddening from Karachentsev et al. (2007) and from the Schlegel extinction maps (Schlegel et al. 1998), respectively. These are affected by uncertainties of $\sim 7\%$ and $\sim 10\%$ of the values listed in Table 2.1. If we let one of these two parameters vary within its errorbars, the isochrones overplotted on the observed CMDs will all be shifted by the same amount.

We first test how the derived median metallicities and the metallicity spreads change if we change the adopted distance value within its errorbars. We find that for distances higher (lower) than the adopted one, the median metallicities are lower (higher) by $\sim 10\%$ (meaning $\sim 0.10 - 0.15$ dex), while the spreads are also higher (lower) by $\sim 20\%$. Similarly, for higher (lower) foreground reddening values the resulting median metallicities will be higher (lower)

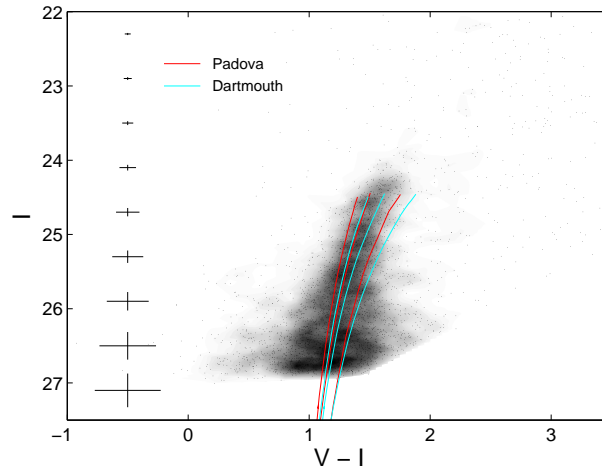


Figure 3.4: Color-magnitude diagram of the dwarf spheroidal galaxy KK189 (black dots), overlaid by a Hess density diagram of its stars (gray areas). We show both Padova (red lines) and Dartmouth (green lines) stellar isochrones, with a fixed age of 10 Gyr and varying metallicity of $[\text{Fe}/\text{H}] = -2.0, -1.5$ and -1.0 (from the blue to the red side).

by $\sim 3\%$ and the spreads lower (higher) by $\sim 10\%$.

Stellar evolutionary models

As a test, we also repeated our entire analysis using Padova isochrones (Marigo et al. 2008), with an identical age and metallicity grid. The results are quite similar overall, from the shape of the MDFs to the presence of metallicity gradients and distinct stellar populations (see next section), but the average metallicities found for each galaxy are systematically higher by ~ 0.3 dex on average. This can be clearly understood if we look at the differences that the two sets of isochrones present in the upper part of the RGB. We show an example in Fig. 3.4, where we plot isochrones with a fixed age of 10 Gyr and varying metallicity ($[\text{Fe}/\text{H}] = -2.0, -1.5$ and -1.0 , corresponding to $Z \sim 0.0002, 0.0006$ and 0.002 for the Padova models, assuming $Z_{\odot} = 0.019$). However, a detailed comparison between different theoretical models goes beyond the goals of our work (for some examples, see Gallart et al. 2005; Glatt et al. 2008a; Glatt et al. 2008b; Goudfrooij et al. 2009; Sarajedini et al. 2009).

3.1.3 Stellar spatial distributions

We now look for metallicity gradients within the target early-type galaxies and for projected spatial variations in their stellar populations.

3.1.3.1 Metallicity gradients?

To take into account that the galaxies do not have a perfectly circular shape, we consider elliptical radii from now on. The determination of the ellipticity for each galaxy follows the method of McLaughlin et al. (1994). In Fig. 3.5 we show the individual metallicity values for the RGB stars as a function of elliptical radius. We plot the data until the last ellipse that is entirely contained within the ACS field of view, because data beyond that point are incomplete

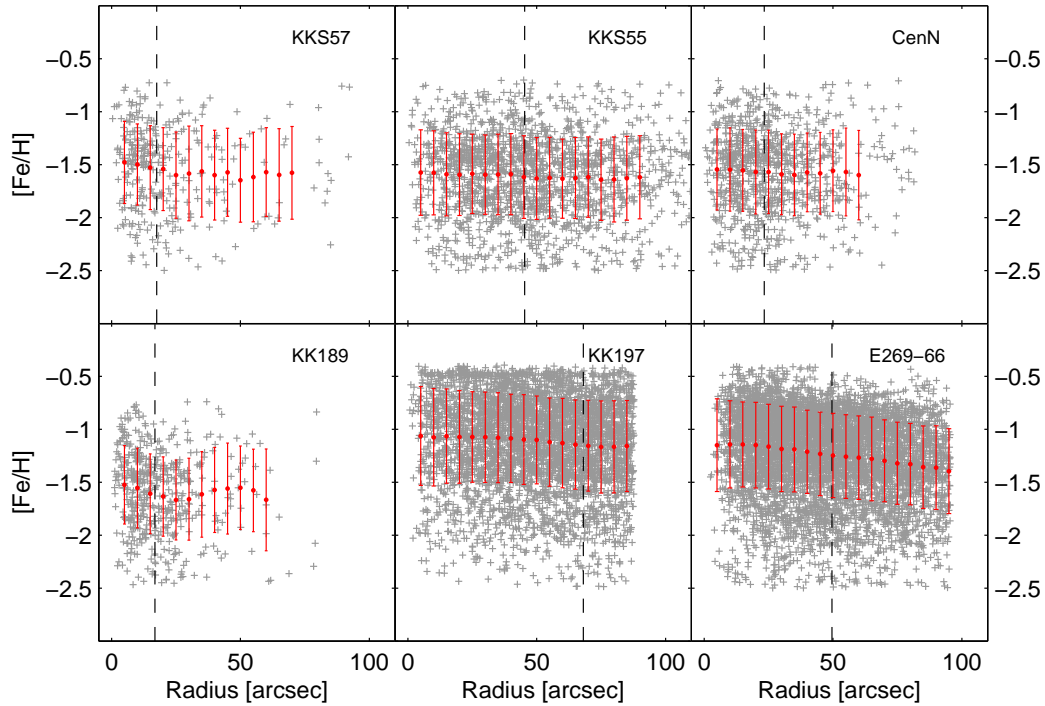


Figure 3.5: Metallicities of individual RGB stars as a function of elliptical radius for the six early-type galaxies. The projected half-light radius r_h is plotted as a dotted line in each subpanel. A running mean (red points) is also drawn for each galaxy.

in metallicity. That is, we could correct the number of stars to account for not observing the entire area of the ellipse, but we could not have any metallicity information about the stars that lie outside the instrumental field of view. For the galaxies KKS55, KK197, and ESO269-66, the instrumental field of view does not cover their whole extent. We also overplot the projected half-light radius for each galaxy, derived as described below.

We compute projected, completeness corrected surface density profiles from our RGB stars, and fit them with 3-parameter King models (King 1962). However, these models only yield poor results when we attempt to simultaneously fit both the very central parts and the outskirts of the dwarf galaxies. We thus also derive I -band surface brightness profiles from star counts, and fit them with Sersic profiles (Sersic 1968). This is a generalized exponential function of the form

$$I(r) \sim I(r_h) \exp[-(r/r_h)^{1/n}],$$

where the surface brightness is expressed in terms of intensity. It should be noted that some authors use the index n instead of $1/n$ for this type of parametrization. The free parameters for the Sersic profile are the effective (half-light) radius r_h , a shape parameter n that characterizes the curvature of the profile and the surface brightness at the radius r_h . The values derived here are reported in Table 3.2. We cannot make direct comparisons with the values previously published for our sample of galaxies because such studies consider surface brightness profiles from different bands (Jerjen et al. 2000a) or perform the fit with a simple exponential profile

Table 3.2: Parameters from Sersic profiles.

Galaxy	r_h^a	$r_{h,red}^b$	n
KKs57	17.5 ± 0.8	14.2 ± 0.6	0.97 ± 0.14
KKs55	45.3 ± 0.6	43.9 ± 0.6	0.79 ± 0.04
CenN	23.3 ± 0.6	22.5 ± 0.5	0.73 ± 0.05
KK189	16.8 ± 0.5	14.9 ± 0.4	0.88 ± 0.06
KK197	68.1 ± 1.5	47.2 ± 1.0	0.60 ± 0.05
ESO269-66	49.6 ± 0.6	43.6 ± 0.5	0.76 ± 0.04

^a computed from surface brightness as a function of elliptical radius.

^b computed from surface brightness as a function of “reduced” radius $r_{red} = \sqrt{ab}$ (see text for details).

(Sharina et al. 2008). The results derived in this work are nevertheless consistent with the ones found in the aforementioned studies. For the sake of clarity, we have to underline that we construct our surface density profiles as a function of elliptical radius. However, other authors often define a “reduced radius” ($r_{red} = \sqrt{ab}$, with a and b as the semi-major and semi-minor axes, respectively) to account for the ellipticity of the galaxy. For a small ellipticity, the two radii are consistent with each other, but in the case of a high ellipticity, they can differ substantially. In our sample, the galaxy KK197 is very elongated so its “reduced” half-light radius would result in a lower value than the one computed from our profiles. For completeness, we apply the correction for ellipticity to our derived half-light radii and also report them in Table 3.2 ($r_{h,red}$). We also use this information later, when looking for different stellar populations within our galaxies.

Coming back to Fig. 3.5, it is not easy to see a possible trend in these plots, so we also compute and plot a running mean for each galaxy (in steps of ~ 5 arcsec). Simple linear fits reveal flat or weak overall gradients. For KKs55, KK197, and ESO269-66, the results are ~ -0.043 , -0.09 , and -0.17 dex per arcmin, respectively (or ~ -0.036 , -0.075 and -0.15 dex per kpc). For the three remaining galaxies, which are less extended than the ones above, a weak gradient is observed in the central regions, while in the outer parts it tends to flatten (and the statistics tend to worsen because of the small number of stars in the outskirts). We find that: for KKs57, within the inner ~ 40 arcsec, we have a gradient of ~ -0.18 dex per arcmin (~ -0.15 dex per kpc); for CenN, the value is ~ -0.078 dex per arcmin (~ -0.065 dex per kpc) in the inner ~ 40 arcsec; for KK189, within the inner ~ 30 arcsec, the linear fit gives ~ -0.36 dex per arcmin (~ -0.3 dex per kpc). Due to the large errorbars reported in Fig. 3.5, we may conclude that an *overall* metallicity gradient is definitely present for ESO269-66, while KKs57 and KK189 only show hints of a gradient in their central regions. Finally, for ESO269-66 we have no information about the stellar population of its nucleus, because it is not resolved in the photometry.

We may further want to check whether there are differences in the stellar population of the galaxies, as observed in some early-type dwarfs in the Local Group. For each galaxy we thus divide the stars with derived metallicities in two subsamples. The first (*metal-poor*) subsample contains stars with metallicity values lower than ($\langle [\text{Fe}/\text{H}] \rangle_{med} - 0.2$), while the second (*metal-rich*) subsample has values higher than ($\langle [\text{Fe}/\text{H}] \rangle_{med} + 0.2$). We thus avoid any significant overlap for the subsamples, by excluding the values around the peak of the metallicity

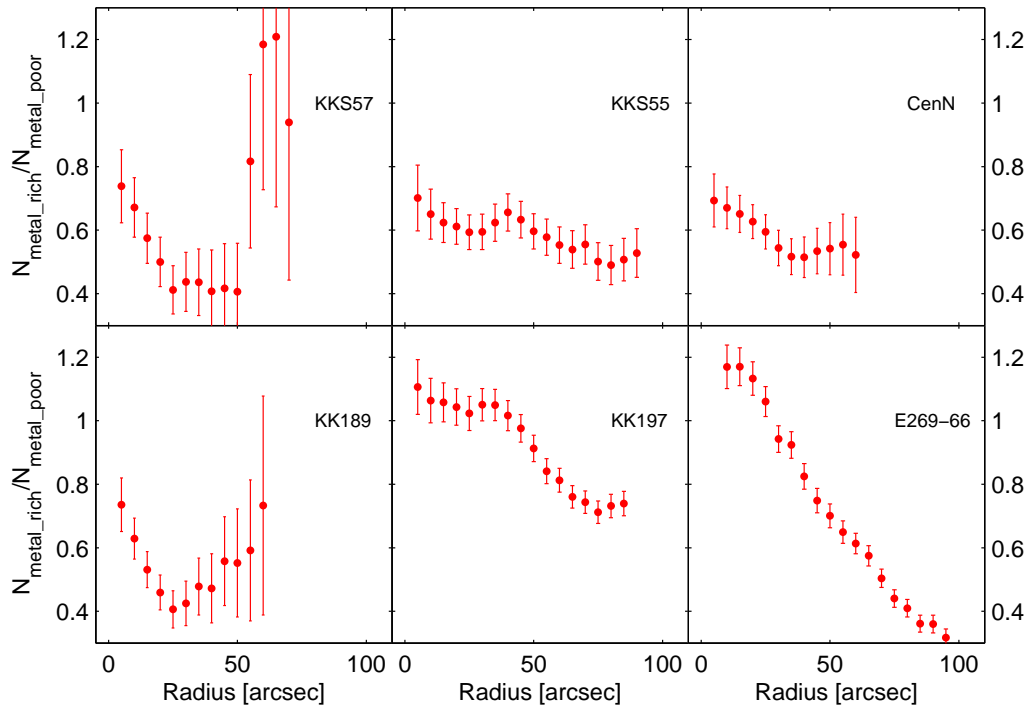


Figure 3.6: Ratio of metal-rich to metal-poor stars as a function of elliptical radius. These stars have metallicity values $> \langle [\text{Fe}/\text{H}] \rangle_{\text{med}} + 0.2$ and $< \langle [\text{Fe}/\text{H}] \rangle_{\text{med}} - 0.2$, respectively.

distribution functions.

First of all, we check the results derived for the metallicity gradients by plotting the ratio of metal-rich to metal-poor stars as a function of elliptical radius (Fig. 3.6, where the errorbars come from the Monte Carlo realizations described above). The ratio is decreasing overall with radius for all of the galaxies. For KKs57, CenN, and KK189, this is valid out to a bit more than the r_h , after which the ratio tends to be dominated by statistical errors and fluctuations. These stem from small-number statistics and our averaging over an elliptical radius, thus not taking asymmetric features into account. For the three other galaxies, the ratio decreases over their whole extent.

3.1.3.2 Population gradients?

For the two metallicity subsamples, we then derive I -band surface brightness profiles from star counts (corrected for radial incompleteness) and plot them in Fig. 3.7 (normalized to the total number of considered stars). Indeed, for KK197 and ESO269-66 we clearly see a difference between the two subpopulations. To quantitatively test whether the two subpopulations are truly separated, we performed two-sided Kolmogorov–Smirnov (KS) tests, again varying the metallicity of each star within its metallicity error. In this way we could assess the robustness of our results. The values derived from the KS tests are reported along the surface brightness profiles in Fig. 3.7: for KKs57, CenN, and KKs55, there is a probability of $\sim 40\%$ (i.e., less than 1σ significance level) that the two subsamples come from the same parent distribution;

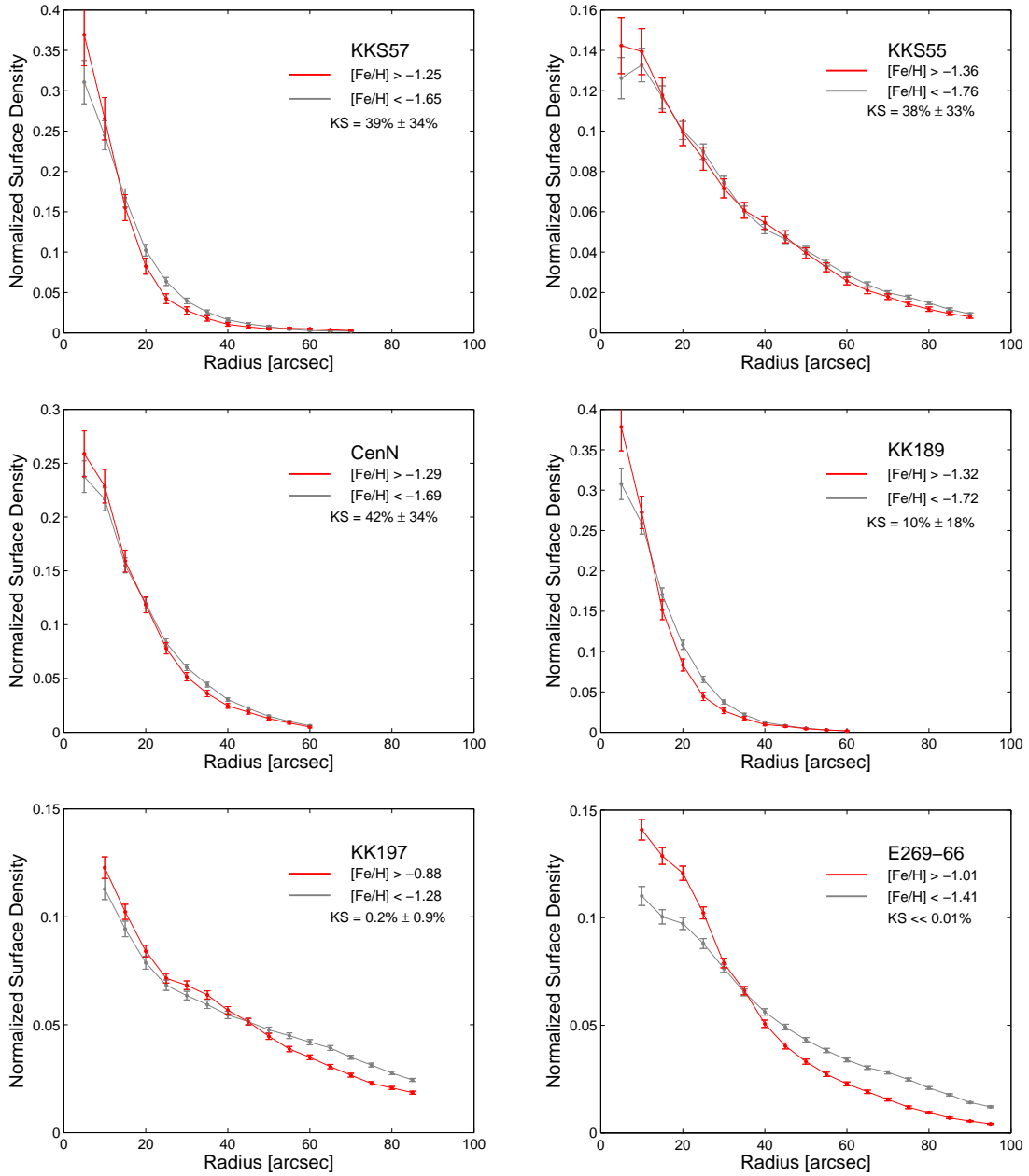


Figure 3.7: Normalized surface brightness profiles as a function of elliptical radius. For each galaxy there is a distinction between *metal-poor* (solid gray lines) and *metal-rich* (solid red lines) stars (with metallicity values $< (<[\text{Fe}/\text{H}]>_{\text{med}} - 0.2)$ and $> (<[\text{Fe}/\text{H}]>_{\text{med}} + 0.2)$, respectively). We also report the result of a KS test on the cumulative distribution functions of the two subsamples, in order to statistically assess whether they belong to the same parent population or not (see text for details).

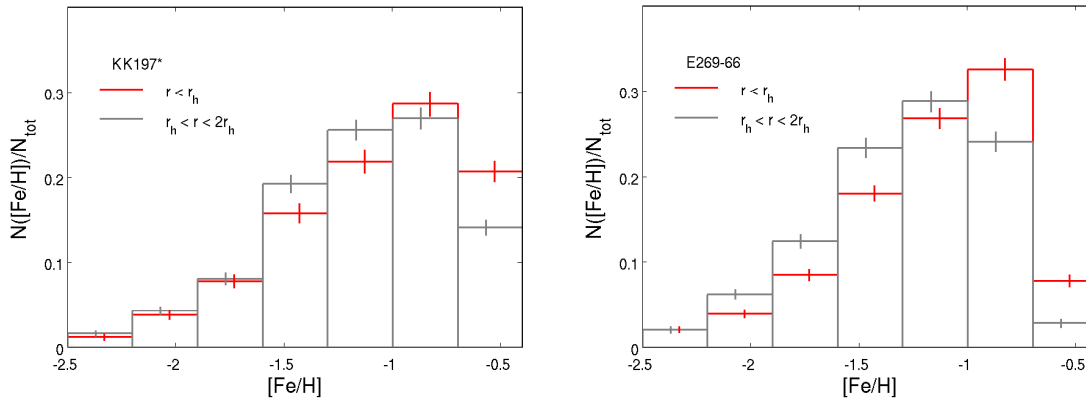


Figure 3.8: Normalized metallicity distribution functions for the inner and outer regions of KK197 and E269-66. The RGB stars are divided into two subsamples, respectively with distances of $r < r_h$ and $r_h < r < 2r_h$ from the galaxy center. For KK197 the data do not go out to $2r_h$, so the second subsample contains stars with distances that go from $r > r_h$ until the borders of the CCD frame (corresponding to $\sim 1.35r_h$).

for KK189, this probability goes down to $\sim 10\%$ ($\sim 2\sigma$); finally, for KK197, and ESO269-66 the null hypothesis can be rejected (with a probability of, respectively, 0.15% and $\ll 0.01\%$), thus these galaxies do show significantly separated subpopulations. This is a robust result, even though our subdivision into subsamples is arbitrary and the radial distribution of the subsamples partly overlaps, but with these data we have no way of investigating whether *more* than two stellar subpopulations are present.

Jerjen et al. (2000a) performed surface photometry in the B - and R -bands of dwarfs in the CenA and Sculptor groups. Their sample contains three of our galaxies (KK189, KK197, and ESO269-66). Jerjen et al. (2000a) had a slightly larger field of view for their observations than provided by our ACS data, but the results are consistent with ours. It is particularly interesting to look at their $B - R$ color profiles as a function of radius: for KK189 the color profile stays constant, while for the other two dwarfs in common with our study, they become redder for radial distances from the center greater than the projected half-light radius. This supports our results regarding an older/more metal-poor population that dominates the outskirts of these galaxies.

We can also divide the stars into two subsamples depending on their distance from the galaxy center, e.g., $r < r_h$ and $r_h < r < 2r_h$. This is done to compare the results for each galaxy with a fixed physical quantity, the half-light radius, and in order to do these comparisons in the future in other studies. We chose the ranges such that there are enough stars in each sample. The ACS data cover (at least) $2r_h$ for (almost) all of our target galaxies. The only exception is KK197, for which the data cover less than $2r_h$, so that the stars in the second subsample have distances ranging from r_h up to $\sim 1.35r_h$. We check for the less extended galaxies whether the results change significantly when choosing a larger second interval ($r_h < r < 3r_h$), but we do not see any evidence of that. We then derive normalized (to the total number of considered stars) MDFs for the two radius-selected subsamples. For the galaxies with no significant signature for two different subpopulations, the normalized MDFs are indistinguishable within the errorbars, but they show a marked difference as expected for KK197 and ESO269-66. We report the normalized MDFs for the last two dwarfs in Fig. 3.8. That the data do not cover the full extent of KK197 within $2r_h$ does not change our conclusions, since a gradient is already clear in the

inner regions of the galaxy. KK197 and ESO269-66 are classified as dwarf ellipticals, they are the most luminous galaxies in our sample, and they are located very close to the central dominant galaxy of the group (see, e.g., Fig. 3.11).

However, in these kinds of analyzes one has to keep two aspects in mind. First, by looking at properties as a function of projected radius, possible non-radial gradients can be averaged out. We thus also compute area density maps for the two subsamples in the following way. At the mean distance of the group (~ 3.8 Mpc), 1 arcsec approximately corresponds to ~ 0.02 kpc. We first count the number of neighbors within ~ 0.03 kpc². This value is chosen to avoid introducing any small-scale noise or artificial substructures, but to permit us to still recognize overall features. Then we convolve the results with a square grid and get a final resolution of 0.01 kpc². The resulting density maps are shown in Fig. 3.9. The color scale is the same for both subsamples of each galaxy, normalized to the peak density value of the *metal-rich* sample, and the values are reported in units of number of stars per 0.01 kpc². We draw 10 equally spaced isodensity contour levels starting at the 1σ significance level up to the 3σ significance level (4σ for KK197 and ESO269-66). In every case, the outer contours have values of many (~ 5 on average) σ above the Galactic foreground level.

The density maps of the two subsamples in each galaxy do not show striking differences. In each case, the subsamples' distributions follow the elongation of the galaxy. However, we can see that the *metal-rich* stars tend to be more centrally concentrated than the *metal-poor* ones in KK197 and ESO269-66. There are some fluctuations and asymmetries within the galaxies, to some extent caused by small-scale substructure and poor sampling in the outskirts. In the most massive galaxies, the ACS gap between its two CCDs is visible in the density maps (a horizontal line at pixel $y \sim 2000$), but this does not affect their general features. For KK197, an unresolved globular cluster is found near the position of the central peak (Georgiev et al. 2008), which may in fact represent a nucleus. For the nucleated galaxy ESO269-66, a depression in the density map is seen at the center, because we chose to leave out the nucleus because of the high crowding in that region.

The second thing that has to be mentioned is that, as seen in the previous section, there is a non negligible IAP in some of our galaxies. The intermediate-age stars could, in principle, bias the derived metallicity gradients. We thus have a qualitative look at the radial distribution of the luminous AGB stars. We computed the number of AGB and RGB stars (selected as described in the previous Section) in elliptical annuli of ~ 4 arcsec width. We corrected the counts for radial incompleteness and also subtracted the estimated number of contaminants for AGB and RGB separately. This has to be done because the amount of relative contamination is very different for the two samples because of having fewer luminous AGB stars than RGB stars. We then computed the ratio between AGB and RGB stars and considered it to be a function of radius. The results are plotted in Fig. 3.10. The strong fluctuations in these plots are just reflecting the poor statistics. In almost every case, this ratio stays nearly constant over the full extent of the galaxy. Only for ESO269-66 do the inner ~ 20 arcsec show a slightly higher AGB to RGB ratio, revealing a small amount of intermediate-age AGB stars concentrated in the inner region of this galaxy. As discussed before, this younger population would - at least qualitatively - increase the number of apparently blue, metal-poor RGB stars, thus biasing the metal-poor subsample. Nonetheless, we see that the more metal-rich stars are clearly more centrally concentrated (Figs. 3.7 and 3.8). On the other hand, the metallicity gradient that we find for this galaxy is still significant, and it could be even more pronounced if some of the central stars that we identify as metal-poor RGB stars were in fact more metal-rich, low-

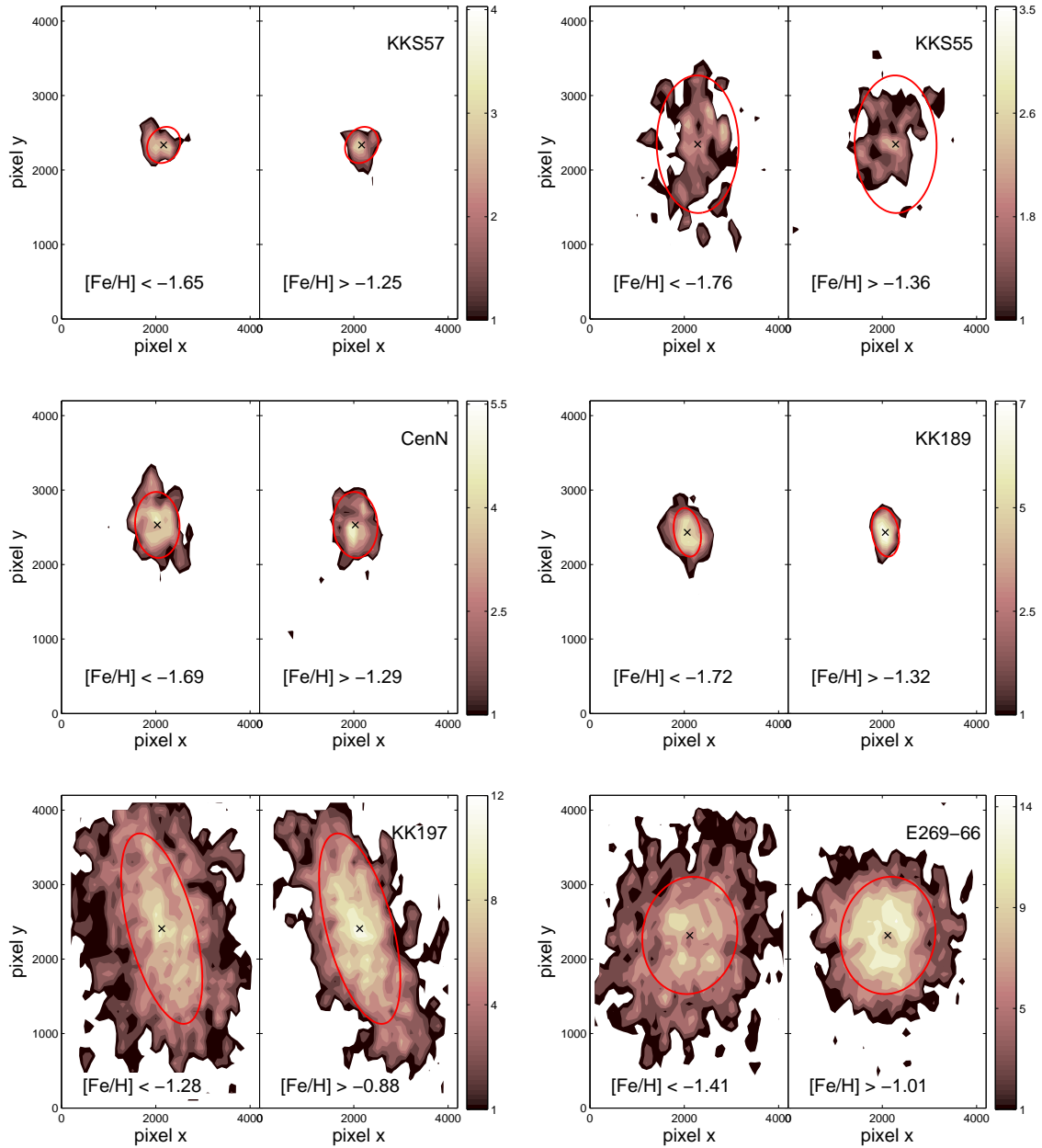


Figure 3.9: Density maps for the early-type galaxies, each divided into two subsamples. For each galaxy, the left (right) panel shows *metal-poor* (*metal-rich*) stars with metallicity values $< (<[\text{Fe}/\text{H}]>_{\text{med}} - 0.2)$ ($> (<[\text{Fe}/\text{H}]>_{\text{med}} + 0.2)$). The color scale is the same for the two subsamples, normalized to the peak density value of the *metal-rich* one, and the density values are listed in units of number of stars per 0.01 kpc^2 . Ten equally spaced isodensity contours are drawn starting at the 1σ up to the 3σ significance level (4σ for KK197 and ESO269-66). The center of each galaxy is indicated with a black cross, and its half-light radius with a red ellipse (see Sect. 3.1.3 for details).

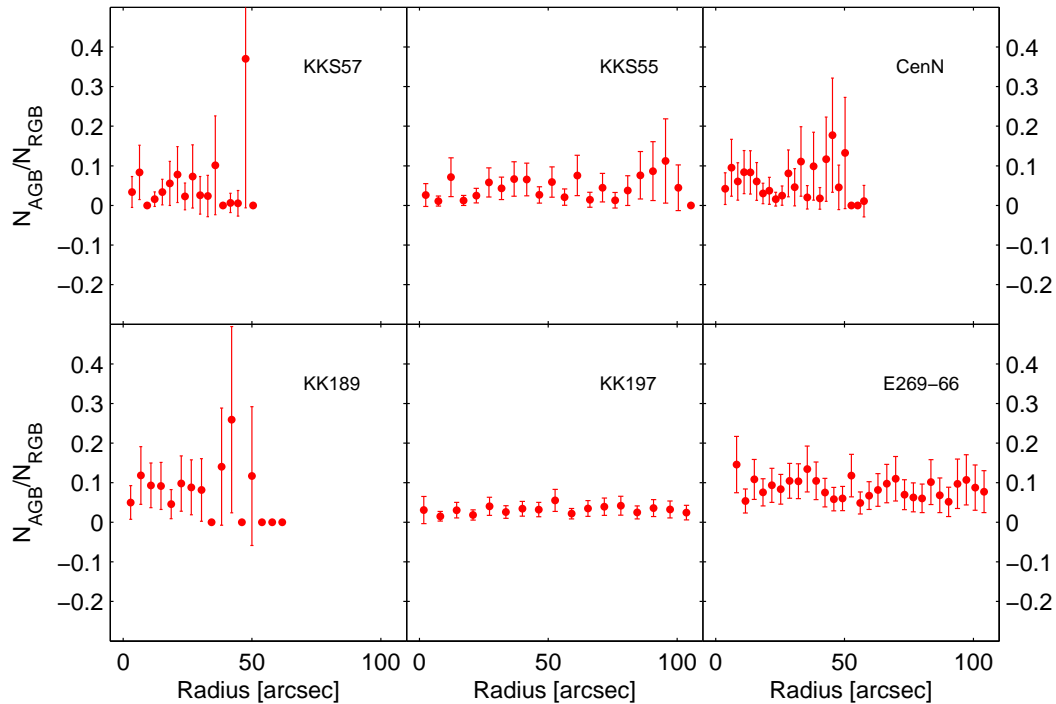


Figure 3.10: Ratio of luminous AGB to RGB stars as a function of elliptical radius (see text for details on the selection of the two subsamples).

luminosity AGB stars superimposed on the RGB.

3.1.4 Discussion

To illustrate where the early-type target galaxies are located within the Centaurus A group, we plot the position in the sky of the galaxies in this group in Fig. 3.11, using the data from Karachentsev et al. (2007). The left panel shows the distribution of dwarfs with positive tidal index (i.e., belonging to the group) around the two giant galaxies CenA and M83, which form two distinct subgroups. In the right panel of the figure, we zoom in around CenA, since all of the early-type galaxies that we study belong to the CenA subgroup. This is obviously quite a dense region, because it contains approximately the same number of galaxies within a fixed radius as our Local Group, with the difference that the census for CenA is likely to be incomplete (e.g., Jerjen et al. 2000a, Rejkuba et al. 2006).

The six early-type dwarfs of our sample have quite a wide range of luminosities (see Table 2.1), and their morphological types vary from dwarf spheroidals (KKs57, KKs55, CenN, and KK189) to dwarf ellipticals (KK197 and ESO269-66, the latter being a nucleated galaxy). What they have in common is the absence of any recent star formation (as traced by $H\alpha$, or young populations from CMD), and there is no significant amount of HI detected that would allow for ongoing or future star formation. For example, Bouchard et al. (2007) investigated the gas content in three of our target dwarfs (KK189, KK197 and ESO269-66) and find only upper limits for their HI masses (< 1.6 , < 2.9 and $< 1.0 \times 10^5 M_{\odot}$). Moreover, only upper limits can be

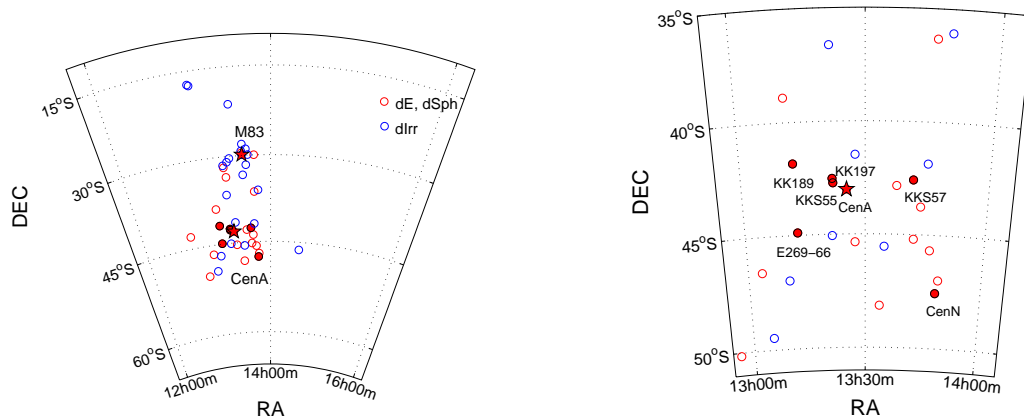


Figure 3.11: *Left panel.* Positions in the sky of the galaxies belonging to the CenA group (from Karachentsev et al. 2007). Red symbols indicate early-type dwarfs (dE and dSph), while blue symbols are for late-type dwarfs (dIrr). Two red stars are drawn at the positions of the two dominant giant galaxies CenA and M83, around which the smaller companions cluster and form two distinct subgroups. The filled circles represent the dwarfs studied here. *Right panel.* Same as the left panel, just zoomed in a smaller region around CenA, where the early-type galaxies studied here are located (as labeled in the plot).

found for the star formation derived from $H\alpha$ emission: for KK189, KK197, and ESO269-66 the values reported by Bouchard et al. (2009) are $< 0.4 \times 10^{-5} M_{\odot} \text{yr}^{-1}$.

The metallicities derived here can be compared to the work of Sharina et al. (2008). These authors derive the mean metallicities for a large sample of nearby dwarfs, among which there are also our target objects. Sharina et al. (2008) apply the empirical formula $[\text{Fe}/\text{H}] = -12.64 + 12.6(V-I)_{-3.5} - 3.3(V-I)_{-3.5}^2$ (Lee et al. 1993), which infers the mean metallicity from the mean color of the RGB at an absolute magnitude of $M_I = -3.5$. Their derived values are all slightly lower ($\sim 10 - 15\%$ in dex) than the values found with our isochrone interpolation method, but still consistent within the errors, if we consider the difference (~ 0.1 dex) between the empirical metallicity scale from the above-mentioned formula and the one used in the Dartmouth isochrone models. This discrepancy is also possibly due to a different selection of stars for the computation of the mean color of the RGB, but Sharina et al. (2008) do not explicitly state how they selected their sample of stars.

Sharina et al. (2008) further plot the color spread as a function of luminosity and suggest that the linear correlation between these two quantities could stem from a more intense star formation in more massive galaxies, probably because of denser gas reservoirs. They do, however, note a very high *color* spread for the galaxy KK197, twice what could be expected for its luminosity. Sharina et al. (2008) suggest this is the consequence of a possible strong mass loss. If we plot our derived *metallicity* spreads as a function of luminosity, KK197 indeed appears to be slightly displaced from the linear relation shown by the other galaxies, and so does also KKs57. Looking at the position of these two galaxies within the group (Fig. 3.11), and also their deprojected distance from CenA (see below), they are located not far from the giant elliptical, but we have no way of adding more information about possible environmental effects because nothing can be said about the orbits that the dwarfs had in the past. However, Bouchard et al. (2007) point out that KK197 and ESO269-66 could both be influenced by the close radio lobes of CenA, through which they may pass during their orbits and which may have contributed to the removal of the neutral gas content. In fact, ESO269-66 appears to have a particularly low HI

gas mass to visual luminosity ratio, suggesting that some external agent could have contributed to the loss of its gas content. Although KKs55 is (in deprojection) located very close to CenA as well, it does seem to contain a slightly greater fraction of intermediate-age stars, as compared to KKs57, KK197 and ESO269-66. This could possibly imply that this galaxy may now be on its first close approach to CenA.

Comparison with Milky Way early-type dwarf companions

Given the restricted amount of information we can derive from the data considered here, it is difficult to make a detailed comparison to the dwarf galaxies of our own Local Group. However, there are some points that suggest that the smallest objects in these two groups may have had a similar history. Like the complex and different SFHs seen in our neighborhood, we see that the metallicity and stellar population properties in our target dwarfs differ from each other (e.g., median metallicity, metallicity spread, fraction of intermediate-age stars). However, it looks like there are no purely old dwarfs in our sample such as Ursa Minor, Draco or Cetus in the Local Group, although our sample is small and moreover the census of CenA companions would need to be extended to lower luminosities to make a definitive statement in this direction.

In our results, all of the studied dwarfs are relatively metal-poor, as is expected for galaxies with such low luminosities. For comparison, dwarf spheroidals in the Local Group that lie in the same range of luminosities have mean values of $[Fe/H] = -1.9$ to -1.3 (see, e.g., Mateo 1998; Grebel et al. 2003; Koch 2009), hence on average slightly more metal-poor than our sample (~ 0.15 dex, see Fig. 3.12). This small difference could come from the measurement techniques, on one hand detailed spectroscopy and on the other photometry. Moreover, as mentioned in the previous Sections, the metallicities derived here could possibly be upper limits because of our assumptions about age and α -enhancement, so we conclude that on average there are no significant differences between the dwarfs of the two groups. Dwarf galaxies with even lower luminosities have recently been found in the Local Group, which have even lower metallicities, but these objects are intrinsically too faint to be observed in the existing surveys at the CenA group distance. This naturally leads us to the metallicity-luminosity relation, already analyzed in detail for the Local Group and other environments by many authors (e.g. Mateo 1998; Grebel et al. 2003; Thomas et al. 2003; Lee et al. 2007; Sharina et al. 2008; Kalirai et al. 2010). The six early-type galaxies analyzed here have already been included in the metallicity-luminosity relation of Sharina et al. (2008, Fig. 9). They show that this relation is very similar for the dwarfs in the Local Group and those in other groups and in the field within a distance of ~ 10 Mpc. They also comment on a few early-type dwarfs that show lower metallicities than all of the others, pointing out that they resemble dwarf irregulars in their metallicity content and could thus be in a transition phase. Among the galaxies with metallicity values lower than expected, there are the three galaxies in common with our study (KKs55, CenN, and KK189). In the upper panel of Fig. 3.12, we again plot the metallicity-luminosity relation with the small sample of values derived in our study and adding the values for dwarf spheroidals that are companions to the MW (taken from the literature compilation by Kalirai et al. 2010). There does not seem to be any major displacement of our target dwarfs from a linear relation that represents Local Group dwarfs.

The other panel in Fig. 3.12 represents the metallicity as a function of the deprojected distance from CenA, and the same is reported also for MW dwarf spheroidals. We compute the distances from the host galaxy by considering the radial distances listed in Karachentsev et al.

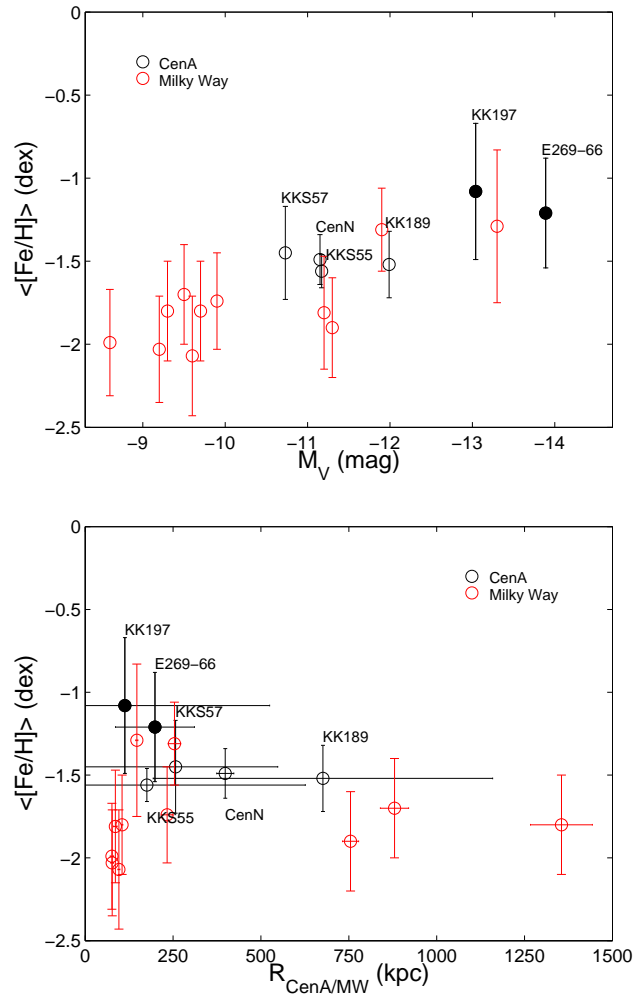


Figure 3.12: Median metallicity plotted as a function of (*upper panel*) absolute V luminosity and (*lower panel*) deprojected distance from the dominant group galaxy. The black symbols represent the CenA group dwarfs studied here (filled circles are dwarf ellipticals, the others dwarf spheroidals), while red symbols are for MW companions. The errorbars represent the intrinsic metallicity spreads.

(2007) and the angular ones derived by Karachentsev et al. (2002b). In this relation, our dwarf spheroidals seem to resemble what is seen for MW companions: neither the CenA nor the MW companions show any obvious trend with galactocentric distance from their massive primary (other than increased scatter in close proximity to a massive galaxy). The two dwarf ellipticals KK197 and ESO269-66 are slightly more metal-rich, similar to the dwarf elliptical companions of M31. There are no such objects in the vicinity of the MW. Finally, we also look for a possible correlation of the metallicity with the tidal index (i.e., a measure of the degree of isolation of a galaxy, with higher values corresponding to denser environments, see also previous Chapter), but find no trend.

The last aspect investigated in our study is the possible presence of subpopulations with a different metallicity content. For the Local Group, photometric, detailed spectroscopic, and in some cases also kinematic studies revealed dwarfs with distinct subpopulations, but also dwarfs that do not present any such trend, and only weak metallicity gradients. It is thus not surprising to find such diversity also in the CenA group. Recent simulations by Marcolini et al. (2008) provide a convincing model for the formation of population gradients and can even account for the formation of subpopulations distinct in metallicity and kinematics. According to this model, population gradients are the natural consequence of “the chemical homogenization of the interstellar matter, together with the combined inhomogeneous pollution by supernovae type Ia”, provided that star formation lasts for several Gyr. In our sample we have two cases (KK197 and ESO269-66) where the metallicities are quite high and where moderate metallicity gradients are found. Defining a metal-poor and a metal-rich subsample of stars, we do find evidence of at least two subpopulations with different radial distributions, even though our separation between the subsamples is arbitrary. This could be the effect of a low, extended star formation at the early stages of these galaxies’ lives, which would enrich the subsequent stellar populations. Since these are the two most luminous galaxies, the retention of some neutral gas due to deeper potential wells could in principle help keep the star formation active for some Gyr. The possible existence of small age gradients in old populations with ages > 10 Gyr cannot be resolved in our data, since the effect of age on the isochrones is too small and we have no other way to disentangle age and metallicity on the upper RGB, but it is almost certainly present and could explain the observed metallicity spreads and gradients.

3.2 NIR data

3.2.1 Combined CMDs

Our goal is to use the combined HST/ACS and VLT/ISAAC data to reliably identify candidate AGB stars. To do this, we first cross-correlate the optical and NIR photometric catalogs. The coordinate transformations are initially derived using the IRAF tasks *geomap* and *geoxytran*. Successively, the combined catalog is obtained with the programme DAOMASTER (Stetson 1987).

The combined lists of stars that have both optical and NIR photometry contain 115, 344, and 919 stars, for KK189, KK197 and ESO269-66 respectively, and in the upper panels of Fig. 3.13, 3.14 and 3.15 we show both the optical and the NIR CMDs of the combined list of stars for each of the three galaxies. We note that these numbers are indeed much lower than the numbers of stars found in the optical photometric catalogs alone (see Sect. 2.1.3.2). This is partly due to the

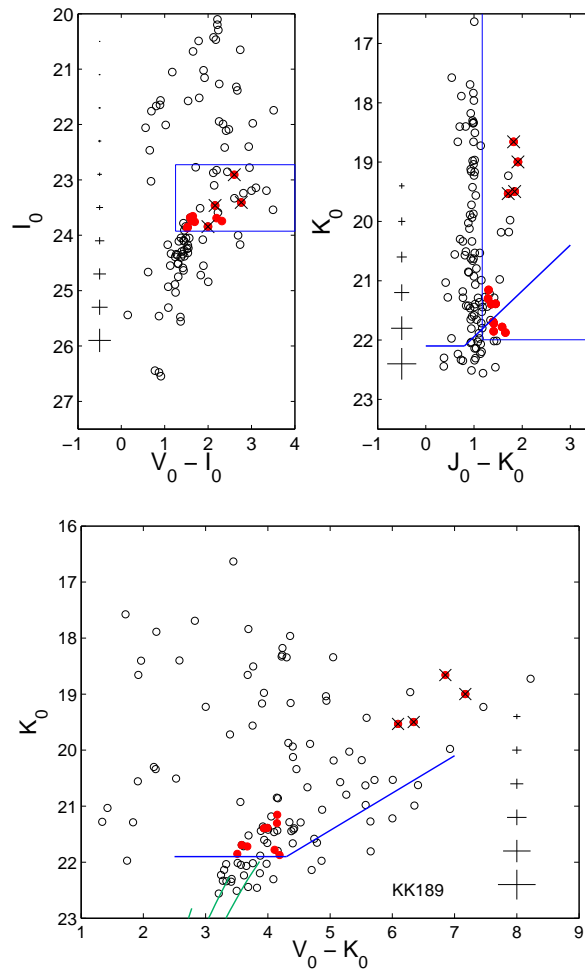


Figure 3.13: *Upper panel.* Optical and NIR (dereddened) CMDs for KK189, showing the stellar point sources cross-identified in both catalogs. Also shown are the boxes used to select luminous AGB candidate stars, and the resulting candidates are plotted as red circles. The objects marked with a black cross are cross-identified in the two datasets, but turn out to be probable background galaxies after visual inspection. Representative photometric errorbars are plotted along the CMDs. The blue solid lines in the NIR CMD indicate the 50% completeness limit. *Lower panel.* Combined CMDs in V_0 - and K_0 -bands for KK189. The stellar sources and the symbols are the same as above. We also plot (green lines) the isochrones with a fixed age of 10 Gyr and spanning the metallicity range of the galaxy, with the same values as in Fig. 2.9. The blue lines have the same meaning as in the upper panel.

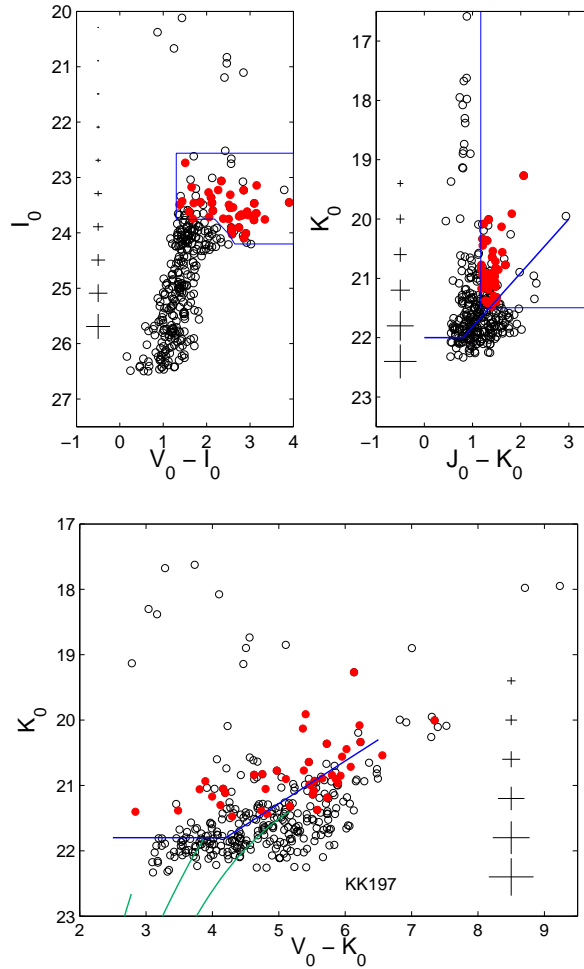


Figure 3.14: Same as in Fig. 3.13, for the galaxy KK197.

fact that the ISAAC field of view is slightly smaller than the ACS one, and partly to the higher resolution and photometric depth of ACS. Unfortunately, this turns into a loss of information in the process of cross-correlation, since there could be some mismatches in the cases where more than one optical source is found in the vicinity of a NIR source. This is particularly true for KK197 and ESO269-66, where the stellar density is higher, and from Fig. 3.14 and 3.15 we see that the NIR foreground sequences are poorly populated because of such mismatches. To avoid a loss of information for the part of the CMD in which we are most interested, we check visually the positions of the stars that are found within our selection boxes (see below) in both NIR and optical catalogs. As a result, we are able to add a few more matches to our combined catalogs.

On the same CMDs, we also overplot the boxes used in both optical and NIR to select candidate AGB stars. For the optical, the box extends from a magnitude of $I_{0,TRGB} - \sigma_I$, where σ_I is the observational error at that magnitude (in order not to select RGB stars with erroneously higher magnitudes because of photometric errors), up until $M_I \sim -5.5$. The color range goes from the bluest edge of the TRGB to $V_0 - I_0 \sim 4$ (there are no stars redder than this value). This should be the magnitude range that luminous AGB stars with the average metallicity of the target

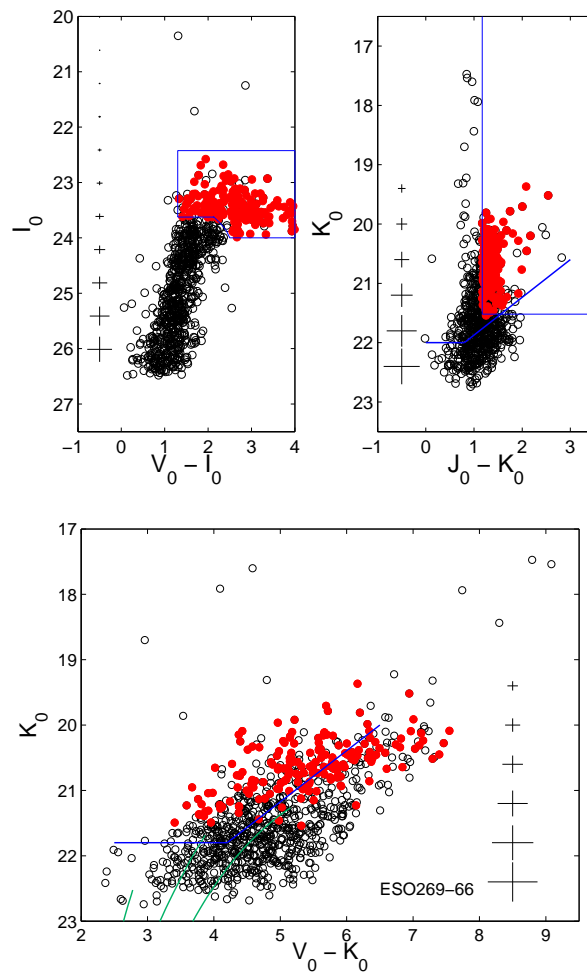


Figure 3.15: Same as in Fig. 3.13 and 3.14, for the galaxy ESO269-66.

galaxies cover (see Rejkuba et al. 2006, and references therein). For KK197 and ESO269-66, we choose to extend the optical selection box based on a few stars with colors $V_0 - I_0 \gtrsim 2.5$ that have magnitudes below that of the TRGB derived from the median metallicity. These stars could belong to the metal-rich population, as the TRGB has in fact slightly fainter magnitudes at increasing metallicities (see, e.g., Fig. 3.1). For the NIR, the selection box contains all the stars that are found above the TRGB in these bands, and redwards of the reddest foreground stars of the vertical plume. Our final “AGB candidates” are those stars that are simultaneously found in the optical and the NIR selection boxes, and are plotted in red on these CMDs. We also overplot the 50% completeness limits to the NIR CMDs, in order to point out that we might be missing the detection of a few luminous AGB stars with colors $J_0 - K_0 \gtrsim 1.0 - 1.5$. This is true in particular for KK197 and for ESO269-66, which have a more metal-rich extension than KK189. Given the number of stars in the low completeness region, we estimate that there could additionally be at least ~ 10 undetected AGB stars for KK197 and ~ 40 for ESO269-66.

There are in total 13 AGB candidates for KK189, 41 for KK197 and 176 for ESO269-66. For KK189, we can see that the four brightest candidates are detached from the rest of the red dots, so we perform a visual inspection of the images and conclude that they are barely

resolved background galaxies. In general, the above reported numbers are lower limits to the total number of luminous AGB stars in the target galaxies, given the NIR incompleteness limits.

The lower panels of Fig. 3.13, 3.14 and 3.15 show the composite $V_0 - K_0$ versus K_0 CMDs for the three studied galaxies. We plot the stars found in the combined lists and mark in red the AGB candidates. To show the expected TRGB position and to stress the metallicity spread of these galaxies, we also plot the same isochrones as in Fig. 2.9. When looking at the combined CMDs, we notice that there are many objects that are found in the region above the TRGB, but are not identified as candidate AGB stars. These sources are mostly foreground contaminants, which are distributed all over the CMDs for these magnitude combination, but some of them might be unresolved background galaxies. In particular, Saracco et al. (2001) study deep ISAAC observations to derive the number counts of unresolved high-redshift galaxies. From their Fig. 1 we estimate a number of galaxies of up to ~ 300 for our field of view, for magnitudes $18 < K_0 < 22$ and distributed on the CMD as shown in their Fig. 3. Due to the combination of high resolution HST data in addition to ISAAC images with excellent seeing, as well as to the quality cuts applied to our PSF photometry, most of these galaxies will be rejected from the final combined catalogs, but there is still the possibility of having a few high-redshift and compact (i.e., point sources with star-like light profiles) contaminants among our AGB candidates, although this cannot be clarified with the current data. The objects found at colors $V_0 - K_0 \gtrsim 8$ are indeed background galaxies, as confirmed by visual inspection.

3.2.2 Intermediate-age populations

From the combined optical and NIR CMD analysis of the previous Section, we are left with 9 luminous AGB candidates for KK189, 41 for KK197 and 176 for ESO269-66. These stars belong to the IAP of the target dwarfs, while a few old and metal-rich AGB stars could be also present for KK197 and ESO269-66, given the red extension of their RGBs. We stress that the old and metal-rich stars in our sample are a very small percentage of the whole luminous AGB population, given the low fraction of stars with $[\text{Fe}/\text{H}] \lesssim -0.7$. Therefore, in the subsequent analysis, we will neglect their contribution, thus considering all our AGB candidates to belong to the IAP. We now want to look at their properties in more detail.

Generally speaking, we only mention that with these data it is not possible to firmly separate carbon-rich from oxygen-rich stars among our AGB candidates. However, for such metal-poor galaxies we would expect to find carbon-rich stars at colors $J_0 - K_0 \gtrsim 1.5$ (e.g. Kang et al. 2006, and references therein), and a few stars with these colors are indeed present in all of our target galaxies.

We check whether our stellar samples contain dust enshrouded AGB stars. This kind of objects are extremely faint or undetected in the optical, very red at NIR wavelengths and thus not easily detectable in the J -band because of our observations' incompleteness effects. We thus search for stars which have good K -band measurement but no J -band counterpart, and find two such objects in KK189, none in KK197 and one in ESO269-66. Of the mentioned sources, in KK189 one is found slightly outside the limiting radius, while the second is close to the center but has a good measurement only for one of the two K -bands; in ESO269-66 the dust enshrouded candidate also has a bad measurement in one of the two bands. We can just mention that these are candidates but could as well be unresolved background galaxies (see previous Section).

3.2.2.1 Variable candidates

We can also look for additional AGB candidates by considering variability, which is an intrinsic characteristic of luminous AGB stars. For all of the target galaxies we have at least two observations in the K -band, so we use the difference between the stellar magnitudes at different epochs (with ~ 20 to ~ 60 days between the different observations) as a variability indicator. For a long period variable star, the typical maximum magnitude difference is of ~ 0.1 to ~ 1.5 mag in K -band, and the period is on the order of $\sim 10^{2-3}$ days (see for example Rejkuba et al. 2003, and references therein). We should thus expect to see variations of a few tens of a magnitude at most, given the observing timescales for our targets (see Tab. 2.3).

For KK189, there are three observations in K -band due to one repeated observation. There are 36 days between the first and the last one (see Tab. 2.3), which are barely enough to put a lower limit on the number of possible long-period variables. We check whether there are variations between any combination of K -band observations, but find none. We then also check the whole combined list of sources, looking for stars that display a magnitude variation of more than 3σ . We find two additional variable sources that lie just below the lower limits of the AGB selection boxes, and thus include them in our AGB candidates list. However, when checking them on the images we find that their profiles look like those of barely resolved background galaxies. In Fig. 3.16 (top panel) we display the K -band magnitude difference between the second and the third epochs, since these are the ones with better seeing, for all the candidate AGB stars except one, because it has a bad measurement in the K_2 -band. Shown (in green) are also the two likely background galaxies.

The K -band observations of KK197 were taken 57 days apart, and three of the AGB candidates display variability (blue dots in the central panel of Fig. 3.16). When considering the entire sample, two stars that lie just leftward of the NIR selection box, and are found inside the optical selection box, are indeed variables by more than 3σ (green symbols). We add the two latter to the number of candidate AGB stars for KK197. Also in this case, one AGB candidate has a bad measurement in the K_2 -band and is thus not shown in the plot.

Finally, for ESO269-66 the timescale for the observations is very short, only 20 days. We are able to see a variability of more than 3σ for only four AGB candidates, as can be seen from the bottom panel of Fig. 3.16. No additional candidates were found for this galaxy.

3.2.2.2 Absolute bolometric magnitudes

We can now use the luminosity of the candidate AGB stars to constrain their ages. This is possible since in this evolutionary stage, at a given metallicity, there is no degeneracy between position in the CMD and age. In particular, the maximum bolometric luminosity in the sample of AGB candidates can tell us when the most recent episode of star formation took place in a galaxy, with the further advantage that the metallicity dependence of the luminosity is weak compared to the age dependence. We refer in particular to Fig. 19 of Rejkuba et al. (2006), where an empirical relationship is found between age and absolute bolometric magnitude of the tip of the AGB, starting from data for LMC and SMC clusters.

We thus first compute the bolometric magnitudes of our luminous AGB candidates for each galaxy. We can apply bolometric corrections to both our optical and NIR results, and see whether they give consistent values. Following Rejkuba et al. (2006) (see also their discussion), we adopt NIR bolometric corrections from Costa & Frogel (1996) and optical ones from

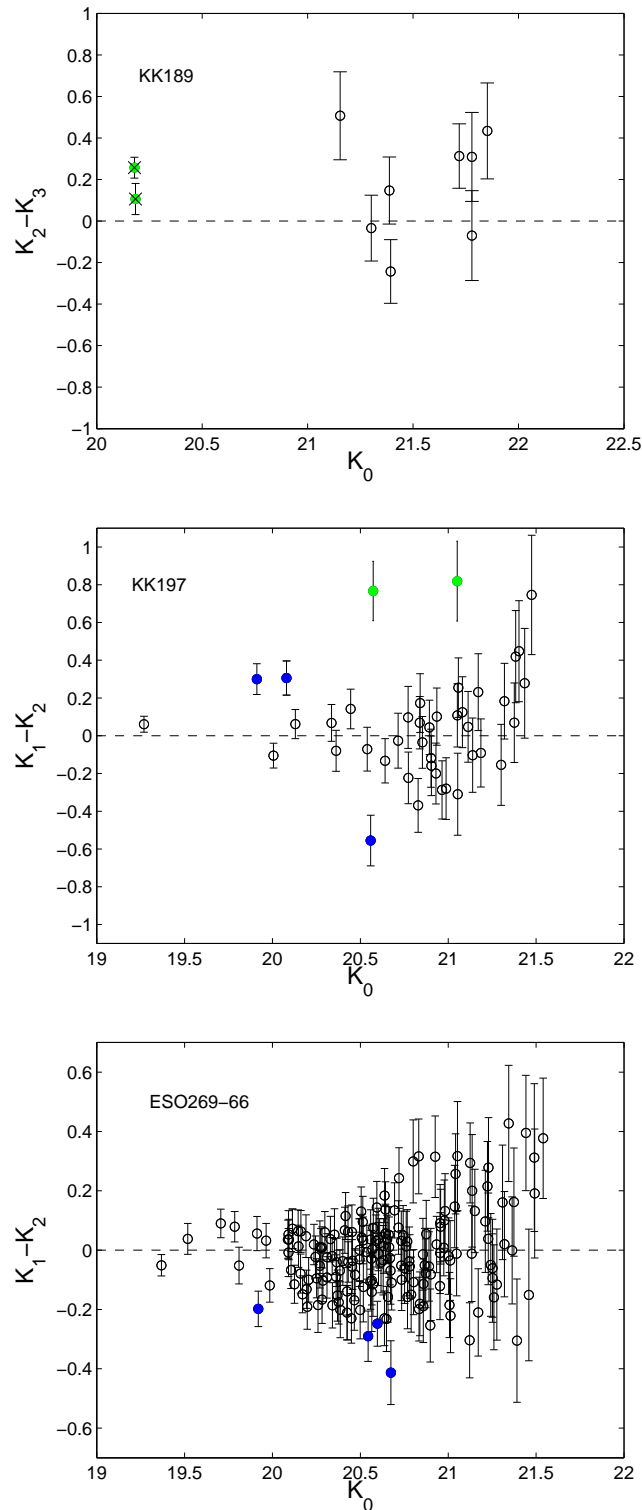


Figure 3.16: K -band magnitude difference from first to second observation (or second and third in the case of KK189), against combined dereddened K magnitude. The target galaxies are ordered by increasing luminosity. We display the magnitude difference for candidate AGB stars, plus for those stars that lie on the edges of the selection boxes but show variability (green dots). For KK189, the latter turn out to be probable background galaxies after visual inspection and have a black cross on top of the circle (see text for details). Blue objects are AGB candidates which vary more than 3σ between the two observations (or between any combination of observations for KK189). Finally, one AGB candidate is not shown for both KK189 and KK197 since it has a bad measurement in one of the two plotted K -bands.

Table 3.3: Magnitudes of the the most luminous (in bolometric magnitude) AGB candidates for each galaxy.

Galaxy	ID	I_0	K_0	$V_0 - I_0$	$J_0 - K_0$	$M_{bol,opt}$	$M_{bol,NIR}$
KK189	420 ^a	23.69 ± 0.03	21.78 ± 0.11	2.20	1.58	-4.14 ± 0.18	-3.24 ± 0.24
	9323 ^a	23.74 ± 0.03	21.87 ± 0.20	2.32	1.65	-4.11 ± 0.18	-3.10 ± 0.25
	9248 ^{a,b}	23.66 ± 0.02	21.15 ± 0.08	1.65	1.30	-4.04 ± 0.18	-4.08 ± 0.22
	168 ^b	23.76 ± 0.02	21.30 ± 0.07	1.69	1.29	-3.95 ± 0.18	-3.94 ± 0.21
	329 ^b	23.71 ± 0.03	21.39 ± 0.07	1.62	1.36	-3.98 ± 0.18	-3.79 ± 0.22
KK197	224 ^a	22.74 ± 0.02	21.40 ± 0.12	1.51	1.36	-4.76 ± 0.17	-3.61 ± 0.28
	1361 ^{a,b}	23.14 ± 0.02	20.08 ± 0.04	3.15	1.24	-4.75 ± 0.17	-5.05 ± 0.27
	1316 ^{a,b}	23.06 ± 0.02	19.27 ± 0.02	2.34	2.06	-4.64 ± 0.17	-5.37 ± 0.48
	1482 ^b	23.45 ± 0.02	20.00 ± 0.03	3.90	1.34	-4.63 ± 0.17	-5.03 ± 0.28
ESO269-66	3689 ^a	22.58 ± 0.01	20.15 ± 0.04	1.94	1.22	-4.89 ± 0.17	-4.86 ± 0.32
	2139 ^a	22.68 ± 0.01	20.24 ± 0.04	2.35	1.31	-4.89 ± 0.17	-4.58 ± 0.34
	4406 ^{a,b}	22.93 ± 0.02	19.99 ± 0.03	3.37	1.17	-4.88 ± 0.17	-5.07 ± 0.32
	3774 ^b	22.93 ± 0.02	19.37 ± 0.18	2.60	2.08	-4.70 ± 0.17	-5.13 ± 0.63
	3170 ^b	23.21 ± 0.02	19.92 ± 0.03	1.92	1.30	-4.25 ± 0.17	-5.01 ± 0.34

Notes. The combined (ISAAC and ACS) and dereddened NIR and optical magnitudes are given with the photometric errors resulting from the photometric package.

^a Among three most luminous objects in the optical.

^b Among three most luminous objects in the NIR.

Da Costa & Armandroff (1990). The results for the three most luminous stars in both optical and NIR wavelengths (which in some cases overlap) are reported in Tab. 3.3 as follows: (1): galaxy name; (2): stellar ID from the combined catalog; (3): dereddened apparent I_0 -band magnitude; (4): dereddened apparent K_0 -band magnitude; (5): dereddened optical color; (6): dereddened NIR color; (7) absolute bolometric magnitude computed from optical values; and (8) absolute bolometric magnitude computed from NIR values.

For KK189, the three most luminous stars in NIR have absolute bolometric magnitudes ranging from $M_{bol,NIR} \sim -4.1 \pm 0.2$ to $\sim -3.8 \pm 0.2$, while the values derived from the optical are $M_{bol,opt} \sim -4.1 \pm 0.2$ to $\sim -4.0 \pm 0.2$ (with one star in common between the two subsamples). The optical data were taken about 20 days later than the NIR data. We take the average M_{bol} from the three most luminous AGB candidates, which are $M_{bol,NIR} \sim -3.9 \pm 0.4$ and $M_{bol,opt} \sim -4.1 \pm 0.3$, respectively. When putting these values on the age-absolute bolometric magnitude of AGB tip relation of Rejkuba et al. (2006), we obtain an age of approximately 9.0 ± 1 Gyr for the most recent episode of star formation, indicating that there was very little activity in this galaxy other than at quite old ages.

In KK197, the three most luminous AGB candidates have $M_{bol,NIR} \sim -5.4 \pm 0.5$ to $\sim -5.0 \pm 0.3$ and $M_{bol,opt} \sim -4.8 \pm 0.2$ to $\sim -4.6 \pm 0.2$. Two out of three stars are the same for the two samples, and the optical data were taken between the two K -band observations. The average values are $M_{bol,NIR} \sim -5.1 \pm 0.6$ and $M_{bol,opt} \sim -4.7 \pm 0.3$, respectively. These bolometric magnitudes lead to ages of $\sim 2.0 \pm 1.5$ Gyr and $\sim 5.0 \pm 2.0$ for the last star formation episode.

For ESO269-66 the three highest luminosity values in NIR range from $M_{bol,NIR} \sim -5.1 \pm 0.6$

to $\sim -5.0 \pm 0.3$, while in optical they all are of $M_{bol,opt} \sim -4.9 \pm 0.2$ (with one common star out of the three most luminous between the subsamples). This galaxy was observed with HST three months later than in the NIR bands. As before we compute the average values for the NIR and optical, $M_{bol,NIR} \sim -5.1 \pm 0.8$ and $M_{bol,opt} \sim -4.9 \pm 0.3$, and derive from these values the time of the most recent star formation, resulting in 2.0 ± 1.5 Gyr and 3.0 ± 1.5 Gyr ago.

We just stress that we may expect the bolometric values to differ somewhat between the optical and NIR results, given that the bolometric corrections may have differences from one set of bands to the other, and also considering the fact that our sources are possibly long-period variable stars. However, in all of the cases we find a very good agreement between the two datasets. We also point out that the optical bolometric corrections from Da Costa & Armandroff (1990) are based on stars with colors $V - I < 2.6$, so for the three objects in KK197 and ESO269-66 that have optical colors redder than this limit (see Tab. 3.3) the corrections are highly uncertain. We can however see that the resulting absolute bolometric values are consistent with the ones derived starting from the NIR. The bolometric corrections from Costa & Frogel (1996) are instead valid for the entire range in NIR colors spanned by our listed stars. We conclude that while for KK197 and ESO269-66 the most luminous AGB stars have comparable bolometric luminosities, and thus similar ages (with ESO269-66 giving slightly younger values), KK189 had no significant star formation over the last ~ 9 Gyr.

3.2.2.3 Spatial distribution

We show the positions of the candidate AGB stars in Fig. 3.17. The coordinate system is the one of the ISAAC instrument (in pixels), and there is complete overlap with the field of view of ACS since the latter is slightly larger. Red crosses indicate the entire sample of NIR sources (after applying the quality cuts). The AGB candidates are shown as cyan diamonds, while blue circles are assigned to candidate variable stars among the AGB stars and filled green circles refer to those stars that are variable but are found outside the selection boxes in the CMDs (see previous Sect.). As a reference, we overplot the half-light radius and limiting galactic radius for KK189 and the half-light radius for KK197 and ESO269-66, since the last two galaxies extend beyond the field of view (values adopted from Tab. 3.2).

From the previous analysis of optical HST data, we find that the ratio of AGB/RGB stars stays roughly constant as a function of radius for KK189 and KK197, while for ESO269-66 there is an indication for the ratio being slightly higher in the central part of the galaxy (see Fig. 3.10). In Fig. 3.17, we can see that in KK189 the candidate AGB stars are not symmetrically distributed, and do not tend to cluster in the center of the galaxy. This displacement is probably due to the small number statistics and to an incomplete spatial sampling. In KK197 the luminous AGB stars are smoothly distributed all across the galaxy, but mostly found within the half-light radius. Finally, although the AGB candidate distribution for ESO269-66 is similar to that for KK197, the former has a higher density of AGB candidates in its central part. For the last two galaxies, we can notice that there are some ‘‘holes’’ in the distribution of the whole stellar sample, and these are due to bright foreground stars. In particular, given the high density of AGB candidates for ESO269-66, these foreground stars might be precluding the detection of additional AGB candidates, up to as much as $\sim 10\%$ of the detected number.

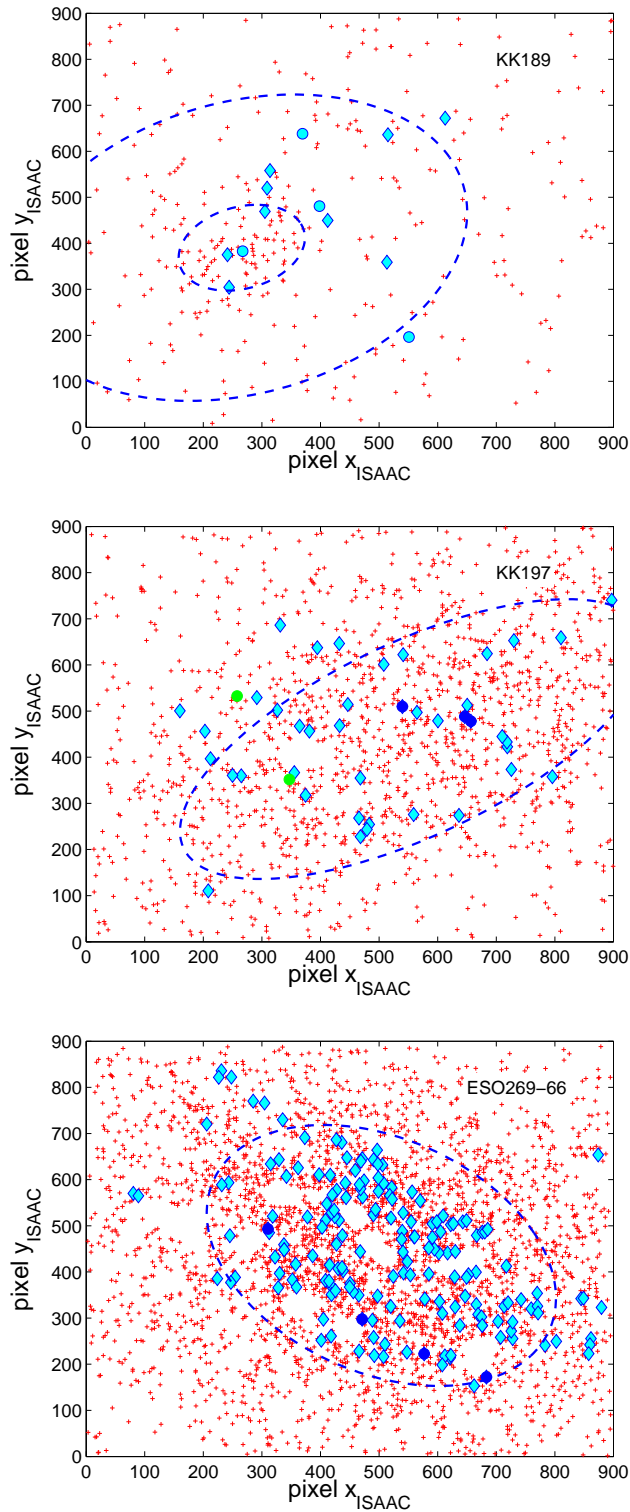


Figure 3.17: Stellar positions projected on the sky for the target galaxies (ordered by increasing luminosity). The pixel coordinates refer to the ISAAC field-of-view. Red crosses indicate the NIR sources. The blue dashed lines are, respectively, the half-light radius and the limiting radius for KK189 and the half-light radius for KK197 and ESO269-66. Cyan diamonds are candidate AGB stars, blue dots are variable stars among the candidates, and green dots are variable stars found just outside the selections boxes (see text for details). The white “holes” in the distribution of stars for KK197 and ESO269-66 are due to bright foreground stars that are overlapping with some possibly underlying galaxy stars.

3.2.3 Discussion

We can now compare our results to what we know for early-type dwarf galaxies in the Local Group. Among companions of the MW, there are many objects that do show a substantial amount of IAPs (stars with ages in the range $\sim 1-9$ Gyr), like for example the dwarf spheroidals Fornax, Carina, Leo I and Leo II (see Grebel & Gallagher 2004 and Tab. 7 of Rejkuba et al. 2006). The stellar populations of the mentioned galaxies contain as much as $\sim 50\%$ of IAPs, where these estimates come from detailed SFH recovery from deep CMDs. Considering the M31 companions, the dwarf elliptical galaxies NGC 205, NGC 185 and NGC 147 (e.g., Demers et al. 2003; Nowotny et al. 2003; Davidge 2005) do show some presence of IAP, but among the dwarf spheroidals only AndII and AndVII contain a small fraction of such young populations (Harbeck et al. 2004; Kerschbaum et al. 2004). Generally, in dwarf galaxies with more recent star formation these populations tend to be more centrally concentrated than the older populations (Harbeck et al. 2001).

We mention again that previous studies have only been able to put upper limits on the HI gas mass of our target galaxies (see also Section 3.1.4). For example, Bouchard et al. (2007) report values of $M_{HI}/L_B < 0.05, 0.01$ and 0.002 for KK189, KK197 and ESO269-66, which are comparable to the values found for Local Group early-type dwarfs with IAPs (see, e.g., Table 1 of Grebel et al. 2003) after considering the lower HI detection limit at the distance of the CenA group. Bouchard et al. (2009) estimate the current rate of star formation (from H α emission) to be $< 0.4 \times 10^{-5} M_{\odot} \text{yr}^{-1}$ for the target galaxies. These results all confirm their morphological classification and absence of a significant amount of ongoing star formation.

When looking at the bolometric luminosities of the brightest AGB stars of dwarfs in both the Local Group and the CenA group, with our small sample we can confirm the results of Rejkuba et al. (2006) and conclude that they are all in the same range, with the exception of KK189 which shows a predominantly old stellar content. The physical properties (total luminosity, mean metallicity and metallicity dispersion, deprojected distance from dominant group galaxy, see Tab. 2.1) of KK197 and ESO269-66 are indeed very similar to those of Fornax and Leo I, and so are also the bolometric luminosities of the brightest AGB stars (e.g., Demers et al. 2002; Menzies et al. 2002; Whitelock et al. 2009; Held et al. 2010), although we are here considering dwarf ellipticals while Fornax and Leo I are dwarf spheroidals. As pointed out by Bouchard et al. (2007), the two CenA group dwarf ellipticals might have been influenced by the radio-lobes of CenA, in the sense that their proximity to the giant elliptical could have played a role in the removal of their gas content. However, we stress that only the current deprojected position of these galaxies can be known, and we do not have information about their orbits so that it is difficult to draw any firm conclusion about possible effects like ram-pressure stripping or tidal interactions. KK189 is on the other hand located further away from CenA ($\sim 670 \pm 480$ kpc, see Tab. 2.1) in our sample, and is thus more similar (in distance from the dominant group galaxy, in its luminosity and metallicity content) to the most distant dwarfs of the Local Group. Its last significant star formation episode is significantly older than for the other galaxies and most probably its SFH was much less influenced by the central giant galaxy of the group. The absence of any sizeable IAP younger than 9 Gyr is somehow unexpected in a system as apparently distant from the dominant group galaxy (see, e.g., Bouchard et al. 2009), but on the other side Tucana and Cetus in the Local Group present similar characteristics to KK189 (see, e.g., Monelli et al. 2010). As a reference, we recompute the deprojected distances of the two CenA dwarf companions AM1339-445 and AM1343-452 analyzed in the previous study by

Rejkuba et al. (2006). We find a distance from CenA of $\sim 300 \pm 330$ kpc and $\sim 310 \pm 120$ kpc, respectively.

IAP fractions

We estimate the fraction of IAP with respect to the total stellar content of our target galaxies in the following way: we compute the ratio of the total number of luminous AGB stars, derived in the previous Section (also including the variable stars we found outside the selection boxes), to the number of stars found in a box that extends down to 0.3 mag below the TRGB in the optical. The latter comprises both old RGB and AGB stars and also a percentage of intermediate-age RGB stars and AGB stars that are still ascending along the RGB. Finally, the number of stars in the box extending below the TRGB has been subtracted for expected foreground stars, using TRILEGAL models. The ratio computed in this way is called P_{IA} . The values for our target galaxies are: ~ 0.07 for KK189; ~ 0.04 for KK197; and ~ 0.11 for ESO269-66. We notice that KK197 has a particularly low P_{IA} , together with a very wide metallicity spread (see Tab. 3.1). KK197 must have been very active at old ages, before loosing its gas reservoir and thus stopping to produce a significant amount of stars, and this could be directly linked to a possible tidal interaction with CenA or a ram-pressure stripping event by the intergalactic medium, although the orbits for our target galaxies cannot be constrained, as pointed out above.

The next step to evaluate the IAP fraction is then to consider stellar population models and compare them to our observational findings. We use the Maraston models (Maraston 2005) and follow the procedure of Rejkuba et al. (2006). Namely, we first assume that there are two main subpopulations in our galaxies, one that is old (13 Gyr) and the second one with an age of 1, 2, 4, 6 or 9 Gyr (one for each different realization). This is of course a first-order simplification of the true situation, since the star formation could also have proceeded more continuously or in more than two episodes during the galaxies' lifetime. Moreover, we underline that with our data we could be missing a certain amount of IAP and even younger stars, if we assume that the star formation rate was, in some periods, so low that an observable amount of AGB stars was simply not produced. Thus, once again, we conclude that the fractions we derive are lower limits for the true fractions of IAP.

The model we adopt has a metallicity of $[Z/H] = -1.35$, which matches well with all of the galaxies in our sample, if we consider that the lifetimes of the AGB phase do not dramatically change as a function of the small differences in metallicity among our target galaxies. We then let the IAP fraction vary among the different realizations (from 0 to 1), and each time compute the P_{IA} ratio given by the models. When we compare the results to the observed values found above, we find that KK189 has an IAP fraction of $\sim 15\%$; for KK197 we get an upper limit of only $\sim 5\%$; while for ESO269-66 the value we find is between $\sim 5\%$ and $\sim 10\%$. Compared to the rough predictions given in Section 3.1.2, the current results are slightly higher for KK189, and lower for both KK197 and ESO269-66. We check whether this would change the results about the metallicity content of KK189, and find that the median metallicity value does not change, while the metallicity spread is smaller by a few percent. For the other two galaxies there are no significant changes. We emphasize though that recent studies have pointed out how stellar evolutionary models tend to overpredict the number of luminous AGB stars for dwarfs with low metallicities, similar to our targets, by a factor of as much as $\sim 3 - 6$ (e.g., Gullieuszik et al. 2008; Girardi et al. 2010; Held et al. 2010; Melbourne et al. 2010). This, together with the arguments mentioned above, reinforces the idea that our results are lower limits for the true

IAP fractions in these galaxies.

Having computed the IAP fractions, even considering that the real fractions could be twice or three times those derived here, we still can clearly see that they are much lower than the fractions found in similar objects of the Local Group. We underline that the relative differences with the Local Group will not be affected by the model uncertainties, since the comparison is observationally based, although the absolute values of both sets might be larger. In particular, we mentioned that the characteristics of KK197 and ESO269-66 are similar to those of Fornax and Leo I, but despite this similarity, the recent star formation has proceeded at a much lower rate for the (so far studied) objects in the CenA group. The latter, denser, environment could thus be responsible for the observed properties of its dwarf members. These results are again in agreement to what is found by Rejkuba et al. (2006), which also found quite low IAP fractions in two dwarf members of this group, that resemble the low luminosity companions of M31. We however stress that currently the sample is too small to draw firmer conclusions, and we would need to have NIR data also for the other CenA dwarfs with existing optical HST data.

“The aim of science is not to open the door to infinite wisdom, but to set a limit to infinite error.”

B. Brecht, *Life of Galileo* (1939)

4

M31 dwarf spheroidal companions

As seen in Chapter 3, although the early-type dwarfs of the CenA group share the metallicity content and spatial properties of their stellar distribution with MW companions of comparable luminosities, one characteristic that is clearly different between the two samples is the content of IAPs and the radial extent. Namely, several (about 1/3) of the early-type dwarfs around our MW show the presence of a substantial amount of recent star formation (e.g., Fornax, Carina, Leo I, Leo II), up to $\sim 50\%$ of their total stellar population. On the other hand, all of the CenA companions studied until now (about half of the total number detected so far) seem to contain low fractions of IAPs (up to $\sim 15\%$, although these are likely lower limits to the true fractions). If we compare these results to M31 dwarf companions, however, the conclusions are different: while the dwarf ellipticals NGC 147, NGC 185 and NGC 205 do contain significant IAP fractions, the lower-mass dwarf spheroidals show very little or no signs of such a population. And II and And VII are the only two M31 dwarf spheroidals (out of the ~ 10 “classical” ones) that have been shown to have a few AGB stars more luminous than the TRGB (indicative of a population aged $\sim 1 - 9$ Gyr, see respective Subsections). It is thus interesting to understand whether there are links between these two dwarf populations, and what could be the reasons for their similarities. We note that in the subsequent analysis, the newly discovered ultra-faint M31 companions will not be considered. HST archival data are available for And XI, And XII and And XIII, but their CMDs are very sparsely populated and, moreover, we do not have such faint objects in our CenA dwarfs sample. The material presented in this Chapter is partly included in the paper by Grebel et al. (2010), in preparation.

4.1 Color-magnitude diagrams

Photometric properties of the M31 classical dwarf spheroidal companions have been studied in a number of contributions over the last decade and before (e.g., Mould & Kristian 1990; Armandroff et al. 1993; Koenig et al. 1993; Da Costa et al. 1996; Armandroff et al. 1998, 1999; Grebel & Guhathakurta 1999; Da Costa et al. 2000; Harbeck et al. 2001; Da Costa et al. 2002; McConnachie et al. 2005; McConnachie & Irwin 2006; McConnachie et al. 2007). In particular, attention has been given to their metallicity content (using Galactic globular cluster fiducials or, in the case of McConnachie et al. 2005, theoretical isochrones), their age (as derived from the HB), and the spatial properties of their stellar populations. Although these galaxies are very close to the MW, and thus it is not always possible to target their whole spatial extent with only one pointing with HST (for example, with the WFPC2 or ACS instruments that were used for some of the mentioned studies), it has been shown that some of these objects do show

Table 4.1: Fundamental properties of the dwarf spheroidal companions of M31 considered for this study.

Galaxy	RA (J2000)	DEC (J2000)	$(m - M)$	D (kpc)	D_{M31} (kpc)	A_V	M_V
And V	01 10 10.0	+47 37 37.8	24.44 ± 0.08	774 ± 28	110 ± 4	0.41	-9.6
And III	00 35 36.0	+36 31 31.6	24.37 ± 0.07	749 ± 24	75 ± 17	0.19	-10.2
And VI	23 51 52.0	+24 34 34.9	24.47 ± 0.07	783 ± 25	269 ± 6	0.21	-11.5
And I	00 45 46.0	+38 02 02.4	24.36 ± 0.07	745 ± 24	59 ± 23	0.18	-11.8
And II	01 16 16.0	+33 25 25.7	24.07 ± 0.06	652 ± 18	185 ± 23	0.21	-12.6
And VII	23 26 27.0	+50 40 40.8	24.41 ± 0.10	763 ± 35	222 ± 6	0.65	-13.3

Notes. Units of right ascension are hours, minutes, and seconds, and units of declination are degrees, arcminutes, and arcseconds. The references for the reported values are McConnachie et al. (2005); McConnachie & Irwin (2006).

metallicity/age gradients in their populations, with stars that are generally more metal-rich or younger being found in the more central regions of the dwarfs compared to the metal-poor or older ones. Very few spectroscopic measurements are available for our target dwarfs. Côté et al. (1999) obtained spectra for a handful of stars in And II and were able to estimate their mean metallicity and velocity dispersion. Guhathakurta et al. (2000) presented spectroscopic results for five dwarf spheroidal companions of M31, deriving their integrated radial velocities and MDFs. The SPLASH Survey (Spectroscopic and Photometric Landscape of Andromeda’s Stellar Halo) is performing systematic spectroscopic measurements of radial velocity and metallicity for individual RGB stars in several M31 dwarf spheroidals (see e.g. Kalirai et al. 2010), in order to disentangle a potential Galactic foreground or M31 field contamination and thus study more accurately their stellar content and their dynamical masses. We now want to apply the same analysis method used for the CenA dwarf companions (see Chapter 3) to the M31 dwarf spheroidals, in order to check its limitations as compared to spectroscopic results and also to get a homogenized sample of results starting from HST data. We will not consider the M31 dwarf elliptical companions here, since the presence of their IAPs would significantly bias the derived metallicities.

Our sample has been chosen in order to have HST (WFPC2 or ACS instruments) images for each galaxy, so that their properties can be derived in a homogeneous way. We have collected archival data from the programs GO-5325 (And I), GO-6514 (And II), GO-7500 (And III), GO-8272 (And V and And VI), and GO-8192 and GO-10430 (And VII). The PSF photometry has been performed by M. Frank (his Diploma Thesis, private communication) using the HSTPHOT and DOLPHOT packages (Dolphin 2000, 2002), for the WFPC2 and ACS images respectively. The quality cuts applied to the resulting photometry are the following: the “object” type must be 1 (to avoid objects that are too sharp or extended); the sharpness parameter has to be $|sharp| \leq 0.2$; we require $\chi < 2.0$; the crowding parameter (i.e., how much the star would be brighter if measured with no close neighbors) must be < 1.5 mag in both filters (generally WFPC2 F450W and F555W, except for And VII, which was observed in F606W and F814W with WFPC2 plus F435W and F555W with ACS); the photometric errors as given by the program must be < 0.2 mag in both filters. The artificial star tests were performed with the same package, following

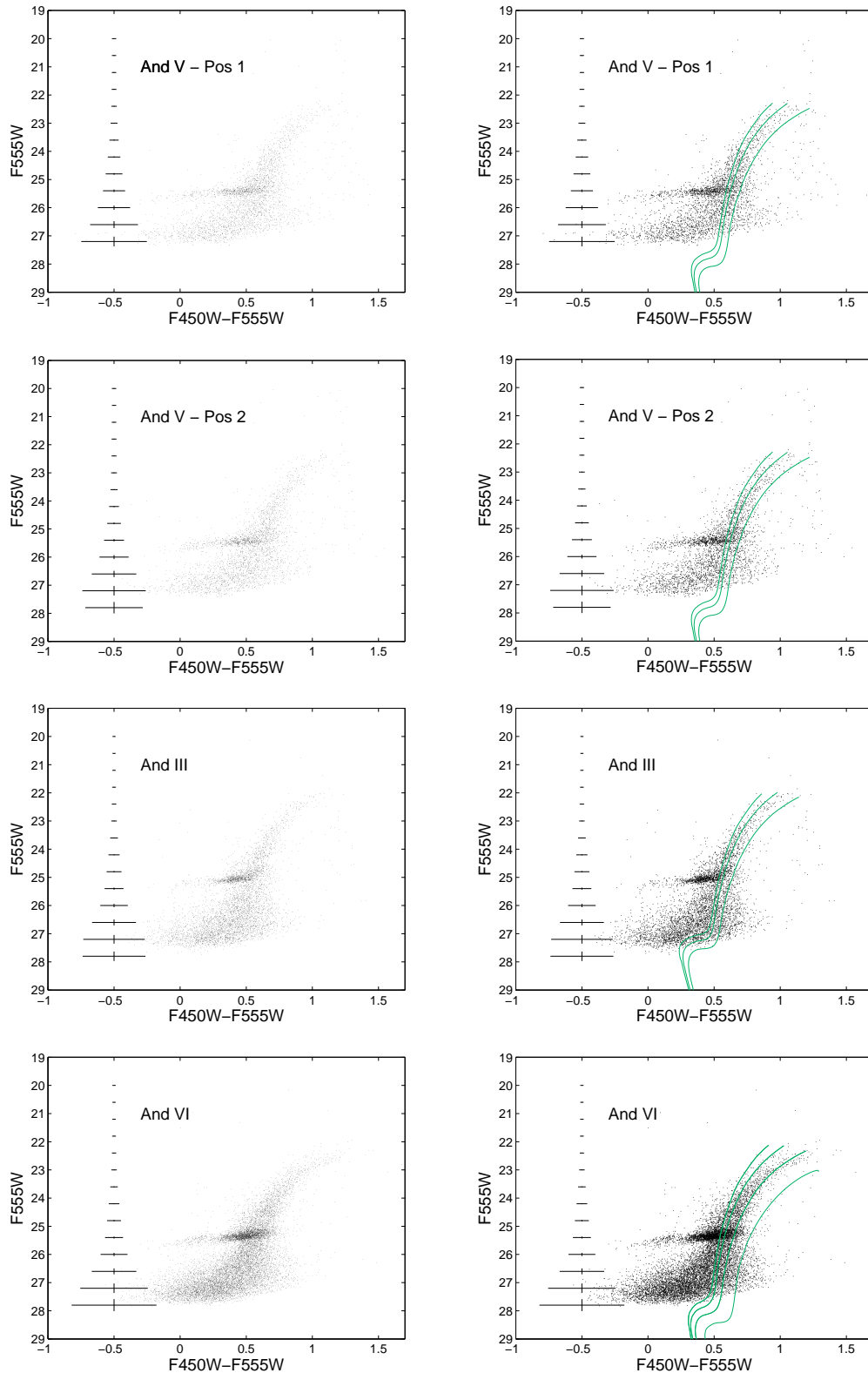


Figure 4.1: *Left panels.* CMDs for three of the M31 target dwarfs, ordered by increasing luminosity. Representative photometric errorbars are shown at different magnitudes along the CMDs. *Right panels.* We overlay on the CMDs the Dartmouth stellar isochrones with a fixed age (derived for each galaxy as explained in the text, and listed in Tab. 4.2), shifted to the distances of the galaxies and reddened according to the values listed in Table 4.1. Their metallicities are: $[\text{Fe}/\text{H}] = -2.5, -1.9, -1.3$, and for And VI also -0.7 (proceeding from the blue to the red part of the CMDs). For And V, images were taken at two (similar) positions, and we thus show the CMDs for both pointings.

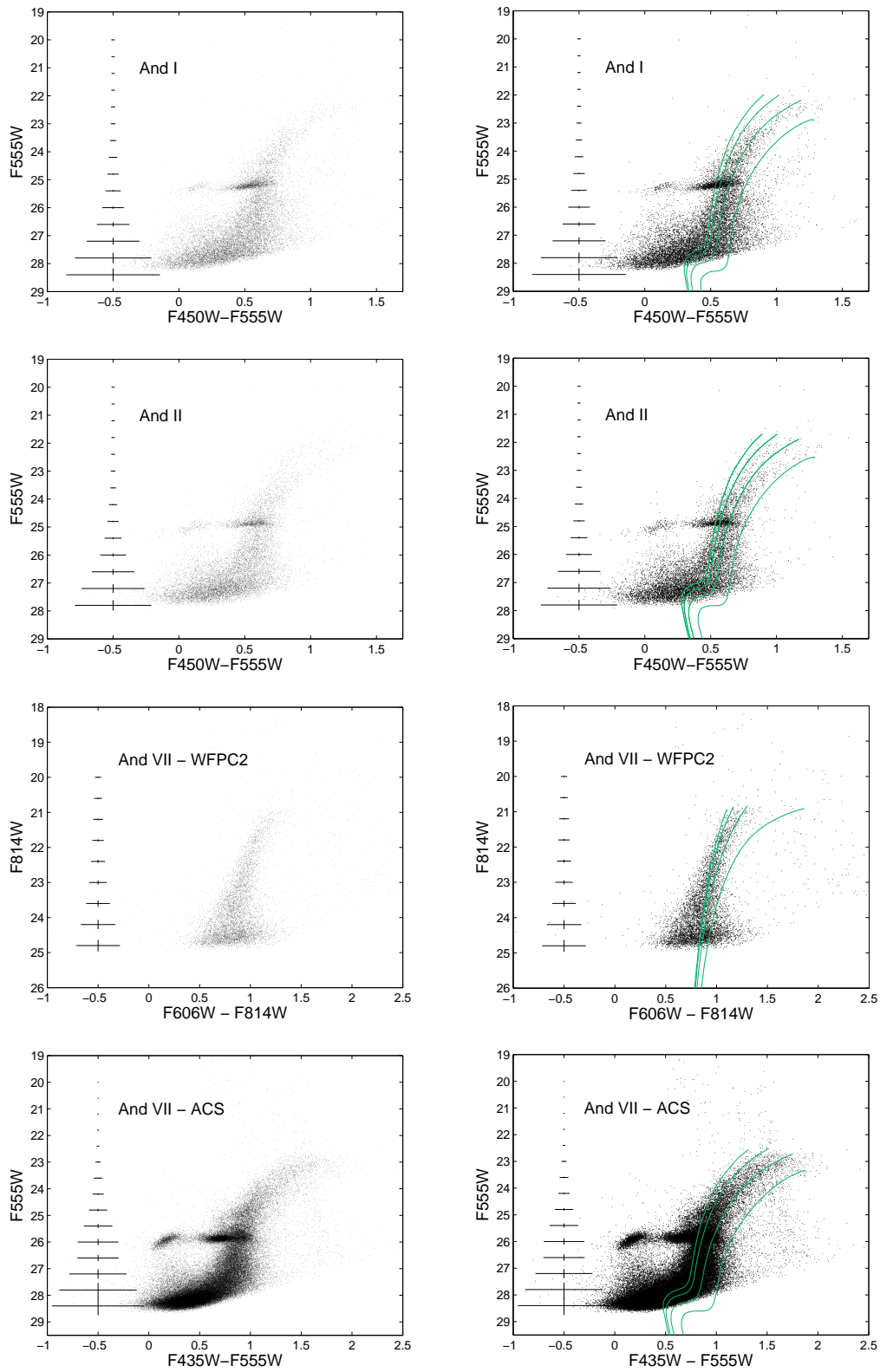


Figure 4.2: CMDs for the three remaining M31 target dwarfs, ordered by increasing luminosity (as in Fig. 4.1). For And VII, we show both the CMD stemming from the WFPC2 observations and the one coming from the ACS observations.

the stellar magnitude distribution for each galaxy and adding a number of fake stars between ~ 10 and 20 times the number of the observed stars. The resulting CMDs for the target galaxies are presented in Fig. 4.1 and 4.2. In the right panels of the two figures, we overlay Dartmouth stellar isochrones of fixed age and varying metallicities on the CMDs of the target dwarfs (see also next Section). We plot the instrumental magnitudes and show representative photometric errorbars derived from the artificial star tests along the CMDs.

The target dwarf spheroidal companions of M31 span a range of luminosities and distances from the dominant galaxy. We list their general properties (the galaxies are ordered by increasing luminosity) in Tab. 4.1 as follows: (1): name of the galaxy; (2-3): equatorial coordinates (J2000); (4): distance modulus (McConnachie et al. 2005); (5): distance (McConnachie et al. 2005); (6): deprojected distance from M31, computed starting from the distance in column (5) and adopting an M31 distance of 785 ± 25 kpc (McConnachie et al. 2005); (7) extinction in the V -band (from the NED database); and (8) V -band absolute magnitude (McConnachie & Irwin 2006).

4.2 Metallicity distribution functions and ages

We derive the photometric MDF for the target galaxies following the procedure described in Chapter 3. We choose the Dartmouth set of stellar evolutionary models (Dotter et al. 2008), given the good match they provide to old globular clusters in comparison with other sets of models (see, e.g., Glatt et al. 2008a,b; Sarajedini et al. 2009). Since the RGB suffers from the well known age-metallicity degeneracy, in which older and more metal-poor RGB stars overlap in the CMD with younger and more metal-rich stars, it is not easy to unambiguously assign a metallicity to each star. However, we know that the upper part of the RGB is more sensitive to metallicity than to age, and much of the observed spread in color of the RGB can then be reasonably explained by a spread in metallicity (once the photometric errors have been subtracted, see previous Chapter). We thus choose a single, fixed age for the stellar population being studied, and interpolate the metallicity value for each RGB star using a range of stellar isochrones with varying metallicity. We adopt $[\alpha/\text{Fe}] = 0.0$, since nothing can be said about the α -element abundance in these objects (see also the discussion in the previous Chapter). While it is very likely that the ancient star formation (≥ 10 Gyr) in dwarf galaxies is extended in time, it is not possible to quantify the age range of their populations without reaching the MSTO of the oldest populations. The star formation could thus in principle have lasted for $\sim 1 - 3$ Gyr at old ages, but we are not able to extract this information from our data. More importantly, this will not heavily affect our results (see previous Chapter).

As mentioned before and as can be seen from the CMDs of the target galaxies in Fig. 4.1 and 4.2, almost all of the M31 dwarf spheroidal companions studied here lack IAPs, as judged from the absence of AGB stars more luminous than the TRGB. The only exceptions are And II and And VII, for which hints of such a population were observed using both optical and NIR photometry (Kerschbaum et al. 2004; Harbeck et al. 2004; McConnachie et al. 2007). However, the fraction of the IAP is very low, as compared to for example other Local Group dwarf spheroidal members like Carina, Fornax, Leo I, Leo II, or the dwarf elliptical companions of M31. In the previous Chapter we showed that the early-type dwarf companions of CenA also contain very small amounts of luminous AGB stars, and estimated how much these IAPs would change our results on the metallicity content of the target dwarfs. We concluded that IAP

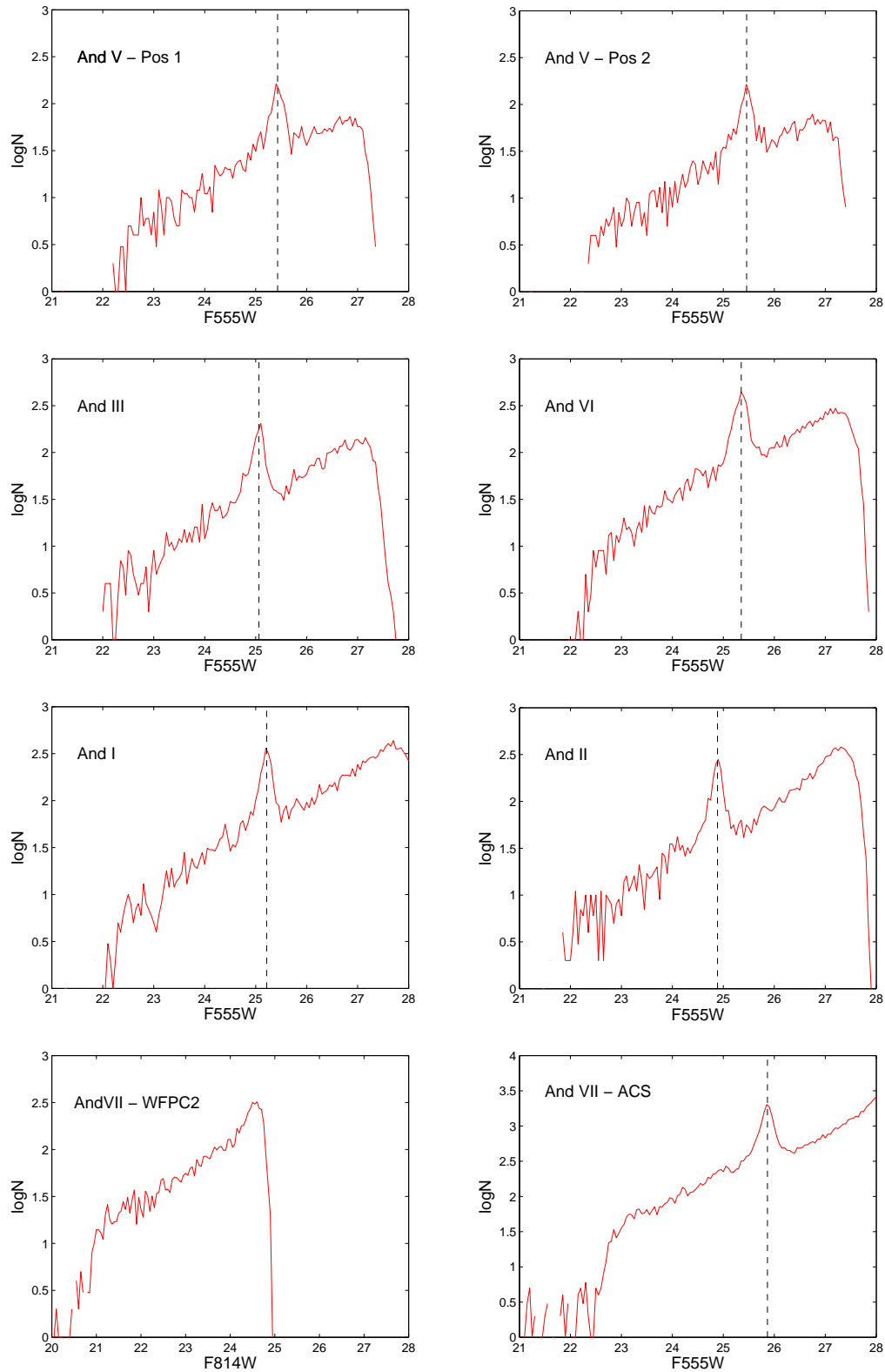


Figure 4.3: Observed luminosity functions for the M31 target dwarfs. The mean luminosity of the HB (derived from a Gaussian fit, see text for details) is shown with a vertical black dashed line. For And V and And VII, we report the luminosity functions derived for each one of the two datasets. For the WFPC2 observations of And VII, the HB is at the limiting magnitude, so we cannot compute its mean magnitude.

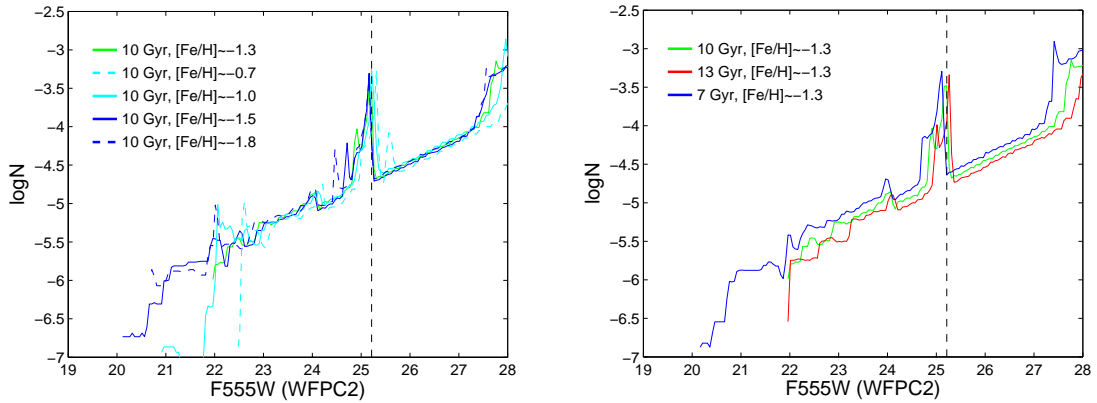


Figure 4.4: Theoretical luminosity functions from Padova evolutionary models (for the WFPC2 instrument, not convolved with observational errors). *Left panel.* Luminosity functions with a fixed age and varying metallicity. *Right panel.* Luminosity functions with a fixed metallicity and varying age (based on the And I median metallicity). We also show the location of the observed mean HB magnitude for And I with a vertical black dashed line.

fractions of up to $\sim 15\%$ would not significantly change our results, since the median metallicity values derived would be underestimated by at most $\sim 5\%$ and the metallicity spreads would be similarly overestimated by $\sim 10\%$ (depending on the single cases). Finally, we stress that the region of the RGB that lies immediately above the HB is unavoidably contaminated by old AGB stars in its bluest edge, and we thus decide to only apply our interpolation method to the upper part of the RGB (down ~ 1.5 mag below the TRGB, see individual magnitude limits for each galaxy in the next Sections).

A further step that we can take is to give a rough estimate of the ages of the target dwarfs. While the CenA companions are too distant for the photometry to reach the HB level, the exquisite dataset of images obtained with WFPC2 and ACS for the M31 companions is deep enough to reach these limits, thus giving us further information about their stellar content. Once the median metallicity value for a galaxy is derived (using isochrones with an arbitrary age of 10 Gyr), we can compare theoretical luminosity functions having that metallicity with the observed luminosity functions. To do this we adopt the Padova stellar evolutionary models (Marigo et al. 2008), since their simulated luminosity functions also take into account phases more evolved than the RGB (i.e., HB stars), contrary to the Dartmouth models. This is fundamental, since the HB is the most prominent feature in our observed luminosity functions. The RGB bump will mostly be blended, partly due to photometric errors, with the red part of the HB at the low metallicities ($[\text{Fe}/\text{H}] \lesssim -1.0$) and at the old ages displayed by these dwarfs, while the AGB bump is more difficult to observe due to the short time spent by stars in this phase and due to the low number of stars itself (see e.g., Alves & Sarajedini 1999; Rejkuba et al. 2005). After deriving the observed luminosity function for each galaxy (shown in Fig. 4.3), we fit the peak of the HB feature with a Gaussian. We then repeat this procedure with the theoretical luminosity functions (reddened and shifted to the distance of the target galaxies according to the values of Tab. 4.1), and by comparing the mean magnitudes found for functions of different ages we assign an indicative age to the observed HB. The position of the HB in the luminosity function does depend on both metallicity and age of the considered galaxy. However, for a simple stellar population with a low mean metallicity, the dependence of the HB luminosity on metallicity is less pronounced than the dependence on age. As can be seen from the example in Fig. 4.4, a

Table 4.2: Metallicity and age values derived for the dwarf spheroidal companions of M31.

Galaxy	N_{RGB}	age (Gyr)	$\langle[\text{Fe}/\text{H}]\rangle_{med}$	$\sigma[\text{Fe}/\text{H}]_{obs}$	$\sigma[\text{Fe}/\text{H}]_{int}$	$[\text{Fe}/\text{H}]_{lit}$	$\sigma[\text{Fe}/\text{H}]_{lit}$
And V	135	10	-1.75	0.44	0.41	-2.20	0.5
And III	83	8	-1.71	0.25	0.21	-1.78	0.27
And VI	279	12	-1.42	0.29	0.26	-1.50	-
And I	216	12	-1.23	0.28	0.26	-1.45	0.37
And II	142	10*	-1.43	0.51	0.50	-1.64	0.34
And VII (WFPC2)	556	10*	-1.46	0.40	0.23	-1.40	-
And VII (ACS)	698	10*	-1.41	0.36	0.33	-1.40	-

* Arbitrary values (see text for details).

Notes. The literature metallicity values have the following references: McConnachie et al. (2005) for And VI and And VII; Mancone & Sarajedini (2008) for And V; and Kalirai et al. (2010) for And I, And II and And III.

shift of $\sim +0.05$ mag for the peak of the HB in the luminosity function corresponds to an age step of ~ 3 Gyr (from 10 to 13 Gyr) or to a metallicity difference of ~ 0.8 dex (from $[\text{Fe}/\text{H}] = -1.8$ to -1.0). Although we first derived the metallicity of the targets using isochrones with fixed age of 10 Gyr, this will not influence the result since, when considering the upper part of the RGB, a change of 2 Gyr in the isochrone's age only brings about a change in metallicity of ~ 0.05 dex. Finally, once the age of the target galaxy has been determined, we proceed to recompute the median metallicity and metallicity dispersion using isochrones with the updated age value. The resulting MDFs are shown in Fig. 4.5. We note that both Galactic foreground contamination and stars belonging to the M31 giant stellar stream are not significantly affecting our results (see the Sections for And I and And VII).

The derived values for the M31 dwarf spheroidal companions are reported in Tab. 4.2 as follows: (1): name of the galaxy; (2): number of stars for which we derive the metallicity; (3) estimate of the age from the HB mean magnitude; (4): median $[\text{Fe}/\text{H}]$ value from the MDF; (5): observed metallicity dispersion (from a Gaussian fit); (6): intrinsic metallicity dispersion (after subtraction of the measurement error); (7): most recent photometric literature value for the mean $[\text{Fe}/\text{H}]$ (Grebel & Guhathakurta 1999; Mancone & Sarajedini 2008; Kalirai et al. 2010); and (8): metallicity spread given in literature.

We will now present and discuss the results for each of the galaxies separately.

4.2.1 And V

And V is the least luminous object in our sample. There are interesting discrepancies in the mean metallicity values found for this galaxy in the literature. Armandroff et al. (1998) give the first photometric estimate of the metallicity in And V, with a resulting mean value of $[\text{Fe}/\text{H}] \sim -1.5$ dex. We note that Guhathakurta et al. (2000) targeted individual RGB stars in some of the M31 dwarf spheroidal companions (And V, And III, And VI and And I) and derive their metallicity. Although they show the resulting MDFs, they do not report their mean values. A further photometric study by Davidge et al. (2002) concludes that the mean metallicity, as derived from the slope of the RGB, is much lower, $[\text{Fe}/\text{H}] \sim -2.2$ dex. McConnachie et al.

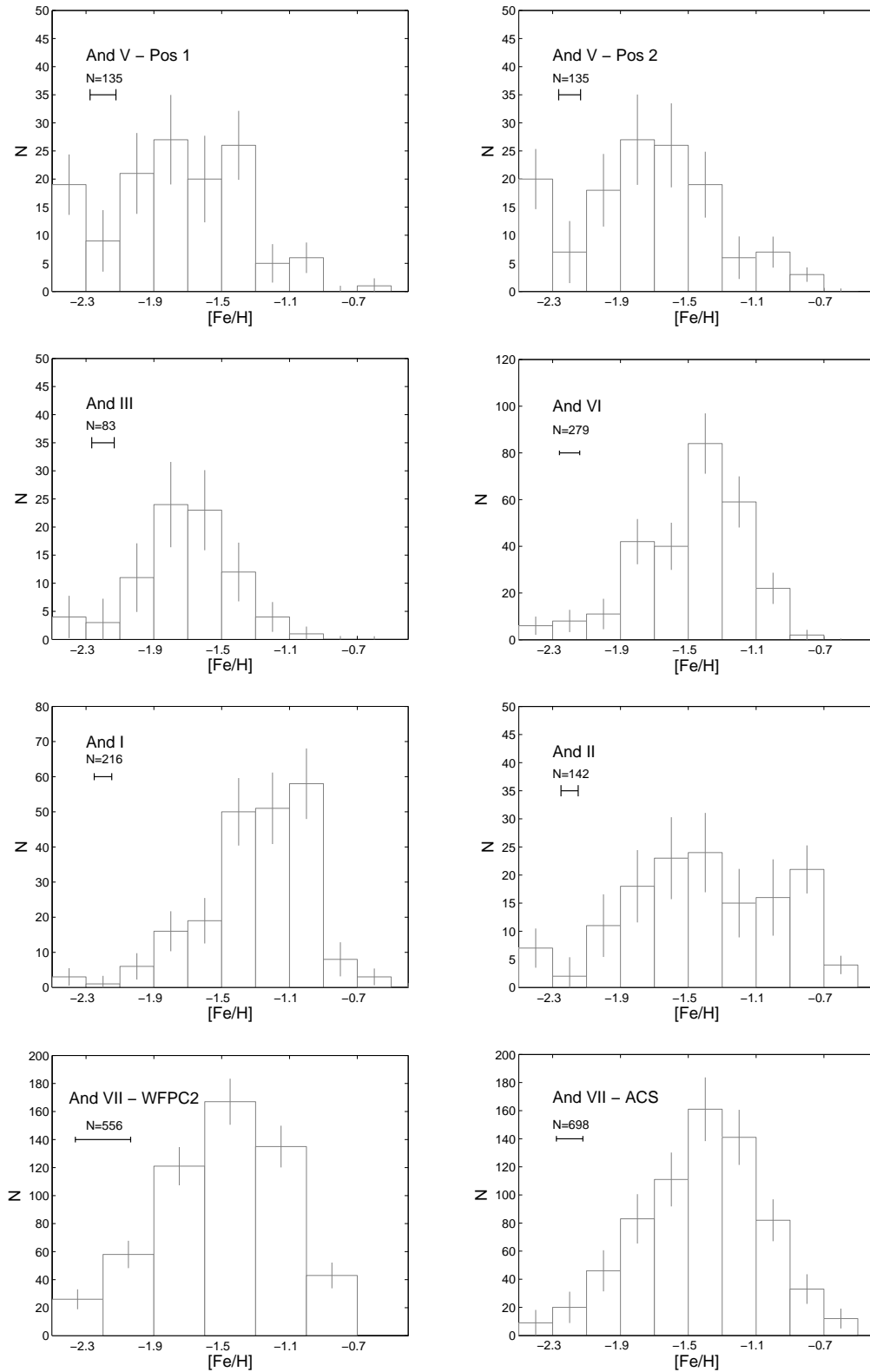


Figure 4.5: Metallicity distribution functions of the target M31 dwarfs, derived via interpolation of Dartmouth isochrones at a fixed age (see Tab. 4.2) and with varying metallicity. Plotted in the upper left corner is the median error on the individual values of $[\text{Fe}/\text{H}]$, and the total number of stars considered (for details see the text). For And V and And VII, we report the results derived for each of the two available datasets. Note that, compared to the other datasets, the binsize is larger for the MDF of the WFPC2 And VII observations due to the larger median metallicity error for the former.

(2005) then find a metallicity value similar to the result of Armandroff et al. (1998), by starting from the Vandenberg et al. (2000) stellar evolutionary models and a new set of data. The latest result comes from the WFPC2 observations that we use for our analysis: Mancone & Sarajedini (2008) use Galactic globular cluster fiducials to get a mean metallicity of $[\text{Fe}/\text{H}] \sim -2.2$ dex for And V, with a metallicity spread of ~ 0.5 dex. A tentative gradient in its HB population was found by Harbeck et al. (2001) by looking at WFPC2 data.

There are two, nearly entirely overlapping, HST/WFPC2 pointings for this galaxy, and the two datasets are (unsurprisingly and reassuringly) similar. The mean HB magnitudes derived from the luminosity functions shown in Fig. 4.3 are respectively $F555W = 25.43$ (dereddened, corresponding to an absolute value of 0.49) and $F555W = 25.46$ (corresponding to an absolute magnitude of 0.51), with dispersion values of ~ 0.1 in both cases (after measurement error subtraction). Given the similar datasets, we average the two median metallicity values found for RGB stars brighter than $F555W = 23.5$ in the two samples and arrive at a final value of $[\text{Fe}/\text{H}] \sim -1.75 \pm 0.41$. Isochrones of 10 Gyr have been used, consistent with the HB magnitude found and in agreement with the results of Mancone & Sarajedini (2008). This value is slightly more metal-rich than the one obtained by Mancone & Sarajedini (2008) using the same dataset, although it lies in the middle of the range of values found in the literature ($[\text{Fe}/\text{H}] \sim -2.2$ to ~ -1.5). Also the metallicity spread we find is in agreement with the Mancone & Sarajedini (2008) value. This little difference in the metallicity values is partly due to the different metallicity scale between the globular cluster fiducials (Zinn & West 1984) and the Dartmouth isochrones. The latter do not adopt an empirical scale but compute $[\text{Fe}/\text{H}]$ values starting from the solar abundances given by Grevesse & Sauval (1998), which result in $[\text{Fe}/\text{H}]$ values in good agreement (~ 0.1 dex) with the Zinn & West (1984) scale. Finally, the small discrepancy between our results and the literature ones could also be due to the slightly younger age of And V with respect to the globular clusters.

4.2.2 And III

The HST/WFPC2 data analyzed here were first studied by Da Costa et al. (2002), in the third of a series of papers dedicated to three M31 dwarf spheroidal companions (And I, And II and And III). Based on globular cluster fiducials, they found a mean metallicity value of $[\text{Fe}/\text{H}] \sim -1.88$ dex for this galaxy, with a dispersion of only ~ 0.12 dex. This value is in agreement with a previous photometric estimate by Armandroff et al. (1993) ($[\text{Fe}/\text{H}] \sim -2.0$) and with the value subsequently found by McConnachie et al. (2005) ($[\text{Fe}/\text{H}] \sim -1.7$). The study of Harbeck et al. (2001) and Da Costa et al. (2002) do not reveal the presence of gradients in the RGB or HB stellar populations of And III. Kalirai et al. (2010) derive and compare photometric and spectroscopic results for some of their target M31 dwarf spheroidals (And I, And II, And III). Both photometry (i.e., the position of the stars on the CMD) and spectroscopy (i.e., radial velocities) are used to identify the stars that most probably belong to the dwarf galaxy. Their results show that photometric (derived starting from the Vandenberg et al. 2006 stellar evolutionary models) and spectroscopic metallicities for the probable member stars are in good agreement with each other above a value of $[\text{Fe}/\text{H}] \sim -2.2$, within the uncertainties involved in the two methods (see their Fig. 9 and the respective discussion). The final value found for the photometric mean metallicity for And III is $[\text{Fe}/\text{H}] \sim -1.78$ and its metallicity dispersion 0.27 dex, in good agreement with previous estimates.

The luminosity function of And III is compared to theoretical luminosity functions, which

suggest its average age to be ~ 8 Gyr, thus slightly younger than the other dwarf spheroidals from the sample. This confirms the estimates from previous authors (e.g., Da Costa et al. 2002; McConnachie et al. 2005). The mean dereddened HB magnitude we find is $F555W = 25.35$ (absolute magnitude of 0.47), with a dispersion of ~ 0.12 . The median metallicity value we derive for the sample of RGB stars with $F555W < 23.0$ is $[Fe/H] \sim -1.71 \pm 0.21$, in good agreement with all the literature values mentioned above.

4.2.3 And VI

Using Galactic globular cluster fiducials, Armandroff et al. (1999) estimate the photometric metallicity of this galaxy to be $[Fe/H] \sim -1.58$ dex with a dispersion of approximately 0.3 dex. Subsequently, with the same method and a different dataset, Grebel & Guhathakurta (1999) give a slightly higher value (~ -1.30 dex), while McConnachie et al. (2005) find $[Fe/H] \sim -1.50$ using the Vandenberg et al. (2000) evolutionary models. A spectroscopic MDF for this galaxy has been derived by Guhathakurta et al. (2000), which shows a peak at $[Fe/H] \sim -1.5$ dex, a more metal-rich tail and a considerable spread. Harbeck et al. (2001) find strong and significant gradients in both the HB and RGB populations for this galaxy from an analysis of the same dataset as we study here, and attribute them primarily to metallicity (which they find to have a mean value of ~ -1.6 dex based on fiducials).

From the luminosity function of And VI, we find that an average age of ~ 12 Gyr is the preferred value for this object. The mean dereddened magnitude for the HB is found to be $F555W = 25.35$, which turns into an absolute value of ~ 0.63 with a dispersion (after photometric error subtraction) of 0.14. Using 12 Gyr old isochrones and considering only RGB stars with $F555W < 23.5$, the resulting median metallicity is $[Fe/H] \sim -1.42$ dex and its dispersion 0.26 dex, thus not inconsistent with the literature values mentioned above. We indeed confirm the significant metallicity spread already spectroscopically found by Guhathakurta et al. (2000). Note, however, that although Guhathakurta et al. (2000) emphasize that the metallicity spread and the width of the RGB in And VI are clearly larger than those of And V, these results are not confirmed by our findings.

4.2.4 And I

The first photometric estimate of the metallicity of And I was given by Mould & Kristian (1990), who report a mean value of $[Fe/H] = -1.4 \pm 0.2$ dex. As for And III, the photometric dataset we consider for this galaxy comes from the study carried out by Da Costa et al. (1996, 2000, 2002). The CMD of And I shows a HB that is predominantly red but with a blue extension. Da Costa et al. (1996) derive a photometric estimate of And I's metallicity using fiducials from Galactic globular clusters. The derived mean value is $[Fe/H] = -1.45$ dex, while the internal metallicity spread has a total range of ~ 0.6 dex as estimated from the width of the RGB, and an internal metallicity dispersion of ~ 0.21 dex. They further analyze the properties of the HB to quantify its age. By computing the difference between the mean color of the HB and that of the red part of the HB, they are able to estimate an age of $\sim 9.5 \pm 2.5$ Gyr for the dominant population of And I. They find a radial gradient in the distribution of HB stars with the bluer ones being found preferentially beyond the core radius of the dwarf. However, when computing the mean metallicity of the RGB for different radial subsamples of stars, they find no evidence for a radial gradient in abundance. These results are confirmed by Harbeck

et al. (2001), who find tentative gradients in both the HB and RGB populations. However, the number of stars used in this analysis is very low, and a more extended spatial coverage would be required to draw firmer conclusions about the existence of gradients. McConnachie et al. (2005) find a mean metallicity value of $[\text{Fe}/\text{H}] = -1.4$ dex for And I. In the study by Kalirai et al. (2010), particular attention is given to the membership of the target stars in And I (the closest dwarf to M31, also in projection), which is partly contaminated by MW foreground dwarfs and partly by the giant stellar stream that And I lies close to. By using both photometric and spectroscopic data (as explained above), they show that the contamination of this sample by Galactic foreground stars is fairly low. On the other hand, stars belonging to the giant stellar stream are easily recognizable because of their higher metallicities ($[\text{Fe}/\text{H}] \gtrsim -0.9$) with respect to the ones derived for the stars belonging to the dwarf, and because they are predominantly found at larger radii (the spatial coverage of their observations of And I goes well beyond the galaxy's core radius). The resulting mean metallicity is $[\text{Fe}/\text{H}] \sim -1.45$, while the metallicity spread is 0.37. These values are in excellent agreement with the photometric estimates given by Da Costa et al. (1996).

We find an age for And I of ~ 12 Gyr. The mean observed magnitude is $F555W = 25.21$, corresponding to an absolute (dereddened) magnitude of ~ 0.64 and with a spread (after photometric error subtraction) of ~ 0.09 . We next derive the MDF for And I based on RGB stars brighter than $F555W = 23.5$, to avoid the contamination from AGB stars along the left side of the RGB (see also Da Costa et al. 1996). The median metallicity value reported in Tab. 4.2 is slightly higher than the previous photometric estimates and also the latest spectroscopic value, as also for And II (next Section). Kalirai et al. (2010) show that stars with $[\text{Fe}/\text{H}] \gtrsim -0.9$ in their sample in fact all belong to the M31 stream. Our sample does not, however, reach the outer parts of And II where the M31 stars are located (see their Fig. 7), so the contamination from the M31 stream should be minimal in our sample. Even when the median metallicity is recomputed without taking into account stars with $[\text{Fe}/\text{H}] \gtrsim -0.9$, we find that its value does not significantly change. Hence, we consider this small discrepancy in metallicity to be due to the isochrone models used.

4.2.5 And II

The first photometric estimate of the mean metallicity for And II was given by Koenig et al. (1993), who report a value of $[\text{Fe}/\text{H}] \sim -1.6$ with a spread of ~ 0.4 dex. Côté et al. (1999) subsequently analyzed a spectroscopic stellar sample for this galaxy, obtaining a mean metallicity value of $[\text{Fe}/\text{H}] = -1.47$ dex with a spread of ~ 0.35 dex. The HST/WFPC2 images for this galaxy were analyzed in the second of a series of papers about M31 dwarf spheroidal companions (Da Costa et al. 1996, 2000, 2002). We use the same dataset in order to derive And II's MDF and age. The mean metallicity value derived for this galaxy by Da Costa et al. (2000) is $[\text{Fe}/\text{H}] = -1.49$ dex, with a large dispersion of ~ 0.36 dex. Interestingly, they also point out that the derived MDF can be fitted well by a double component, with the first one having a mean metallicity of $[\text{Fe}/\text{H}] \sim -1.60$ dex and the second, less prominent one, displaying a value of $[\text{Fe}/\text{H}] \sim -0.95$ dex. In the same study, it was suggested that And II could contain both an old population and an intermediate-age one, given the morphology of the HB and the possible presence of luminous AGB stars. A small number of carbon stars is indeed found by Kerschbaum et al. (2004) for this object. Finally, Da Costa et al. (2000) showed that the HB population has a spatial gradient, although this is not seen in the RGB population. Harbeck

et al. (2001) later also considered the same data but did not find significant gradients in the two subpopulations. In their study, McConnachie et al. (2005) assign a value of $[\text{Fe}/\text{H}] \sim -1.5$ dex to the mean metallicity of And II, starting from the Vandenberg et al. (2000) stellar isochrones. Perhaps the most interesting study of And II is by McConnachie et al. (2007). The authors analyze a new photometric dataset, from which they conclude that a RC (stemming from the superposition of red HB, RGB and intermediate-age helium-burning stars) is definitely present in And II, the first to be observed in the M31 dwarf spheroidal companions. Their data provide a large spatial coverage of the target galaxy and they are able to show that the RGB population has an old and extended component plus a slightly younger (by ~ 3 Gyr) subpopulation, with the latter being more centrally concentrated. They find mean values of $[\text{Fe}/\text{H}] \sim -1.5$ and $[\text{Fe}/\text{H}] \sim -1.0$ for the two subpopulations, respectively, with the latter also having a larger spread. Finally, McConnachie et al. (2007) suggest that the two mentioned subpopulations are likely to be dynamically separated (although kinematic data are needed to support this claim). The mean metallicity value derived for this galaxy by Kalirai et al. (2010) is $[\text{Fe}/\text{H}] = -1.64$ dex, with a dispersion of ~ 0.34 dex, however their MDF does not show signs of a double component. They attribute this to the limited spatial coverage of their data with respect to the McConnachie et al. (2007) ones.

We derive an age estimate of this galaxy of ~ 10 Gyr by comparing the luminosity function of And II to the theoretical ones. We use this age as an arbitrary value to derive our MDF, since it is likely to be biased given that there are two distinct age components in this galaxy (see the detailed analysis by McConnachie et al. 2007). The mean magnitude of the RC for And II is $F_{555W} = 24.89$, which can be translated to an absolute magnitude of ~ 0.58 with a dispersion of $\sigma_{F_{555W}} = 0.09$ (after subtraction of photometric errors). The MDF shown in Fig. 4.5 comes from the RGB stars that have $F_{555W} = 23.0$, in order to avoid as much as possible contamination from the presence of AGB stars, and the resulting median metallicity is $[\text{Fe}/\text{H}] \sim -1.43$ dex. This value is slightly higher than the literature ones. Also our MDF clearly shows signs of a double component, and a double Gaussian fit leads to peak metallicity values of $[\text{Fe}/\text{H}] = -1.51$ and $[\text{Fe}/\text{H}] = -0.94$ dex for the subcomponents, in excellent agreement with the results of Da Costa et al. (2000) and McConnachie et al. (2007).

4.2.6 And VII

There are only two photometric estimates for the metallicity of And VII. Grebel & Guhathakurta (1999) give a mean value of $[\text{Fe}/\text{H}] \sim -1.40$ dex starting from fiducials, which is subsequently confirmed by the study of McConnachie et al. (2005). No further analysis has been performed for this object. And VII presents a very well populated HB, and this is particularly true for its red part (see Fig. 4.2). We note that And VII lies at a Galactic latitude of only $b \sim -10^\circ$, making it the most foreground contaminated object in this sample. However, as we show in Fig. 4.6 by using the Besançon Galactic models (see also previous Chapter), this does not significantly influence our results. The most affected part of the RGB is just its upper, reddest edge in the ACS observations ($\sim 10\%$ contamination). Even if we were to subtract the Galactic foreground, the net effect would only be a slightly smaller number of stars in the three most metal-rich bins of our MDFs, and a mean metallicity value that is lower by a few percent.

The mean HB magnitude we find here is $F_{555W} = 25.9$ from the ACS data (the WFPC2 observations are not deep enough for us to estimate the HB position, see Fig. 4.3). This translates to an absolute magnitude of 0.7 and the dispersion has a value of 0.1. However, when

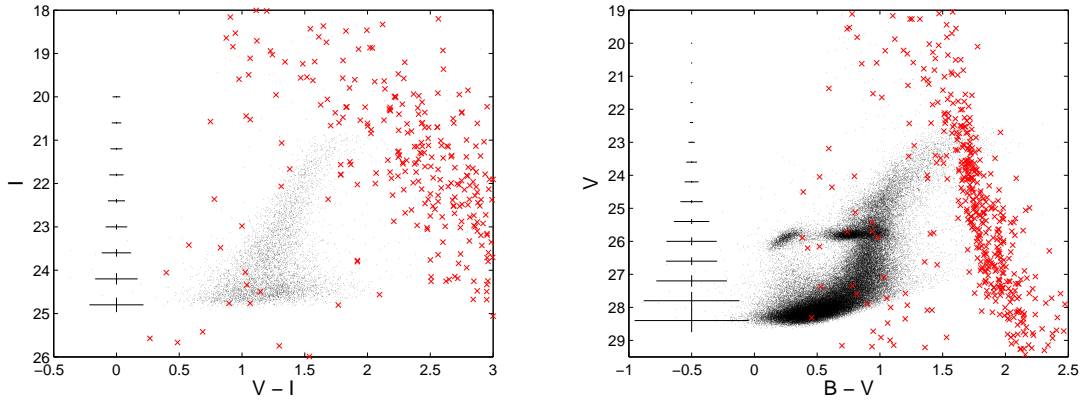


Figure 4.6: CMDs for And VII (from both WFPC2, *left panel*, and ACS, *right panel*, observations). Representative photometric errorbars are shown at different magnitudes along the CMDs. We overlay on the CMDs the predicted Galactic foreground contamination (obtained with the Besançon models) as red crosses. The simulated stars do not include incompleteness effects or photometric errors.

comparing the observed luminosity function for And VII reported in Fig. 4.3 to the theoretical ones of the Padova stellar evolutionary models (shown in Fig. 4.7), we can clearly see that a discrepancy is present. And VII would need to be older than ~ 13 Gyr *and* at least as metal-rich as $[\text{Fe}/\text{H}] \sim -1.0$ at the same time, in order for the models to reproduce the observed HB luminosity. If we were to adopt an age of 13 Gyr, then the resulting metallicity would be *lower* and not higher, so this would not solve the issue. The problem could be hidden in the evolutionary models (specifically, in the transformations from theoretical to observational plane) for this particular choice of filters. Alternatively, an α -element enhancement could also mimic an older age (see also previous Chapter), but the Padova models do not simulate isochrones with α values different from solar, and this is a question that only accurate spectroscopy would be able to answer. A scatter in the α -element abundance values is observed from spectroscopy of MW dwarf spheroidal companions (see Fig. 1.8), so a small enhancement of these elements (up to $[\alpha/\text{Fe}] \sim +0.3$) cannot be excluded. And VII definitely deserves more attention, starting from a more extended radial coverage and proceeding with a detailed study of the HB, or possibly the RC in case IAPs are present.

We thus compute the median metallicity for the two samples (ACS and WFPC2 observations) using isochrones with an arbitrary age of 10 Gyr. We consider stars brighter than $F555W = 23.5$ for the ACS observations and stars brighter than $F814W = 22.5$ for the WFPC2 ones. The two resulting values agree very well with each other (see Tab. 4.2), and with the previous literature estimates mentioned above. In Fig. 4.5, we plot the MDF derived from the WFPC2 observations with a larger binsize compared to the other MDFs, because the median metallicity error for this dataset has a slightly higher value. The metallicity dispersion computed starting from the WFPC2 data is just slightly smaller than the one derived from the deeper ACS data. This could be due to the differences between stellar isochrones produced for different filters, but also due to observational errors.

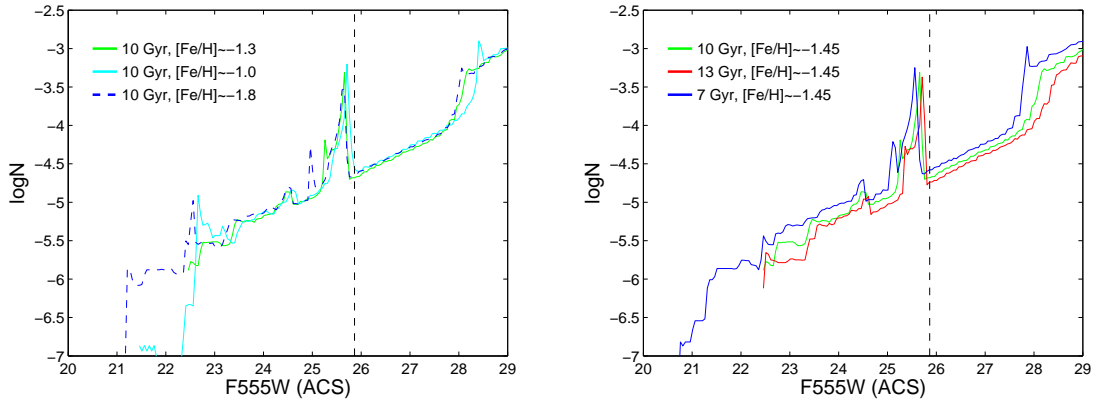


Figure 4.7: Theoretical luminosity functions from Padova evolutionary models (not convolved with observational errors). *Left panel.* Luminosity functions with a fixed age and varying metallicity. *Right panel.* Luminosity functions with a fixed metallicity and varying age (based on And VII median metallicity). We also show the location of the observed mean HB magnitude for And VII with a vertical black dashed line.

4.3 Discussion

The sample of M31 dwarf spheroidal companions we present comes entirely from HST data and the photometry of this exquisite set of data has been performed in a homogeneous way in our analysis. The derivation of the MDFs was done using the Dartmouth stellar isochrones, that have recently proven to be a very good match to old globular clusters, see also Section 4.2. The MDFs for some of these objects have been previously presented in the literature, but mostly with the use of Galactic globular cluster fiducials, and never for such a large sample. Other studies (e.g., McConnachie et al. 2005) have derived the structural parameters and integrated quantities for our entire sample of targets, including the mean metallicity, but without producing MDFs and starting from ground-based data. Finally, the ongoing SPLASH Survey makes use of both photometry and spectroscopy to accurately derive physical parameters for the M31 dwarf companions (including the newly discovered faint ones), but this is still far from being completed. With this analysis, we can further check the validity of the method presented in Chapter 3 for deriving MDFs, and moreover estimate the ages of our target objects thanks to the depth of the available photometry.

It almost goes without saying that the MDFs we derive are all very different from one another, again supporting the evidence that dwarf galaxies have extremely diverse SFHs. As can be seen from Tab. 4.2, the results we obtain with our method are generally in good agreement with previous literature values. In the cases where differences exist, we find no indications for any *systematic* offset between our values and the ones found in literature, the differences depending on the individual cases. Both in the case of And VI and And VII, the comparisons were made with the values found by McConnachie et al. (2005), where Vandenberg et al. (2000) isochrones were used. The differences in the mean metallicity are still less than ~ 0.1 dex. We underlined an interesting discrepancy between the theoretical and the observed luminosity functions for And VII, which makes it difficult to estimate the age for this object. This galaxy definitely deserves further study. We also note that for this object we have not only deep photometric data that reach below the HB level, but also a second dataset that is much shallower, thus very similar to the sample we have for the CenA early-type dwarf companions. In this way, we verify that

the results derived from the two datasets are in very good agreement, although the metallicity spread derived from the shallow dataset is lower by ~ 0.1 dex. In the previous Chapter, we already mentioned that our resulting metallicity spreads are most probably lower limits to the true ones. The difference we find for the two And VII datasets quantifies the uncertainty of our method, as it probably comes both from the stellar evolutionary models as well as from the observational errors.

Moving on to the other galaxies of our M31 sample, the mean metallicity we find for And V has a value in between the (discrepant) ones previously given in literature. Our result is slightly more metal-poor than the latest literature value. The latter comes from using the same dataset but from adopting Galactic globular cluster fiducials, so the difference could be due to the different metallicity scales involved and the younger age we find for this galaxy with respect to globular clusters (see the discussion in the And V Section). And I, And II and And III have their photometric MDFs derived by Kalirai et al. (2010), based on a combined photometric and spectroscopic analysis. Our MDFs for And I and And III are similar to their results, while for And II Kalirai et al. (2010) do not find a bimodal distribution that has, however, been observed in previous studies (e.g., Da Costa et al. 2002; McConnachie et al. 2007). They justify this result as most probably due to the limited spatial coverage of their observations. The latter could be one of the reasons for the small differences between the Kalirai et al. (2010) mean metallicities and the ones we find for these three objects. The differences are more pronounced for And I and And II, in the sense that our values are more metal-rich by ~ 0.2 dex, but this is still a very good agreement if we consider the age uncertainty and the different sets of isochrones employed (in the case of Kalirai et al. 2010, these are the Vandenberg et al. 2006 ones). While for And II our metallicity spread is larger than the one of Kalirai et al. (2010) (due to the more metal-rich, and probably younger component that they do not resolve, see also McConnachie et al. 2007), for And I and And III our spreads are slightly smaller, indicating again that we are probably obtaining lower limits to the true values.

Comparison with Centaurus A early-type dwarf companions

Last but not least, we can compare these results to what is known about the MW dwarf spheroidal companions, and to what we derived for the CenA early-type dwarf companions. As mentioned in the introduction of this Chapter, if we consider dwarf galaxies from the three subsamples which lie in the same range of luminosities, the most striking difference among them is that the CenA dwarfs (or at least the ones for which the IAP was analyzed in detail), together with the M31 companions, both show the absence of a significant IAP. It is not at all clear what the reason for this difference could be. It could be that the M31 and CenA environments, as opposed to the MW one, have somehow truncated the star formation of their smallest (and closest) companions earlier. In the MW surroundings, there is evidence for a mild trend of the amount of IAPs with distance from the dominant group galaxy, with the furthest dwarfs having a slightly higher percentage of IAPs (see, e.g., the discussion in van den Bergh 1999; Da Costa et al. 2002). Environmental processes, such as ram-pressure stripping from a hot corona or from the intra-group medium, or even the UV flux from the dominant group galaxy, could be responsible for the observed trend (e.g., Grebel et al. 2003). M31 is known to have a higher stellar density than the MW at a radius of ~ 20 kpc, and the large amount of substructures observed in M31's halo suggest a very active accretion history (see, e.g., Kalirai et al. 2010, and references therein). At the same time, the elliptical CenA has also experienced substantial mergers in its recent past

and shows the presence of radio lobes, and the surrounding group is believed to be a dense environment that possibly favors ram-pressure stripping thus making gas retention difficult for its dwarf members (see the discussion in Chapter 3). The conclusion is that some process must have somehow lead to a loss of gas, thus halting the star formation in the M31 and CenA dwarf companions earlier than in the MW subgroup (we underline that the IAP fractions are confirmed to be very low only for five early-type dwarfs around CenA, so further studies will be necessary to confirm this trend). It is however extremely difficult to disentangle possible external causes from the internal processes that influence the evolution of a dwarf galaxy. On the other hand, recent studies have not only proved that the brightest of the M31 dwarf spheroidal companions have much larger half-light radii than MW dwarfs of similar luminosity (McConnachie & Irwin 2006), but also suggest that their populations are dynamically colder, and thus they might reside in less dense dark matter haloes (Kalirai et al. 2010; Collins et al. 2010). This would imply a substantial difference in the physics of these small objects.

We plot some of the fundamental properties of our target galaxies in Fig. 4.8, and compare them to the MW and CenA companions (see also previous Chapter). In the top panel, we show again the luminosity-metallicity relation, and add the values found here for the M31 companions. As expected, they nicely follow the linear relation found for the MW dwarfs. The amount of metal-enrichment observed in a galaxy namely depends on its mass, since a low-mass object is at the same time producing stars less efficiently compared to a more massive object, and is also less capable to retain the products of stellar evolution (e.g., galactic outflows). The luminosity-metallicity relation seems to be universal, as proved for MW and M31 companions (see, e.g., Kalirai et al. 2010), and as also seen for dwarfs outside the Local Group (e.g., Sharina et al. 2008). The central panel shows the dependence of metallicity on the deprojected distance from the dominant group galaxy (computed starting from the distances of McConnachie et al. 2005), and confirms the absence of a trend for this relation, as already seen in the previous Chapter. Finally, we check whether there could be similarities in the relation of half-light radius versus luminosity. We transform the values found for the CenA dwarfs and reported in Tab. 3.2 from units of arcsec to units of pc, depending on the individual galaxy distances, and plot the results (together with the MW and M31 values listed in Kalirai et al. 2010, who also show a complete plot of all the MW and M31 companions) in the bottom panel of Fig. 4.8. There is no striking evidence for the CenA dwarfs being larger than the MW or M31 counterparts, except maybe for KKs55 and for the two dwarf ellipticals (ESO269-66 and KK197). In the analysis of the previous Chapter, we also did not find any definite spatial dependence of the amount of IAPs in our targets. The entire discussion about which aspects are commonly shared by the M31 and CenA dwarfs and what makes them different from the MW companions thus remains an open and intriguing question, that definitely deserves further attention.

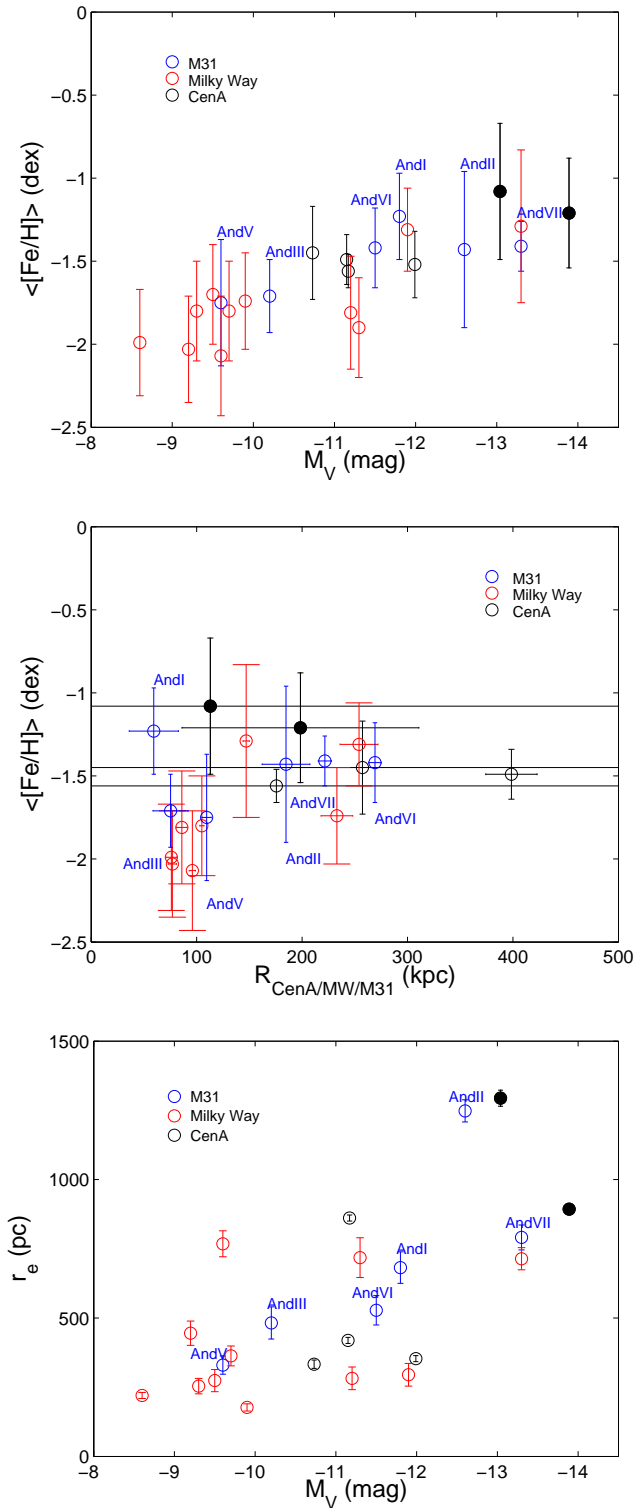


Figure 4.8: *Top panel.* Median metallicity plotted as a function of absolute V luminosity. *Central panel.* Median metallicity plotted as a function of deprojected distance from the dominant group galaxy. *Bottom panel.* Half-light radius plotted as a function of absolute V luminosity (see text for details). Blue symbols are for the M31 dwarf spheroidal studied in this Chapter, black symbols represent the CenA group dwarfs studied in Chapter 3 (open symbols for dwarf spheroidals and filled circles for dwarf ellipticals), while red symbols denote the MW dwarf spheroidal companions.

“The heaventree of stars hung with humid nightblue fruit.”

J. Joyce, *Ulysses*, (1922)

5

Late-type dwarfs

In the previous Chapters, we have shown how we can derive properties like the metallicity content, the spatial distribution and the star formation episodes of the intermediate-age and old populations for early-type dwarf galaxies. For the CenA group, the drawback of our analysis lies in the fact that the information available from the resolved stellar populations of these objects is limited by their distance from us. As already seen in Chapter 2.1.3.3, late-type dwarfs are more generous in the amount of information that can be extracted from their CMDs, since the young stellar populations permit us to reconstruct in detail their most recent ($\lesssim 1$ Gyr) SFH. In Section 5.1 we describe the synthetic CMD modeling method used for this study (which was developed by A. A. Cole, who also derived the SFHs discussed in this Chapter), and present separately the results for the M83 and CenA subgroups. In Section 5.2 we then study the spatial distribution of the stellar populations distinct (in age) for the individual target galaxies. The material presented in this Chapter is partly included in the following papers: Crnojević et al. (2010c), A&A submitted, and Crnojević et al. (2010d), in preparation.

5.1 Recent star formation histories

Starting from Padova stellar evolutionary models (Marigo et al. 2008), the adopted code (see, e.g., Skillman et al. 2003; Cole et al. 2007) builds synthetic CMDs with a wide range of physical parameters. We make assumptions about the initial mass function (IMF) and the binary fraction. In particular, the chosen IMF is log-normal between 0.08 and 1 M_{\odot} (Chabrier 2003) and it follows a Salpeter power-law above 1 M_{\odot} . For the binary fraction, prescriptions from Duquennoy & Mayor (1991) and Mazeh et al. (1992) are used. Distance moduli and reddening values are taken from Karachentsev et al. (2007) (derived via the TRGB method) and from the Schlegel extinction maps (Schlegel et al. 1998) respectively. Where available, we also use literature values to constrain a priori the present-day iron abundance computed starting from oxygen abundances (available for IC4247, ESO381-20 and KK196, see below for details).

We do not make any assumption about a possible age-metallicity relation. This would, in fact, not change the amount of star formation, but it would slightly affect the age and duration of each star formation episode. Due to the low amount of information available from the CMDs, any attempt to impose such a relation would be arbitrary and poorly constrained. We initially choose 5 different isochrone metallicities to construct the synthetic CMDs ($Z = 0.0001, 0.00024, 0.0004, 0.0006$ and 0.001).

We also choose not to take into account differential reddening internal to the galaxies. This is almost certainly present, due to the presence of (not uniformly distributed) young stars. How-

ever, Cignoni & Tosi (2010), in their review paper about star formation modeling techniques, show that the effects of not taking differential reddening into account for the SFH reconstruction are minor and not systematic, as compared for example to the adopted foreground reddening value. Moreover, since we are dealing with metal-poor dwarf galaxies, the amount of dust is generally low.

Finally, we make use of the artificial star tests to take into account photometric errors and incompleteness effects in our observations. We can now look for the synthetic SFH that produces a CMD that has the maximum likelihood to match with the observed one. This is done exploring the parameter space via a simulated annealing algorithm (described in Skillman et al. 2003; Cole et al. 2007). This procedure gives for each galaxy the SFR at each chosen time interval (SFH), and a corresponding best-fit metallicity value. We show the results in Fig. 5.1, 5.3, 5.5, and 5.6.

The first thing to point out is that we plot the SFHs with a logarithmic age axis. This is done because the age resolution decreases with increasing age. The age bins will be broader when there is less information available from the CMD, and finer where there is more. For example, in Fig. 2.6 we see that the oldest MSTO detectable in our data is visible for stars no older than ~ 50 Myr ($I \sim 26$). For the recent SFH we can then rely on the upper MS and the bright helium-burning phases. The CMDs do not reach the HB (which at these distances would be expected at an I -band magnitude of ~ 28). Also, the RC is not recognizable in our data. This means that for ages older than ~ 1 Gyr it is very difficult to put any firm age constraint on star formation episodes from the evolved population alone. We can put constraints on the intermediate-age SFR (~ 1 to ~ 9 Gyr) by looking at luminous AGB stars, but we are not able to resolve any bursty episode of star formation at these ages, and so the time bins become very large as age increases. Each bin size is thus considered as a horizontal errorbar.

The vertical errorbars for the star formation, shown in the upper panels of Fig. 5.1, 5.3, 5.5, and 5.6, come from the maximum likelihood process, and extend to all of the values that produce solutions within 1σ from the best-fit star formation value. In the lower panels we also report the evolution of metallicity as a function of time. Unfortunately, due to the age-metallicity degeneracy for the old stars of the RGB and due to the limited amount of information for younger ages, it is very difficult to constrain the metallicity for our target galaxies. We thus underline that only the mean metallicity values derived are reliable, while the evolution with time and potential metallicity spreads cannot be analyzed any further from the available data. However, for all of the galaxies the best-fit metallicity is consistent with the other information available, and it shows an almost constant metallicity value over the whole galaxy's lifetime. The errorbars in metallicity show the range, in each age bin, from the 10th to the 90th percentile from the best-fit SFH.

As an additional test, we compute the total number of stars formed during the whole galaxy's lifetime from our SFH, and compare it to estimates of the stellar mass coming from the total luminosity and an assumption for the stellar mass-to-light ratio. The latter has normally a value of ~ 1 for gas-rich dwarf galaxies (e.g., Banks et al. 1999; Read & Trentham 2005, and references therein). Côté et al. (2000) analyze dwarf irregulars in the CenA and Sculptor groups. We have one galaxy, ESO381-20, in common with their sample. Looking for the best-fit stellar mass-to-light ratio from their HI rotation curves, they derive values larger than 1 (~ 2 to ~ 4) for some of the galaxies including ESO381-20, so we decide to additionally assume a stellar mass-to-light ratio of 2 when computing stellar masses for our sample. We find good agreement between the results for the the two different estimates, and we list the exact values in

the individual galaxies' description.

We note however that there is disagreement between our derived [Fe/H] values and previous literature works (Karachentsev et al. 2007, Sharina et al. 2008), in the sense that our values are higher for all of the target dwarfs. In those studies, the mean metallicity of the target galaxies was computed through the empirical formula by Lee et al. (1993) considering stars on the upper RGB. The aforementioned formula is valid only for predominantly old populations, while in our target galaxies there is clear evidence for intermediate-age stars. This younger stellar components will bias the old RGB in the sense that it will be highly contaminated by intermediate-age RGB stars, which have bluer colors than old RGB stars at a fixed metallicity and luminosity (see, e.g., Cole et al. 2005). When adopting the Lee et al. (1993) formula, RGB stars younger than ~ 10 Gyr will thus be considered to be old, metal-poor RGB stars, and the resulting metallicity will be underestimated by about 0.5-1 dex. In addition, faint AGB stars along the RGB locus can bias the derived metallicities to erroneously low values.

To better understand the SFH, we also present some parameters to facilitate the comparison of the results among individual galaxies and to other literature studies (e.g., Scalo 1986; Weisz et al. 2008). We compute the ratio of the SFR in a certain time period to the average SFR during the galaxy's lifetime (b_{100} over the last 100 Myr, b_{500} over the last 500 Myr, b_{1G} over the last 1 Gyr, and b_{14G} for ages older than 1 Gyr ago). We also derive the fractions of stars formed from 0 – 1 Gyr (f_{1G}), from 1 – 4 Gyr (f_{4G}) and from 4 – 14 Gyr (f_{14G}), to assess the efficiency of the star formation process in different time periods. These parameters would have the following values if a constant SFR were adopted: $f_{1G} = 0.07$, $f_{4G} = 0.36$ and $f_{14G} = 0.57$. The values that we derive for these parameters, together with the lifetime average metallicity values, are reported in Tab. 5.1, as follows: column (1): name of the galaxy; (2): average SFR over the whole lifetime; (3): b_{100} ; (4): b_{500} ; (5): b_{1G} ; (6): b_{14G} ; (7): f_{1G} ; (8): f_{4G} ; (9): f_{14G} ; and (10): average metallicity over the whole lifetime.

We now comment separately the results obtained for each individual galaxy.

5.1.1 The M83 subgroup

ESO443-09, KK170

The faintest and least dense galaxy in our sample is ESO443-09. This object also contains the smallest amount of HI gas ($M_{HI} \sim 10^7 M_{\odot}$, Georgiev et al. 2008), and it is the most isolated one, having a tidal index of -0.9 (Karachentsev et al. 2007, see definition in Chapter 2). Its distance from us is 5.97 ± 0.46 Mpc, and its deprojected distance from M83 is $\sim 1.2 \pm 0.4$ Mpc (computed using the radial distance and the coordinates from Karachentsev et al. 2007). ESO443-09 has not yet been studied in $H\alpha$. We detect only ~ 1900 stars in its CMD (Fig. 2.5). ESO443-09 indeed contains very few massive MS stars and no evidence of currently ongoing star formation as judged from its CMD. There is, however, a considerable presence of BL stars, on top of the old component seen in the RGB; the RSG and an IAP (luminous AGB) are almost absent. Hence, overall this galaxy exhibits the properties of a typical transition-type dwarf (e.g. Grebel et al. 2003).

The SFH derived for ESO443-09 and shown in Fig. 5.1 confirms that this galaxy has been almost constantly active in its early history, although with a low average SFR ($\sim 0.0008 \pm 0.0007 M_{\odot} \text{yr}^{-1}$). From now on we adopt a standard Λ CDM cosmology with $t_0 = 13.7$ Gyr, $H_0 = 71 \text{ km s}^{-1} \text{ Mpc}^{-1}$, $\Omega_{\Lambda} = 0.73$ and $\Omega_m = 0.27$. If we assume that the galaxy was born

Table 5.1: Star formation parameters derived for our sample of late-type galaxies (companions of M83 and CenA).

Galaxy	$\langle \text{SFR} \rangle$ ($10^{-2} M_{\odot} \text{yr}^{-1}$)	b_{100}	b_{500}	b_{1G}	b_{14G}	f_{1G}	f_{4G}	f_{14G}	$\langle [\text{Fe}/\text{H}] \rangle$ (dex)
ESO443-09, KK170	0.08 ± 0.07	6.48	3.02	0.91	1.01	0.11	0.06	0.83	-1.46 ± 0.14
ESO381-18	0.35 ± 0.26	1.71	0.93	1.91	0.95	0.13	0.11	0.76	-1.40 ± 0.13
ESO444-78, UGCA365	0.63 ± 0.36	0.66	0.48	0.40	1.07	0.03	0.11	0.86	-1.37 ± 0.21
IC4247, ESO444-34	1.01 ± 0.66	0.90	0.89	1.42	0.99	0.10	0.06	0.84	-1.43 ± 0.11
ESO381-20	0.70 ± 0.48	4.36	3.41	1.76	0.92	0.15	0.06	0.79	-1.45 ± 0.17
HIPASS J1348-37	0.14 ± 0.05	1.56	1.78	1.73	0.88	0.12	0.28	0.60	-1.50 ± 0.07
KK196, AM1318-444	0.20 ± 0.11	–	0.99	0.66	1.04	0.07	0.19	0.74	-1.43 ± 0.25
KK182, Cen6	0.10 ± 0.14	5.72	6.78	3.37	0.85	0.24	0.35	0.41	-1.46 ± 0.21
ESO384-16	0.60 ± 0.23	0.14	0.54	0.37	1.09	0.03	0.27	0.70	-0.97 ± 0.15
ESO269-58	6.79 ± 3.93	0.12	0.31	0.21	1.11	0.01	0.22	0.76	-0.98 ± 0.20

Notes. The b parameter is the ratio of star formation rate over the indicated time period (0.1, 0.5, 1 and from 1 to 14 Gyr respectively) to the average star formation over the whole lifetime; the f parameter is the fraction of stars born in a certain time interval (0 – 1, 1 – 4 and 4 – 14 Gyr).

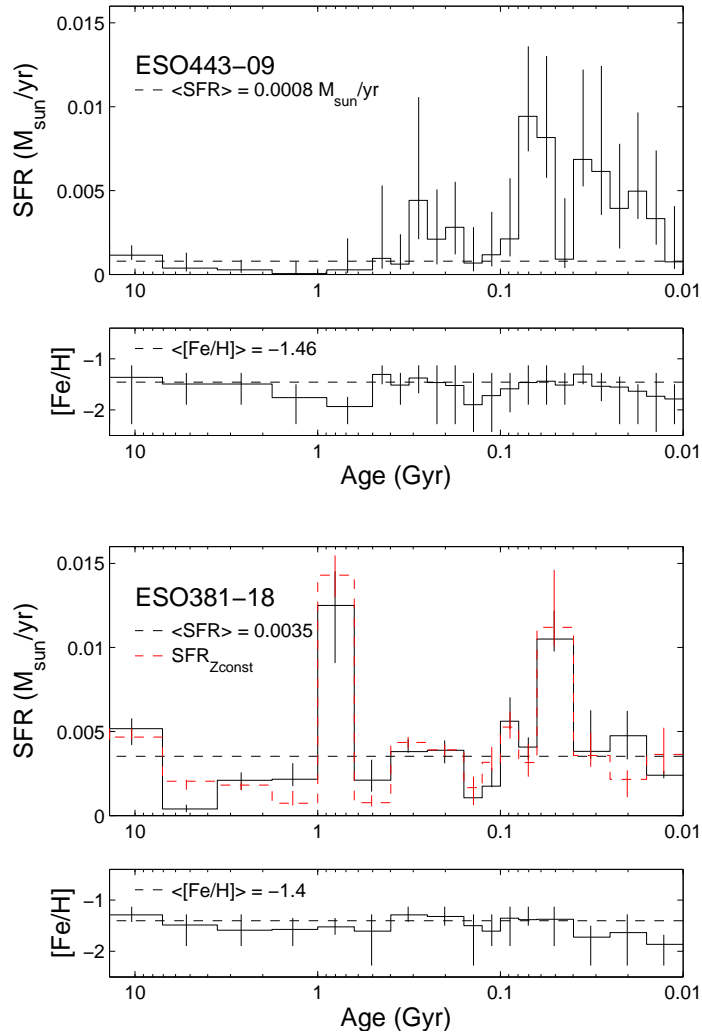


Figure 5.1: *Upper panels.* Star formation histories derived for two of the studied galaxies in the M83 subgroup (ESO443-09 and ESO381-018, ordered by increasing absolute magnitude). For each galaxy, the star formation rate is plotted as a function of time, with the oldest age being on the left side and the most recent time bin on the right edge of the (logarithmic) horizontal axis. Note that the size of the time bins is variable, due to the different amount of information obtainable from each CMD for each stellar evolutionary stage. The black dotted line indicates the mean star formation over the whole galaxy’s lifetime. The red dotted line for ESO381-18 indicates the alternative star formation history solution obtained when restricting the metallicity range in the parameter space (see text for details). *Lower panels.* Metallicity as a function of time, with the same axes convention as above. The black dotted line represents the mean metallicity over the galaxy’s lifetime. Note that the metallicity evolution is poorly constrained.

~ 13.5 Gyr ago, the fraction of stars that had formed by 8 Gyr ago (which corresponds to $z \sim 1.1$) and by 5 Gyr ago ($z \sim 0.5$) is $\sim 60\% \pm 10\%$ and $\sim 75\% \pm 10\%$, respectively. This is just a rough estimate, since we cannot derive precisely the age of the oldest stellar populations with these data. A fairly large fraction ($> 10\%$) of stars was however formed in the last Gyr. In particular, the values of b_{100} and b_{500} (Tab. 5.1) are quite high, showing a non-continuous episode of star formation from 10 to 200 Myr ago.

The metallicity is fairly constant within the errorbars. However, for this and for almost all of the other galaxies (except for ESO381-20), the present-day values appear to be slightly lower than the average ones. We will return to this issue in the next Subsection.

We first compute the total stellar mass by integrating the stellar mass produced by our SFH, which yields $1.1 \times 10^7 M_{\odot}$. We note that this is not a precise estimate, since we are not subtracting off the mass of the stars that died off due to their evolution. This implies that we are overestimating the stellar masses by $\sim 25\%$. Starting from the B -band luminosity and assuming a stellar mass-to-light ratio of 1 or 2, we obtain values of $0.8 \times 10^7 M_{\odot}$ and $1.6 \times 10^7 M_{\odot}$, respectively, thus consistent with our SFH derivation.

ESO381-18

ESO381-18 is another rather isolated galaxy ($\Theta = -0.6$), found at a deprojected distance of $\sim 1.1 \pm 0.1$ Mpc from M83 (computed using the radial distance from Karachentsev et al. 2007). As for ESO443-09, neutral gas has been detected ($M_{HI} \sim 3 \times 10^7 M_{\odot}$, Banks et al. 1999; Georgiev et al. 2008), but there is no evidence of ongoing star formation (poorly populated upper MS, not observed in $H\alpha$). Also the BL and RSG phases are very sparsely populated, but a clump of AGB stars is visible in the CMD in Fig. 2.5, which contains a total of ~ 7300 stars. ESO381-18 has a particularly high stellar density, with a peak stellar density of 909 stars per 0.1 kpc^2 (down to the limiting magnitude $I \sim 27$) in its central regions.

This galaxy formed $55\% \pm 3\%$ of its stars prior to 8 Gyr ago, while $72\% \pm 3\%$ were in place 5 Gyr ago. The SFR was higher than the average value of $\sim 0.0008 \pm 0.0007 M_{\odot} \text{ yr}^{-1}$ at more recent times (see b_{100} and b_{1G}). The derived SFH in Fig. 5.1 suggests the occurrence of two strong recent bursts, the first from 600 Myr to 1 Gyr ago and the second one, shorter, from 20 to 100 Myr ago.

Some difficulties were met when deriving the SFH for this galaxy. In particular, the color of the old RGB and young BL populations and the TRGB were not well fitted by isochrones with the average metallicity that we derive for this galaxy (see Tab. 5.1), and with the reddening and distance modulus adopted. We thus first tried to slightly change the reddening and distance modulus. The best-fitting values found to reproduce the observed CMD were $E(B - V) = 0.1$ instead of 0.06, and $(m - M)_0 = 28.56$ instead of 28.63 ± 0.14 , which is still consistent with the original value within the errorbars. LEDA¹ reports an internal extinction value in the B -band of 0.42 mag due to the inclination of the galaxy, which may explain part of the discrepancy. However, the region above and redward of the RGB in the best-fit synthetic CMD does not match the observed one well. We plot the Hess diagram for the data and the best-fit model in Fig. 5.2 to show where the fit yields poor results. Note the bin size is big due to the low number statistics. The discrepancy is partly due to inconsistencies in the isochrone models, which cannot reproduce simultaneously the colors of RGB and RSG/BL stars at these low

¹<http://leda.univ-lyon1.fr/>.

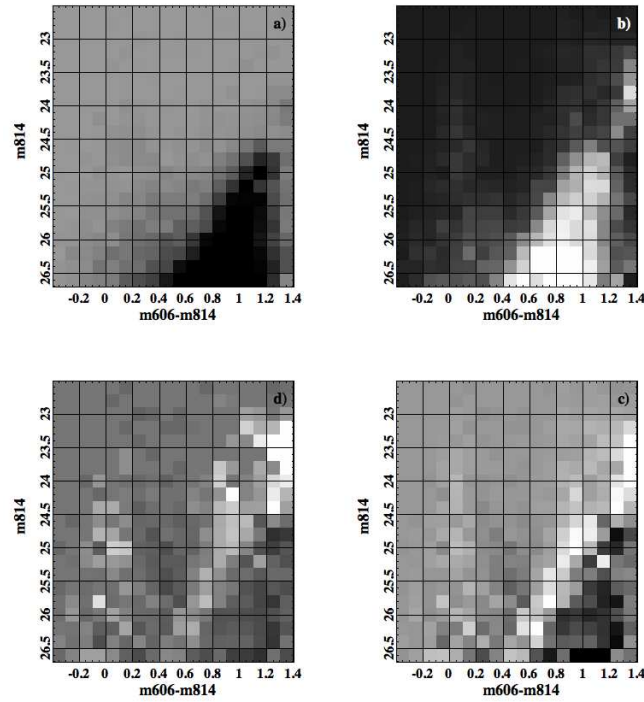


Figure 5.2: Hess diagrams (displayed using ACS filters) for ESO318-18. *Panel a*). Data. *Panel b*). Best-fit synthetic model, with a reverse color scale with respect to the data to facilitate comparison. *Panel c*). Difference between the data and best-fit model. *Panel d*). Significance of the difference between the data and best-fit model.

metallicities (e.g. Úbeda et al. 2007), together with the poor number statistics and the possible presence of differential reddening.

Another point is that the metallicity seems to be decreasing with time (see Fig. 5.1), and the problem is again related to the color of the RGB, which is not well fitted by the chosen set of old isochrones. The metallicity value for the RGB (as high as $Z \sim 0.004$ if we compare its color to models) is well above the values one would expect for such a small galaxy, also considering the low metallicity of the young populations we derive with the SFH recovery ($[\text{Fe}/\text{H}] \sim -1.4$, corresponding to $Z \sim 0.0008$). Apart from the reddening issue, another plausible explanation could be an α -element enhancement at early times, which would make the RGB redder. We perform the following test: we run the SFH recovery process again, but this time with a restricted range of metallicities ($Z = 0.0004, 0.0006$ and 0.001). This will force the metallicity to vary very little, thus not giving us any information about the chemical evolution itself, but it will show how much the RGB color issue can affect our derived SFH. The results show a synthetic CMD that is almost identical to the first one, and the SFH (plotted in red in Fig. 5.1) is comparable to our originally derived SFH within the errorbars. The second oldest time bin changes slightly to a higher SFR, but this age range is in any case quite uncertain, and the overall features (the two recent burst episodes) are still clearly distinguishable. Also the two most recent time bins show little change, but this is due to the higher metallicity imposed (with respect to the first model). We thus conclude once again that the derived SFH is fairly robust, but the constraints on the metallicity are weak.

Finally, we compare the stellar mass found from the SFH ($4.7 \times 10^7 M_{\odot}$) with a mass estimate coming from the galaxy's luminosity and an adopted stellar mass-to-light ratio of 1 or 2. We

find values of $2.2 \times 10^7 M_{\odot}$ or $4.4 \times 10^7 M_{\odot}$, respectively, thus again matching well the result of our SFH (even after correcting for the evolutionary effects).

ESO444-78, UGCA365

The dwarf irregular ESO444-78 is the closest one to M83 within our sample (only $\sim 110 \pm 500$ kpc deprojected distance, again adopting the values reported by Karachentsev et al. 2007), and is also located in the densest environment, with respect to the other targets of our study ($\Theta = 2.1$). According to LEDA, also in this case there is a high internal extinction in the B -band due to the inclination (0.88 mag). As the previous two galaxies, ESO444-78 contains little neutral gas (see Tab. 2.2), but it was detected in $H\alpha$ (Côté et al. 2009). From the CMD alone (~ 11400 stars), the old stellar component seems predominant, while there are few, smoothly distributed stars in the young and intermediate-age phases, with a smaller concentration in the luminous AGB.

Indeed, ESO444-78 formed already $65\% \pm 5\%$ of its stars more than 8 Gyr ago, and $82\% \pm 5\%$ more than 5 Gyr ago. The fraction of the galaxy's total stellar content formed prior to 8 Gyr is the largest for this galaxy, compared to the others in the sample. The average SFR for ESO444-78 is $\sim 0.0063 \pm 0.0036 M_{\odot} \text{yr}^{-1}$. For ages younger than 8 Gyr, ESO444-78 seems to have experienced an almost constant and low level of activity (see Tab. 5.1), with only 3% of its stars born in the last Gyr. The current SFR is estimated to be only $\sim 0.000032 M_{\odot} \text{yr}^{-1}$ from its one HII region (Côté et al. 2009). We do not plot this value in the SFH of Fig. 5.3, since we are not able to recover a significant SFR for the youngest time bin (< 10 Myr). Also in this case, the metallicity seems rather constant, excluding the time bin between 1 and 2 Gyr ago, which has a lower value. This could be easily due to the fact that there is not much information for these ages in the CMD, so it may not be relevant.

The stellar mass from the derived SFH is $8.4 \times 10^7 M_{\odot}$. Assuming a mass-to-light ratio of 1 or 2 to estimate the galaxy's stellar mass, together with its luminosity, we find values of $2.7 \times 10^7 M_{\odot}$ and $5.3 \times 10^7 M_{\odot}$, respectively. These masses are slightly lower than the first mass estimate: for this galaxy, we may be overestimating the low-mass end, given that the SFR at ages older than ~ 4 Gyr is particularly uncertain due to the low amount of information obtainable from the CMD.

IC4247, ESO444-34

IC4247 has the highest stellar density in our sample, with a peak stellar density of 1040 stars per 0.1 kpc^2 (down to the limiting magnitude $I \sim 27$). This galaxy is located at a deprojected distance of $\sim 280 \pm 400$ kpc from M83, with a positive tidal index (see Tab 2.2). Its neutral gas content is $M_{HI} \sim 3.5 \times 10^7 M_{\odot}$ (Banks et al. 1999; Georgiev et al. 2008), and this galaxy is detected also in $H\alpha$ (Lee et al. 2007). In the CMD in Fig. 2.5, the RGB, luminous AGB stars, blue and red helium-burning stars, and some upper MS stars are clearly visible, with a total number of ~ 18000 recovered stars. As for ESO381-18 and ESO444-78, this galaxy has a high internal extinction due to its inclination ($A_B \sim 0.74$ mag).

The recovered SFH is shown in Fig. 5.3. The average SFR is $\sim 0.0101 \pm 0.0066 M_{\odot} \text{yr}^{-1}$. This galaxy formed $\sim 65\% \pm 5\%$ of its stars prior to 8 Gyr ago and $\sim 80\% \pm 5\%$ of its stars more than 5 Gyr ago. IC4247 was certainly not constant in its SFR, but the most prominent feature recognizable here is the episode of enhanced star formation that lasted from 500 Myr to 1 Gyr ago. Other short-lived enhancements in the SFR are seen in the last few tens of Myr.

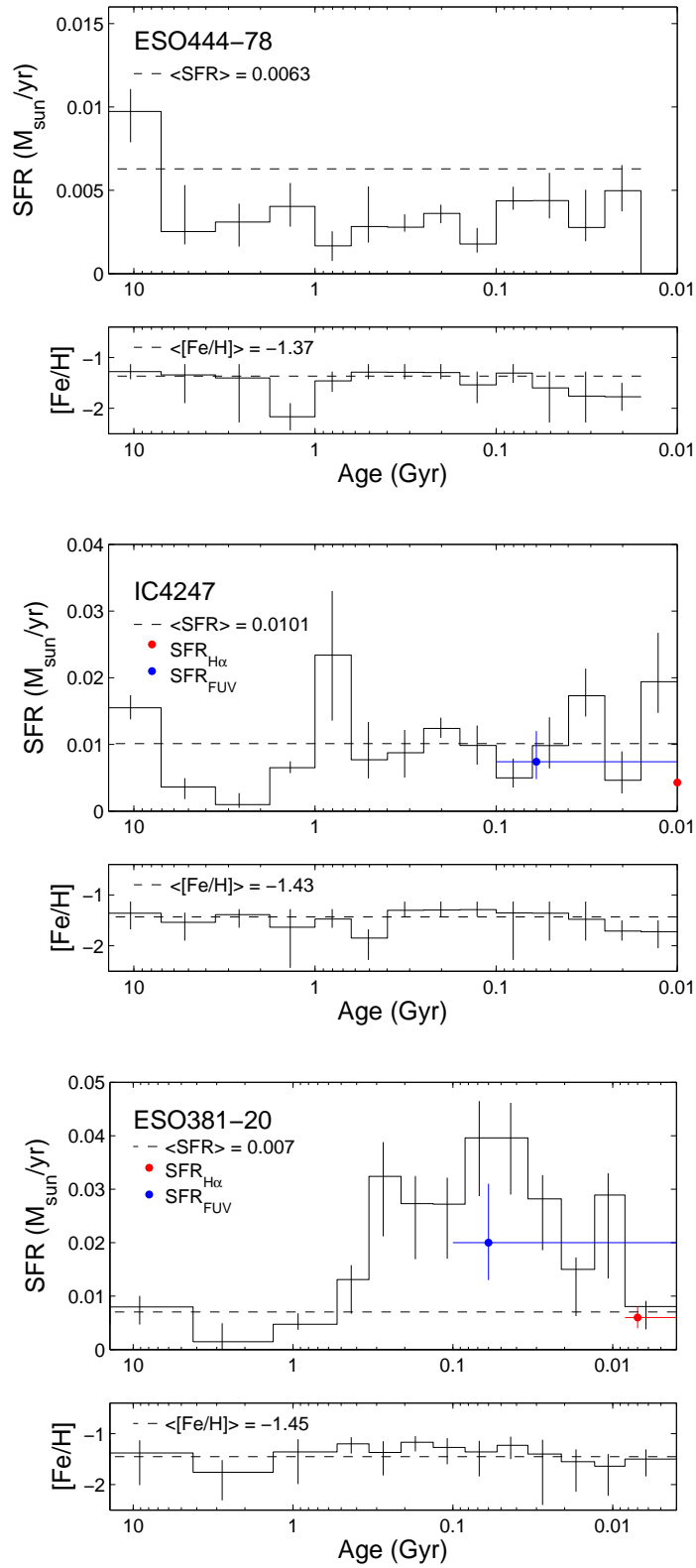


Figure 5.3: Same as Fig. 5.1, for the galaxies ESO444-78, IC4247 and ESO381-20 (ordered by absolute increasing magnitude). The red dots report the current star formation rate derived from $\text{H}\alpha$ observations reported in the literature, while the blue dots indicate the recent star formation rate derived from FUV observations (see text for references).

An estimate of the star formation within the last ~ 100 Myr is given by the far ultraviolet (FUV) non-ionizing continuum. IC4247 is included in the sample of Lee et al. (2009), who consider nearby luminous and dwarf galaxies to compare the SFRs derived from $H\alpha$ and FUV observations. In Fig. 5.3 we plot the SFR derived from FUV, and find it to be consistent with our results. At the present day, there is not very much star formation occurring as seen from the CMD, and we do not extend our SFH to ages younger than 10 Myr. The $H\alpha$ flux coming from the interstellar medium in the central region of the galaxy (taken from Lee et al. 2007) can be used to compute the current SFR. In particular, the relation between $H\alpha$ flux and SFR can be written as (see Bouchard et al. 2009, and references therein)

$$SFR = \frac{L(H\alpha)}{1.26 \times 10^{41} \text{ergs s}^{-1}} M_{\odot} \text{yr}^{-1}$$

where the $H\alpha$ luminosity (in erg s^{-1}) is given by $L(H\alpha) = 4\pi d^2 F(H\alpha)$, and d is the line of sight distance (in cm), while $F(H\alpha)$ is the flux (in $\text{erg s}^{-1} \text{cm}^{-2}$).

This value turns out to be $\sim 0.0045 M_{\odot} \text{yr}^{-1}$, and we show it as reference in Fig. 5.3, even though it refers to an age bin that we do not plot (the lifetime of massive ionizing stars and thus of $H\alpha$ emission is $\lesssim 10$ Myr). We mention that, as for ESO381-18, it was rather difficult to match the color of the RGB with the other features in the CMD in the isochrone-fitting process. We thus had to use a value of $E(B - V) = 0.12$ instead of 0.06, and the distance modulus was rearranged to $(m - M)_0 = 28.33$ instead of 28.48 ± 0.21 , which is still within the errorbars. As discussed before, adjustments in the metallicity values would not lead to any major change in the derived SFH.

The value of $[Fe/H]$ looks constant over the history of IC4247. The mean value of $[Fe/H] = -1.43 \pm 0.11$ dex is lower than the value we derive from the oxygen abundances of Lee et al. (2007) ($[Fe/H] = -1.03 \pm 0.2$). The HII regions of this galaxy are rather small and concentrated in its central parts, and their enhanced metal content is the consequence of a recent short episode of star formation, which shows the inhomogeneity of the enrichment process. If the youngest populations have a higher metallicity, it is very difficult for us to recover this information just from the few MS stars, which are degenerate with age and metallicity and are blended with the BL at the faintest magnitudes of our CMD. More in general, even though the interstellar medium is enriched by star formation episodes, dwarf galaxies are not always able to retain the enriched gas (Lanfranchi & Matteucci 2004; Marcolini et al. 2006, 2008). Furthermore, they are often not well mixed (e.g., Kniazev et al. 2005; Glatt et al. 2008a; Koch et al. 2008a,b). IC4247, with its high stellar density, follows this trend, having some young ‘‘pockets’’ more enriched in the central regions where the potential is deeper.

From the SFH of IC4247 we estimate a stellar mass of $1.4 \times 10^8 M_{\odot}$. Considering, instead, its luminosity and a stellar mass-to-light ratio of 1 or 2, we get values of $0.6 \times 10^8 M_{\odot}$ and $1.3 \times 10^8 M_{\odot}$, respectively, thus consistent with the previous estimate.

ESO381-20

The irregular galaxy ESO381-20 is located in the outskirts of the CenA/M83 group and is rather isolated (its tidal index Θ is negative, Karachentsev et al. 2007). Its distance as found by Karachentsev et al. (2007) is 5.44 ± 0.37 Mpc, its deprojected distance from the closest massive neighbor (M83) is $\sim 1.1 \pm 0.1$ Mpc. Its CMD (Fig. 2.5) contains ~ 20000 stars, and shows an old RGB, an intermediate-age luminous AGB and young MS, BL and RSG stars. This galaxy has

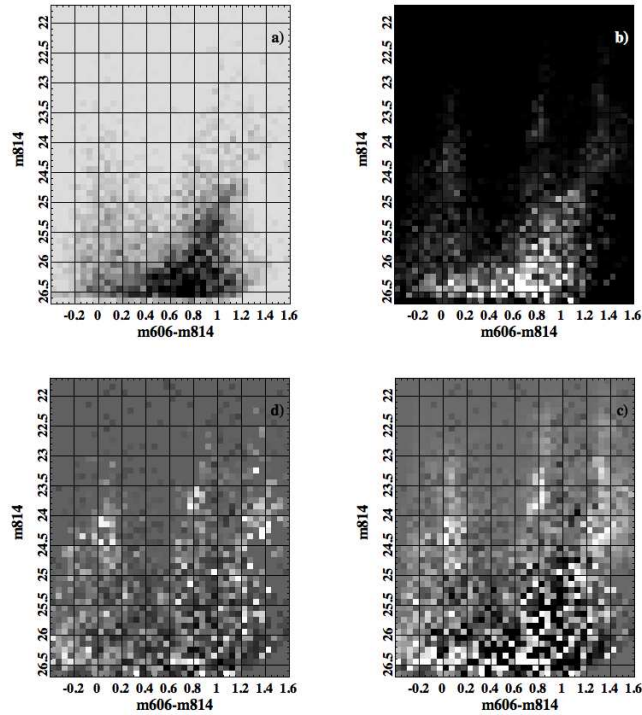


Figure 5.4: Hess diagrams (displayed using ACS filters) for ESO318-20. *Panel a*). Data. *Panel b*). Best-fit synthetic model, with a reverse color scale with respect to the data to facilitate comparison. *Panel c*). Difference between data and best-fit model. *Panel d*). Significance of the difference between data and best-fit model.

a very high content of neutral gas ($M_{HI} \sim 2 \times 10^8 M_{\odot}$, Banks et al. 1999; Georgiev et al. 2008), which extends much further than the apparent optical galaxy. There is thus a high potential to form stars, and indeed its $H\alpha$ maps shows regions of very active star formation (Lee et al. 2007; Bouchard et al. 2009). Some of these star forming regions seem to coincide with local maxima in the HI distribution (Côté et al. 2000). The extinction due to the inclination is about 0.57 mag in the B -band (taken from LEDA). ESO381-20 is also the only galaxy within this sample that contains a globular cluster (Georgiev et al. 2008).

ESO381-20 seems to have experienced a relatively high continuous star formation during its lifetime (with an average of $\sim 0.007 \pm 0.0048 M_{\odot} \text{yr}^{-1}$), which then increased substantially from 10 to 500 Myr ago. This increased star formation activity was more than twice the average rate (see also the parameter b_{500} in Tab. 5.1). Following the recent discussion by McQuinn et al. (2009), we may definitely say that this is a period of a global starburst for the galaxy. The result does not change if we consider only the average SFR over the last ~ 4 Gyr, as McQuinn et al. (2009) do to avoid “contamination” from old ages. We will further discuss this starburst in the following Sect. We report in Fig. 5.3 the estimate of the SFR in the last ~ 100 Myr, derived from the FUV continuum by Lee et al. (2009), which is in good agreement with our results. For the most recent age bin (for this galaxy we are able to derive the SFR for ages as young as ~ 4 Myr), the value derived here is consistent with the SFH derived by Bouchard et al. (2009) considering the $H\alpha$ flux of the galaxy ($\sim 0.006 \pm 0.002 M_{\odot} \text{yr}^{-1}$, shown in Fig. 5.3), but a factor of two higher than the $H\alpha$ SFR inferred by Côté et al. (2009). After a visual examination of the HII regions selected in the two papers, we conclude that the discrepancy may be due to a slightly different selection of the emission regions, which summed up to give the total flux. The star formation

in the last few Myr has a value consistent with the average SFR from our SFH, as confirmed by the presence of only few MS stars compared to blue and red helium-burning stars. We note that the SFRs derived from FUV and from H α differ from each other. Lee et al. (2009) show that, for dwarf galaxies, there is a systematic discrepancy between these two methods of deriving SFRs. In the case of ESO381-20, this seems to be due simply to the fact that the two tracers represent different star formation timescales. Already $\sim 50\% \pm 5\%$ of the stars of ESO381-20 were formed more than 8 Gyr ago, while $70\% \pm 5\%$ were in place 5 Gyr ago, but a substantial fraction was formed in the last Gyr (see Tab. 5.1).

Finally, in Fig. 5.4 we show the Hess diagrams for the observed CMD and the best-fit synthetic CMD. We can see that, given the higher number of stars for this galaxy, the resulting Hess diagrams are divided into smaller bins than in the case of ESO318-18 (Fig. 5.2), from which the information needed to reconstruct the SFH is then evaluated. In the case of ESO381-20 the overall fit is better, with the biggest discrepancies between the data and the synthetic CMD being found in the less populated and most difficult to model regions (upper BL, upper RSG and luminous AGB).

Also in this case, the [Fe/H] value seems to be fairly constant during the entire galaxy lifetime. For comparison with our results, the oxygen abundances of the HII regions derived by Lee et al. (2007) are combined into a mean [Fe/H] value using the empirical formula found by Mateo (1998), and the result is -1.4 ± 0.2 dex, consistent with our value within the errorbars (see Tab. 5.1). However, there are strong variations in the values for the individual HII regions (the nominal range is from [Fe/H]= -1.87 to -0.90). These findings would support the previous interpretation of the high metallicities found for the two HII regions of IC4247, indicative of an inhomogeneous enrichment, in contrast with the value we derive from the SFH recovery.

For ESO381-20, the total stellar and dynamical masses were computed in Côté et al. (2000) via modeling of its rotation curve. They get a value of $2.3 \times 10^8 M_{\odot}$ for the stellar mass, with a best-fit stellar mass-to-light ratio of 2.3 and a total mass-to-light ratio of about 20. From our method the result is $\sim 1 \times 10^8 M_{\odot}$, thus slightly lower. If we recompute the mass starting from the *B*-band luminosity and assuming a stellar mass-to-light ratio of 1 or 2, we get values of ~ 0.9 and $\sim 1.8 \times 10^8 M_{\odot}$, respectively. This is consistent with our SFH. Since the depth of our CMDs is limited, it is plausible that in our resolved stellar study we are losing part of the mass coming from the oldest population, which results in a lower mass when compared to the integrated light study of Côté et al. (2000). As a check, we use the GALEV models (Kotulla et al. 2009) with our derived SFH as an input to compute the resulting total luminosity of the galaxy, which turns out to be almost identical to the true one reported in Tab. 2.2.

5.1.2 The CenA subgroup

HIPASS J1348-37

Within the CenA subgroup of late-type dwarfs, HIPASS J1348-37 is the faintest one (together with KK196, see Table 2.2), and the galaxy with the lowest density. Due to its large deprojected distance from CenA ($\sim 2.1 \pm 0.7$ Mpc, computed starting from the radial distance found in Karachentsev et al. 2007), we also try to compute its deprojected distance from M83, and find that HIPASS J1348-37 is actually closer to the latter than to CenA ($\sim 1.0 \pm 0.5$ Mpc). The subgroup membership of our late-type targets was initially assigned following the classification of Karachentsev (2005). However, with the new and more precise distance measurements of

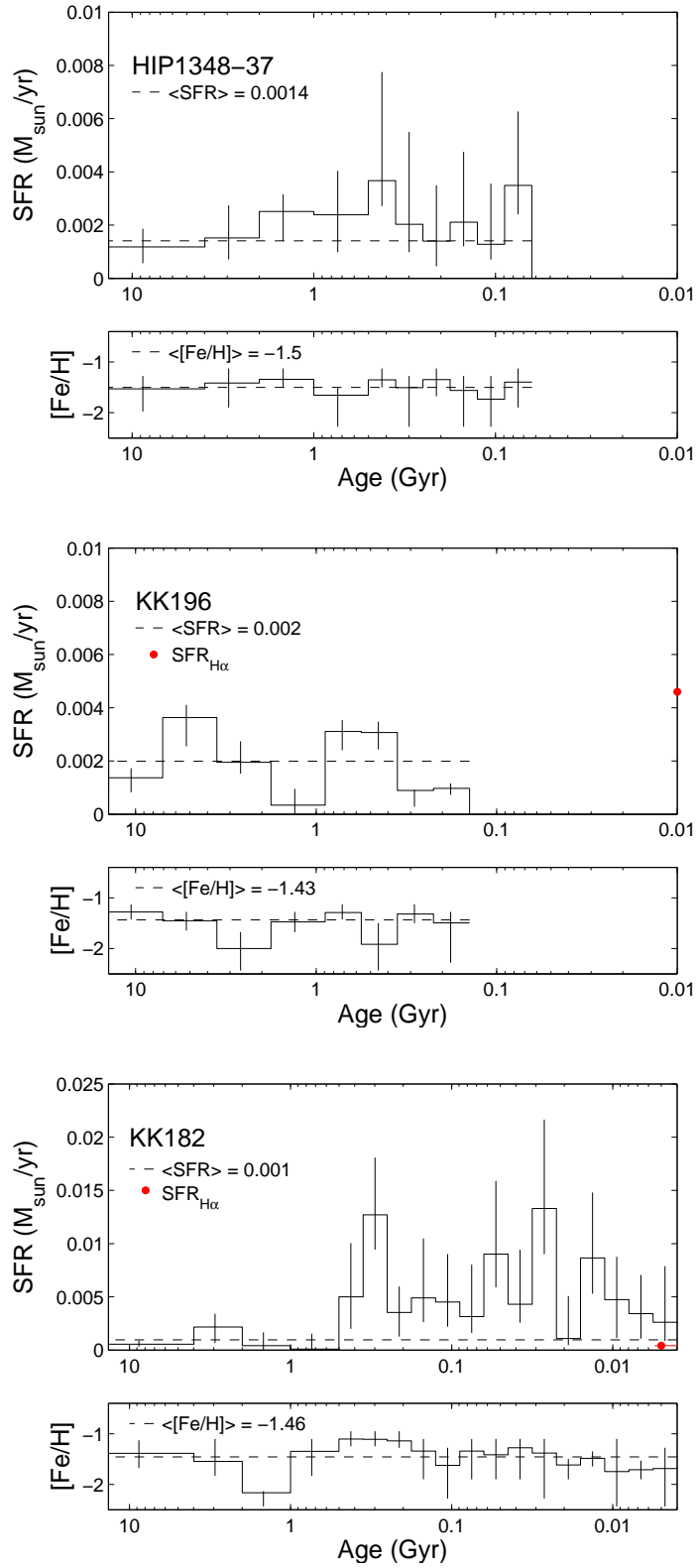


Figure 5.5: Same as Fig. 5.1, for three of the studied galaxies in the CenA subgroup (HIPASS1348-37, KK196 and KK182, ordered by increasing absolute magnitude). The red dots report the current star formation rate derived from $H\alpha$ literature observations.

Karachentsev et al. (2007), HIPASS J1348-37 (together with other two galaxies of this subsample, namely KK182 and ESO384-16) is found to have a negative tidal index (-1.2 , Karachentsev et al. 2007) instead of the positive one that was reported in older papers, and thus turns out to be a rather isolated galaxy. In our subsequent analysis, we will consider this information, as explained more in detail in the next Section.

HIPASS J1348-37 contains a few $\sim 10^7 M_{\odot}$ of neutral gas (Banks et al. 1999; Georgiev et al. 2008), but has not been studied in $H\alpha$ yet. Its CMD, presented in Fig. 2.5 and containing ~ 3300 stars, indeed shows very little sign of recent or intermediate-age star formation, as judged from the absence of MS stars and presence of a small number of BL, RSG and luminous AGB stars. As ESO444-78 in the previous sample, from the characteristics of its CMD HIPASS J1348-37 could be classified as transition-type dwarf (e.g. Grebel et al. 2003).

We derive the SFH for HIPASS J1348-37, although the information stemming from the CMD is mainly based on the old RGB stars and on a few intermediate-age stars, and plot it in Fig. 5.5. It is not possible to derive the SFR for ages younger than ~ 60 Myr, and the average SFR from ages older than that is $\sim 0.0014 \pm 0.0005 M_{\odot} \text{yr}^{-1}$. Assuming the formation epoch of the galaxy to be around ~ 13.5 Gyr ago, we estimate that HIPASS J1348-37 has formed $\sim 35\% \pm 5\%$ of its stellar content by 8 Gyr ago ($z \sim 1.1$), and $\sim 55\% \pm 5\%$ by 5 Gyr ago ($z \sim 0.5$). In particular, this galaxy has been slightly more active in its last ~ 1 Gyr of life, as also indicated by the parameters listed in Table 5.1, with moderate enhancements of the star formation ~ 80 and ~ 400 Myr ago. The star formation episode at ~ 400 Myr ago is very uncertain, because this is the oldest age where the blue loop stars are included in the CMD and it may indicate increased noise at the lower end of the CMD instead of a real increase in star formation. However, the enhancement in the $\sim 250 - 1000$ Myr range is real because of the large number of stars on the blue side of the RGB (they are too blue to be ancient, metal-poor stars).

The average metallicity of HIPASS J1348-37 derived from the SFH recovery is $[\text{Fe}/\text{H}] = -1.50 \pm 0.07$. We compute the total stellar mass for the galaxy as in the previous Sections, and find a value of $1.9 \times 10^7 M_{\odot}$ from our SFH (with the reminder that this value could overestimate the true one by $\sim 25\%$, because we do not take into account stars that already ended their lives). On the other hand, if we consider the B -band luminosity and assume a stellar mass-to-light ratio of 1 or 2, we can estimate the stellar mass to be $0.9 \times 10^7 M_{\odot}$ to $1.7 \times 10^7 M_{\odot}$, which is consistent with the previous estimate.

KK196, AM1318-444

As faint as HIPASS J1348-37, but with a higher stellar density, KK196 is the next object considered in our sample, with ~ 7300 stellar sources detected. Although its CMD presents features similar to HIPASS J1348-37 (Fig. 2.5, few BL and RSG stars, with a small stellar concentration in the luminous AGB region), KK196 is located much closer to CenA, at a deprojected distance of $\sim 260 \pm 390$ kpc and in a denser environment ($\Theta = 2.2$, Karachentsev et al. 2007). It thus has properties similar to ESO444-78 and IC4247 in the M83 subgroup, however, KK196 is not detected in HI (e.g., Karachentsev et al. 2007). Curiously, this dwarf shows almost no sign of a MS in its CMD, but it has an $H\alpha$ detection from Lee et al. (2007). Finally, LEDA reports an internal extinction value due to inclination of $A_B \sim 0.50$ mag for this galaxy.

We show the result of our SFH recovery in Fig. 5.5. As for HIPASS J1348-37, we were not able to constrain the most recent (~ 100 Myr) SFH from the information in the CMD alone. The average SFR is $\sim 0.002 \pm 0.0011 M_{\odot} \text{yr}^{-1}$, with an enhancement at $\sim 400 - 900$ Myr ago, preceded

by ~ 1 Gyr of low activity. In the period $\sim 3.5 - 7$ Gyr ago, KK196 also experienced a SFR slightly higher than the average one, although at such old ages we do not have the resolution to see smaller fluctuations. Overall, this galaxy has not been very active in the most recent period (see Table 5.1), and the $H\alpha$ detection mentioned above can be the result of a short, or weak, burst of star formation, which does not produce enough stars to be significantly detected in the CMD. Indeed, if we look at the HST image of KK196 and check where our detected stars are, the (small) central region where $H\alpha$ was detected by Lee et al. (2007) is not resolved. From the $H\alpha$ data we are able to compute the current SFR for KK196 (for details see the Section about IC4247), which has a value of $\sim 0.0046 \pm 0.0004 M_{\odot} \text{yr}^{-1}$, and which we also plot in Fig. 5.5 although it is not comparable to our results. KK196 has formed $30\% \pm 5\%$ of its stars more than 8 Gyr ago, while $60\% \pm 5\%$ were formed more than 5 Gyr ago.

From the SFH recovery, we derive an average metallicity value of $[\text{Fe}/\text{H}] = -1.43 \pm 0.25$, which is in excellent agreement with the value we compute starting from the oxygen abundance listed in Lee et al. (2007) ($[\text{Fe}/\text{H}] = -1.43 \pm 0.02$). If we compute the total stellar mass for KK196 from our SFH, we get a value of $2.7 \times 10^7 M_{\odot}$; when we assume a stellar mass-to-light ratio of 1 or 2 and compute the total stellar mass starting from the B -band luminosity, the values are $0.9 \times 10^7 M_{\odot}$ and $1.7 \times 10^7 M_{\odot}$, thus slightly higher than our first estimate. As for the case of ESO444-78, we might be overestimating the low-mass end of the SFH due to lack of information from the CMD.

KK182, Cen6

The CMD for KK182 (Fig. 2.5) has some ~ 4100 stars, and shows a fairly well populated MS/BL region, although there are comparatively few RGB and luminous AGB stars. This galaxy has a high deprojected distance from CenA ($\sim 2.0 \pm 0.6$ Mpc) but it is actually closer to M83 ($\sim 1.3 \pm 0.3$ Mpc), with a negative tidal index that makes it a quite isolated object (Karachentsev et al. 2007). KK182 contains a moderate amount of neutral gas ($\sim 5 \times 10^7 M_{\odot}$) and has also been detected in $H\alpha$ (Côté et al. 2009). The internal extinction (due to inclination) given by LEDA is $A_B \sim 0.78$. Finally, the optical image of KK182 reveals a peculiar triangular shape for this object.

When deriving the SFH for this object, we notice that the intermediate-age and old populations provide very little information (Fig. 5.6). The average SFR for this dwarf is the lowest of this sample, and has a value of $\sim 0.001 \pm 0.0014 M_{\odot} \text{yr}^{-1}$. KK182 has experienced most of its star formation in the past ~ 0.5 Gyr, with many short-lived episodes of star formation ($\sim 10 - 100$ Myr in duration), the strongest of which had strengths of several times the average SFR. This is reflected in the high values of b_{100} , b_{500} , and b_{1G} reported in Table 5.1. KK182 thus formed only $25\% \pm 5\%$ of its stars more than 8 Gyr ago, while $35\% \pm 5\%$ were in place 5 Gyr ago. This result is extremely similar to the SFH for ESO443-09 in the M83 subgroup, the latter being also a very isolated object. The star formation value we derive for the youngest time bin (resolving ages of ~ 4 Myr) is not in disagreement with the value that Côté et al. (2009) find starting from the $H\alpha$ flux of this galaxy ($\sim 0.0004 M_{\odot} \text{yr}^{-1}$, see also Fig. 5.6), considering its off-center star forming region. Their study does not give errorbars, but it is likely that the two values are similar once the observational errors are considered.

The metallicity content of this galaxy is low and in line with its luminosity ($[\text{Fe}/\text{H}] = -1.46 \pm 0.21$). The stellar mass as obtained from the SFH is $1.3 \times 10^7 M_{\odot}$. If we compute again the stellar mass from the luminosity of KK182 and a given stellar mass-to-light ratio (1 or 2), we

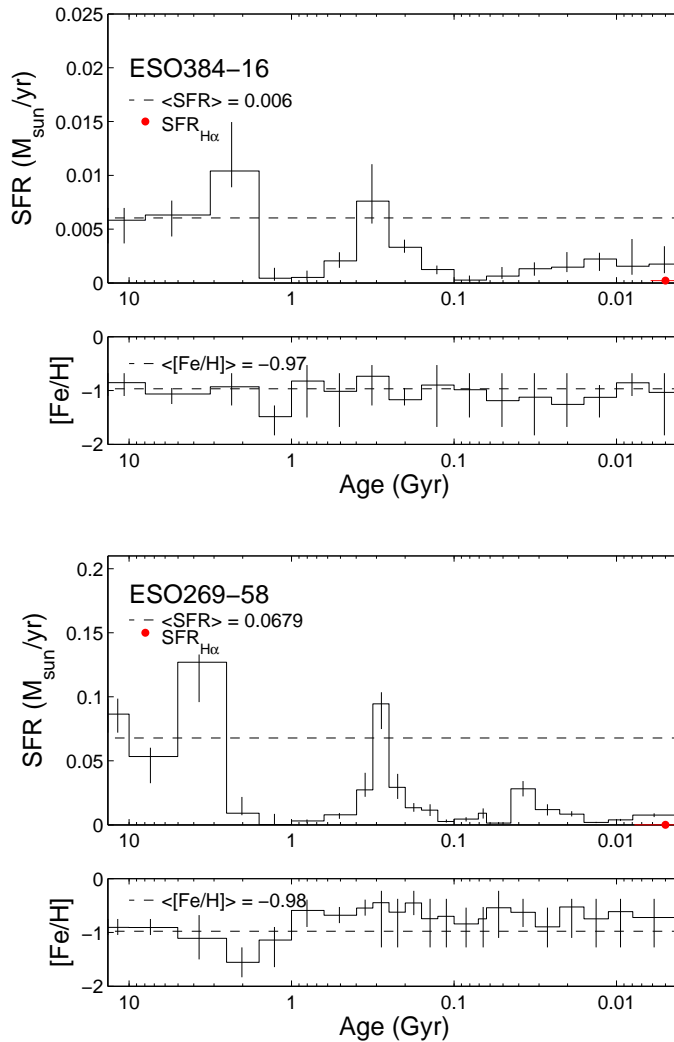


Figure 5.6: Same as Fig. 5.5, for the galaxies ESO384-16 and ESO269-58 (ordered by absolute increasing magnitude). The red dots report the current star formation rate derived from $H\alpha$ literature observations.

get $1.5 \times 10^7 M_{\odot}$ and $3.0 \times 10^7 M_{\odot}$. In this case we are thus slightly underestimating the stellar mass, and this is likely to happen because of the small number of old RGB stars present in the CMD.

ESO384-16

ESO384-16 is considered to be a transition-type or lenticular dwarf (e.g., Jerjen et al. 2000a; Beaulieu et al. 2006; Bouchard et al. 2007), with a rather regular elliptical shape and a high central stellar density (~ 9 stars per arcsec²). The latter characteristic marks the separation between early-type dwarfs and dwarf lenticulars (see also the discussion in Beaulieu et al. 2006), together with a higher M_{HI}/L_B ratio than the typically close to zero ratio for early-type dwarfs. In the mentioned study, the neutral gas mass is reported to be $\sim 10^6 M_{\odot}$, and its spatial distribution is described as asymmetric. For this reason, Beaulieu et al. (2006) suggest that ESO384-16 is actually falling toward the center of the group. Bouchard et al. (2007) also suggest that this

galaxy may be experiencing a mild ram-pressure stripping from the intra-group medium, based on the properties of its HI content. In its CMD, which has ~ 17200 stars, we identify an overdensity of luminous AGB stars above a prominent RGB, but the BL and RSG regions are sparsely populated, indicating very little presence of recent star formation. However, this galaxy was detected in $H\alpha$ by Bouchard et al. (2009). ESO384-16 is located halfway between the dominant giants of the group, at a deprojected distance of $\sim 1.0 \pm 0.4$ Mpc from CenA and $\sim 0.9 \pm 0.4$ Mpc from M83, and has a negative tidal index (Karachentsev et al. 2007). According to Georgiev et al. (2008), ESO384-16 hosts two globular clusters.

When deriving its SFH, we immediately notice that this galaxy has been one of the most active in our CenA sample, with an average SFR of $\sim 0.006 \pm 0.0023 M_{\odot} \text{yr}^{-1}$. As reported in Table 5.1, the parameter b_{14G} is the only one being > 1 , meaning a SFR higher than the average for ages older than 1 Gyr ago. About $35\% \pm 5\%$ of the stars in ESO384-16 were born more than 8 Gyr ago, and $60\% \pm 5\%$ more than 5 Gyr ago. The recovered SFH (Fig. 5.6) shows two episodes of enhanced star formation, one taking place $\sim 250 - 400$ Myr ago, and an older one occurring between 2 and 3 Gyr ago. However, for the latter, old ages, there is a high uncertainty given that the main feature in the CMD is the RGB, clearly degenerate in age and metallicity. In fact, we have to slightly change the initial values of distance and reddening reported in Table 2.2 to find the best-fitting synthetic CMD for our SFH recovery. The new values we adopt are $E(B - V) = 0.12$ (instead of 0.08), and $(m - M)_0 = 28.18$ (instead of 28.28 ± 0.14 found by Karachentsev et al. 2007), which however lie within the errorbars of the previous values. Coming to the most recent star formation, for ages as young as ~ 4 Myr ago our SFR lies on the upper limit of the $H\alpha$ measurement given in Bouchard et al. (2009) (who report a current SFR of $\sim 0.00023 \pm 0.00006 M_{\odot} \text{yr}^{-1}$). These authors find that the $H\alpha$ emission in ESO384-16 is quite faint and diffuse, thus being in agreement with the evidence from its resolved populations.

As mentioned before, the age-metallicity degeneracy in the RGB phase makes it difficult to constrain the average metallicity for ESO384-16. Considering the relatively high average SFR for this galaxy, the best-fit result of $[\text{Fe}/\text{H}] = -0.97 \pm 0.15$ is appropriate for its luminosity (related to the total mass). We estimate the total stellar mass to be $8.0 \times 10^7 M_{\odot}$ from our SFH, while the values derived assuming a stellar mass-to-light ratio of 1 or 2 are $3.0 \times 10^7 M_{\odot}$ and $5.6 \times 10^7 M_{\odot}$, respectively. The reported values are consistent with each other, if we consider that the number obtained from the SFH is likely to be overestimated and that the information extracted from the CMD is limited for this object.

ESO269-58

ESO269-58 is perhaps the most intriguing object in this sample, as can already be seen from its rich CMD (~ 136000 stars). While relatively few BL and RSG stars are present in this galaxy, the most prominent features are a very broad RGB and an extremely well populated luminous AGB region (see Fig. 2.5). This peculiar irregular galaxy shows a prominent dust lane in its central regions, and contains $\sim 25 \times 10^6 M_{\odot}$ of neutral gas. There exists only one measurement of the $H\alpha$ flux for this galaxy, carried out by Phillips et al. (1986). The $H\alpha$ emission is extremely weak. ESO269-58 also has an internal extinction of $A_B \sim 0.50$, according to LEDA. Its position within the CenA subgroup is rather central, being only $\sim 300 \pm 50$ kpc away from CenA and with a tidal index close to 2 (Karachentsev et al. 2007). Finally, ESO269-58 contains as many as 8 globular clusters (Georgiev et al. 2008).

The average rate at which ESO269-58 has been forming stars is the highest in our sample

($\sim 0.07 \pm 0.04 M_{\odot} \text{yr}^{-1}$). Just as KK196 and ESO384-16, this object had a SFR higher than the lifetime average value just for ages > 1 Gyr ago. ESO269-58 formed $45\% \pm 3\%$ of its stellar content more than 8 Gyr ago, and $63\% \pm 3\%$ more than 5 Gyr ago. The SFH recovery of this object has been made more difficult by the high crowding exhibited by this object. Its peak stellar density is ~ 10 stars per arcsec² (down to $I \sim 27$), and the 1σ photometric errors at a magnitude of $I = 25$ are already 0.15 mag in magnitude and 0.24 mag in color, which has the effect to significantly broaden the observed features in the CMD. The observed broadening could in part also be due to differential reddening, but the fact that the TRGB is not stretched along the reddening vector, and that the MS does not look heavily affected, points toward ordinary crowding effects. We find new best-fitting values for the reddening and the distance modulus, namely $E(B - V) = 0.15$ instead of 0.10, and $(m - M)_0 = 27.80$ instead of 27.90 ± 0.16 . As can be seen from the SFH plotted in Fig. 5.6, ESO269-58 experienced an enhanced star formation between ~ 3 and 5 Gyr ago, which was followed by a rapid chemical enrichment. This is confirmed by the curvature of the RGB and the metal-rich extent of the luminous AGB (see Fig. 2.5), and the resulting mean metallicity ($[\text{Fe}/\text{H}] = -0.98 \pm 0.20$) is in agreement with the absolute luminosity of this galaxy. A second, mild enhancement occurred ~ 300 Myr ago, but overall the activity of this galaxy has been much lower than the average SFR in the last 1 Gyr (the fraction of stars born in this period is only 1%, see Table 2.2). The $\text{H}\alpha$ flux reported by Phillips et al. (1986) is compared to the most recent bin of our SFH, being however slightly smaller than our derived value.

We mention that Davidge (2007) also studied the resolved stellar populations of ESO269-58 in its outskirts, using ground-based optical data. This study reports a mean metallicity value of $[\text{Fe}/\text{H}] \sim -1.8$, derived by comparing the RGB to stellar isochrones. The study also concludes that ESO269-58 harbors a small IAP (with stars not younger than 1 Gyr), which accounts for a few percent of the galaxy's stellar mass. According to Davidge (2007), these stars are the result of an episode of enhanced star formation no more than ~ 1 Gyr ago. The reason for the discrepancy between this study's metallicity value and our results could be due to the blue extension of the RGB. Davidge (2007) does not resolve stars younger than 1 Gyr, while our CMD shows such populations (the depth of the CMDs are comparable). As a test, we look at the stellar spatial distributions of a sample of stars along the blue edge of the RGB ($0.5 \lesssim V - I \lesssim 0.9$) and of a second sample of stars along the mean locus of the RGB ($0.5 \lesssim V - I \lesssim 0.9$), at a magnitude of $I \sim 25$. The latter is clearly distributed across the whole spatial extent of the galaxy, while the bluer stars are more centrally concentrated, and indicative of a younger population. It is thus plausible that Davidge (2007) interpreted them as truly metal-poor RGB stars.

We compute the total stellar mass stemming from the recovered SFH, which results in a value of $8.8 \times 10^8 M_{\odot}$. On the other hand, when we assume a stellar mass-to-light ratio of 1 or 2, the expected stellar mass values are between $1.0 \times 10^8 M_{\odot}$ and $2.1 \times 10^8 M_{\odot}$. The explanation for this small discrepancy is most probably again coming from the difficulties in the analysis of the degenerate RGB.

5.2 Spatial distribution of stellar populations as a function of time

Dwarf irregulars are known to have scattered, clumpy regions of active star formation, with the less massive dwarfs usually containing only one such active region (for a review, see Grebel 2004, and references therein). This is, for example, reflected in the shape these galaxies show when imaged in $H\alpha$. We now want to look for possible differences in the spatial distribution of stellar subpopulations.

The stellar subsamples into which the CMDs of the galaxies are divided were described in Chapter 2, and are (ordered by increasing age): MS, BL, RSG, AGB and RGB. For each of the subsamples, only stars with photometric errors smaller than ~ 0.1 mag in magnitude and ~ 0.15 mag in color are considered, since some features in the CMDs strongly overlap when the photometric errors are larger (e.g., MS and BL stars, see Fig. 2.6). This limit also corresponds to a $\sim 80\%$ completeness level. We report in Fig. 5.7 and 5.8 the density maps of the five mentioned stellar subsamples for eight of the target late-type galaxies. For HIPASS J1348-37 and KK196, the number of stars in the MS, BL and RSG stages was too small to draw density maps, so we do not plot them for the mentioned objects. Also ESO384-16 lacks a significant MS population for which we can derive density maps (see Fig. 5.8).

We compute density maps for the subsamples in the following way. The target galaxies are located at distances between ~ 4 and ~ 6 Mpc, at which 1 arcsec corresponds to $\sim 0.02 - 0.03$ kpc. We assign to each star of a given evolutionary phase the number of neighbors found within $\sim 0.03 - 0.07$ kpc², depending on the distance of the galaxy (value chosen such that we do not add too much substructure but we still retain the overall features). We then convolve the result with a square grid. The final resolution of the density maps is $0.01 - 0.02$ kpc². For each map there are 10 equally spaced isodensity contours. They start from a 1σ significance level, or 0.5σ where the number counts are too low, up to the peak significance level, different for each map and indicated in the caption of Fig. 5.7 and 5.8. The colorbars indicate the stellar density for each subsample, in units of stars per 0.1 kpc². To facilitate comparisons among the stellar subsamples, we show with a black cross the center of the galaxy (i.e., coordinates listed in Tab. 2.2), and with an ellipse the projected major axis radius at the isophote level 25 mag arcsec⁻¹ in I -band (taken from Sharina et al. 2008).

The youngest stars (MS in a range of ~ 10 to 20 Myr and BL in a range of $\sim 10 - 20$ to 150 Myr) are mostly concentrated in small “pockets” close to the center of the galaxy. Given typical lifetimes of star forming complexes (~ 100 Myr, see e.g. Dohm-Palmer et al. 1997, and references therein), it is reasonable to assume that these stars are still close to their birth place. They appear to form preferentially close to the central regions of the galaxies, where the potential is deeper. In some of the targets (e.g., ESO443-09, ESO444-78, ESO381-20) the most recent star formation episode took place in a region displaced from the center (as shown in Fig. 5.7 and 5.8), while the BL stars reveal a similar off-centered activity region as well as activity in the galactic center. For populations older than a few hundred Myr, the stellar distribution evens out. The RSG stars are approximately ~ 50 to $\sim 400 - 500$ Myr old and appear slightly more smoothly distributed. Finally, the intermediate-age and old populations (luminous AGB and RGB) are distributed basically over most of the galaxy’s extent, with a quite regular elliptical shape. This reflects the migration and redistribution of stars within the galaxy over long timescales. It is interesting to note that ESO381-20 has a very broad distribution for both

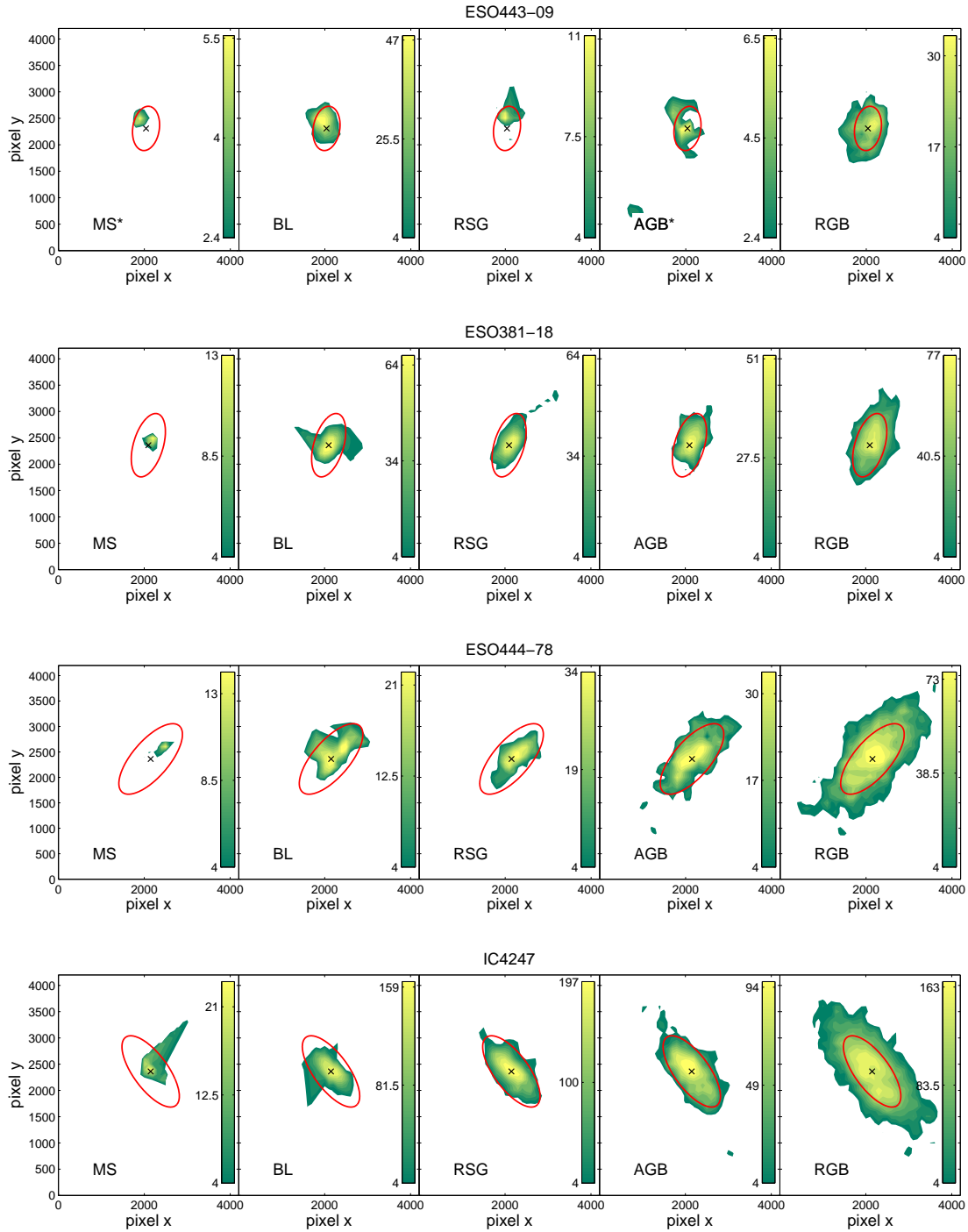


Figure 5.7: Density maps for four of the M83 late-type galaxies (ESO443-09, ESO381-018, ESO444-78, and IC4247, ordered by absolute magnitude), each divided in five stellar evolutionary phases. These are: MS, BL, RSG, luminous AGB and RGB, ordered by increasing age. The stellar density values are listed along the colorbars, in units of number of stars per 0.1 kpc². 10 equally spaced isodensity contours are drawn starting at the 1 σ significance level up to the peak significance level. For the subpanels with an asterisk, the number counts are low and thus the contours start at the 0.5 σ significance level. The peak levels are: for ESO443-09: MS=1.4 σ , BL=3.5 σ , RSG=2 σ , AGB=1.4 σ , RGB=3 σ ; for ESO381-018: MS=2 σ , BL=3.8 σ , RSG=3.8 σ , AGB=3.6 σ , RGB=4 σ ; for ESO444-78: MS=2 σ , BL=2.5 σ , RSG=3 σ , AGB=3 σ , RGB=4 σ ; for IC4247: MS=2.6 σ , BL=4.7 σ , RSG=5 σ , AGB=4.2 σ , RGB=4.7 σ . The center of each galaxy is indicated with a black cross. Just as a reference among different frames, we also overplot the ellipse corresponding to the projected major axis radius at the isophote level 25 mag arcsec⁻¹ in I-band (taken from Sharina et al. 2008).

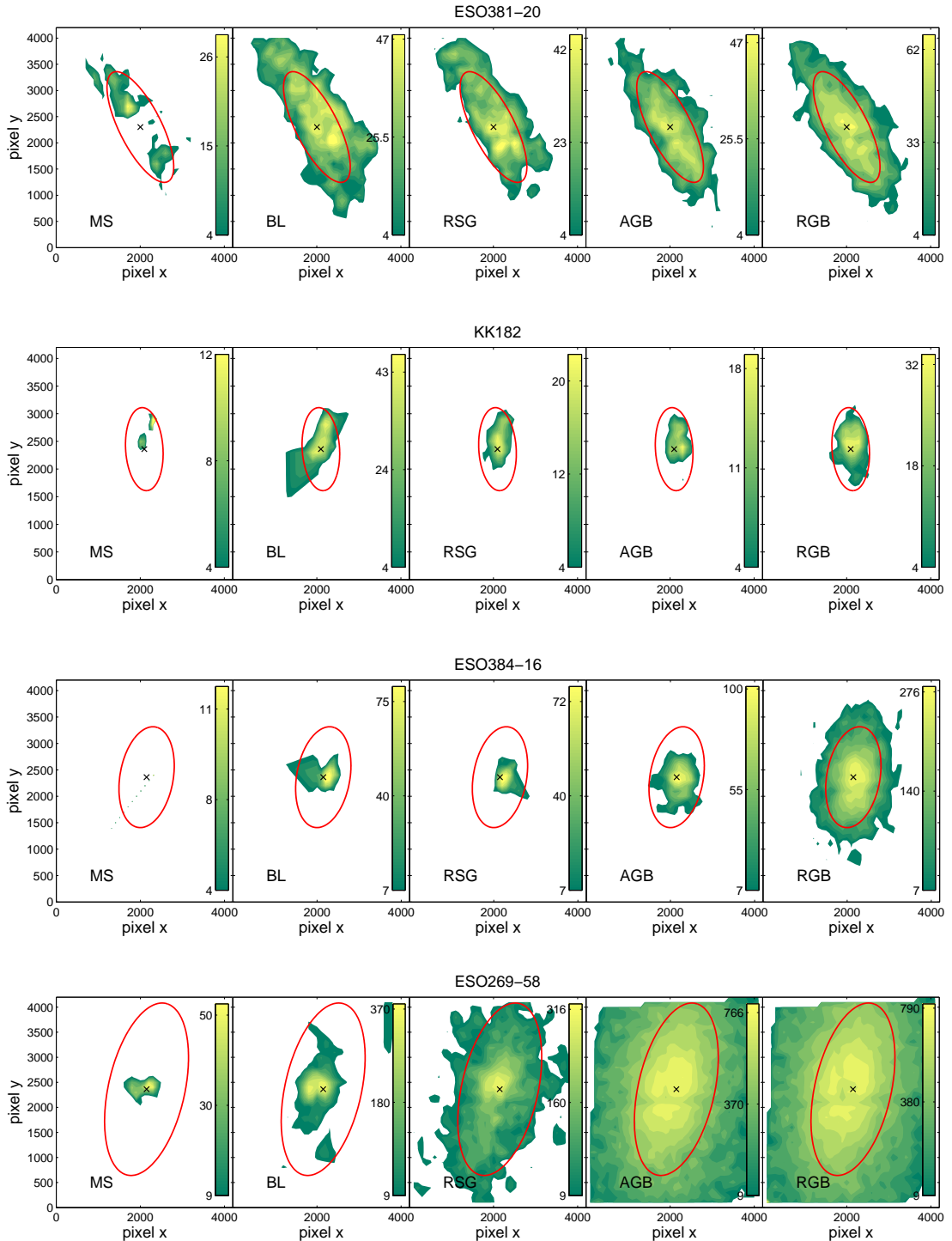


Figure 5.8: Same as Fig. 5.7, for one of the M83 companions (ESO381-20), and for three of the CenA companions (KK182, ESO384-016 and ESO269-58, ordered by absolute magnitude). 10 equally spaced isodensity contours are drawn starting at the 1σ significance level up to the peak significance level. The peak levels are: for ESO381-20: MS= 3σ , BL= 3.5σ , RSG= 3.4σ , AGB= 3.5σ , RGB= 3.7σ ; for KK182: MS= 2σ , BL= 3.4σ , RSG= 2.6σ , AGB= 2.5σ , RGB= 3.1σ ; for ESO384-16: MS= 1.5σ , BL= 3.4σ , RSG= 3.4σ , AGB= 3.7σ , RGB= 4.7σ ; for ESO269-58: MS= 2.7σ , BL= 4.7σ , RSG= 4.5σ , AGB= 5.4σ , RGB= 5.5σ .

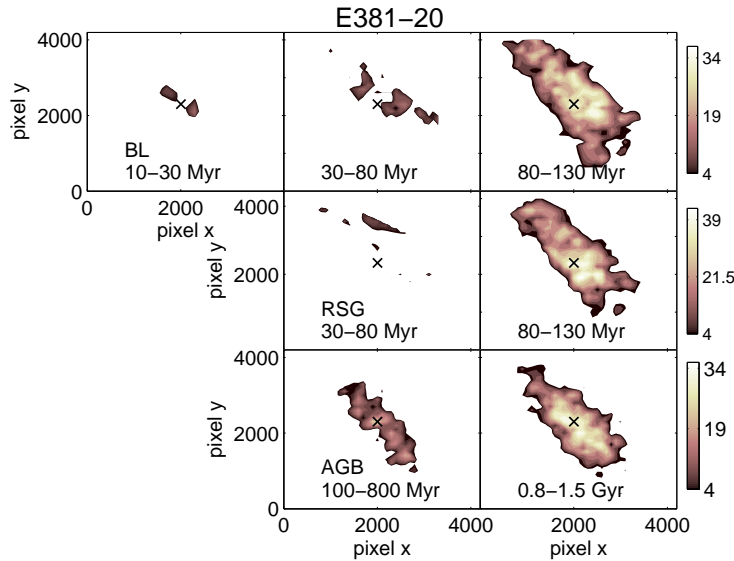


Figure 5.9: Density maps for one of the M83 companions (ESO381-20), divided into different evolutionary stages. These are: in the top row BL stars; in the middle row RSG stars; in the bottom row luminous AGB stars. For each panel in each row, there is an age range as indicated. The color scale is the same within each row, normalized to the peak density of the densest (= oldest) subsample, and the stellar density values are listed along the colorbars (in units of number of stars per 0.1 kpc^2). For each map there are 10 equally spaced isodensity contours, starting at the 1σ significance level up to the peak significance level. The peak levels are (from the youngest to the oldest sample): BL= 1.6σ , 1.6σ , 3.2σ , RSG= 1.3σ , 3.2σ , AGB= 2.3σ , 3.1σ . The center of the galaxy is indicated with a black cross.

BL and RSG stars. This is due to the fact that it experienced a strong burst of star formation in the last ~ 500 Myr, that must have taken place over the whole spatial extent of the galaxy. A similar behavior is seen also for KK182, although less pronounced. We note that the RGB sample is likely to be contaminated by a fraction of intermediate-age and old AGB stars, which are less luminous than the TRGB.

We now discuss in more detail the helium-burning and luminous AGB samples. The position of a star in a CMD is determined, among other parameters, by age and metallicity, which in some evolutionary stages suffer a degeneracy, meaning that older and more metal-poor stars are found at the same location as younger and more metal-rich stars. This is particularly true in the RGB phase. Moreover, for the MS older and younger stars of the same mass occupy roughly the same position on the CMD. On the other hand, in their BL and RSG stages, stars with different ages are well separated in the CMD (see Fig. 2.6). Given that in our galaxies we do not resolve metallicity variations with time, we can safely assume that the age-metallicity degeneracy is minimal and we can assign to each star in the BL and RSG phase a single age based on its position in the CMD. We want to use this information to better understand the distribution of stars at different lookback times, and see how the stellar populations are evolving.

We adopt the method described by Dohm-Palmer et al. (1997) to separate the BL, RSG and AGB samples into older and younger subsamples, using Padova stellar isochrones as reference. We then again compute density maps as described before, this time for three age subsamples for the BL stars, and two subsamples for RSG and luminous AGB. This is because it is easier to separate ages for the BL as compared to the other two evolutionary stages. We stress that for the luminous AGB phase the age determination for ages > 1 Gyr is quite uncertain, since stars

with different ages almost overlap in the region above the TRGB in $I, V - I$ color-magnitude space. We thus cannot evaluate precisely the age of the oldest AGB bin, and the age reported in the plot is just indicative. We report one example for this kind of density maps (ESO381-20), which is plotted in Fig. 5.9.

For all of the studied objects, the youngest populations are again generally found in concentrated, actively star forming regions, while the stars with older ages are more broadly distributed. Theoretical expectations tell us that such complexes can have diameters up to several hundred pc in size, and contain OB associations and open clusters (for a discussion, see Appendix A in Dohm-Palmer et al. 1997). The former will quickly dissolve (within $\sim 10 - 30$ Myr), but their stars will remain in the complex for $\sim 50 - 100$ Myr, while open clusters are more long-lived and disrupt after several hundred Myr due to internal dynamics. It is not easy to put observational constraints on the lifetime of such complexes, because we are not able to follow them closely for long enough timescales. For Sextans A, Dohm-Palmer et al. (2002) find a lower-limit age of ~ 100 Myr, based on the spatially resolved SFH derived from BL stars. In our sample, ESO381-20 is the only galaxy that contains a substantial BL population, suitable for this kind of study, so we will now concentrate on this object.

ESO381-20

ESO381-20 experienced a strong enhancement in star formation in the last ~ 500 Myr, approximately three times higher than the average value. ESO381-20 also contains a higher number of BL stars as compared to the other galaxies in our sample, and thus we can take a closer look at its spatially resolved SFH.

Fig. 5.9 shows how the location of the peaks in stellar density in the BL phase changes with time. However, it is not straightforward to compare the density maps to each other. When sorting the subsamples by age, we are considering stars with different masses, and so the star formation needed to produce the observed densities will be different. We thus have to normalize the density maps for the IMF, and to do so we use the relations described by Dohm-Palmer et al. (1997). We zoom in on the central region of the galaxy, recompute the density maps for the BL subsamples, this time with a resolution of 0.01 kpc^2 , and finally normalize them to get units of $M_{\odot} \text{ Myr}^{-1} 0.1^{-1} \text{ kpc}^{-2}$. The results are shown in the upper panel of Fig. 5.10.

We can see that the galaxy has kept forming stars overall within this age range, with several localized enhancements. This supports the idea of self-propagating stochastic star formation (see Seiden et al. 1979; Dohm-Palmer et al. 2002; Weisz et al. 2008), for which the star formation is intermittently turning on and off in adjacent cells within the galaxy. It is not clear what the main mechanism is that triggers this mode of formation. Turbulence in the interstellar medium may locally enhance the gas density above the threshold for star formation (Elmegreen et al. 1996), or the reason could lie in the balancing process between heating (from stellar feedback) and cooling (inefficient at low metallicities) of the interstellar medium (Hirashita 2000). These mechanisms would lead to large star forming complexes, with sizes of up to several hundred pc and lifetimes of ~ 100 Myr. As mentioned before, some of the HII regions in ESO381-20 coincide with HI peaks. Looking at Fig. 5.10, we can see how the peaks in star formation are moving as time proceeds, but unfortunately the low number of stars in the youngest bin only permits us to detect the two most prominent, intensively star forming regions. The peaks have diameters of ~ 100 pc, thus consistent with the expectations. For reference, the physical distance from the center of the galaxy (black cross) to the highest density peak in the rightmost panel is ~ 0.8

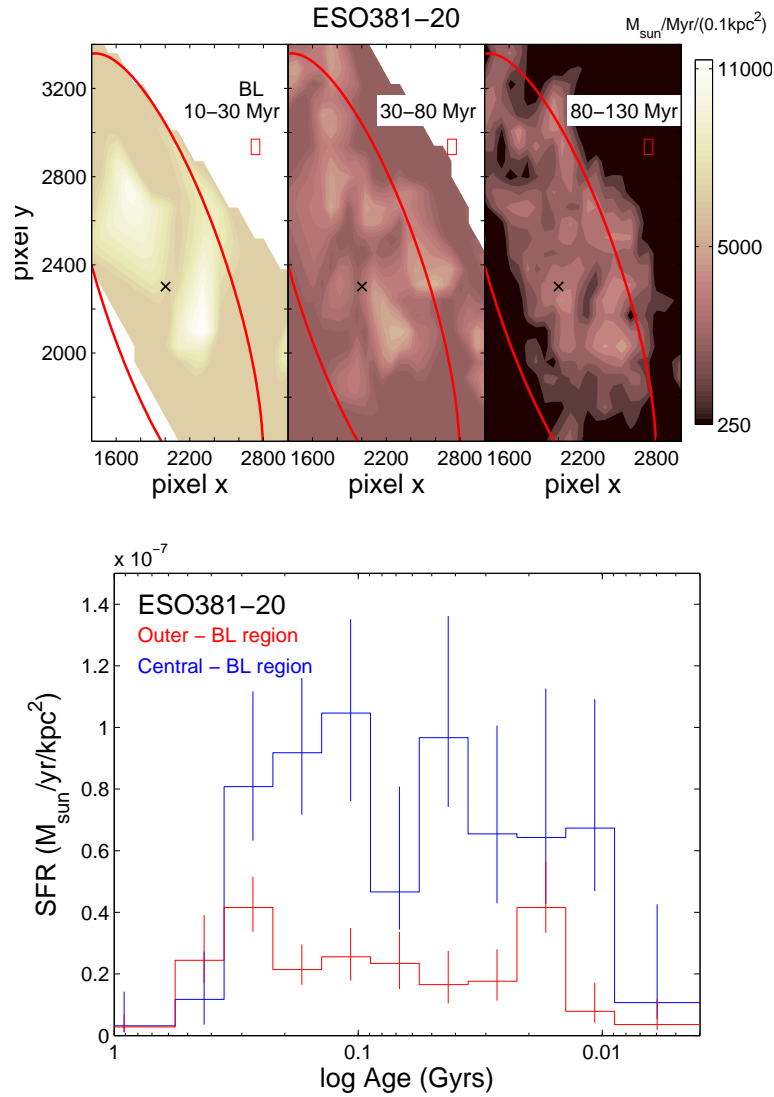


Figure 5.10: *Upper panel.* Spatially resolved star formation history for the central region of ESO381-20, as from BL stars of different ages (as indicated in the subpanels). The SFR per unit area is indicated on the colorbar, with the same color scale for all of the subsamples. The angular resolution of the maps is marked with a red square in each subpanel. The center of the galaxy is indicated with a black cross. Just as a reference among different frames, we also overplot the ellipse corresponding to the projected major axis radius at the isophote level $25\text{ mag arcsec}^{-1}$ in I -band (taken from Sharina et al. 2008). *Lower panel.* Spatially resolved star formation history (via synthetic CMD modeling) of ESO381-20 within the last 1 Gyr. We select two subsamples of stars, found in the “inner” and in the “outer” regions of the galaxy, by looking at the density maps of the BL stars (Fig. 5.9, see text for details). The star formation rate for each region (normalized to the area of the considered region) as a function of time is plotted, with the oldest age being on the left side and the present time on the right side of the (logarithmic) horizontal axis.

kpc. Their duration is more difficult to determine, given the small timescale resolvable. We can however notice that the peaks of star formation in the youngest age bin are already present, even though with a lower efficiency, in the 30 – 80 Myr panel, so activity there has lasted for at least ~ 80 Myr. Several of the smaller peaks present in the oldest time bin are disappearing in the young ones, but adjacent cells are seemingly turning on. There does not seem to be any obvious spatially directed progression of the star formation, but from these data it is not possible to draw firm conclusions. A high-resolution HI map would be helpful to study in more detail the substructures in this galaxy (see, e.g., Weisz et al. 2009b). We note that similar star formation characteristics and timescales have also been found in other irregulars, e.g., the LMC (Grebel & Brandner 1998; Glatt et al. 2010), and may be typical for these galaxies.

Moreover, star formation may be overall enhanced within galactic scales for long time periods ($\sim 0.5 - 1$ Gyr, see e.g. Dohm-Palmer et al. 1997, McQuinn et al. 2009), due to a global starburst in the galaxy. ESO381-20 seems to have experienced such a high star formation period, and this was recent enough that we can try to look at the spatially resolved SFH within different parts of the galaxy, as derived from synthetic CMD modeling. Following McQuinn et al. (2009), we separate the galaxy in two smaller subregions, and we do that according to the BL density maps in Fig. 5.9. We consider the inner region to be the one where the star formation activity has been high in the last ~ 100 Myr, producing a high density of BL stars. The outer, currently less luminous, region is the one where stars younger than 130 Myr are found, but excluding the previously mentioned central region. We then want to see whether the enhancement in star formation has affected the galaxy as a whole, possibly with intermittent episodes, or whether it was localized in the central region. We compare the SFHs derived for these two subsamples, scaling them for the area of the regions, and plot them in the lower panel of Fig. 5.10. The outer region is producing overall fewer stars compared to the central one, but apart from that we do not see any obvious trend from the derived SFHs. On the contrary, the SFR is randomly varying with time around the average value. Even though the area normalized SFHs clearly show that the star formation in the faint region is on average more than two times lower than in the bright region, it still is enhanced by a factor of two with respect to the average SFR of the faint region itself. This simply tells us that the observed burst of star formation was a period in which the whole galaxy produced stars at a higher rate, and the phenomenon was not only localized to the currently bright central region.

5.3 Discussion

Just as the dwarf irregular galaxies of the Local Group, the target objects of our sample show considerable variety in their SFHs. The galaxies studied here cover a range of ~ 2.5 mag in magnitude, they have neutral gas masses of few 10^7 to few $10^8 M_\odot$, and the sample includes galaxies with both positive and negative tidal indices.

For almost all of our sample dwarfs, a period of old star formation (≥ 5 Gyr) at the lifetime average rate is followed by a lower-level activity for intermediate ages, with some exceptions where there is pronounced intermediate-age activity (e.g., ESO384-16 and ESO269-58). We emphasize that episodes of enhanced star formation could also be present at these old ages, but the time resolution of our CMDs does not allow us to recover such episodes. Only in the last ~ 1 Gyr are we able to resolve increased star formation activity above the average rate, for which ESO381-18 and ESO381-20 are the most striking examples. The enhancements

in star formation found for all of the galaxies are usually a factor of 2-3 times the average lifetime value. For some cases the situation is different. For example, in ESO444-78 the star formation activity is high only for the first few Gyr, after which it stays rather constant and always below the average value. Côté et al. (2009) suggest that this object could be a transition-type galaxy, given the absence of strong H α emission. Its SFH resembles that of Local Group transition-type dwarfs such as Phoenix or LGS3 (see, e.g., Dolphin et al. 2005), with two major differences. First, ESO444-78 is almost three magnitudes brighter than these Local Group dwarfs, and second, its neutral gas content is also higher by a factor of 10–100 (see our Tab. 2.2 and Tab. 1 in Grebel et al. 2003). However, we are not able to make more detailed comparisons between these objects, since our photometric depth does not permit us to resolve enhanced star formation episodes at ages older than ~ 5 Gyr. On the other hand, for HIPASS1348-37 and KK196 the SFR remains lower than the average SFR in the first Gyr, subsequently proceeds with mild peaks, and almost disappears in the last ~ 100 Myr. Given that there is an H α detection for KK196 (although HI gas is not detected), out of these two objects only HIPASS1348-37 is a candidate transition-type dwarf. In the cases of ESO384-16 and ESO269-58, the SFR was more pronounced between ~ 2 and $\sim 3 - 4$ Gyr ago, after which the SFR has been well below the average value but shows a single peak a few hundred Myr ago. ESO384-16 is indeed classified as a transition-type dwarf and, given their similarities, ESO269-58 should also be (see the respective Subsections). Both galaxies contain several globular clusters, although like ESO444-78 the neutral gas content and the luminosities are larger than those of Local Group transition-type dwarfs.

The derived SFHs (Fig. 5.1, 5.3, 5.5 and 5.6) seem to confirm the general trend found for objects in the Local Group, with quite long periods of star formation (~ 100 to 500 Myr) separated by quiescent epochs when the star formation is low but constantly active (“gasping” regime, Marconi et al. 1995). The *average* SFRs are of the order of $\sim 10^{-3}$ to $\sim 6 \times 10^{-2} M_{\odot} \text{yr}^{-1}$, which is slightly higher than the values found for Local Group dwarf irregulars in the same magnitude range, but comparable to the sample of objects in the M81 interacting group studied by Weisz et al. (2008). Given the high activity seen for the giant galaxies in the CenA group, Côté et al. (2009) also look for enhancements in the SFR of its dwarf members with respect to the Local Group, but they do not find evidence for this using the *current* SFR. Note that we are looking at lifetime average values, rather than the current rate. Finally, some of our targets seem to have formed at least 50% of their stellar content before $z \sim 1$ ($\lesssim 8$ Gyr ago). These are all the M83 companions, while for the CenA subsample the fraction of stars formed more than 8 Gyr ago is generally smaller, 25% – 45%. We however point out that two of the CenA companions that were originally classified as such are actually isolated objects that are closer to M83, and we thus exclude an obvious correlation with environment. It is more plausible that we are seeing a variety of SFHs, just as observed in the Local Group. Namely, in the LG we have cases where most of the dwarfs’ stellar content were formed at ancient times ($\gtrsim 10$ Gyr), but also cases where the bulk of star formation occurred at ages younger than that (e.g., IC1613 or Leo A, see Skillman et al. 2003; Cole et al. 2007). We will come back to this point later.

The position of our ten galaxies in the CenA/M83 group and a blow-up of the CenA and M83 subgroups are shown in Fig. 5.11 (the positions are taken from Karachentsev et al. 2007). An important difference between the two subgroups is that the M83 subgroup, as opposed to the CenA subgroup, contains many more dwarf irregulars (shown in blue). A high number of gas-rich dwarf irregulars is often taken as sign of a relatively unevolved group. Apart from the dwarfs that are likely bound members of the two subgroups, we also plot the positions of

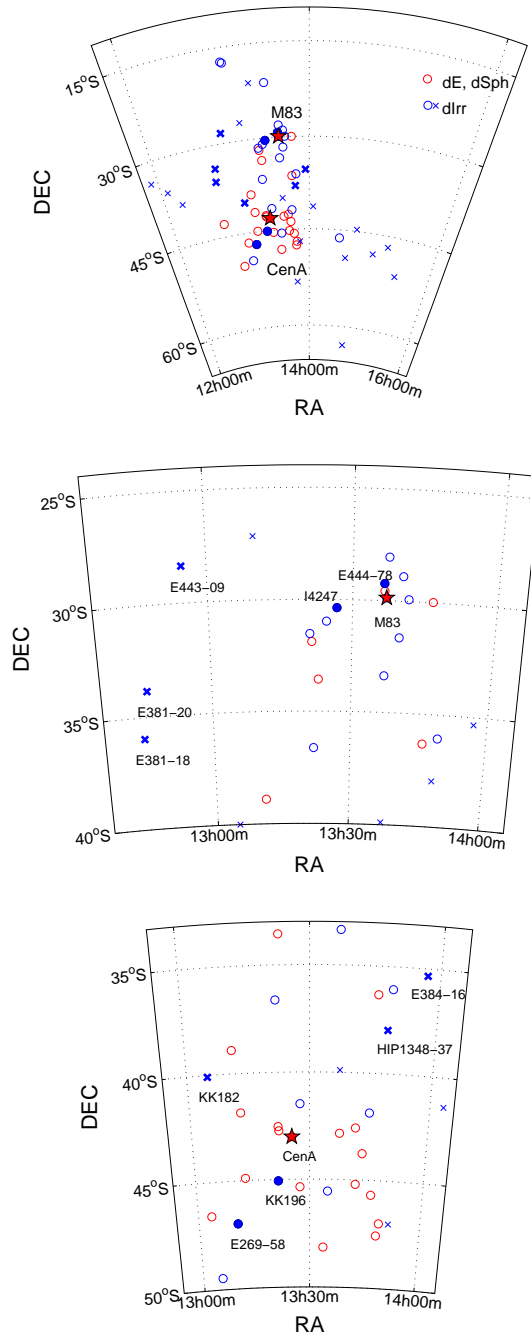


Figure 5.11: *Top panel.* Sky positions in the sky of the galaxies belonging to the CenA/M83 complex (from Karachentsev et al. 2007). Red symbols indicate early-type dwarfs (dwarf ellipticals, dEs, and dwarf spheroidals, dSphs), while blue symbols indicate late-type dwarfs (dIrrs). The circles are objects with positive tidal indices, while the crosses denote objects with a negative tidal index. Two red stars are drawn at the positions of the two dominant giant galaxies CenA and M83, around which the smaller companions cluster, forming two distinct subgroups. The filled circles and thick crosses represent the dwarfs studied here. *Central panel.* Same as above, but zoomed-in for a smaller region around M83. The late-type galaxies studied that belong to this subgroup are labeled in the plot. *Bottom panel.* Same as above, but zoomed-in for a smaller region around CenA.

galaxies with negative tidal indices (i.e., isolated dwarfs), of which there are six within our target sample. We would like to compare the properties of the dwarfs studied, also bearing in mind their position within the group. The most isolated objects are ESO443-09, ESO381-18, ESO381-20, HIPASS1348-37, KK182, and ESO384-16, located at a deprojected distance of > 900 kpc from either M83 or CenA. Some of these galaxies appear to have undergone periods of enhanced star formation in the last few hundred Myr (relative to their lifetime average), while others show an extremely low SFR in the same time range. There is thus no clear indication for an environmental influence on their evolution. Internal processes may shape the star formation in these small objects as suggested by ESO381-18 and IC4247 (in the M83 sample) having similarly shaped recent SFHs, even though the first one is currently quite isolated while the second one is the second closest to the dominant galaxy and lives in a dense environment. The same is also true for HIPASS1348-37 and KK196 in the CenA sample, and a very similar SFH is shared also by ESO384-16 and ESO269-58.

A puzzling property of the CenA/M83 group is the higher neutral gas mass to visual luminosity ratio of its members (Grossi et al. 2007), as compared to the Local Group or the Sculptor group, which are both less dense environments. When considering galaxy density, the stripping of the neutral gas from the dwarfs would thus in principle be more favored in the CenA environment (e.g., Bouchard et al. 2007). This issue is extensively discussed by Grossi et al. (2007), who are unable to find a definite answer. Bouchard et al. (2007) study the HI content of ESO444-78 and, from an asymmetric elongation of the HI distribution, conclude that ram-pressure stripping could be at work for this object. The same authors derive a similar conclusion also for ESO384-16, which they suggest to be falling toward the center of the group from asymmetries in its HI distribution. When we compute the ratio of the present-day neutral gas content over the lifetime average SFR for our targets, we see that for ESO444-78 and IC4247 (located at deprojected distances of ~ 104 kpc and ~ 280 kpc from M83, respectively) it would take ~ 3.5 Gyr to consume their entire HI amount at this rate. In the CenA subgroup, ESO269-58 (~ 320 kpc from CenA) would need only ~ 350 Myr to exhaust its neutral gas content, while the other CenA companion with positive tidal index, KK196, has no HI gas detected. This could be a hint of a possible environmental effect on the neutral gas content of these dwarfs, since the galaxies of our sample that currently have a negative tidal index show instead high $M_{HI}/\langle\text{SFR}\rangle$ ratios ($\geq 10^{10}$). The exception is ESO384-16, which has a $M_{HI}/\langle\text{SFR}\rangle$ ratio of 850 Myr but, as mentioned before, this object could possibly be experiencing ram-pressure stripping (Bouchard et al. 2007). Lee et al. (2007) and Côté et al. (2009) do not find any obvious trend of the neutral gas fraction as a function of tidal index or distance from the dominant galaxy (the first work considers projected distances, while the second one uses deprojected distances), using data for many dwarfs in different nearby groups. On the other hand, Bouchard et al. (2009) find that the neutral gas fraction is generally lower in denser environments, in agreement with our results, so the overall trend seems to be unclear.

We further analyze the specific properties of our targets as a function of different parameters. In Fig. 5.12 we plot the average SFR as a function of absolute magnitude, tidal index and deprojected distance from the closest giant galaxy. First of all, if we assume that to first order light traces the baryonic mass, then we expect the average SFR to be linearly increasing with luminosity (see, e.g., Grebel 2004, and references therein). Indeed, this is what we see from the top panel of Fig. 5.12, however ESO269-58 seems to be an outlier for this relation. Namely, its average SFR is higher than that found for galaxies of similar magnitude. There is no clear correlation between the average SFR and the tidal index of our galaxies, and the same is also

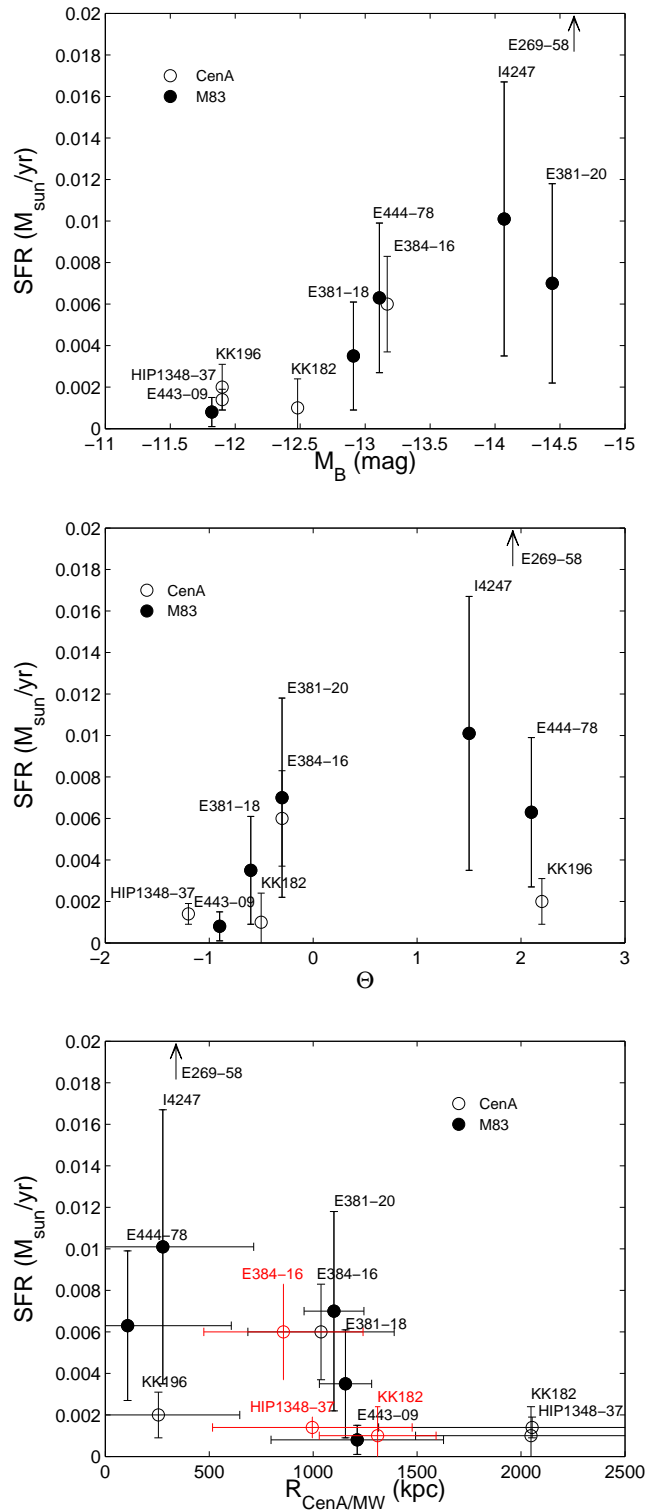


Figure 5.12: Lifetime average star formation rate plotted as a function of (*top panel*) absolute B luminosity, (*central panel*) tidal index, and (*bottom panel*) deprojected distance from the dominant subgroup galaxy. The black circles represent the CenA subgroup late-type dwarfs, while the filled circles are M83 subgroup members. Red symbols indicate the distances that we recompute for three of the CenA subgroup members, as indicated, as they are actually closer to M83 than to CenA (see text for details). For ESO269-58, the SFR is much higher than those for the other objects ($\sim 0.07 \pm 0.04 M_{\odot} \text{yr}^{-1}$), so this value falls outside our plot limits. In the panels, we only indicate its luminosity/tidal index/deprojected distance values with an arrow.

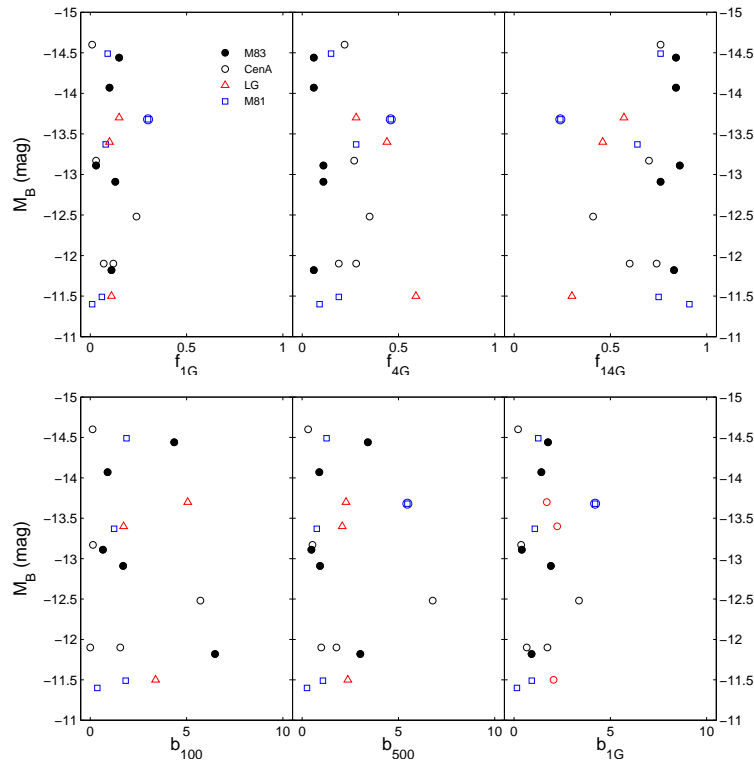


Figure 5.13: Absolute B luminosity plotted as a function of: (*upper panel*) the fraction of stars formed in the past 0 – 1 Gyr (f_{1G}), 1 – 4 Gyr (f_{4G}) and 4 – 14 Gyr (f_{14G}); (*lower panel*) the ratio of SFR to the lifetime average SFR over the last 100 Myr (b_{100}), 500 Myr (b_{500}) and 1 Gyr (b_{1G}). The black open circles represent the CenA subgroup late-type dwarfs, the black filled circles are M83 subgroup members, red triangles indicate Local Group late-type dwarf members and blue squares the M81 group late-type dwarfs. Holmberg IX is a candidate tidal dwarf, and we mark it with an additional blue circle since this object is not a typical dwarf galaxy (see text for details).

true for the deprojected distance. For the latter, we plot the distances based on the original group classification, and then also add the recomputed data points for the three CenA companions that are actually closer to M83 (HIPASS1348-37, KK182, and ESO384-16). If we consider these three objects as part of the CenA subgroup, it could be possible to claim that a mild trend is present, where the SFR is decreasing with increasing distance from the dominant galaxy. However, after recomputing their distances from M83, no clear correlation is seen between SFR and distance, only a scatter in the values of the sample. The absence of a trend seems reasonable if we bear in mind that the positions of the galaxies in the group have changed with time, and so the present-day position is not necessarily indicative of the distance from other galaxies in the past. We have no way of reconstructing the past orbits of our sample galaxies within the group. Also in this case, ESO269-58 appears to be an outlier given its high average SFR. This result still holds if we use the SFR to L_B ratio instead of the SFR alone.

We also computed parameters to quantify the amount of star formation in certain time periods, relative to the average value, and the fraction of stars born at recent, intermediate-age and old epochs (Tab. 5.1). We now want to investigate how these parameters behave as a function of luminosity, tidal index and deprojected distance from M83. A similar study has been done by Weisz et al. (2008), concentrating on M81 and Local Group dwarf irregulars with a larger luminosity range than the one considered here. However, the CMDs and the adopted techniques

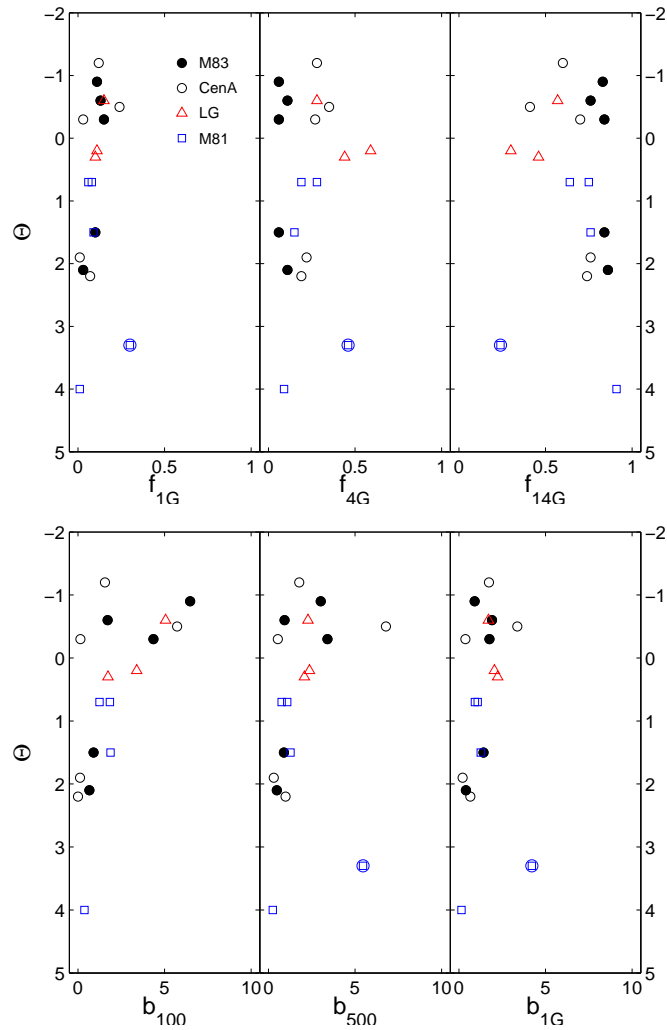


Figure 5.14: Tidal index plotted as a function of: (*upper panel*) the fraction of stars formed in the past 0 – 1 Gyr (f_{1G}), 1 – 4 Gyr (f_{4G}) and 4 – 14 Gyr (f_{14G}); (*lower panel*) the ratio of SFR to the lifetime average SFR over the last 100 Myr (b_{100}), 500 Myr (b_{500}) and 1 Gyr (b_{1G}). The black open circles represent the CenA subgroup late-type dwarfs, the black filled circles are M83 subgroup members, red triangles indicate Local Group late-type dwarf members and blue squares the M81 group late-type dwarfs. Holmberg IX is a candidate tidal dwarf, and we mark it with an additional blue circle since this object is not a typical dwarf galaxy (see text for details).

are similar, so their sample can be compared to ours. They do not find any clear trend of the luminosity with any of the parameters, and the values for the interacting M81 group and the Local Group do not reveal any substantial difference. They conclude that, given that the average SFR within their galaxy sample is almost consistent with a constant SFR over a Hubble time, the observed intrinsic scatter in the parameters may indicate the stochastic nature of the star formation process for these objects. We consider the galaxies from their sample (both from the M81 and the Local Group) that are in the same luminosity range as those in our sample, and investigate the cited parameters as a function of luminosity. Some of our results are very similar to theirs. For example, we do not find any correlation between absolute B luminosity and f (fraction of stars formed in certain time periods) or b (ratio of the SFR in a certain time period to the lifetime average SFR) parameters, which are plotted in Fig. 5.13. We show the values for dwarf galaxies belonging to three different groups (CenA/M83 group, Local Group and M81 group), and we do not see a clear trend in their values. We note that one of the M81 group members (Holmberg IX) is classified as a candidate tidal dwarf. This type of dwarf is supposed to have formed out of the baryonic material coming from a close interaction episode of the parent galaxy (in this case, the spiral M81), and thus a tidal dwarf should be a dark matter-free object (e.g., Toomre & Toomre 1972; Duc et al. 1997, 2000). One of the peculiarities of tidal dwarfs is that they contain very few old populations (most probably coming from the parent galaxy), and a more pronounced young population, born after the interaction event. They will thus not share the common properties of a typical dwarf galaxy, and we decide to mark Holmberg IX as an outlier in the relations discussed here.

We further plot the tidal index as a function of the f and b parameters in Fig. 5.14. If we do not consider Holmberg IX, we can see that there is a clear trend between the tidal index and both b_{100} and b_{500} (which tells us how active a galaxy has been in the past 100 and 500 Myr, respectively). There is also a hint for such a trend with b_{1G} , but less pronounced. The conclusion is that galaxies with a positive tidal index have generally had a low activity in their recent SFHs, while the ones which are more isolated have a range of different properties. The result confirms what has already been found by Bouchard et al. (2009) about the current SFR being lower in denser environments. They use a large sample of dwarfs in the Local Group, the CenA group and the Sculptor group, relating the dwarfs' physical properties to the local luminosity density. Considering the fraction of stars born at different ages, the f_{4G} and f_{14G} parameters present a larger scatter for a tidal index $\lesssim 0.5$. This translates into a common property for galaxies embedded in a denser environment, namely that they have all formed most of their stellar content more than 4 Gyr ago. On the other hand, galaxies that are currently sitting in less dense environments have a larger range of values for f_{4G} and f_{14G} .

As a last step we also plot the deprojected distance from the dominant group galaxy as a function of the f and b parameters in Fig. 5.15. For this quantity, only data for the CenA/M83 group are shown. We can see that the results are similar to the ones found for the tidal index. All the dwarf galaxies that are located closer than ~ 500 kpc from a giant galaxy clearly produced stars at a rate much lower than the lifetime average SFR in the last ~ 1 Gyr. Their more distant companions, on the other hand, produced stars with a range of different rates. This effect is particularly pronounced within the last 100 Myr. As before, this still holds when considering the fraction of stars born at different times. We conclude that the star formation in late-type dwarfs has a considerable range of properties in the field, while those objects that live in an environment with a high galaxy density and close to a giant galaxy have their star formation suppressed within the last 1 Gyr. The details of the SFHs will of course depend on the details

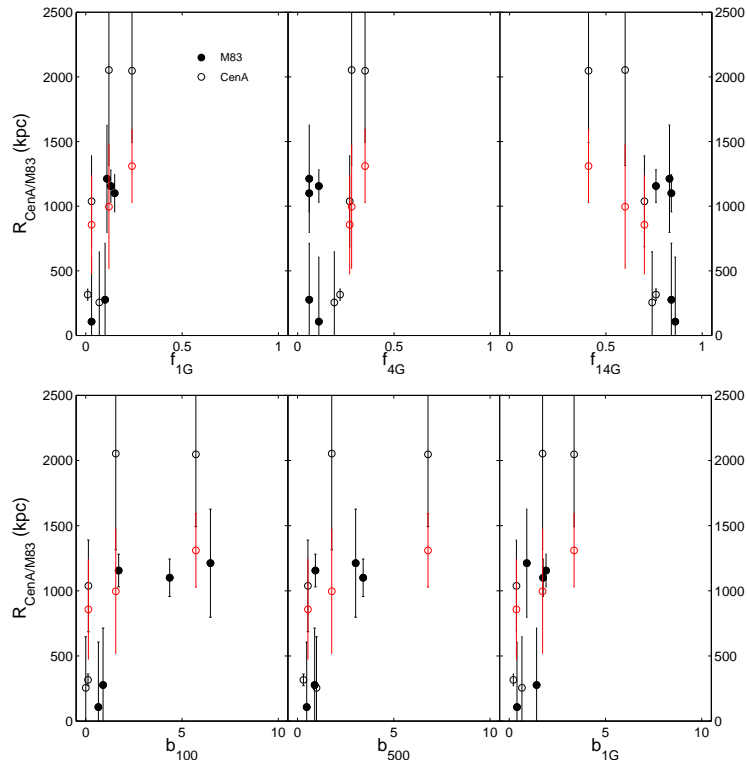


Figure 5.15: Deprojected distance from the dominant subgroup galaxy (either CenA or M83) plotted as a function of: (*upper panel*) the fraction of stars formed in the past 0 – 1 Gyr (f_{1G}), 1 – 4 Gyr (f_{4G}) and 4 – 14 Gyr (f_{14G}); (*lower panel*) the ratio of SFR to the lifetime average SFR over the last 100 Myr (b_{100}), 500 Myr (b_{500}) and 1 Gyr (b_{1G}). The black open circles represent the CenA subgroup late-type dwarfs and the black filled circles are M83 subgroup members. Red symbols indicate the distances that we recompute for three of the CenA subgroup members, as they actually are closer to M83 than to CenA (see also Fig. 5.12).

of the galactic orbit within the group, but the orbits of our targets are unknown due to their distances. As discussed in the previous Chapter, ram-pressure stripping could be a possible culprit for the observed suppression of star formation in the CenA group. We have already seen that the environment also affects the SFHs of the early-type dwarf members of the group. Bouchard et al. (2009) suggest that the proximity to a large number of galaxies (i.e., a dense group environment) could be accompanied by a dense enough intergalactic medium in order for ram-pressure stripping to happen. According to them, another possibility is that galaxies in a dense environment have a higher fraction of ionized gas, because of a higher ionizing flux coming from the neighboring galaxies.

Regarding the metallicity results, we emphasize again that with the current data we are not able to constrain the metallicity evolution with time and that our photometric metallicities are uncertain, but we can provide lifetime average values. Most of our targets are metal-poor ($[Fe/H] \sim -1.4$ dex). This suggests that the galaxies may have been locally enriched within small-scale regions during periods of intense star formation, as can be seen from their $H\alpha$ emission, but that they afterward have experienced strong ejection of newly formed metals from star forming regions. The ejection can happen through galactic winds and SNe explosions (see e.g. Bradamante et al. 1998), and the dwarfs may have also accreted some primordial gas during their lifetime. Alternatively, the enriched gas may still be in a hot phase, and thus not possible

to detect at optical wavelengths (e.g., Recchi et al. 2000, 2006). It is indeed likely that dwarf galaxies embedded in a dominant dark matter halo, but with baryonic masses as low as the ones in our sample ($\sim 10^8 M_{bar}$), will not be able to retain almost any of the metal-enriched gas coming from the star formation episodes (Mac Low & Ferrara 1999). We also note that two of the most luminous galaxies in our sample, ESO384-16 and ESO269-58, have slightly higher metallicities ($[Fe/H] \sim -1.0$ dex) with respect to the others, thus showing a hint of a metallicity-luminosity relation. Previous studies indeed suggest that the metallicity-luminosity relation for galaxies in other groups and clusters is similar to the one found in the Local Group. We have already shown that this holds for our sample of early-type dwarfs (see Chapter 3). We note that Sharina et al. (2008) consider the same dataset that we study, and compute the metallicities of the target dwarfs with the empirical formula by Lee et al. (1993), considering stars on the upper RGB. They find an offset between early-type dwarfs and late-type dwarfs, similar to the one displayed by MW companions (Gebel et al. 2003). However, as suggested in Sect. 5.1, their metallicities for the dwarf irregulars may be underestimated. Unfortunately, it is difficult to compare our results to theirs in more detail, or to the metallicities found for our early-type sample. This is because we used the Dartmouth stellar evolutionary models for our previous study, while for the SFH recovery we adopted the Padova set of models (since only these models cover the full range of ages that we need). As already discussed in Section 3.1.2, the use of the two models gives metallicity results that differ by approximately 0.3 dex (judging from the upper part of the RGB). Moreover, the estimate of the metallicity for the late-type dwarfs includes the youngest stars, while the metallicity values for early-type dwarfs come only from their old populations. It is thus not possible to compare the metallicities derived in Chapter 3 to the ones derived in this Chapter, because the involved models yield different results due to their different input physics and to the differences in the transformation to the observational plane from theoretical quantities (like temperature and luminosity).

“Now is no time to think of what you do not have. Think of what you can do with what there is.”

E. Hemingway, *The Old Man and the Sea* (1952)



Summary and outlook

Dwarf galaxies are fundamental ingredients for the assembly of the present-day Universe. Despite their small size, they surprise us with a variety of morphologies, chemical compositions and evolutionary histories. Their physical properties are as much complex within our own Local Group, as they are still unexplored beyond its boundaries. With state-of-the-art observing instruments and analysis tools, in the last decades we have learned many of the nuances of dwarfs inhabiting our backyard. With this study, we go beyond our doorstep and explore the techniques that will help us to unveil the secret mechanisms of galaxy formation and evolution. By looking at dwarfs in nearby groups of galaxies, we can extract the information embedded in their resolved stellar populations, which trace their past history. We are particularly interested in the role that the surrounding environment plays in the evolution of these objects. This Thesis is one of the first studies to look at the resolved stellar populations of dwarfs in nearby groups in great detail.

The Centaurus A/M83 group has been the main character of this Thesis. It is one of the closest galaxy agglomerates to us (located at an average distance of ~ 4 Mpc), and shows characteristics very similar to the Local Group. However, there is also evidence for it to be an environment that is more dense in galaxies and perhaps in a more advanced evolutionary stage compared to our own. More than 50 dwarf members of different morphologies and stellar contents form two subgroups around the dominant giants (the peculiar elliptical CenA and the spiral M83). The Centaurus A/M83 is thus a very appealing target in which to study these small objects and to seek possible similarities or differences with dwarf populations in other group environments.

For our study, we use both archival optical data from the HST (ACS instrument) and proprietary NIR data taken at the VLT (ISAAC instrument). We perform stellar point-source photometry on these images and derive CMDs for sixteen target dwarfs belonging to the Centaurus A/M83 group. Although the CMDs are not as deep as those obtainable for Local Group members (due to their larger distance), we are able to study the physical properties and the evolutionary histories of the target dwarfs with the help of theoretical isochrones. More specifically, we derive photometric metallicity-distribution functions, investigate the presence of radial metallicity gradients and quantify the amount of intermediate-age star formation for our six early-type dwarf targets. Furthermore, we test the validity of our analysis techniques on the deeper CMDs of six low-mass M31 early-type companions that show similar characteristics as our target objects. For our ten late-type dwarf targets, we reconstruct their recent (~ 1 Gyr) star formation histories in detail and study the time-dependent spatial distribution of their stellar populations. We then look for a connection between the derived properties and the location of the targets within the group.

We can summarize our results as follows.

- *Early-type dwarfs*

We studied deep HST/ACS images of four dwarf spheroidals and two dwarf ellipticals in the CenA group. These are the deepest photometric data available to date for CenA dwarf members. They allow us to investigate their metallicity content and to put constraints on their star formation episodes through the study of their resolved stellar populations. Our goal is to estimate whether there are similarities or differences with the early-type dwarf population of our own Local Group, and thus to better understand the interplay between internal processes and external forces in shaping dwarf galaxy evolution. With the current instrumentation, spectra for individual RGB stars at these distances (~ 4 Mpc) cannot be obtained, and thus the only possibility to look in detail at stellar metallicities is to take advantage of their photometric properties. *This is the first time that photometric metallicity distribution functions are derived for dwarf galaxies outside the Local Group.* On the other hand, early-type dwarfs were originally believed to have simple star formation histories given their absence of neutral gas and recent star formation. However, some of the Local Group early-type dwarf members have revealed significant amounts of intermediate-age populations, and furthermore there is a tendency for dwarfs more distant from the dominant giant galaxy to have higher fractions of such populations. Some external gas removal mechanism could thus be acting on these galaxies, perhaps also leading to a morphological transformation from late-type to early-type dwarf. The study of intermediate-age populations in early-type dwarfs of nearby groups is fundamental in order to shed light on how external forces influence the dwarfs' evolution in different environments.

The optical CMDs of the CenA early-type dwarf companions show broad RGBs without any evidence of young (< 1 Gyr) populations, so we assume a predominantly old age for their stellar content. We note that our target galaxies also exhibit a small number of luminous AGB stars above the tip of their RGBs, indicative of an intermediate-age population ($\sim 1 - 9$ Gyr). However, a precise quantification of such populations is not possible from optical data alone, given that the Centaurus A group lies at a mean Galactic latitude of $b \sim 20^\circ$, and is thus affected by Galactic foreground contamination. To derive photometric metallicities for the luminous red giants in our sample, we chose Dartmouth isochrones, since they have been shown to provide an excellent fit to the full extent of CMDs of both old and intermediate-age star clusters. Fixing the age of the isochrones at 10 Gyr and assuming a solar-scaled α -element abundance, we allowed the metallicity to vary and interpolated between the isochrones to obtain individual metallicity values for stars on the RGB. We further estimated the amount of bias in our results due to the presence of intermediate-age stars (which we estimate to account for $\sim 10\%$ to $\sim 20\%$ of the entire population), and found that the metallicity spreads were likely to be the result of this contamination for two of the target galaxies. For the other objects, we show that the presence of extended early-star formation episodes (which are indeed very likely) and a range of α -element abundances would eventually broaden the derived metallicity spreads, and make the median metallicities lower by $\sim 15\%$.

In terms of metallicity content (derived from the optical CMDs), the CenA early-type companions resemble the properties of Local Group dwarfs. They are moderately *metal-*

poor ($\langle[\text{Fe}/\text{H}]\rangle = -1.56$ to -1.08), and *metallicity spreads are observed* for almost all of them (internal dispersions of $\sigma[\text{Fe}/\text{H}] = 0.10 - 0.41$ dex). The CenA companions follow closely the luminosity-metallicity relation originally discovered for Local Group members and subsequently found to extend also to other nearby environments. The shapes of the resulting metallicity-distribution functions are overall very similar to the ones spectroscopically derived for Local Group dwarfs, and stem from the combination of supernovae-driven enrichment and galactic outflows. A more detailed comparison is not possible because of the intrinsic uncertainties of our analysis method. Some of our targets additionally show the presence of metallicity gradients, and also of statistically distinct stellar subpopulations (in metallicity), which is again similarly observed for Local Group early-type dwarfs and can be reproduced by the theoretical models. We do not find any clear trend in median galaxy metallicity versus tidal index (i.e. degree of isolation) or versus (present-day) distance from the central galaxy of the group. While the orbits of our target galaxies are not known, this suggests an important role of internal processes (governed by galactic mass) in the shaping of the physical properties of these dwarfs.

However, an intriguing difference emerges when we look at the intermediate-age populations of the early-type dwarfs in CenA in more detail. To do this, we exploit the combination of our deep high-resolution optical images and NIR data, where the Galactic foreground contamination is more easily separable from the galactic populations and where upper AGB stars appear more luminous. NIR observations are available for three of our target early-type dwarfs. We select common stars from the combined optical and NIR CMDs, and isolate candidate luminous AGB stars in our targets. We then compute the absolute bolometric magnitudes for the most luminous AGB candidates of each galaxy, and correlate the values obtained with the age of the most recent significant star formation episode in these galaxies. We find that the most recent significant star formation episode took place between ~ 2 and ~ 9 Gyr ago in the target dwarfs. By comparing the number of candidate luminous AGB stars to stellar evolutionary models, we are able to compute the fraction of intermediate-age populations and find values of up to $\sim 15\%$ of the total population. These values could be higher by a factor of two/three, if we consider the observational limitations and the recent literature discussion about the uncertainties in theoretical models. When comparing our results to dwarf galaxies of the Local Group, we clearly see that despite sharing similar physical properties and positions within the two groups, *the objects in the CenA group tend to have lower intermediate-age population fractions* (the relative differences are not affected by model uncertainties). These results confirm previous literature work on two early-type CenA dwarf companions. We suggest that this difference might be due to environmental effects, which lead to the earlier loss of the neutral gas for the dwarfs in this dense group. This seems preferentially to be the case for objects that are closest to the dominant elliptical CenA. However, we stress that our sample, together with the two objects considered in the mentioned previous study, consists of only five galaxies.

According to the CenA membership list by Karachentsev et al. (2007), there are sixteen early-type dwarf companions to CenA. For five of these objects, the results presented in Rejkuba et al. (2006) and complemented in this Thesis clearly point toward a low fraction of intermediate-age populations in them. For the remaining three dwarfs studied here, we have indirect evidence that this trend is still true. We can thus claim that at least half

of the early-type dwarfs (so far detected) in this group had their star formation halted at some point within the last ~ 9 Gyr. For the Local Group, the same statement is true for about 1/3 of the classical dwarf spheroidals around the Milky Way. On the other hand, all of the M31 dwarf spheroidal companions lack a significant intermediate-age stellar component (with the exception of the three dwarf ellipticals). It is thus interesting to try to understand whether there could be similarities between our target objects and the M31 dwarf companions, and we decided to further investigate this aspect (see below). Coming back to the CenA group, there are six additional early-type dwarfs that have so far not been observed with the HST, and two that have WFPC2 observations (which, however, only cover part of the galaxy bodies). The next step of the present study will thus be to propose both HST optical observations of these objects with the newly installed WFPC3 instrument, and further, to follow them up with NIR data (using the VLT/HAWK-I instrument, more sensitive and with a larger field-of-view than ISAAC). There are additionally four other M83 early-type companions for which the same observations would be recommendable, given the fact that this subgroup has a much lower early-type to late-type dwarfs ratio and is thus probably in a less advanced evolutionary stage than the CenA subgroup.

We emphasize again that this is one of the first studies in which intermediate-age populations for dwarfs in nearby groups are investigated from their resolved stellar populations. The theoretical stellar evolutionary models, which are particularly challenging to calibrate for the delicate stage of luminous AGB stars, would definitely benefit from this kind of study, helping to put further constraints on the properties of this evolutionary phase. The natural extension of this work would then be to include other nearby groups of galaxies, in order to be able to additionally target diverse environments (e.g., the loose Sculptor filament or the as yet unvirialized Canes Venatici Cloud) and investigate the effects of environment on dwarf galaxy evolution. In these less evolved groups, one would in principle expect higher fractions of intermediate-age populations, if we assume that the environment is what causes this effect in the CenA group. It would, finally, also be desirable to complete the galactic census of the CenA/M83 group itself, which would most probably reveal quite a number of early-type members fainter than $M_B \sim -12$ (e.g., see the luminosity function reported by Jerjen et al. 2000a), although this is an observationally challenging task.

- *M31 early-type dwarf companions*

We have considered six dwarf spheroidal companions of M31, which, just like the studied CenA dwarfs, lack significant amounts of intermediate-age populations. Our aim is to understand whether the environment they live in is the culprit for the truncation of their star formation at recent epochs. The data considered come entirely from HST observations, and we can check our photometric metallicity distribution function derivation method using the CMDs of these objects. We thus provide *the first homogeneous sample of observations for which metallicity distribution functions are derived by applying the same data processing and analysis technique throughout.* Given that spectroscopic metallicities of individual RGB stars are available from literature for some of the M31 targets, by studying these objects we can additionally test our photometric results against the precise spectroscopic estimates. We find very good agreement and confirm that our derived

metallicity spreads are likely to be lower limits of the true values. Due to the depth of the CMDs (thanks to their vicinity), we are additionally able to give an estimate for the age of these objects. We do this by comparing the observed luminosity functions to theoretical ones produced with the Padova stellar evolutionary models (these include the HB stage in their simulations). We underline that And VII, among the M31 companions, is a particularly interesting target. Namely, we find that its observed luminosity function is not well represented by any combination of age and metallicity of the theoretical models, which could stem from uncertainties in the model calibrations. Furthermore, And VII shows hints of an intermediate-age population, but a detailed analysis of its stellar populations with a complete radial coverage of the galaxy is still missing, and follow-up observations are going to be proposed for this object.

Recent studies suggest that the dwarf spheroidal M31 companions might possess larger half-light radii with respect to their MW counterparts, and that they might inhabit less dense dark matter haloes. This could be partly due to external effects, such as ram-pressure stripping from a dense intra-group medium or a strong UV flux from the dominant spiral, or could exotically arise from different underlying physics. What is the reason for the observed structural properties and for the apparent truncation of star formation in these objects? The comparison between the properties of M31 and CenA companions do not straightforwardly provide a definitive answer to this fascinating dilemma. This is an additional reason for which more observational data should be obtained for both of the environments studied.

- *Late-type dwarfs*

As for our early-type targets, it is interesting to study late-type dwarfs in environments different from the Local Group to understand the mechanisms that most influence their evolutionary histories. Late-type dwarfs have undergone recent star formation and this is reflected in their CMDs, which show a wealth of information for these young stellar populations. Our ten target objects show different luminosities and neutral gas contents, and reside at different locations within the group (two close to the giant spiral M83, two close to the giant elliptical CenA and six isolated objects in the outskirts of the group). This is thus a very suitable sample to look for possible environmental effects on galactic evolution. We perform synthetic color-magnitude diagram modeling for each object, which is a powerful tool for extracting the star formation rate as a function of time, and we do this by starting from Padova stellar isochrones. Given the fair amount of luminous young stars, the star formation histories we derive are detailed for the past $\sim 1 - 2$ Gyr, while for older ages the time resolution becomes coarser but still allows us to give average values for the star formation. The lifetime average star formation values range from $\sim 10^{-3}$ to $\sim 10^{-2} M_{\odot} \text{yr}^{-1}$, which are typical values for low-mass galaxies. The individual star formation histories appear to be very different from each other, with some of the target dwarfs having already formed most of their stellar content more than 8 Gyr ago, some others having been significantly active only at recent times, some being possibly in a transition phase from late-type to early-type morphology, and some having just experienced a strong burst. Overall, the general trend is one where *the star formation takes place rather constantly over the galaxy's lifetime, with global enhancements of 2-3 times the average value lasting up to 300-500 Myr*. With this method, it is also possible to

derive an average value of metallicity for our targets (although we lack the CMD depth to be able to put constraints on its time evolution), and they all turn out to have a metal-poor stellar content. The late-type dwarfs studied do seem to follow a metallicity-luminosity relation, but a more detailed comparison to CenA or Local Group early-type members is made difficult by the uncertainties stemming from the analysis method and because of the different theoretical models involved.

We have presented the stellar spatial distribution for stars of different ages within our galaxies, in order to study how star formation proceeds in these objects. We confirm previous results about the oldest populations being more extended and having a regular shape compared to the youngest stars, which show a more clumpy distribution. This trend reflects the migration and redistribution of stars within the galaxy with increasing time. Specifically, an analysis of the youngest populations of massive core helium-burning stars allows us to spatially resolve the recent star formation histories for one of our targets. The positions in a CMD of stars found in this evolutionary stage are, namely, not degenerate for age and metallicity, and thus permit us to assign to each star a specific age with high precision. From the density maps of these young stars we can then infer that this galaxy recently experienced a prolonged period of high star formation activity involving the galaxy as a whole, with several localized and short-lived enhancements. We conclude that *the actively star forming regions have sizes of ~ 100 pc and lifetimes of $\gtrsim 100$ Myr*, in excellent agreement with literature studies of other, closer dwarf irregulars, and thus suggesting a stochastic star formation mode for the target late-type dwarf galaxies. The overall similar properties in the star formation histories of different galaxy groups (Local Group, CenA/M83, the interacting M81 group), and the intrinsic scatter in the parameters characterizing the star formation support this scenario.

The dwarfs studied have average star formation rates slightly higher than their analogues in the Local Group, but comparable to those in the M81 group. We find no significant differences among the three groups of galaxies when looking at the galaxies' individual star formation efficiencies at various epochs and also looking at the shape of the star formation histories themselves. If we consider their average star formation rates as a function of tidal index or of deprojected distance from the closest giant galaxy, we do not find any trend. This is a reasonable result, given that the average properties depend on the whole galaxy's history, and we only have information about the current position of the objects within the group because their orbits are unknown. However, we compute the ratio of the star formation in the last $\sim 0.5 - 1$ Gyr to the lifetime average value and we find that it correlates with environment, confirming previous studies. Namely, dwarfs that are closest to the dominant giant galaxy and found in a denser environment have lower such ratios compared to the more isolated objects. We can thus conclude that *the star formation within the last ~ 1 Gyr is quenched in dense group environments, while more isolated objects show a vast range of different histories* (i.e., their evolution is primarily regulated by intrinsic properties).

Finally, the neutral gas content of the sample dwarfs also does seem to be affected by the group environment: galaxies within denser regions have a much lower ratio of neutral gas mass to average star formation rate than the isolated ones do, meaning that they will exhaust their gas reservoirs more quickly. Also for late-type dwarfs, we notice that there is a tight interplay between internal and external processes that regulate their evolutionary

histories. It would certainly be interesting to look at the neutral gas mass distribution for these objects in more detail, since it extends further out than the stellar populations. Distortions or asymmetries in its distribution would increase our understanding of the possible external forces that act on these galaxies. Finally, we look forward to comparing the star formation histories we derive from the resolved stellar populations to the ones obtained from integrated spectra for some of our target galaxies. These data are already being analyzed, and will be extremely useful for the calibration of the latter method, which is the only method available for disentangling the properties of galaxies beyond ~ 18 Mpc.

Take-home message

Although the dwarf galaxies studied here exhibit physical characteristics that are on the whole comparable to those of the Local Group members, our results suggest that the (dense) CenA/M83 environment could have played a role in the suppression of its dwarf companions' star formation. This is a very interesting result which certainly deserves more observational evidence. The CenA/M83 group has proven to be a very promising target, in which the resolved stellar populations of the dwarf members can be analyzed to ultimately better understand the details of galactic evolution. The study presented in this Thesis should thus be an appetizer, and stimulate the curiosity for the research that has started to be pursued for nearby groups of galaxies that cover a range of different environments.

Bibliography

- Adelman-McCarthy, J. K., Agüeros, M. A., Allam, S. S., et al. 2008, *ApJS*, 175, 297
- Adén, D., Wilkinson, M. I., Read, J. I., et al. 2009, *ApJ*, 706, L150
- Aloisi, A. & Leitherer, C. 2001, in *Astronomical Society of the Pacific Conference Series*, Vol. 245, *Astrophysical Ages and Times Scales*, ed. T. von Hippel, C. Simpson, & N. Manset, 439
- Aloisi, A., Tosi, M., & Greggio, L. 1999, *AJ*, 118, 302
- Alves, D. R. & Sarajedini, A. 1999, *ApJ*, 511, 225
- Aparicio, A., Carrera, R., & Martínez-Delgado, D. 2001, *AJ*, 122, 2524
- Aparicio, A. & Gallart, C. 2004, *AJ*, 128, 1465
- Aparicio, A., Gallart, C., Chiosi, C., & Bertelli, G. 1996, *ApJ*, 469, L97
- Armandroff, T. E., Da Costa, G. S., Caldwell, N., & Seitzer, P. 1993, *AJ*, 106, 986
- Armandroff, T. E., Davies, J. E., & Jacoby, G. H. 1998, *AJ*, 116, 2287
- Armandroff, T. E., Jacoby, G. H., & Davies, J. E. 1999, *AJ*, 118, 1220
- Banks, G. D., Disney, M. J., Knezek, P. M., et al. 1999, *ApJ*, 524, 612
- Battaglia, G., Helmi, A., Tolstoy, E., et al. 2008, *ApJ*, 681, L13
- Battaglia, G., Tolstoy, E., Helmi, A., et al. 2006, *A&A*, 459, 423
- Beaulieu, S. F., Freeman, K. C., Carignan, C., Lockman, F. J., & Jerjen, H. 2006, *AJ*, 131, 325
- Begeman, K. G., Broeils, A. H., & Sanders, R. H. 1991, *MNRAS*, 249, 523
- Bellazzini, M., Ferraro, F. R., Origlia, L., et al. 2002, *AJ*, 124, 3222
- Belokurov, V., Walker, M. G., Evans, N. W., et al. 2010, *ApJ*, 712, L103
- Belokurov, V., Zucker, D. B., Evans, N. W., et al. 2006, *ApJ*, 647, L111
- Binggeli, B. 1994, in *European Southern Observatory Conference and Workshop Proceedings*, ed. G. Meylan & P. Prugniel, Vol. 49, 13
- Bosler, T. L., Smecker-Hane, T. A., & Stetson, P. B. 2007, *MNRAS*, 378, 318
- Bouchard, A., Da Costa, G. S., & Jerjen, H. 2009, *AJ*, 137, 3038
- Bouchard, A., Jerjen, H., Da Costa, G. S., & Ott, J. 2007, *AJ*, 133, 261
- Boyer, M. L., Skillman, E. D., van Loon, J. T., Gehrz, R. D., & Woodward, C. E. 2009, *ApJ*, 697, 1993
- Bradamante, F., Matteucci, F., & D'Ercole, A. 1998, *A&A*, 337, 338

- Brown, T. M., Smith, E., Guhathakurta, P., et al. 2006, *ApJ*, 636, L89
- Bullock, J. S. 2010, *ArXiv:1009.4505*
- Bullock, J. S., Kravtsov, A. V., & Weinberg, D. H. 2000, *ApJ*, 539, 517
- Carpenter, J. M. 2001, *AJ*, 121, 2851
- Carrera, R., Aparicio, A., Martínez-Delgado, D., & Alonso-García, J. 2002, *AJ*, 123, 3199
- Chabrier, G. 2003, *ApJ*, 586, L133
- Cignoni, M. & Tosi, M. 2010, *Advances in Astronomy*, 2010, 3
- Cole, A. A. 2010, *Publications of the Astronomical Society of Australia*, 27, 234
- Cole, A. A., Skillman, E. D., Tolstoy, E., et al. 2007, *ApJ*, 659, L17
- Cole, A. A., Tolstoy, E., Gallagher, III, J. S., & Smecker-Hane, T. A. 2005, *AJ*, 129, 1465
- Coleman, M. G. & de Jong, J. T. A. 2008, *ApJ*, 685, 933
- Collins, M. L. M., Chapman, S. C., Irwin, M. J., et al. 2010, *MNRAS*, 1119
- Costa, E. & Frogel, J. A. 1996, *AJ*, 112, 2607
- Côté, P., Oke, J. B., & Cohen, J. G. 1999, *AJ*, 118, 1645
- Côté, S., Carignan, C., & Freeman, K. C. 2000, *AJ*, 120, 3027
- Côté, S., Draginda, A., Skillman, E. D., & Miller, B. W. 2009, *AJ*, 138, 1037
- Côté, S., Freeman, K. C., Carignan, C., & Quinn, P. J. 1997, *AJ*, 114, 1313
- Crnojević, D., Grebel, E. K., & Koch, A. 2010, *A&A*, 516, A85
- Da Costa, G. S. & Armandroff, T. E. 1990, *AJ*, 100, 162
- Da Costa, G. S., Armandroff, T. E., & Caldwell, N. 2002, *AJ*, 124, 332
- Da Costa, G. S., Armandroff, T. E., Caldwell, N., & Seitzer, P. 1996, *AJ*, 112, 2576
- Da Costa, G. S., Armandroff, T. E., Caldwell, N., & Seitzer, P. 2000, *AJ*, 119, 705
- Dalcanton, J. J., Williams, B. F., Seth, A. C., et al. 2009, *ApJS*, 183, 67
- Davidge, T. J. 2005, *AJ*, 130, 2087
- Davidge, T. J. 2007, *AJ*, 134, 1799
- Davidge, T. J., Da Costa, G. S., Jørgensen, I., & Allington-Smith, J. R. 2002, *AJ*, 124, 886
- Davis, L. E. 1993, in *Astronomical Society of the Pacific Conference Series*, Vol. 52, *Astronomical Data Analysis Software and Systems II*, ed. R. J. Hanisch, R. J. V. Brissenden, & J. Barnes, 420

- Dekel, A. & Silk, J. 1986, *ApJ*, 303, 39
- Demers, S., Battinelli, P., & Letarte, B. 2003, *AJ*, 125, 3037
- Demers, S., Dallaire, M., & Battinelli, P. 2002, *AJ*, 123, 3428
- Dohm-Palmer, R. C., Skillman, E. D., Mateo, M., et al. 2002, *AJ*, 123, 813
- Dohm-Palmer, R. C., Skillman, E. D., Saha, A., et al. 1997, *AJ*, 114, 2527
- Dolphin, A. E. 2000, *PASP*, 112, 1383
- Dolphin, A. E. 2002, *MNRAS*, 332, 91
- Dolphin, A. E., Weisz, D. R., Skillman, E. D., & Holtzman, J. A. 2005, *ArXiv:0506430*
- Dotter, A., Chaboyer, B., Jevremović, D., et al. 2008, *ApJS*, 178, 89
- Duc, P., Brinks, E., Springel, V., et al. 2000, *AJ*, 120, 1238
- Duc, P., Brinks, E., Wink, J. E., & Mirabel, I. F. 1997, *A&A*, 326, 537
- Duquennoy, A. & Mayor, M. 1991, *A&A*, 248, 485
- Durrell, P. R., Harris, W. E., & Pritchett, C. J. 2001, *AJ*, 121, 2557
- Einasto, J., Saar, E., Kaasik, A., & Chernin, A. D. 1974, *Nature*, 252, 111
- Elmegreen, B. G., Elmegreen, D. M., Salzer, J. J., & Mann, H. 1996, *ApJ*, 467, 579
- Fleming, D. E. B., Harris, W. E., Pritchett, C. J., & Hanes, D. A. 1995, *AJ*, 109, 1044
- Frebel, A., Simon, J. D., Geha, M., & Willman, B. 2010, *ApJ*, 708, 560
- Gallart, C., Freedman, W. L., Aparicio, A., Bertelli, G., & Chiosi, C. 1999, *AJ*, 118, 2245
- Gallart, C., Zoccali, M., & Aparicio, A. 2005, *ARAA*, 43, 387
- Geha, M., van der Marel, R. P., Guhathakurta, P., et al. 2010, *ApJ*, 711, 361
- Geisler, D., Wallerstein, G., Smith, V. V., & Casetti-Dinescu, D. I. 2007, *PASP*, 119, 939
- Georgiev, I. Y., Goudfrooij, P., Puzia, T. H., & Hilker, M. 2008, *AJ*, 135, 1858
- Gerhard, O. 2010, *ArXiv:1009.3380*
- Gilmore, G., Wilkinson, M. I., Wyse, R. F. G., et al. 2007, *ApJ*, 663, 948
- Girardi, L., Groenewegen, M. A. T., Hatziminaoglou, E., & da Costa, L. 2005, *A&A*, 436, 895
- Girardi, L., Williams, B. F., Gilbert, K. M., et al. 2010, *ArXiv:1009.4618*
- Glatt, K., Gallagher, III, J. S., Grebel, E. K., et al. 2008a, *AJ*, 135, 1106
- Glatt, K., Grebel, E. K., & Koch, A. 2010, *A&A*, 517, A50

- Glatt, K., Grebel, E. K., Sabbi, E., et al. 2008b, *AJ*, 136, 1703
- Goudfrooij, P., Puzia, T. H., Kozhurina-Platais, V., & Chandar, R. 2009, *AJ*, 137, 4988
- Grcevich, J. & Putman, M. E. 2009, *ApJ*, 696, 385
- Grebel, E. K. 1997, in *Reviews in Modern Astronomy*, ed. R. E. Schielicke, Vol. 10, 29
- Grebel, E. K. 2001, *Astrophysics and Space Science Supplement*, 277, 231
- Grebel, E. K. 2004, in *Origin and Evolution of the Elements, Carnegie Observatories Centennial Symposia*, Cambridge University Press, ed. A. McWilliam & M. Rauch, 234
- Grebel, E. K. 2007, in *Groups of Galaxies in the Nearby Universe*, ed. I. Saviane, V. D. Ivanov, & J. S. Borissova, 3
- Grebel, E. K. & Brandner, W. 1998, in *Magellanic Clouds and Other Dwarf Galaxies*, ed. T. Richtler & J. M. Braun, Shaker Verlag, 151
- Grebel, E. K. & Gallagher, III, J. S. 2004, *ApJ*, 610, L89
- Grebel, E. K., Gallagher, III, J. S., & Harbeck, D. 2003, *AJ*, 125, 1926
- Grebel, E. K. & Guhathakurta, P. 1999, *ApJ*, 511, L101
- Grevesse, N. & Sauval, A. J. 1998, *Space Science Reviews*, 85, 161
- Grillmair, C. J., Mould, J. R., Holtzman, J. A., et al. 1998, *AJ*, 115, 144
- Grossi, M., Disney, M. J., Pritzl, B. J., et al. 2007, *MNRAS*, 374, 107
- Guhathakurta, P., Reitzel, D. B., & Grebel, E. K. 2000, in *Society of Photo-Optical Instrumentation Engineers (SPIE) Conference Series*, ed. J. Bergeron, Vol. 4005, 168
- Gullieuszik, M., Held, E. V., Rizzi, L., et al. 2008, *MNRAS*, 388, 1185
- Gullieuszik, M., Held, E. V., Saviane, I., & Rizzi, L. 2009, *A&A*, 500, 735
- Han, M., Hoessel, J. G., Gallagher, III, J. S., Holtzman, J., & Stetson, P. B. 1997, *AJ*, 113, 1001
- Harbeck, D., Gallagher, III, J. S., & Grebel, E. K. 2004, *AJ*, 127, 2711
- Harbeck, D., Grebel, E. K., Holtzman, J., et al. 2001, *AJ*, 122, 3092
- Harris, G. L. H. 2010, *ArXiv:1004.4907*
- Harris, G. L. H. & Harris, W. E. 2000, *AJ*, 120, 2423
- Harris, G. L. H., Harris, W. E., & Poole, G. B. 1999, *AJ*, 117, 855
- Harris, G. L. H., Rejkuba, M., & Harris, W. E. 2009, *ArXiv:0911.3180*
- Harris, J. & Zaritsky, D. 2002, in *Astronomical Society of the Pacific Conference Series*, Vol. 274, *Observed HR Diagrams and Stellar Evolution*, ed. T. Lejeune & J. Fernandes, 600

- Harris, J. & Zaritsky, D. 2004, *AJ*, 127, 1531
- Harris, J. & Zaritsky, D. 2009, *AJ*, 138, 1243
- Harris, W. E. & Harris, G. L. H. 2002, *AJ*, 123, 3108
- Harris, W. E., Harris, G. L. H., Layden, A. C., & Wehner, E. M. H. 2007, *ApJ*, 666, 903
- Held, E. V., Gullieuszik, M., Rizzi, L., et al. 2010, *MNRAS*, 404, 1475
- Helmi, A., Irwin, M. J., Tolstoy, E., et al. 2006, *ApJ*, 651, L121
- Hirashita, H. 2000, *PASJ*, 52, 107
- Hui, X., Ford, H. C., Ciardullo, R., & Jacoby, G. H. 1993, *ApJ*, 414, 463
- Hunter, D. A. & Elmegreen, B. G. 2004, *AJ*, 128, 2170
- Hurley-Keller, D., Mateo, M., & Grebel, E. K. 1999, *ApJ*, 523, L25
- Hurley-Keller, D., Mateo, M., & Nemeč, J. 1998, *AJ*, 115, 1840
- Ikuta, C. & Arimoto, N. 2002, *A&A*, 391, 55
- Isserstedt, J. 1984, *A&A*, 131, 347
- Jerjen, H., Binggeli, B., & Freeman, K. C. 2000a, *AJ*, 119, 593
- Jerjen, H., Freeman, K. C., & Binggeli, B. 2000b, *AJ*, 119, 166
- Kalirai, J. S., Beaton, R. L., Geha, M. C., et al. 2010, *ApJ*, 711, 671
- Kang, A., Sohn, Y., Kim, H., et al. 2006, *A&A*, 454, 717
- Karachentsev, I. D. 2005, *AJ*, 129, 178
- Karachentsev, I. D., Dolphin, A. E., Geisler, D., et al. 2002a, *A&A*, 383, 125
- Karachentsev, I. D., Grebel, E. K., Sharina, M. E., et al. 2003a, *A&A*, 404, 93
- Karachentsev, I. D., Karachentseva, V. E., Huchtmeier, W. K., & Makarov, D. I. 2004, *AJ*, 127, 2031
- Karachentsev, I. D., Kashibadze, O. G., Makarov, D. I., & Tully, R. B. 2009, *MNRAS*, 393, 1265
- Karachentsev, I. D. & Makarov, D. I. 1999, in *IAU Symposium, Vol. 186, Galaxy Interactions at Low and High Redshift*, ed. J. E. Barnes & D. B. Sanders, 109
- Karachentsev, I. D., Makarov, D. I., Sharina, M. E., et al. 2003b, *A&A*, 398, 479
- Karachentsev, I. D., Sharina, M. E., Dolphin, A. E., et al. 2002b, *A&A*, 385, 21
- Karachentsev, I. D., Sharina, M. E., Dolphin, A. E., et al. 2003c, *A&A*, 398, 467

- Karachentsev, I. D., Tully, R. B., Dolphin, A., et al. 2007, *AJ*, 133, 504
- Karachentseva, V. E. & Karachentsev, I. D. 1998, *A&AS*, 127, 409
- Kerschbaum, F., Nowotny, W., Olofsson, H., & Schwarz, H. E. 2004, *A&A*, 427, 613
- King, I. 1962, *AJ*, 67, 471
- Kirby, E. N., Simon, J. D., Geha, M., Guhathakurta, P., & Frebel, A. 2008, *ApJ*, 685, L43
- Klypin, A., Kravtsov, A. V., Valenzuela, O., & Prada, F. 1999, *ApJ*, 522, 82
- Kniazev, A. Y., Grebel, E. K., Pustilnik, S. A., Pramskij, A. G., & Zucker, D. B. 2005, *AJ*, 130, 1558
- Koch, A. 2009, *Astronomische Nachrichten*, 330, 675
- Koch, A., Grebel, E. K., Gilmore, G. F., et al. 2008a, *AJ*, 135, 1580
- Koch, A., Grebel, E. K., Kleyna, J. T., et al. 2007a, *AJ*, 133, 270
- Koch, A., Grebel, E. K., Wyse, R. F. G., et al. 2006, *AJ*, 131, 895
- Koch, A., McWilliam, A., Grebel, E. K., Zucker, D. B., & Belokurov, V. 2008b, *ApJ*, 688, L13
- Koch, A., Wilkinson, M. I., Kleyna, J. T., et al. 2007b, *ApJ*, 657, 241
- Koenig, C. H. B., Nemec, J. M., Mould, J. R., & Fahlman, G. G. 1993, *AJ*, 106, 1819
- Koleva, M., de Rijcke, S., Prugniel, P., Zeilinger, W. W., & Michielsen, D. 2009, *MNRAS*, 396, 2133
- Koposov, S., Belokurov, V., Evans, N. W., et al. 2008, *ApJ*, 686, 279
- Kormendy, J., Fisher, D. B., Cornell, M. E., & Bender, R. 2009, *ApJS*, 182, 216
- Kotulla, R., Fritze, U., Weilbacher, P., & Anders, P. 2009, *MNRAS*, 396, 462
- Kravtsov, A. V., Gnedin, O. Y., & Klypin, A. A. 2004, *ApJ*, 609, 482
- Krist, J. 1995, in *Astronomical Society of the Pacific Conference Series*, Vol. 77, *Astronomical Data Analysis Software and Systems IV*, ed. R. A. Shaw, H. E. Payne, & J. J. E. Hayes, 349
- Lanfranchi, G. A. & Matteucci, F. 2004, *MNRAS*, 351, 1338
- Lee, H., Grebel, E. K., & Hodge, P. W. 2003, *A&A*, 401, 141
- Lee, H., Zucker, D. B., & Grebel, E. K. 2007, *MNRAS*, 376, 820
- Lee, J. C., Gil de Paz, A., Tremonti, C., et al. 2009, *ApJ*, 706, 599
- Lee, M. G., Freedman, W. L., & Madore, B. F. 1993, *ApJ*, 417, 553
- Lianou, S., Grebel, E. K., & Koch, A. 2010, *ArXiv:1003.0861*

- Mac Low, M. & Ferrara, A. 1999, *ApJ*, 513, 142
- Makarova, L., Karachentsev, I., Rizzi, L., Tully, R. B., & Korotkova, G. 2009, *MNRAS*, 397, 1672
- Makarova, L., Koleva, M., Makarov, D., & Prugniel, P. 2010, *MNRAS*, 406, 1152
- Makarova, L. & Makarov, D. 2008, in *IAU Symposium, Dark Galaxies and Lost Baryons*, Vol. 244, Cambridge University Press, ed. J. Davies & M. Disney, 326
- Makarova, L. N., Karachentsev, I. D., Grebel, E. K., & Barsunova, O. Y. 2002, *A&A*, 384, 72
- Makarova, L. N., Karachentsev, I. D., Grebel, E. K., et al. 2005, *A&A*, 433, 751
- Mancone, C. & Sarajedini, A. 2008, *AJ*, 136, 1913
- Maraston, C. 2005, *MNRAS*, 362, 799
- Marcolini, A., D'Ercole, A., Battaglia, G., & Gibson, B. K. 2008, *MNRAS*, 386, 2173
- Marcolini, A., D'Ercole, A., Brighenti, F., & Recchi, S. 2006, *MNRAS*, 371, 643
- Marconi, G., Tosi, M., Greggio, L., & Focardi, P. 1995, *AJ*, 109, 173
- Marigo, P., Girardi, L., Bressan, A., et al. 2008, *A&A*, 482, 883
- Martin, N. F., McConnachie, A. W., Irwin, M., et al. 2009, *ApJ*, 705, 758
- Martínez-Delgado, D., Gabany, R. J., Crawford, K., et al. 2010, *AJ*, 140, 962
- Mateo, M. L. 1998, *ARAA*, 36, 435
- Matteucci, F. & Brocato, E. 1990, *ApJ*, 365, 539
- Mayer, L., Kazantzidis, S., Mastropietro, C., & Wadsley, J. 2007, *Nature*, 445, 738
- Mazeh, T., Goldberg, D., Duquennoy, A., & Mayor, M. 1992, *ApJ*, 401, 265
- McConnachie, A. W., Arimoto, N., & Irwin, M. 2007, *MNRAS*, 379, 379
- McConnachie, A. W. & Irwin, M. J. 2006, *MNRAS*, 365, 1263
- McConnachie, A. W., Irwin, M. J., Ferguson, A. M. N., et al. 2005, *MNRAS*, 356, 979
- McLaughlin, D. E., Harris, W. E., & Hanes, D. A. 1994, *ApJ*, 422, 486
- McQuinn, K. B. W., Skillman, E. D., Cannon, J. M., et al. 2009, *ApJ*, 695, 561
- Meier, D. L., Jauncey, D. L., Preston, R. A., et al. 1989, *AJ*, 98, 27
- Melbourne, J., Williams, B., Dalcanton, J., et al. 2010, *ApJ*, 712, 469
- Menzies, J., Feast, M., Tanabé, T., Whitelock, P., & Nakada, Y. 2002, *MNRAS*, 335, 923

- Mighell, K. J. & Burke, C. J. 1999, *AJ*, 118, 366
- Mighell, K. J. & Rich, R. M. 1996, *AJ*, 111, 777
- Milgrom, M. 1983a, *ApJ*, 270, 371
- Milgrom, M. 1983b, *ApJ*, 270, 365
- Mirabel, I. F., Laurent, O., Sanders, D. B., et al. 1999, *A&A*, 341, 667
- Monelli, M., Hidalgo, S. L., Stetson, P. B., et al. 2010, *ApJ*, 720, 1225
- Moore, B., Ghigna, S., Governato, F., et al. 1999, *ApJ*, 524, L19
- Mouhcine, M., Ibata, R., & Rejkuba, M. 2010, *ApJ*, 714, L12
- Mould, J. & Kristian, J. 1990, *ApJ*, 354, 438
- Noël, N. E. D., Aparicio, A., Gallart, C., et al. 2009, *ApJ*, 705, 1260
- Norris, J. E., Yong, D., Gilmore, G., & Wyse, R. F. G. 2010, *ApJ*, 711, 350
- Nowotny, W., Kerschbaum, F., Olofsson, H., & Schwarz, H. E. 2003, *A&A*, 403, 93
- Orban, C., Gnedin, O. Y., Weisz, D. R., et al. 2008, *ApJ*, 686, 1030
- Pasetto, S., Grebel, E. K., Berczik, P., Chiosi, C., & Spurzem, R. 2010, *ArXiv:1009.2758*
- Payne-Gaposhkin, C. 1972, in *IAU Colloq. 17: Age des Etoiles*, ed. G. Cayrel de Strobel & A. M. Delplace, 3
- Phillips, M. M., Jenkins, C. R., Dopita, M. A., Sadler, E. M., & Binette, L. 1986, *AJ*, 91, 1062
- Pietrinferni, A., Cassisi, S., Salaris, M., & Castelli, F. 2004, *ApJ*, 612, 168
- Piotto, G. 2009, in *IAU Symposium, Vol. 258, IAU Symposium*, ed. E. E. Mamajek, D. R. Soderblom, & R. F. G. Wyse, 233
- Read, J. I. & Trentham, N. 2005, *Royal Society of London Philosophical Transactions Series A*, 363, 2693
- Recchi, S., Hensler, G., Angeretti, L., & Matteucci, F. 2006, *A&A*, 445, 875
- Recchi, S., Matteucci, F., & D'Ercole, A. 2000, in *Astronomical Society of the Pacific Conference Series, Vol. 215, Cosmic Evolution and Galaxy Formation: Structure, Interactions, and Feedback*, ed. J. Franco, L. Terlevich, O. López-Cruz, & I. Aretxaga, 140
- Rejkuba, M., Da Costa, G. S., Jerjen, H., Zoccali, M., & Binggeli, B. 2006, *A&A*, 448, 983
- Rejkuba, M., Greggio, L., Harris, W. E., Harris, G. L. H., & Peng, E. W. 2005, *ApJ*, 631, 262
- Rejkuba, M., Minniti, D., Silva, D. R., & Bedding, T. R. 2001, *A&A*, 379, 781
- Rejkuba, M., Minniti, D., Silva, D. R., & Bedding, T. R. 2003, *A&A*, 411, 351

- Renzini, A. & Buzzoni, A. 1986, in *Astrophysics and Space Science Library*, Vol. 122, *Spectral Evolution of Galaxies*, ed. C. Chiosi & A. Renzini, 195
- Revaz, Y., Jablonka, P., Sawala, T., et al. 2009, *A&A*, 501, 189
- Richardson, J. C., Ferguson, A. M. N., Mackey, A. D., et al. 2009, *MNRAS*, 396, 1842
- Robin, A. C., Reyl e, C., Derri ere, S., & Picaud, S. 2003, *A&A*, 409, 523
- Sabbi, E., Gallagher, J. S., Tosi, M., et al. 2009, *ApJ*, 703, 721
- Sadakane, K., Arimoto, N., Ikuta, C., et al. 2004, *PASJ*, 56, 1041
- Salaris, M. & Cassisi, S. 2005, *Evolution of Stars and Stellar Populations*, ed. Salaris, M. & Cassisi, S.
- Sanna, N., Bono, G., Stetson, P. B., et al. 2010, *ArXiv:1009.3917*
- Saracco, P., Giallongo, E., Cristiani, S., et al. 2001, *A&A*, 375, 1
- Sarajedini, A., Dotter, A., & Kirkpatrick, A. 2009, *ApJ*, 698, 1872
- Sarajedini, A., Grebel, E. K., Dolphin, A. E., et al. 2002, *ApJ*, 567, 915
- Saviane, I., Held, E. V., & Bertelli, G. 2000, *A&A*, 355, 56
- Scalo, J. M. 1986, *Fundamentals of Cosmic Physics*, 11, 1
- Schlegel, D. J., Finkbeiner, D. P., & Davis, M. 1998, *ApJ*, 500, 525
- Schulte-Ladbeck, R. E., Hopp, U., Crone, M. M., & Greggio, L. 1999, *ApJ*, 525, 709
- Seiden, P. E., Schulman, L. S., & Gerola, H. 1979, *ApJ*, 232, 702
- Sersic, J. L. 1968, *Atlas de galaxias australes*, ed. Sersic, J. L.
- Sharina, M. E., Karachentsev, I. D., Dolphin, A. E., et al. 2008, *MNRAS*, 384, 1544
- Shetrone, M., Venn, K. A., Tolstoy, E., et al. 2003, *AJ*, 125, 684
- Shetrone, M. D., C ot e, P., & Sargent, W. L. W. 2001, *ApJ*, 548, 592
- Sirianni, M., Jee, M. J., Ben itez, N., et al. 2005, *PASP*, 117, 1049
- Skillman, E. D., Terlevich, R., Teuben, P. J., & van Woerden, H. 1988, *A&A*, 198, 33
- Skillman, E. D., Tolstoy, E., Cole, A. A., et al. 2003, *ApJ*, 596, 253
- Smecker-Hane, T. A., Cole, A. A., Gallagher, III, J. S., & Stetson, P. B. 2002, *ApJ*, 566, 239
- Starkenburger, E., Hill, V., Tolstoy, E., et al. 2010, *A&A*, 513, A34
- Stetson, P. B. 1987, *PASP*, 99, 191

- Stetson, P. B. 1994, *PASP*, 106, 250
- Stetson, P. B., Hesser, J. E., & Smecker-Hane, T. A. 1998, *PASP*, 110, 533
- Strigari, L. E., Bullock, J. S., Kaplinghat, M., et al. 2008, *Nature*, 454, 1096
- Tafelmeyer, M., Jablonka, P., Hill, V., et al. 2010, *ArXiv:1008.3721*
- Thomas, D., Bender, R., Hopp, U., Maraston, C., & Greggio, L. 2003, *Ap&SS*, 284, 599
- Tollerud, E. J., Bullock, J. S., Strigari, L. E., & Willman, B. 2008, *ApJ*, 688, 277
- Tolstoy, E., Battaglia, G., Beck, R., et al. 2010, *ArXiv:1009.4103*
- Tolstoy, E., Hill, V., & Tosi, M. 2009, *ARAA*, 47, 371
- Tolstoy, E., Irwin, M. J., Helmi, A., et al. 2004, *ApJ*, 617, L119
- Toomre, A. & Toomre, J. 1972, *ApJ*, 178, 623
- Tosi, M., Focardi, P., Greggio, L., & Marconi, G. 1989, *The Messenger*, 57, 57
- Tosi, M., Greggio, L., Marconi, G., & Focardi, P. 1991, *AJ*, 102, 951
- Trentham, N. & Tully, R. B. 2002, *MNRAS*, 335, 712
- Úbeda, L., Maíz-Apellániz, J., & MacKenty, J. W. 2007, *AJ*, 133, 932
- Valenti, E., Ferraro, F. R., & Origlia, L. 2004, *MNRAS*, 354, 815
- van den Bergh, S. 1999, *A&A Rev.*, 9, 273
- van Dyk, S. D., Puche, D., & Wong, T. 1998, *AJ*, 116, 2341
- VandenBerg, D. A., Bergbusch, P. A., & Dowler, P. D. 2006, *ApJS*, 162, 375
- VandenBerg, D. A., Swenson, F. J., Rogers, F. J., Iglesias, C. A., & Alexander, D. R. 2000, *ApJ*, 532, 430
- Weisz, D. R., Skillman, E. D., Cannon, J. M., et al. 2008, *ApJ*, 689, 160
- Weisz, D. R., Skillman, E. D., Cannon, J. M., et al. 2009a, *ApJ*, 691, L59
- Weisz, D. R., Skillman, E. D., Cannon, J. M., et al. 2009b, *ApJ*, 691, L59
- Whitelock, P. A., Menzies, J. W., Feast, M. W., et al. 2009, *MNRAS*, 394, 795
- Wilkinson, M. I., Kleyana, J. T., Evans, N. W., et al. 2004, *ApJ*, 611, L21
- Willman, B., Dalcanton, J. J., Martinez-Delgado, D., et al. 2005, *ApJ*, 626, L85
- Wolf, J., Martinez, G. D., Bullock, J. S., et al. 2010, *MNRAS*, 406, 1220
- Zinn, R. & West, M. J. 1984, *ApJS*, 55, 45

Zucker, D. B., Belokurov, V., Evans, N. W., et al. 2006a, *ApJ*, 650, L41

Zucker, D. B., Belokurov, V., Evans, N. W., et al. 2006b, *ApJ*, 643, L103

Zucker, D. B., Kniazev, A. Y., Martínez-Delgado, D., et al. 2007, *ApJ*, 659, L21

Acknowledgements

“I can only note that the past is beautiful because one never realises an emotion at the time. It expands later, and thus we don’t have complete emotions about the present, only about the past.”

V. Woolf, *A Sketch of the Past* (1939)

Now that these three years are completed, my feelings about them are hardly contained in a couple of closing pages. This is for the wonderful people that helped me to make it happen in the best way possible.

My gratitude goes first of all to those that made it possible for me to be here. Thanks to my supervisor Eva Grebel, to the International Max Planck Research School for Astronomy and Cosmic Physics and the Graduate School for Fundamental Physics at the University of Heidelberg, and to the Astronomisches Rechen Institut for choosing me and offering me a great support. In particular, thanks to Christian Fendt, who is without any doubt the best Graduate School responsible ever! Thank you Eva for teaching to me with patience, for giving me great freedom while guiding me along this path, but also for always having a smile and a good advice about newts, and for ultimately allowing me to get far more sunny days than what we had agreed on. I am grateful to my Thesis Committee, Thorsten Lisker, you were always there when I needed an advice, and Matthias Bartelmann, thank you for laughing together in front of paper airplanes. I would really like to thank my collaborators, who always stimulated my scientific curiosity and got me a lot of help during these years. Thanks to Andrew Cole, thank you so much for your infinite patience and for everything that I learned from you. Thanks to Andreas Koch, for your scientific comments and even more for the book advice. Hvala to Marina Rejkuba, it is a real pleasure to work and discuss about science with you, *la tua gentilezza è una cosa rara in questo ambiente*. Thanks to Gary Da Costa, for the always extremely fruitful discussions, and to Helmut Jerjen. I also want to thank Jay Gallagher, for his contagious enthusiasm and his kindness. Thanks to Hans-Walter Rix for agreeing to be the referee of my Thesis, and to Andreas Quirrenbach and Karlheinz Meier for being part of my examination Committee. I am deeply grateful also to Paolo Tozzi, who always followed and supported me from Trieste.

A big hug goes to the entire Grebel-Group! You guys are all so great. It always makes me smile to look at you and see so many different colors and habits, but such a unique sense of family that you were able to give me. It has been so good to talk to you about our work, and even better to enjoy our little trips and everyday-life experiences together. Thanks Raoul and Johannes, for being so nice and for your jokes and for your help. Thank you Anna, Sarah and Xiaoying, a simple smile from you always makes me feel better, your energy is contagious. Thank you Matthias, because talking to you just feels so simply good, whether science-related or not. I really appreciate your way of understanding me, and last but not least thank you for your scientific contribution to this work. A big, special thanks to my girls! Gracias Veronica! Although there was little time to be together, I think it has been so natural to get to know you, I love your colors, your pavos, your humor and your cookies. Thank you Sonia, your wisdom has always helped so much, you took care of me when you knew I most needed it, and you can always find a smile from inside to donate, although the weather is gray outside and the mood even worse. Katrin and Katharina, you have been here from the beginning, always ready to help, always nice in front of my continuous complaining, doing for me much more than what I would ask for, thank you for making me laugh and for much, much more. Katharina, thank

you also for the big help with the Thesis! Shoko, I have spent most of my time in the office with you, and I am so glad this went well beyond the science we daily discuss. It has been a continuous surprise to know you, to share papers, little problems among the funny moments, sweets and advice, and feelings. After all, as C. Dickens would say, “there is nothing better than a friend, unless it is a friend with chocolate.” Once more, grazie for the immense help you gave me with the correction of the Thesis! Thanks also to Gernot Burkhardt, for always being willing to help and for an extremely careful reading of the Thesis. Noch ein danke an Prof. Schubart, für immer so nett zu sein.

Vielen vielen Dank zu meinen lieben Freunden von Rudern! Meine Freizeit war mit euch immer toll, ich habe mich so wohl im Klub und an den Wettkämpfen gefühlt. Danke auch an Ariane, Patci und meinen Haus-Männern. So liebevolle Mitbewohnern kann man nicht überall finden, danke für die Lächeln, für auf mich aufzupassen und auch für langweilig zusammen zu sein!

Grazie agli amici di una patria un pochino più lontana dopo questi tre anni, ma pur sempre viva grazie a voi. Grazie Fra per essere un sostegno immancabile e per capire, sempre. Grazie Cesca e Nico per non cambiare mai e per ricordarvi sempre di me. Grazie Sara e Stefy perché nonostante tutto è bello passare una serata con voi come ai vecchi tempi. Grazie Rita per essere come sei, vicine e quasi uguali nelle pieghe di un tortuoso percorso in evoluzione. Grazie Irene per la tua dolcezza e la tua umanità, per le parole giuste e perché ogni volta che ti leggo o penso, sorrido.

Grazie ai miei genitori ed alla mia bambina, per questi ultimi anni ma soprattutto per avermi accompagnata fino a qui. Sono felice che abbiate sempre creduto in me, che mi abbiate insegnato ad essere determinata nei miei obiettivi, grazie per avermi tirata su di morale quando il cielo era grigio qui. Mi dispiace di potervi vedere molto meno di quanto vorrei. Cotta, sei qui con me anche se non posso abbracciarti ogni sera prima di addormentarmi, e sono sempre fiera di te. Hvala Bajo i Duško, od uvijek me pratite i čuvate iz daleka, Pirovac je nikad bijo tako ljep kao u ovim zadnjih godinama.

A huge thanks to all of my IMPRS friends, you have been a wonderful group! How many friday nights, how much laughing, discussing, complaining, you have made this cute german city my second home. An infinite smile goes to the people I have shared most of my little adventures with, especially Nicola, Kelly, Federica, Gisella, Giovanni. With you I have explored and enjoyed everything that hides behind a “scientific” style of life, and I will just miss you so much. Olga, that is particularly true for the cooking and for you always making me laugh, how could I do without you! Baybars, you have been a mirror for me, a root of wise advice, you always understand without judging and smile whatever happens, thank you for letting me laugh, shout, cry. Massimo, it has been eight years now, I think we have grown a lot together. A thank you would not be enough for how much your presence here meant to me, for our long happy and sad conversations, for the almost daily phone calls. You know almost everything about me and you are a fixed point in this long path.. an endless hug to you.

Stefano, I owe you everything I have become in the years here. You have taught me things about myself that I did not know, you have walked along with me, and the most precious presents from you have been your trust and your infinite patience. With you I discovered the meaning of a real smile, that knows how to shine even stronger when everything else around is dark and complicated. Grazie per aver imparato assieme ad essere Noi.